Scattering on compact body spacetimes

Thomas Paul Stratton

A thesis submitted for the degree of Doctor of Philosophy

School of Mathematics and Statistics
University of Sheffield

March 2020

Summary

In this thesis we study the propagation of scalar and gravitational waves on compact body spacetimes. In particular, we consider spacetimes that model neutron stars, black holes, and other speculative exotic compact objects such as black holes with near horizon modifications. We focus on the behaviour of time-independent perturbations, and the scattering of plane waves.

First, we consider scattering by a generic compact body. We recap the scattering theory for scalar and gravitational waves, using a metric perturbation formalism for the latter. We derive the scattering and absorption cross sections using the partial-wave approach, and discuss some approximations. The theory of this chapter is applied to specific examples in the remainder of the thesis.

The next chapter is an investigation of scalar plane wave scattering by a constant density star. We compute the scattering cross section numerically, and discuss a semiclassical, high-frequency analysis, as well as a geometric optics approach. The semiclassical results are compared to the numerics, and used to gain some physical insight into the scattering cross section interference pattern.

We then generalise to stellar models with a polytropic equation of state, and gravitational plane wave scattering. This entails solving the metric perturbation problem for the interior of a star, which we accomplish numerically. We also consider the near field scattering profile for a scalar wave, and the correspondence to ray scattering and the formation of a downstream cusp caustic.

The following chapter concerns the scalar wave absorption spectrum of exotic compact objects, modelled as black holes with a partially reflective surface just above the event horizon. We discuss the systems natural modes of vibration, and derive low and high-frequency approximations for the absorption spectra.

Finally, we apply complex angular momentum (CAM) techniques to the perturbed constant density stellar model. We compute Regge poles (CAM resonance modes) by numerically solving a four-term recurrence relation. The utility of the CAM method is demonstrated by reproducing the scattering cross sections calculated earlier using partial waves.

Acknowledgements

I would like to thank my supervisor Sam Dolan for all of his advice, patience, and encouragement over the last four years. I am immensely grateful for all the wisdom he has shared with me, at work and down the pub.

It has also been a great pleasure to collaborate with Caio Macedo and Luís Crispino, which resulted in the work presented in chapter 5. I thank them for taking me under their wing whilst I visited The Federal University of Pará, and for their collaborative spirit. During this visit I was also deeply touched by the welcome of all the students and staff in the Grav@zon group.

In Sheffield, the friendship and support of all of the members of the Cosmology, Relativity and Gravitation group has been invaluable. In particular, thanks go to my past and present office mates: Tom Morley, Jake Percival, Jake Shipley, David Dempsey, Luiz Leite, Elisa Maggio, Vis Balakumar, Jonny Betts, and Axel Polaczek. Additional thanks go to Mohamed Ould El Hadj, my unofficial second supervisor and collaborator. He taught me a great deal and it was the "icing on the cake" to work together on the material presented in chapter 6.

I acknowledge the financial support of the Engineering and Physical Sciences Research Council, and the European Union's Horizon 2020 research and innovation programme.

Outside of academia, my thanks go to the folks at Snakebite Korfball Club. Most of all, I would like to thank my parents, Andy and Mandy, and my sister Kathryn, for their unwavering support in everything. I could not have done this without you.

Contents

Chapter 1

Introduction

In September 2019, a catalogue of gravitational wave detections was published by the LIGO and Virgo collaborations [1]. Ten of the signals are consistent with the gravitational radiation resulting from a black hole binary merger, as predicted by Einstein's theory of general relativity (GR). Another observation, GW170817, is thought to have originated in the merger of two neutron stars [2]. This event was also observed across the electromagnetic spectrum [3]. These developments constitute the inception of gravitational-wave astronomy, and multi-messenger astronomy.

Gravitational waves (GWs) are ripples in space-time that are passing through us all the time, travelling at the speed of light $c \approx 3 \times 10^8$ m/s. They are so minuscule that (thankfully) we do not experience any day-to day consequences. For example, the strain amplitude of GW170817 when it reached the Earth was of the order of $h \sim 10^{-22}$, meaning the laser interferometers of LIGO detected a change in distance four orders of magnitude smaller than the diameter of an atom.

Einstein predicted GWs as a consequence of his general theory of relativity over a century ago in 1916 [4]. Another prediction of GR that has captured the imagination of many scientists and science-fiction fans is black holes. These are bounded space-time regions that nothing can escape from, not even light, due to their extreme gravitational attraction. The boundary of such a region is known as the event horizon.

A mathematical description of a spherically symmetric, static black hole was discovered by Schwarzschild in 1916 [5]. Other black hole solutions to Einstein's equations were found later that endowed the hole with charge (the Reissner-Nordström solution [6, 7]), or angular momentum (the Kerr black hole [8]), or both (the Kerr-Newman black hole [9]).

Black holes may arise in nature as the end states of collapsing stars. In 1939, Oppenheimer and Snyder described such a process using Einstein's field equations [10]. As a star collapses, the light it emits is increasingly red-shifted, and can escape over a narrower range of angles, due to the increasing curvature at the collapsing surface. To a distant observer the star's surface would become dimmer and never quite seem to reach the horizon. In addition, because of the red shift, the surface will appear to cool down. For this reason, the end-states were referred to as frozen stars.

Supermassive black holes are thought to reside in the centres of almost all galaxies, including our own [11]. Recently, the shadow of a supermassive dark body at the centre of the galaxy M87 has been observed by the Event Horizon Telescope using very-long-baseline-interferometry (VLBI) [12]. The observations are consistent with the object being a Kerr black hole with the mass of 6.5 billion suns.

The other well-motivated astrophysical body with a compactness comparable to a black hole is the neutron star. To get a feeling of the extreme gravitational curvature induced by a neutron star, consider that the escape velocity at their surface is roughly half the speed of light. Like black holes, they are a possible end point of stellar collapse.

Stellar collapse occurs when a star has exhausted all of its nuclear fuel and no longer generates sufficient pressure to balance the gravitational attraction holding it together [13]. As the star contracts, the core becomes more dense, compacting the atoms so closely together that the Pauli exclusion principle gives rise to an electron degeneracy pressure great enough to balance the gravitational force. At this stage there are two possible outcomes: (1) the core remains in equilibrium as the outer layers of the star are lost into the cosmos via the stellar wind, leaving behind a white dwarf, this happens if the initial star has a mass less than roughly 10 solar masses; (2) the degenerate core grows above the Chandrasekhar mass limit [14], $M_{\mathrm{C}} \approx 1.4$ solar masses [13], and undergoes a further collapse. In the latter case, it becomes energetically favourable for protons and electrons to combine and form neutrons and neutrinos. The core collapse may then be halted by neutron degeneracy pressure. Part of the immense gravitational energy released during the core collapse causes the outer layers to be blown off into space in a supernova explosion [13], leaving behind the newly-born neutron star. Depending on the initial star's properties, even the neutron degeneracy pressure of the core may be unable to halt collapse, resulting in a black hole [15].

There is still much to be learnt about neutron stars and black holes, including the details of their formation as stellar remnants briefly summarised above (see e.g. reference [13] for more details). Neutron stars are natural laboratories for understanding the nature of matter at the highest imaginable densities, and the equation of state for neutron star matter is a fertile research area [13]. Black holes in GR possess un-physical curvature singularities, where it is assumed classical physics breaks down and a theory successfully combining quantum mechanics and GR is needed. They are therefore a natural testing ground for postulated theories of quantum gravity.

One theory of quantum gravity, string theory, has provided motivation for black hole models with a partially reflecting surface just outside the horizon [16–18]. Another possibility is that black holes are not (all) the canonical Kerr black holes of GR, but some other object that mimics their behaviour such as boson stars composed of dark matter [19]. Together, these compact bodies are sometimes called exotic compact objects [20].

In this thesis, we consider the interaction of fundamental fields with neutron stars, black holes, and exotic compact objects. We use the framework of perturbation theory, whereby any back reaction of the fields on the metric is considered negligible. In particular, we focus on scattering and absorption of a massless scalar field, and of GWs. Scalar waves serve as a useful proxy for more well motivated yet technically challenging fields (e.g. electromagnetic and GW). They capture the key features of scattering studies, and are a natural place to begin a systematic study [21].

1.1 Scattering

One of the earliest studies of scattering by black holes using perturbation techniques was by Vishveshwara, who simulated GWs scattering from a Schwarzschild black hole [22]. He considered an initial disturbance composed of a Guassian wavepacket and computed the subsequent outgoing radiation. The result was that the scattered GW contained characteristic frequencies of the black hole that were excited by the initial pulse (see figure 1.1). Such characteristic oscillations and their frequencies are referred to as quasinormal modes (QNMs) and quasinormal frequencies (QNFs) respectively [23].

QNM ringing is independent of the type of initial perturbation, it could be caused by an infalling particle, or a newly formed black hole 'ringing down'. The QNFs are determined entirely by the black hole's two parameters mass M and angular momentum J. By measuring at least two modes it is possible to infer M and J, and characterise the black hole. This program of study is termed black-hole spectroscopy [24]. Analysing the GW data from the binary black hole merger event GW150914, Isi *et al* have recently proposed that the ringdown part of the signal is well described by a superposition of two QNMs [25]. In chapter 5 we will discuss an exotic compact object that can 'mimic' part of the ringdown of a black hole [26, 27].

Stellar matter oscillation modes have a long history, and are well modelled using Newtonian gravity [28]. However, for neutron stars relativistic effects should not be ignored [29, 30]. In the relativistic model, stellar modes lose energy in the form of GWs, and thus decay over time. All the types of mode familiar from Newtonian treatments have corresponding quasinormal modes in the relativistic picture [31].

The study of QNMs in GR is a key part of understanding wave propagation on curved spacetimes, and thus understanding the physics of compact objects. The review by Kokkotas and Schmidt [32] provides a thorough discussion on QNMs of black holes and neutron stars.

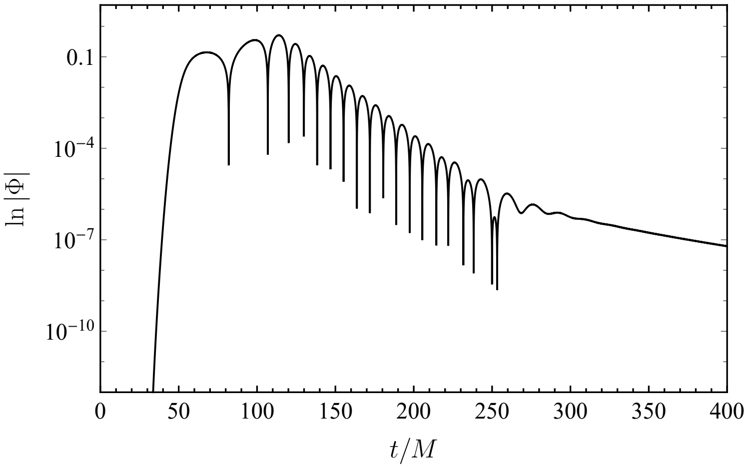

Figure 1.1: The response of a Schwarzschild black hole of mass M to an axial gravitational wave Gaussian pulse. The initial pulse has unit amplitude, is centred at the radial (tortoise) coordinate $r_* \approx 30M$ (see equation (2.7)), and has the form $\exp[-(r_* - 30M)/(18M)]$. The plot shows the time evolution of the axial gravitational wave angular mode $\Phi(r_*, t)$ with $l = 2$, for an observer at $r_* \approx 80M$. We use geometric units setting $G = c = 1$.

In this thesis, we are also focused on understanding the theory of wave propagation on curved spacetimes. In doing so we concentrate on *time-independent* perturbations. In particular we are interested in plane wave scattering and absorption. This is a typical thought experiment in many areas of theoretical physics. From quantum mechanics, to surface water waves, to classical electromagnetism and the theory of the rainbow, time-independent scattering theory is ubiquitous. As a consequence, the theory developed in one area can often be translated to another. This ubiquity will be a continuing thread of this thesis. In chapter 3 we will make us of semiclassical scattering techniques from quantum mechanics [33] to understand plane wave scattering by a neutron star, and draw an analogy with the atmospheric rainbow. Later, we will turn to the complex angular momentum picture of scattering, initially developed to understand propagation of radio waves around the Earth [34].

The scattering and absorption of plane waves by black holes has received considerable attention over the years. Much of this work is presented in a monograph by Futterman, Handler and Matzner [21], drawing on earlier studies

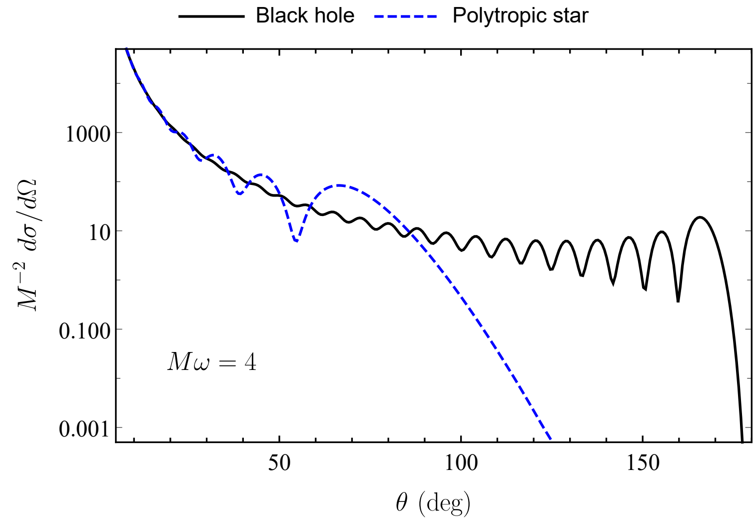

Figure 1.2: The scattering cross sections for a plane gravitational-wave with circular frequency ω incident on compact bodies with mass M, where $M\omega = 4$. The black solid line is for a Schwarzschild black hole, and the blue dashed line is for a polytropic star with a tenuity $R/M = 6$ comparable to a neutron star, where R is the star's radius. Calculations are done using the `Mathematica` programming package [66].

[35–45]. More recent work includes [46–61]. Scattering by neutron stars and exotic compact bodies has received comparatively less attention in the time-independent context. This is the main focus of this thesis, much of which appears in references [62–65].

The scattering cross sections of compact bodies can exhibit significant structure. For example, the cross section for a massless plane wave scattering from a black hole may display a characteristic maximum in the backwards direction, known as a glory [37]. At lower angles regular oscillations are seen, with an angular width controlled by the ratio of the incident waves wavelength and the black hole's radius. This can be understood in a high frequency approximation as components of the wave (which may be modelled as a congruence of rays) 'orbiting' about the black hole, and interfering in the far field.

In chapters 3 and 4 we will see that the cross section of a massless wave scattered by a neutron star should display an interference pattern known as rainbow scattering (see figure 1.2 for a preview). Similar effects have been observed in nuclear scattering [67]. In chapter 5 we will discuss the absorption properties of modified black holes, and see that they display characteristic absorption lines similar to those seen in atomic spectroscopy. The absorption lines are found at the quasinormal frequencies of the body. These phenomena are all 'fingerprints' of compact objects, that in principle could inform us of their properties and shed light on gravitational and nuclear physics.

Following the footsteps of time independent scattering theory in other physical regimes (see e.g. [68]), we study a type of 'resonance' conceptually different to QNMs. These are modes with real frequency and complex angular momentum (CAM). They are referred to as Regge-poles, after Tulio Regge who applied CAM to the Schrödinger wave equation [69] familiar from quantum mechanics. Andersson and Thylwe have shown that the Regge poles of a Schwarzschild black hole can be interpreted as 'surface waves' [46, 47], that propagate close to the unstable photon orbit at $r = 3M$ [70]. Décanini *et al.* have cemented the surface wave interpretation and provided a link between the dual concepts of Schwarzschild Regge poles and QNMs [71]. We will discuss CAM Regge pole modes in more detail in chapter 6, and apply the theory to a simple neutron star model.

In principle, scattering scenarios can distinguish between different types of compact bodies, in both transient and effectively time independent processes. Transient or direct scattering modelled with a time dependent framework is certainly the more promising (and proven) in terms of learning new physics [1, 24, 25, 72], and it is unlikely that long lasting scattering giving rise to diffraction phenomena (figure 1.2) could be observed any time soon. However, the time-independent picture should still be studied for the following reasons:
(1) In order to gain a complete understanding of wave propagation on curved spacetime. For example the complex angular momentum picture has allowed a deeper comprehension of the resonant behaviour of black holes.
(2) It is of fundamental interest to consider. Since scattering theory is so ubiquitous, ideas developed in this context could well find employment in other areas of physics [73, 74].

(3) Future GW detectors [75] will be able to detect long lasting practically monochromatic GW sources (i.e. compact object binaries during their inspiral [76]) for periods of up to a month, opening up the possibility of detecting GW diffraction phenomena [77].

Einstein thought there was ‘no hope’ of observing the gravitational lensing of light [78], and yet now it is a ‘booming part of astrophysics’ [79]. Powerful telescopes have enabled people to determine the chemical constituents of distant exoplanets by observing absorption lines [80], a fundamentally wave-like phenomena. If the past is anything to go by, gravitational scattering of waves by compact bodies could yet prove to be relevant to GW astronomy, and our knowledge of fundamental physics.

1.2 Thesis outline

In chapter 2 we present the theory of scalar and gravitational perturbations on a general spherically symmetric spacetime (with a Schwarzschild exterior region). We will then discuss plane wave scattering of these perturbations, much of which is presented in the monograph ‘*Scattering from black holes*’ by Futterman, Handler, and Matzner [21] (hereafter referred to as FHM). In doing so we recall how to overcome the difficulties associated with defining a plane wave on a background with a long range effective potential, the issue of convergence of the partial wave sum defining the scattering amplitude, and a gauge invariant definition of gravitational wave energy [81–83]. In an extension of FHM, we discuss how to deal with all compact bodies (limited to the non-rotating case). This is a fairly modest generalistation, since the exterior vacuum region of all spherically symmetric spacetimes is described by the Schwarzschild metric, a result known as Birkhoff’s theorem [84, 85]. Therefore all the results relevant to setting up the scattering problem in the far field carry over from the black hole case. To analyse GW scattering, we use the metric perturbation formalism initiated by Regge and Wheeler [69], and presented in a modern form by Martel and Poisson [86, 87] (a selection of key works in the intervening period include [82, 83, 88–90]).

The theory reviewed in chapter 2 is applied to the case of scalar waves scattered by a constant density compact body with radius R and mass M in chapter 3. We investigate tenuities R/M that model a neutron star ($R/M \approx 6$) and tenuities $R/M < 3$ corresponding to ultra compact objects (UCOs) [20] endowed with an unstable closed light ring in their exterior. A semiclassical analysis is used in the high frequency limit, following methods developed by Ford and Wheeler for studying quantum scattering in the classical limit [33] (hence 'semiclassical', even though our work considers purely classical fields to begin with). This provides a link between the scattering of rays and high frequency waves and enables physical interpretation.

In chapter 4 we consider GWs scattering from a star with a polytropic equation of state. The stellar background is constructed by numerically solving the Tolman-Oppenheimer-Volkof equations [10, 91]. To study the perturbations of the interior we build on the formalism of Allen *et al.* [92] and Kojima [93]. For earlier works on stellar perturbations see [29, 30, 94–102]. We apply a numerical method to determine the scattering cross sections, and compare with our results from chapter 3 and black hole scattering (e.g. [35]). We discuss the astrophysical implications of chapters 3 and 4 in the concluding remarks.

Chapter 5 is an investigation of the absorption properties of hyopthetical exotic compact objects. We present a simple parametrised model for such objects that include near-horizon modifications to black holes. A low frequency limit for the absorption cross section, σ_{abs}, is derived by generalising the method of Unruh [103]. We then make numerical calculations of σ_{abs} at moderate frequencies. It is shown that σ_{abs} exhibits strong spectral lines at the characteristic frequencies of the ECO, and that the lines are well approximated by a Breit-Wigner formula [104]. In addition we consider a modified Nariai spacetime model that shares the qualitative features of the ECO. The wave equation on this 'Nariai-ECO' spacetime can be solved exactly [105] and thus allows analytic approximations describing the spectral lines.

The application of CAM theory to perturbations of the compact bodies introduced in chapter 3 is considered in chapter 6. We investigate the scalar field Regge-pole spectrum of two models with $R/M = 6$ and $R/M = 2.26$. Using a combination of numerical methods, a WKB approximation, and by appealing to analogous scattering scenarios in e.g. [68], we provide some interpretation of the Regge-pole spectra. To finish the chapter we demonstrate the utility of the CAM method by reproducing scattering cross sections calculated previously in chapter 3.

Chapter 2

Scattering by compact objects

Time-independent scattering of waves by a black hole has been the subject of numerous studies. In the 1960s Hildreth [106] and Matzner [39] both considered the scattering of scalar waves by a Schwarzschild black hole, concentrating on the low frequency limit s-wave ($l = 0$). Mashhoon considered electromagnetic waves scattering from black holes, noting that for spinning black holes an initially unpolarized plane wave would be expected to polarize when scattered [42]. Significant progress was made by Sanchez [37] who performed the numerical computations necessary to obtain scattering cross sections for a range of energies.

The monograph '*Scattering from black holes*' by Futterman Handler and Matzner (FHM), first published in 1988, gives a unified treatment of massless fields with spin $s \in \{0, 1/2, 1, 2\}$ [21]. FHM treat the fields as perturbations of the Kerr metric and make use of the Newman-Penrose formalism [107]. More recent black hole scattering studies include: an extension to massive fermionic fields by Dolan *et al.* [108]; highly accurate calcuations on rotating black hole backgrounds, overcoming numerical difficulties associated with high frequency incident waves [48, 50, 55, 109]; and the application of complex angular momentum methods [46, 57, 58].

Whilst most scattering studies focus on black holes, there has been some investigation of scattering by other compact bodies such as neutron stars [98], and many studies of pulsating stars and the resulting gravitational wave emission using perturbative techniques [29, 92, 97, 98, 110].

In this chapter we outline scattering theory for scalar and gravitational plane waves on general spherically symmetric backgrounds. We concentrate on the asymptotics that define the scattering problem, and defer detailed discussion of model dependent boundary conditions and interior perturbations to later chapters. The exterior vacuum for all spherically symmetric gravitating bodies is described by the Schwarzschild solution [111], and hence much of the work on the scattering asymptotics that has been done for black holes is applicable here also. However, for GWs we have developed the scattering theory in terms of metric perturbations, as opposed to Riemann tensor perturbations which has been the formalism of choice for previous studies (e.g. references [21, 50]).

Later the formalism presented here will be used to consider scattering by compact bodies including models of neutron stars (chapters 3 and 4), absorption by Schwarschild black holes with near horizon modifications (chapter 5), and the complex angular momentum approach to relativistic scattering (chapter 6).

2.1 Spherically symmetric spacetime metric

A static spherically-symmetric spacetime in Schwarzschild coordinates $\{t, r, \theta, \phi\}$, is described by the line element

$$ds^2 = g_{\mu\nu} dx^\mu dx^\nu = g_{ab} dx^a dx^b + r^2 \Omega_{AB} dx^A dx^B. \tag{2.1}$$

Lower case Latin indices run over $\{t, r\}$, upper case Latin indices run over $\{\theta, \phi\}$, and Greek indices run over all coordinates. We have

$$g_{ab} dx^a dx^b = -A(r)\, dt^2 + B^{-1}(r)\, dr^2, \qquad \Omega_{AB} dx^A dx^B = d\theta^2 + \sin^2\theta\, d\phi^2. \tag{2.2}$$

Latin indices are lowered with g_{ab} and Ω_{AB}, and raised with the corresponding inverse metrics. Greek indices are lowered and raised with $g_{\mu\nu}$ and its inverse $g^{\mu\nu}$.

This space-time is an example of a “warped product” of two pseudo-Riemannian manifolds [112]: the radial-temporal plane $\mathcal{M}_2$ with metric g_{ab}, spanned by the coordinates x^a; and the two-sphere S_2 with metric Ω_{AB}, spanned by the coordinates x^A. In this language, the 4D spherically symmetric space-time is described by $\mathcal{M}_4 = \mathcal{M}_2 \times {}_w S_2$, with metric $g_{\mu\nu}$. The radial-temporal plane is known as the “base space” of $\mathcal{M}_4$, and the surfaces of spherical symmetry are the “fibres”. Each fibre is a direct product of a point $p \in \mathcal{M}_2$ and S_2. The “warping function” in this case is $w = r^2$, so named because it warps the product metric $g_{\mu\nu}$ on each fibre $p \times S_2$.

2.2 Scalar field perturbations

A scalar field Φ, on a background $g_{\mu\nu}$, is governed by the Klein-Gordon equation

$$\Box\Phi \equiv \frac{1}{\sqrt{-g}}\partial_\mu\left(\sqrt{-g}g^{\mu\nu}\partial_\nu\Phi\right) = -\mu^2\Phi, \tag{2.3}$$

where g is the metric determinant, μ is the rest mass of the scalar field, and $\Box$ is the Laplace-Beltrami operator. The general solution to equation (2.3) for a spherically symmetric background can be found using a separation of variables,

$$\Phi = \int_{-\infty}^{\infty} e^{-i\omega t}\sum_{l=0}^{\infty}\sum_{m=-l}^{m=l}\frac{u_{lm\omega}(r)}{r}Y_{lm}(\theta,\phi)\,d\omega, \tag{2.4}$$

where Y_{lm} are the spherical harmonics (appendix A). The radial functions $u_{lm\omega}(r)$ are solutions of the wave equation

$$\sqrt{AB}\frac{d}{dr}\left[\sqrt{AB}\frac{du_l}{dr}\right] + \left(\omega^2 - V_l^{\text{eff}}(r)\right)u_l = 0, \tag{2.5}$$

where we have dropped the subscripts (m,ω) for clarity and V_l^{eff} is an effective potential

$$V_l^{\text{eff}}(r) = A\left(\frac{l(l+1)}{r^2} + \frac{B}{2r}\left(\frac{A'}{A} + \frac{B'}{B}\right)\right). \tag{2.6}$$

The wave equation is simplified by introducing a 'tortoise' coordinate, r_*, defined by

$$\frac{dr}{dr_*} = \sqrt{AB}, \tag{2.7}$$

so that

$$\frac{d^2 u_l}{dr_*^2} + \left(\omega^2 - V_l^{\text{eff}}(r)\right) u_l = 0. \tag{2.8}$$

By Birkhoff's theorem, for the exterior ($r > R$) of all spherically symmetric solutions to Einstein's field equations (EFE) we have that

$$A(r) = B(r) = 1 - \frac{2M}{r}. \tag{2.9}$$

Then, $V_l^{\text{eff}}(r) \to 0$ as $r \to \infty$. The general solution has asymptotic behaviour in the far field

$$u_l(r) \sim C_l^+ e^{i\omega r_*} + C_l^- e^{-i\omega r_*}, \tag{2.10}$$

where C_l^- and C_l^+ are the ingoing and outgoing coefficients of the mode.

2.2.1 Comparison to Coulomb scattering

In this section we outline some similarities between the quantum mechanics treatment of Rutherford scattering and the gravitational scattering of scalar waves. Rutherford scattering is the elastic scattering of charged particles due to the Coulomb (electrostatic) force. It is also referred to as Coulomb scattering.

Let us define the function $\bar{u}_l \equiv (AB)^{1/4} u_l$, where u_l obeys equation (2.5). Then $\bar{u}_l$ satisfies

$$\frac{d^2 \bar{u}_l}{dr^2} + \left[\omega^2 + \frac{4\omega^2 M}{r} - \frac{l(l+1)}{r^2} - U(r)\right] \bar{u}_l = 0. \tag{2.11}$$

where

$$U(r) \equiv -\frac{12\omega^2 M^2}{r^2} + H(R-r)V_{\text{int}}(r) + O(r^{-3}). \tag{2.12}$$

Here we have used the Heaviside step-function $H(\cdot)$, and defined a 'short-range' interior potential $V_{\text{int}}(r)$ which is only effective for $r < R$ (the form of V_{int} does not matter for our purposes). The long range nature of the gravitational field is manifest in the $1/r$ attractive coupling between the 'energy density' $4\omega^2$ and the body's mass M. Equation (2.11) facilitates a comparison to Coulombic scattering of two nuclei with atomic numbers Z_1 and Z_2. The Sommerfeld parameter η is defined by

$$\eta \equiv \frac{\alpha Z_1 Z_2}{\nu / c}, \tag{2.13}$$

where α is the fine structure constant and ν is the speed of the incident nucleus (in the target nucleus rest frame). Equation (1.1) of reference [113] for modified Coulomb scattering is equivalent to equation (2.11) if we replace the Sommerfeld parameter according to

$$\eta \to -2M\omega. \tag{2.14}$$

Thus the exact solution for $\bar{u}_l$ is directly comparable to *modified* Coulomb scattering with the modifying short range potential $U(r)$ of equation (2.12).

Matzner went a step further with his comparison of scalar wave scattering by a Schwarzschild black hole to Coulombic scattering [39]. His argument extends to general spherically symmetric solutions with a finite interior region, and we paraphrase it here. We expect $|\bar{u}_l|$ to be negligible for $r < r_0$ where the turning point $r_0 \sim \sqrt{l(l+1)}/\omega$ when l is large. That is to say, for a given ω, if l is large enough then we can consider solutions of the 'comparison Coulomb problem'

$$\frac{d^2\bar{u}}{dr^2} + \left[\omega^2 + \frac{4\omega^2 M}{r} - \frac{l(l+1)}{r^2}\right]\bar{u} = 0 \tag{2.15}$$

to be good approximations to the true solution (see section C of Matzner [39]). This is also referred to as 'Newtonian scattering' [48]. In essence, partial waves with large l incident from the far field will not penetrate the region where the short range potential $U(r)$ becomes significant.

2.2.2 Boundary conditions

The boundary conditions imposed on the scalar field depend on the compact body being considered. In the case of a Scharzschild black hole, the physically motivated boundary condition is that the mode must be purely ingoing at the event horizon. This boundary condition is part of the reason that 'mathematical' black holes are surprisingly simple models. The modes that satisfy this causal condition are known as IN modes, and satisfy

$$u_l^{\mathrm{in}}(r) \sim \begin{cases} e^{-i\omega r_*}, & r_* \to -\infty \\ A_l^+ e^{i\omega r_*} + A_l^- e^{-i\omega r_*}, & r_* \to \infty \end{cases}. \tag{2.16}$$

Another set of solutions are the OUT modes, corresponding to purely outgoing radiation at the horizon. These are the time-reversal of IN modes, which for real frequencies and in Schwarzschild coordinates corresponds to complex conjugation. Another set of two solutions are the UP and DOWN modes. The UP mode satisfies

$$u_l^{\mathrm{up}}(r) \sim \begin{cases} B_l^+ e^{i\omega r_*} + B_l^- e^{-i\omega r_*}, & r_* \to -\infty \\ e^{i\omega r_*}, & r_* \to \infty \end{cases}, \tag{2.17}$$

where B_l^+ and B_l^- are constants. The DOWN mode is the time reversal of the UP mode.

Rescaling the IN and OUT modes gives standard one dimensional scattering solutions, corresponding to an initial unit amplitude wave travelling to the left (towards the black hole) and right (towards infinity) respectively. Transmission and reflection coefficients, $\mathcal{T}_{\mathrm{in/up}}$ and $\mathcal{R}_{\mathrm{in/up}}$, are encapsulated in the $\mathcal{S}$-matrix [90],

$$\mathcal{S} \equiv \begin{pmatrix} \mathcal{T}_{\mathrm{in}} & \mathcal{R}_{\mathrm{up}} \\ \mathcal{R}_{\mathrm{in}} & \mathcal{T}_{\mathrm{up}} \end{pmatrix} = \begin{pmatrix} \dfrac{1}{A_l^-} & \dfrac{B_l^-}{B_l^+} \\ \dfrac{A_l^+}{A_l^-} & \dfrac{1}{B_l^+} \end{pmatrix}. \tag{2.18}$$

By considering Wronskian relations between the black hole IN and UP modes one may derive the following relations between the mode coefficients:

$$A_l^- = B_l^+, \tag{2.19a}$$

$$A_l^+ = -\bar{B}_l^-, \tag{2.19b}$$

where an overbar denotes complex conjugation. The fact that the Wronskian of the IN and UP modes with their respective complex conjugate solutions is constant yields the conservation laws (assuming ω and l are real)

$$|A_l^-|^2 - |A_l^+|^2 = 1, \tag{2.20a}$$

$$|B_l^+|^2 - |B_l^-|^2 = 1. \tag{2.20b}$$

It can also be instructive to consider objects with ingoing and outgoing radiation at the surface (corresponding to a linear combination of UP/DOWN or IN/OUT modes in the exterior). This encompasses a variety of stellar models, as well as more speculative objects such as black holes with near horizon modifications motivated by quantum gravity [16, 17], gravastars [114], and boson stars [115] (note that we are referring to non-rotating models, with an exterior that is described by the Schwarzschild solution. There is no generalisation of Birkhoff's theorem to a rotating vacuum solution). Rather than considering each object separately, a simple first step is to impose a generic boundary condition near the surface, $r = R$ ($r_* = R_*$). This condition is parametrised by a 'reflectivity' coefficient $\mathcal{K}_l \in \mathbb{C}$,

$$u_l(r) \sim \begin{cases} e^{-i\omega r_*} + \left(\mathcal{K}_l e^{-2i\omega R_*}\right) e^{i\omega r_*}, & r_* \to R_*^+ \\ C_l^+ e^{i\omega r_*} + C_l^- e^{-i\omega r_*}, & r_* \to \infty \end{cases}. \tag{2.21}$$

The Wronskian of this solution with its complex conjugate is constant which yields

$$|C_l^-|^2 - |C_l^+|^2 = 1 - |\mathcal{K}_l|^2. \tag{2.22}$$

This model allows us to capture generic features of such models, whilst not being concerned with the details of the interior. A black hole model with physical boundary conditions (equation (2.16)) is recovered by setting $\mathcal{K}_l = 0$ and $R = 2M$ ($R_* = -\infty$).

If we wish to probe the interior of the object we must solve the wave equation in this region, subject to suitable boundary conditions. A simple example is a polytropic fluid sphere. In this case, the method of Frobenius may be used to find two independent solutions to equation (2.5) near $r = 0$. These are

$$u_l^1(r) \sim r^{l+1}, \qquad u_l^2(r) \sim r^{-l}. \tag{2.23}$$

When $l > 0$ we select the regular solution u_l^1. Numerically integrating this solution out to $r > R$, with suitable care taken at the surface $r = R$, transmutes the regularity boundary condition into a specific choice of $\mathcal{K}_l$.

A similar generic boundary condition can be applied to other perturbations on spherically symmetric spacetimes. For example, gravitational perturbation modes for a gravastar were studied by Pani *et al.* [116]. Inside the gravastar, they found an analytic solution for the odd parity sector, and matched to the corresponding exterior functions using junction conditions. They showed that the mode structure was completely different to that of a black hole. To conclude, the specific boundary conditions formally encode vital information about the object, but the formalism and methods for the exterior do not need to be adapted for every case. This is the power of Birkhoff's theorem. We shall explore some specific objects in later chapters and discuss the physical interpretations.

2.2.3 Probability current

From the Klein Gordon equation (equation (2.3)), it follows that

$$\Phi^* \Box \Phi - \Phi \Box \Phi^* = 0, \tag{2.24}$$

for real frequencies ω. Rearranging this using definition 2.3 yields the conservation law

$$J^{\mu}{}_{;\mu} = 0, \tag{2.25}$$

$$J_\mu = \frac{1}{2i}\left(\Phi^* \partial_\mu \Phi - \Phi \partial_\mu \Phi^*\right), \tag{2.26}$$

where we have defined the four vector J^μ which may be interpreted as the conserved four-current of the scalar field. The number density of the field is given by the time component J^t, and current densities by J^i where i runs over spatial indices.

2.2.4 Scalar plane waves

A massless scalar plane wave of frequency ω, propagating in the $\hat{\mathbf{n}}$ direction, with unit amplitude, can be decomposed into spherical harmonics

$$\Phi_{\text{plane}}(\hat{\mathbf{n}}, t) = e^{i\omega(\hat{\mathbf{n}}\cdot\mathbf{r}-t)} = 4\pi \sum_{l=0}^{\infty} \sum_{m=-l}^{l} i^l j_l(\omega r) Y_{lm}(\theta, \phi) \bar{Y}_{lm}(\hat{\mathbf{n}}) e^{-i\omega t}, \qquad (2.27)$$

where j_l is the spherical Bessel function [117]. The spherical harmonics can be expressed in terms of associated Legendre polynomials P_l^m [117],

$$Y_{lm}(\theta, \phi) = c_{lm} P_l^m(\cos\theta) e^{im\phi}, \qquad (2.28)$$

$$c_{lm} \equiv (-1)^m \left(\frac{2l+1}{4\pi} \frac{(l-m)!}{(l+m)!} \right)^{1/2}, \qquad (2.29)$$

where

$$P_l^m(\cos\theta) = (-1)^m (1-\cos^2\theta)^{m/2} \frac{d^m}{d(\cos\theta)^m} \left[P_l(\cos\theta) \right]. \qquad (2.30)$$

Along the z axis, $\theta = 0$, and by equation (2.30), $P_l^m(\cos 0) = \delta_{m0}$. Thus

$$\Phi_{\text{plane}}(\hat{\mathbf{z}}, t) = e^{i\omega(z-t)} = \sum_{l=0}^{\infty} i^l j_l(\omega r)(2l+1) P_l(\cos\theta) e^{-i\omega t}. \qquad (2.31)$$

There is a subtlety to defining plane waves (and thus a scattering problem) on curved space. Namely, the plane wave (equation (2.31)) cannot be asymptotically matched to a solution on Schwarzschild (equation (2.10)). A practical solution is to make the replacement $r \to r_*$ in equation (2.31), and instead define a 'distorted' plane wave:

$$\Phi_{\text{dist}}(\hat{\mathbf{z}}, t) = \sum_{l=0}^{\infty} i^l j_l(\omega r_*)(2l+1) P_l(\cos\theta) e^{-i\omega t}, \qquad (2.32)$$

which does satisfy the Klein-Gordon equation in the far field. This can be seen by considering the asymptotic form of the spherical Bessel functions [117],

$$j_l(\omega r_*) \sim \frac{1}{\omega r_*} \sin\left(\omega r_* - \frac{l\pi}{2}\right), \quad \omega r_* \to \infty, \tag{2.33}$$

which implies

$$\Phi_{\text{dist}}(\hat{\mathbf{z}}, t) \sim \frac{\pi}{2i\omega} \sum_{l=0}^{\infty} \sum_{m=-l}^{l} \frac{1}{r} \left(e^{i\omega r_*} + (-1)^{l+1} e^{-i\omega r_*}\right) Y_{lm}(\theta, \phi) \bar{Y}_{lm}(\hat{\mathbf{z}}) e^{-i\omega t}, \tag{2.34}$$

as $r_* \to \infty$.

The prescription of replacing the radial coordinate with a tortoise coordinate is standard for defining distorted plane waves on black hole spacetimes [21]. In vacuum

$$r_* = r + 2M \log\left(\frac{r}{2M} - 1\right). \tag{2.35}$$

The presence of a logarithmic term that ‘distorts’ a plane wave is also standard in quantum mechanical scattering by a Coulomb potential [118]. In fact, it is necessary for scattering governed by a Schrödinger-type equation with any potential that decays as $1/r$ as $r \to \infty$. Potentials that satisfy this, such as the gravitational and Coulomb potentials are referred to as ‘long-ranged’.

2.2.5 Scattering cross section

We wish to analyse the component of the field corresponding to the purely outgoing scattered radiation in the far field ($r_* \to \infty$),

$$\Phi_{scat} \sim \frac{\hat{f}(\theta)}{r} e^{i\omega(r_* - t)}, \tag{2.36}$$

which (by symmetry) has no ϕ dependence. Here, $\hat{f}(\theta)$ is the scattering amplitude.

The number density of the scalar field is given by the time component of the conserved current, J^t, (as seen by a stationary observer). The scattering cross section is the intensity of the scalar flux scattered to infinity per unit solid angle, and is defined as

$$\frac{d\sigma}{d\Omega} = \lim_{r\to\infty}\left[r^2\frac{J^t_{scat}}{J^t_{dist}}\right]. \tag{2.37}$$

By equation (2.26), the cross section is

$$\frac{d\sigma}{d\Omega} = |\hat{f}(\theta)|^2. \tag{2.38}$$

Matching the plane wave and scattered radiation to a general solution in the far field, equation (2.10), yields an expression for the scattering amplitude in terms of the mode coefficients C_l^- and C_l^+,

$$\hat{f}(\theta) = \frac{1}{2i\omega}\sum_{l=0}^{\infty}(2l+1)\left(e^{2i\delta_l}-1\right)P_l(\cos\theta), \tag{2.39}$$

where the phase shifts δ_l are defined by

$$e^{2i\delta_l} = S_l = (-1)^{l+1}\frac{C_l^+}{C_l^-}. \tag{2.40}$$

Equation (2.40) also defines the scattering matrix-element S_l.

Approximations

Phase shifts for scattering by a Coulomb potential are known in analytic form [118]. Making the appropriate changes for the comparison Newtonian/Coulomb problem of section 2.2.1, one then obtains the Newtonian scattering amplitude [21, 48]

$$\hat{f}_{\rm N}(\theta) = M\frac{\Gamma(1-2i\omega M)}{\Gamma(1+2i\omega M)}\left(\sin\frac{\theta}{2}\right)^{-2+4i\omega M}, \tag{2.41}$$

and phase shifts

$$e^{2i\delta_l^{\rm N}} = \frac{\Gamma(l+1-2i\omega M)}{\Gamma(l+1+2i\omega M)}. \tag{2.42}$$

The Newtonian scattering cross section is [21, 48]

$$\frac{d\sigma}{d\Omega}_{\mathrm{N}} = \frac{M^2}{\sin^4(\theta/2)}. \tag{2.43}$$

This can be compared with the geodesic weak field scattering cross section found using the Einstein deflection angle [21]

$$\frac{d\sigma}{d\Omega}_{\mathrm{Ein}} = \frac{M^2}{(\theta/2)^4}. \tag{2.44}$$

For a discussion of geodesic scattering see section 3.2. Other approximations based on semiclassical methods will be discussed in chapter 3.

2.2.6 Absorption cross section

The number of particles absorbed by a symmetric body per unit time is given by

$$\frac{dN}{dt} = -\int_S \sqrt{-g} J^r dS, \tag{2.45}$$

where S is a sphere of radius r enclosing the body. By the conservation law equation (2.25) the flux through a closed sphere at the objects radius is equal to the flux through a closed sphere at any radius. In the far field $J^r = J_r$ and by equation (2.26) we have

$$\frac{dN}{dt} = \int_S \frac{1}{2i} \left(\Phi^* \partial_r \Phi - \Phi \partial_r \Phi^*\right) r^2 d\Omega. \tag{2.46}$$

The current density of the initial plane wave in the z direction is simply

$$|J^z| = \omega. \tag{2.47}$$

The absorption cross section is the ratio of total ingoing flux through the body/shell divided by the flux of the initial wave,

$$\sigma_{\mathrm{abs}} \equiv \frac{1}{\omega} \frac{dN}{dt}. \tag{2.48}$$

Using the far field solutions (equation (2.10)), which are normalised by matching the ingoing radiation to the plane wave (equation (2.32)), and substituting into equation (2.46), it can be shown that

$$\sigma_{\text{abs}} = \frac{\pi}{\omega^2} \sum_{l=0}^{\infty} (2l+1)\Gamma_{l\omega}, \tag{2.49}$$

where Γ_{lw} is the lth partial waves transmission factor

$$\Gamma_{lw} \equiv 1 - \left| \frac{C_l^+}{C_l^-} \right|^2 . \tag{2.50}$$

2.2.7 Schwarzschild black hole

Here we present some scalar plane-wave scattering and absorption cross sections for a Schwarzschild black hole, as an example of applying the theory presented above. These are calculated by first numerically solving the wave equation (equation (2.8)) subject to the black hole boundary conditions (equation (2.16)). This determines the mode coefficients $A_l^{\pm}$. Then we use equations (2.49) and (2.50) to find the absorption cross section and equations (2.39) and (2.40) for the scattering cross section. For more details on the method see chapter 3.

These results are shown elsewhere in the literature (e.g. [21, 36, 41, 119, 120]), and agreement with previous studies serves as a useful check on our code which we apply to novel scenarios in later chapters.

Figure 2.1 shows the absorption cross section for a non-rotating black hole of mass M as a function of frequency, reproducing the result found by Sanchez [36]. At low frequencies the absorption cross section is entirely due to the $l = 0$ wave, and is equal to $4\pi(2M)^2$ (see reference [103] and section 5.4 for more details). As $M\omega$ increases, σ_{abs} increases up to and oscillates about the classical value predicted by a geometric ray analysis, $\sigma_{\text{abs}} = 27\pi M^2$. The size of the oscillations scales as $(\sqrt{2}M\omega)^{-1}$ and their period is approximately $\Delta(M\omega) \approx 0.19$ [36]. Each maximum arises from a peak in the transmission amplitude (equation (2.50)) for a given l mode.

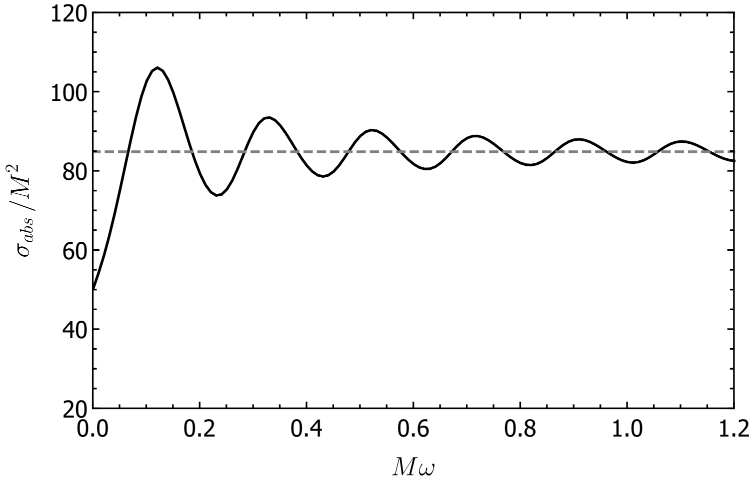

Figure 2.1: Absorption cross section for a massless scalar on a Schwarzschild black hole with mass M. The dashed line is at $\sigma_{\text{abs}} = 27\pi M^2$.

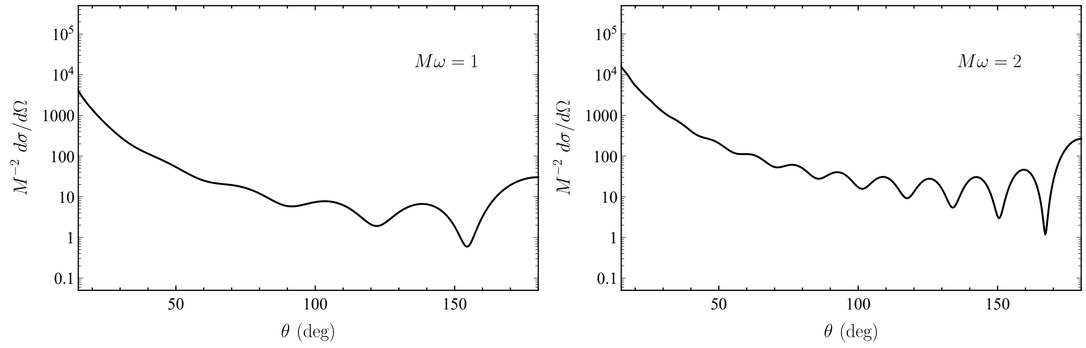

(a)

(b)

Figure 2.2: Scattering cross sections for a massless scalar plane wave with angular frequency ω incident on a Schwarzschild black hole of mass M. Two examples are shown with (a) $M\omega = 1$ and (b) $M\omega = 2$.

In 2011, Décanini, Esposito-Farèse and Folacci [121] showed that the high frequency oscillations in σ_{abs} are remarkably well described by one additional term, and extra terms can be added for increased accuracy. These contributions are derived using complex angular momentum techniques (see chapter 6), and correspond to decaying surface waves localised near the photon sphere at $r = 3M$.

In figure 2.2 we show a reproduction of scattering cross sections for a scalar plane wave impinging on a Schwarzschild black hole with (a) $M\omega = 1$ and (b) $M\omega = 2$. They exhibit a divergence in the forward direction predicted by the 'comparison Newtonian' formula, equation (2.43). There is constructive interference in the backwards direction, $\theta = \pi$, known as a glory. In addition, there is significant structure at intermediate observation angles. This can be understood by considering the initial wave as a congruence of rays. These rays may orbit the black hole and multiple rays scattered by the same net angle give rise to this interference pattern. This is discussed in more detail in section 3.4.2 and, for example, reference [21].

2.3 Gravitational perturbations

Gravitational perturbations are conceptually different to scalar, electromagnetic, and other test fields. Instead of considering an additional field on a given spacetime $g_{\mu\nu}$, the metric itself is perturbed. That is,

$$g_{\mu\nu} = g^0_{\mu\nu} + h_{\mu\nu}, \tag{2.51}$$

where $g^0_{\mu\nu}$ is a known solution to EFE, and $h_{\mu\nu}$ is considered small ($g^0_{\mu\nu} = O(1)$, and $h_{\mu\nu} = O(\epsilon)$).

An effective approach to the Schwarzschild perturbation problem is to substitute equation (2.51) into EFE, neglect any second order terms in $h_{\mu\nu}$ (linearise), then solve for $h_{\mu\nu}$ by decomposing it into tensor harmonics and using a separation of variables. Because the spacetime is static and spherically symmetric, the time and angular dependence separate out. The tensor harmonics used are characterised by angular quantum numbers l and m, as well as their parity $p = \pm 1$. Regge and Wheeler examined perturbations of the Schwarzschild spacetime in this manner, motivated by the question of stability [122].

After such a decomposition, the perturbed EFEs will give ten equations for each $\{l, m, \omega, p\}$ mode. After some algebraic manipulation, these ten equations can be reduced to a second order radial equations for a 'master function'. This reduction was first achieved for the odd parity sector by Regge and Wheeler [122], and for the even parity sector by Zerilli [88]. The resulting radial equations are named after the authors. We will give some more details on a similar, modern decomposition introduced by Martel and Poisson [87] in section 2.3.2.

As far as we know, the metric perturbation procedure sketched above has not been successfully applied to the Kerr spacetime. On a rotating black hole there is no longer full spherical symmetry, only axial symmetry, and so it is not possible to separate the solutions into spherical harmonics. At best, the problem should reduce to coupled differential equations in a radial and angular coordinate.

In a seminal work, Teukolsky developed a powerful approach to perturbations on Kerr using the Newman-Penrose (NP) formulation of general relativity [89, 123]. The NP-formalism is a special type of tetrad calculus [107]. The tetrad is a basis of four null vectors defined at each point in spacetime $\{\mathbf{l}, \mathbf{n}, \mathbf{m}, \bar{\mathbf{m}}\}$, and quantities of interest are projected onto them. For example, the quantities that completely describe non-trivial gravitational perturbations are the Weyl scalar components

$$\Phi_0 \equiv C_{\alpha\beta\gamma\delta} l^\alpha m^\beta l^\gamma m^\delta, \qquad \Phi_4 \equiv C_{\alpha\beta\gamma\delta} n^\alpha \bar{m}^\beta n^\gamma \bar{m}^\delta, \tag{2.52}$$

where $C_{\alpha\beta\gamma\delta}$ is the Weyl tensor.

Teukolsky derived decoupled equations for the perturbations of Φ_0 and Φ_4 on any Type-D background (such as Kerr), and then showed that a separation of variables could be achieved on Kerr for Φ_0 and $\rho^{-4}\Phi_4$, where $\rho = \rho(r, \theta)$ is a spin coefficient [123]. In fact, Teukolsky derived a radial and angular equation for a perturbation of any spin $s \in \{0, {}^1\!/\!{}_2, 1, 2\}$. Early scattering studies on Kerr and Schwarzschild make use of these powerful Teukolsky equations, for example to derive the scattering amplitude of a perturbative gravitational plane wave on Kerr [43]. The result in reference [43] can be applied to a gravitational plane wave on any spherically symmetric spacetime, since by Birkhoff's theorem the exterior must be Schwarzschild, which is a special case of Kerr. However, we have instead employed Martel and Poisson's metric formalism to examine the GW scattering problem, complementing the original works which are summarised in the monograph by Futterman Handler and Matzner [21].

Another reason for choosing a metric perturbation formalism is that it is well developed for stellar models [29, 92, 93, 97, 98, 124]. For a non-vacuum spherically symmetric spacetime, the problem can be reduced to a single second order radial equation for the odd parity sector, and a fourth-order system for the even parity sector [92, 97]. The reason for the added complexity is the presence of matter fields which can couple to the even parity gravitational perturbations. We will further discuss perturbations for the interior of a star in chapter 4.

2.3.1 Choice of gauge and gauge invariance

The Principle of General Covariance, that guided the development of general relativity, consists of two requirements. For a physical equation to hold in a gravitational field, it must a) also hold in the absence of gravitation and b) satisfy general covariance, i.e. preserve its form under a coordinate transformation $x^\mu \to x'^\mu$. For more details and discussion see for example chapter 4 of Weinberg's textbook [125]. Consider a small coordinate transformation of the form

$$x^\mu \to x'^\mu = x^\mu + \xi^\mu, \tag{2.53}$$

where ξ^μ and its derivatives are at the same order as $h_{\mu\nu}$. Under this transformation, the metric of equation (2.51) transforms as

$$g_{\mu\nu} \to g'_{\mu\nu} = g^0_{\mu\nu} + h'_{\mu\nu} + O(\epsilon^2), \tag{2.54}$$

where

$$h'_{\mu\nu} = h_{\mu\nu} - \mathcal{L}_\xi g^{(0)}_{\mu\nu} = h_{\mu\nu} - 2\xi_{(\nu;\mu)}, \tag{2.55}$$

and $\mathcal{L}_\xi$ is the Lie derivative with respect to the vector field ξ^μ. If $h_{\mu\nu}$ is a valid solution of the linearised EFEs on the background $g^0_{\mu\nu}$, then so is $h'_{\mu\nu}$. The general covariance of Einstein's full equations leads to the gauge invariance of the linear perturbation equations.

This gauge freedom can be helpful, often simplifying the field equations. It must also be kept in mind that any physical quantities that could be measured experimentally must be gauge invariant. Sir Arthur Eddington used a coordinate invariant approach to show that certain types of gravitational wave solutions, which could travel at an arbitrary velocity, had no objective existence [126]. He concluded that these waves were 'merely sinuosities in the coordinate system'.

Let

$$T^{a_1 a_2 \ldots a_j}{}_{b_1 b_2 \ldots b_k} = T^{(0)a_1 a_2 \ldots a_j}{}_{b_1 b_2 \ldots b_k} + \delta T^{a_1 a_2 \ldots a_j}{}_{b_1 b_2 \ldots b_k} \tag{2.56}$$

be a general rank (j, k) tensor on a perturbed background (equation (2.51)), where $\delta T^{a_1 a_2 \ldots a_j}{}_{b_1 b_2 \ldots b_k}$ is first order in $h_{\mu\nu}$. Under a gauge transformation (equation (2.53)), $T^{a_1a_2\ldots a_j}{}_{b_1b_2\ldots b_k}$ transforms according to

$$T^{a_1a_2\ldots a_j}{}_{b_1b_2\ldots b_k} \to \tilde{T}^{a_1a_2\ldots a_j}{}_{b_1b_2\ldots b_k} = T^{a_1a_2\ldots a_j}{}_{b_1b_2\ldots b_k} - \mathcal{L}_\xi T^{(0)a_1a_2\ldots a_j}{}_{b_1b_2\ldots b_k} . \tag{2.57}$$

This implies that any tensor which is zero on the background,

$$T^{(0)a_1a_2\ldots a_j}{}_{b_1b_2\ldots b_k} = 0, \tag{2.58}$$

is gauge invariant on the perturbed spacetime. This includes the Ricci tensor $R_{\mu\nu}$ on perturbed vacuum spacetimes, and the Weyl scalars of maximal spin weight (see equation (2.52)) on perturbed Kerr-Newman spacetimes. sor

Although measurable quantities must be gauge invariant, perturbation calculations are usually carried out in a particular gauge. For example: the Regge-Wheeler gauge makes the decomposition of the perturbation equations on a spherically symmetric spacetime particularly simple [29, 88, 92, 122]; Martel and Poisson show that outgoing GWs can be expressed most elegantly in a 'radiation gauge'; and the asymptotic plane wave solution (section 2.3.5) is expressed in a transverse-traceless gauge. The transverse traceless part of a plane GW is the only part that carries energy, and is a physically intuitive gauge to work in. Sometimes, a problem may require working in several gauges, and transforming between them can be technically challenging. This difficulty can be curtailed by using gauge invariant quantities as much as possible. Martel and Poisson's master functions are gauge invariant, which is another reason for choosing to use their formalism in section 2.3.2.

2.3.2 Schwarzschild metric perturbations

Building on previous works, Martel and Poisson have developed a gauge-invariant metric perturbation formalism for the Schwarzschild background [87]. They develop a covariant approach to the metric decomposition on the sub-manifolds $\mathcal{M}_2$ and S_2 (see section 2.1). On the radial-temporal plane $\mathcal{M}_2$ they introduce

$$r_a \equiv \frac{\partial r}{\partial x^a}, \tag{2.59}$$

and the antisymmetric Levi-Civita tensor ϵ_{ab} (The Levi-Civita volume form on $\mathcal{M}_2$ is $\epsilon \equiv \epsilon_{ab}dx^a dx^b \equiv \sqrt{|g|}dt \wedge dr$). On the two sphere they define scalar, vector and tensor spherical harmonics. Like the Regge-Wheeler harmonics, these are classified by angular mode numbers $\{l, m\}$ and parity $p = \pm 1$. Axial (odd-parity) harmonics are labelled $p = -1$ and polar (even-parity) harmonics $p = 1$. Under an inversion of the spatial coordinates (the parity transformation) axial and polar spherical harmonics are multiplied by a factor of $(-1)^{l+1}$ and $(-1)^l$ respectively. In Newtonian theory and seismology axial perturbations are also known as toroidal, and polar ones as spheroidal. This terminology originates in the type of fluid pulsations that the perturbation generates [32].

Under rotations on the two sphere metric perturbation components transform as three scalars, h_{00}, h_{01} and h_{11}; two vectors, h_{0A} and h_{1A}; and a tensor, h_{AB}. Each component is decomposed into the appropriate spherical harmonics. The scalar spherical harmonics, Y^{lm}, have even parity ($p = 1$). Vector and tensor spherical harmonics are denoted by X_A^{lmp} and X_{AB}^{lmp} respectively. For their definitions and properties see appendix A. The decomposition of the metric perturbation begins by splitting the perturbation into the two parity sectors

$$h_{\mu\nu} = h^+_{\mu\nu} + h^-_{\mu\nu}. \tag{2.60}$$

We will use the superscript ± to denote the parity $p = \pm 1$. Following [87], the even parity sector is decomposed as

$$h^+_{ab} = \sum_{l,m} h^{lm}_{ab} Y^{lm}, \tag{2.61a}$$

$$h^+_{aB} = \sum_{l,m} j^{lm}_a X^{lm+}_B, \tag{2.61b}$$

$$h^+_{AB} = r^2 \sum_{l,m} \left(K^{lm} \Omega_{AB} Y^{lm} + G^{lm} X^{lm+}_{AB} \right), \tag{2.61c}$$

and the odd parity components are

$$h^{-}_{ab} = 0, \tag{2.62a}$$

$$h^{-}_{aB} = \sum_{l,m} h^{lm}_{a} X^{lm-}_{B}, \tag{2.62b}$$

$$h^{-}_{AB} = \sum_{l,m} h^{lm}_{2} X^{lm-}_{AB}, \tag{2.62c}$$

where h^{lm}_{ab}, j^{lm}_{a}, h^{lm}_{a}, G^{lm}, K^{lm}, and h^{lm}_{2} are functions of x_0 and x_1. We will refer to these decomposition coefficients as MP (Martel-Poisson) functions. We use the shorthand $\sum_{l,m} \equiv \sum_{l=2}^{\infty} \sum_{m=-l}^{l}$. The lower multipoles $l = 0, 1$, which are not radiative in character, are discussed in [87]. These introduce a shift in the Schwarzschild mass parameter $M \to M + \delta M$, a slow rotation to the black hole, and a pure gauge term that can be removed. For our purposes they are essentially set to zero.

It is helpful to write some tensor components explicitly in terms of scalar spherical harmonics in Schwarzschild coordinates. In the following s and c are shorthand for $\sin\theta$ and $\cos\theta$ respectively. The h_{aB} components are

$$h_{a\theta} = \sum_{l,m} \left[j^{lm}_{a} \partial_\theta - \frac{1}{s} h^{lm}_{a} \partial_\phi \right] Y^{lm}, \tag{2.63a}$$

$$h_{a\phi} = \sum_{l,m} \left[j^{lm}_{a} \partial_\phi + s h^{lm}_{a} \partial_\theta \right] Y^{lm}. \tag{2.63b}$$

The angular (h_{AB}) components are

$$h_{\theta\theta} = \sum_{l,m} \left[r^2 K^{lm} + \frac{1}{2} r^2 G^{lm} D_2 - \frac{1}{2s} h^{lm}_{2} D_1 \right] Y^{lm}, \tag{2.64a}$$

$$h_{\phi\phi} = \sum_{l,m} \left[r^2 s^2 K^{lm} - \frac{1}{2} r^2 s^2 G^{lm} D_2 + \frac{1}{2} s h^{lm}_{2} D_1 \right] Y^{lm}, \tag{2.64b}$$

$$h_{\theta\phi} = \sum_{l,m} \left[\frac{1}{2} r^2 G^{lm} D_1 + \frac{1}{2} s h^{lm}_{2} D_2 \right] Y^{lm}, \tag{2.64c}$$

where we make use of the differential operators

$$D_1 \equiv 2\left[\partial_\theta - \frac{c}{s}\right]\partial_\phi, \tag{2.65a}$$

$$D_2 \equiv \partial_\theta^2 - \frac{c}{s}\partial_\theta - \frac{1}{s^2}\partial_\phi^2, \tag{2.65b}$$

introduced in [127]. To isolate the MP-functions we use combinations and derivatives of the various tensor components. For the even parity sector

$$\sum_{l,m} l(l+1) j_a^{lm} Y^{lm} = -\left(\frac{1}{s^2}\partial_\phi h_{a\phi} + \frac{1}{s}\partial_\theta s h_{a\theta}\right), \tag{2.66a}$$

$$\sum_{l,m} 2r^2 K^{lm} Y^{lm} = h_{\theta\theta} + s^{-2} h_{\phi\phi}, \tag{2.66b}$$

$$\sum_{l,m} \frac{1}{2} r^2 G^{lm}(l-1)l(l+1)(l+2) Y^{lm} = s^{-3} D_1[s h_{\theta\phi}] + \frac{1}{2} s^{-2} D_2[s^2 h_{\theta\theta} - h_{\phi\phi}]. \tag{2.66c}$$

For the odd parity sector

$$\sum_{l,m} l(l+1) h_a^{lm} Y^{lm} = \frac{1}{s}\left(\partial_\phi h_{a\theta} - \partial_\theta h_{a\phi}\right), \tag{2.67a}$$

$$\sum_{l,m} \frac{1}{2} h_2^{lm}(l-1)l(l+1)(l+2) Y^{lm} = s^{-2} D_2[s h_{\theta\phi}] - \frac{1}{2} s^{-3} D_1[s^2 h_{\theta\theta} - h_{\phi\phi}]. \tag{2.67b}$$

Equations (2.61a), (2.66) and (2.67) will come in handy later when we calculate the MP-functions that asymptotically match to a plane wave solution (section 2.3.5).

The MP gauge-invariant master function for the even parity sector is known as the Zerilli-Moncrief function [88, 128] ,

$$\Phi^+_{lm} \equiv \frac{2r}{l(l+1)}\left[\tilde{K}^{lm} + \frac{2}{\Lambda}\left(r^a r^b \tilde{h}^{lm}_{ab} - r r^a \nabla_a \tilde{K}^{lm}\right)\right], \tag{2.68}$$

where

$$\tilde{K}^{lm} \equiv K^{lm} + \frac{1}{2}l(l+1)G^{lm} - \frac{2}{r}r^a\epsilon_a^{lm}, \tag{2.69}$$

$$\epsilon_a^{lm} \equiv j_a^{lm} - \frac{1}{2}r^2\nabla_a G^{lm}, \tag{2.70}$$

$$\tilde{h}_{ab}^{lm} \equiv h_{ab}^{lm} - \nabla_a\epsilon_b^{lm} - \nabla_b\epsilon_a^{lm}, \tag{2.71}$$

and

$$\Lambda \equiv (l-1)(l+2) + \frac{6M}{r}. \tag{2.72}$$

The odd-parity master function is the Cunningham-Price-Moncrief function [95],

$$\Phi_{lm}^{-} \equiv \frac{2r}{(l-1)(l+2)}\epsilon^{ab}\left(\partial_a h_b^{lm} - \frac{2}{r}r_a h_b^{lm}\right), \tag{2.73}$$

recalling that ϵ_{ab} is the antisymmetric Levi-Civita tensor.

As a consequence of the perturbated EFEs, it can be shown that the master functions $\Phi_{lm}^{\pm}$ obey a wave equation. A derivation (with source terms) is in [129]. We work in frequency space with the Fourier modes $\tilde{\Phi}_{lm}^{\pm}(r,\omega)$ defined by

$$\Phi_{lm}^{\pm}(r,t) = \frac{1}{2\pi}\int_{-\infty}^{\infty} d\omega\, \tilde{\Phi}_{lm}^{\pm}(r,\omega)e^{-i\omega t}. \tag{2.74}$$

Assuming there is no perturbing stress-energy source terms, the master functions obey the second order ODEs

$$\frac{d^2\tilde{\Phi}_{lm}^{\pm}}{dr_*^2} + \left(\omega^2 - V_l^{\pm}(r)\right)\tilde{\Phi}_{lm}^{\pm} = 0. \tag{2.75}$$

Here $V_l^{-}(r)$ is the Regge-Wheeler potential,

$$V_l^{-}(r) \equiv A\left(\frac{l(l+1)}{r^2} - \frac{6M}{r^3}\right), \tag{2.76}$$

and $V_l^{+}(r)$ the Zerilli potential

$$V_l^{+}(r) \equiv \frac{A}{\Lambda^2}\left[\mu^2\left(\frac{\mu+2}{r^2} + \frac{6M}{r^3}\right) + \frac{36M^2}{r^4}\left(\mu + \frac{2M}{r}\right)\right], \tag{2.77}$$

with $\mu \equiv (l-1)(l+2)$. Once the master functions have been found by solving equation (2.75), the metric perturbation can be reconstructed from them and their derivatives (see appendix A of [86] for a reconstruction in Regge-Wheeler gauge). The radiative parts of the metric perturbation in spherical coordinates scale as

$$h^{\text{rad}}_{ab} \sim r^{-1}, \quad h^{\text{rad}}_{aB} \sim r^{0}, \quad h^{\text{rad}}_{AB} \sim r^{1}. \tag{2.78}$$

Reconstructing the metric in the far field ($r \to \infty$) is particularly simple in a specific radiation gauge in which $t^a h_{ab} = 0 = t^a h_{aB}$, where t^a is the timelike Killing vector [87]. In this gauge, $h^{\text{rad}}_{ab} = 0 = h^{\text{rad}}_{aB}$ in the far field, and

$$h^{\text{rad}}_{AB} = r \sum_{p=\pm 1} \sum_{l\geq 2}^{\infty} \sum_{m=-l}^{m=l} \Phi^{p}_{lm}(r=\infty, t) X^{lmp}_{AB}(\theta, \phi). \tag{2.79}$$

For the case of a black hole, to evaluate the perturbation at the horizon Martel and Poisson similarly impose the condition $t^a h_{ab} = 0 = t^a h_{aB}$ at $r = 2M$. They find that

$$h^{\text{rad,EH}}_{AB} = 2M \sum_{p=\pm 1} \sum_{l\geq 2}^{\infty} \sum_{m=-l}^{m=l} p \cdot \Phi^{p}_{lm}(r=2M, t) X^{lmp}_{AB}(\theta, \phi). \tag{2.80}$$

2.3.3 Boundary conditions

The boundary conditions for GWs on a black hole background are specified in analogy with the scalar case (section 2.2.2). The IN modes are purely ingoing at the horizon,

$$\tilde{\Phi}^{\text{in}}_{lmp}(r, \omega) \sim \begin{cases} e^{-i\omega r_*}, & r_* \to -\infty \\ A^{+}_{lp} e^{i\omega r_*} + A^{-}_{lp} e^{-i\omega r_*}, & r_* \to \infty \end{cases}, \tag{2.81}$$

and UP modes have the asymptotic behaviour

$$\tilde{\Phi}^{\text{up}}_{lmp}(r, \omega) \sim \begin{cases} B^{+}_{lp} e^{i\omega r_*} + B^{-}_{lp} e^{-i\omega r_*}, & r_* \to -\infty \\ e^{i\omega r_*}, & r_* \to \infty \end{cases}. \tag{2.82}$$

If we wish to consider a general object with radius R ($r_* = R_*$), a generic boundary condition can be imposed at or just outside the surface (analogous to equation (2.21) for the scalar field),

$$\tilde{\Phi}^{\text{in}}_{lmp}(r,\omega) \sim \begin{cases} e^{-i\omega r_*} + \left(\mathcal{K}_{lp} e^{-2i\omega R_*}\right) e^{i\omega r_*}, & r_* \to R_*^+ \\ C^+_{lp} e^{i\omega r_*} + C^-_{lp} e^{-i\omega r_*}, & r_* \to \infty \end{cases} . \tag{2.83}$$

Black hole scattering boundary conditions (equation (2.81)) are recovered by setting $\mathcal{K}_{lp} = 0$ and $R = 2M$ ($R_* = -\infty$). In our notation the various coefficients for $s = 2$ perturbations ($A^{\pm}_{lp}$...) are distinguished from the $s = 0$ coefficients ($A^{\pm}_{l}$...) by the extra dependence on parity p. The various relations between coefficients for the scalar case, equations (2.19), (2.20) and (2.22), also apply for GWs.

For a compact body, equation (2.83) may be derived from a junction condition joining a perturbed interior solution, $g_{\mu\nu}$, to the perturbed Schwarzschild exterior. We will return to this in chapter 4.

2.3.4 Gravitational wave energy

Defining the stress-energy of a GW with respect to a background spacetime $g^0_{\mu\nu}$ necessitates going beyond linear perturbation theory. The stress-energy is second order in $h_{\mu\nu}$, and in order to define it in a gauge invariant way it must be averaged over multiple wavelengths. This averaging is denoted by angular brackets $\langle \cdots \rangle$, and the stress-energy for a GW is [83]

$$T^{\text{BH}}_{\mu\nu} = \frac{1}{32\pi} \left\langle h^{\rho\tau}{}_{;\mu} h_{\rho\tau;\nu} \right\rangle . \tag{2.84}$$

The superscript BH refers to Brill and Hartle, who devised a space-time averaging process when considering gravitational geons [81]. The term Brill-Hartle averaging was coined by Isaacson [82, 83], who developed a rigorous approach to defining the stress energy of a GW, building on earlier works [81, 130]. An important underlying assumption in the derivation is that the GW wavelength is much smaller than the radius of curvature of the background space-time.

Since we are interested in the stress energy of a GW in the far field of an asymptotically flat space-time, this assumption is perfectly valid.

The energy flux in the radial direction is given by T^{rt} [131]. As $r \to \infty$,

$$T^{\mathrm{BH}}_{rt} \sim \frac{1}{r^4}\frac{1}{32\pi}\left\langle \partial_r h^{AB} \partial_t h_{AB} \right\rangle , \tag{2.85}$$

where h_{AB} is given by equation (2.79).

2.3.5 Plane gravitational waves

We consider a circularly-polarized gravitational plane wave of angular frequency ω, travelling up the z axis, and expressed in a spherical coordinate system in tranverse traceless gauge. On flat space this is

$$h_{\mu\nu} = \mathrm{Re}\,\{He^{i(2\phi-\chi)} \begin{bmatrix} 0 & 0 & 0 & 0 \\ \bullet & s^2 & rsc & irs^2 \\ \bullet & \bullet & r^2c^2 & ir^2sc \\ \bullet & \bullet & \bullet & -r^2s^2 \end{bmatrix}\}, \tag{2.86}$$

where H is the amplitude of the wave, $\chi \equiv \omega(t-z)$, and s and c are shorthand for $\sin\theta$ and $\cos\theta$, respectively. This wave is left circularly polarised (positive helicity) for $\omega > 0$ and right circularly polarised (negative helicity) for $\omega < 0$. The terms denoted by $\bullet$ may be inferred from the property $h_{\mu\nu} = h_{\nu\mu}$.

The plane wave in equation (2.86) is not a valid solution on the Schwarzschild background, even in the far-field region, due to the long-range $1/r$ nature of the field. Following convention (see [21]) we replace it with a distorted plane wave by making the substitution $r \to r_*$ in the exponent of equation (2.86) (i.e. $z \to z_* = r_* \cos\theta$). From this metric perturbation, we may compute the master variables $\Phi^{\mathrm{plane}}_{lmp}$, as outlined in section 2.3.2. We must first take some preliminary steps to do this.

In section 2.2.4 we showed that the function $e^{i\omega z}$ can be expressed as a sum over Legendre polynomials. Using recurrence relations for associated Legendre polynomials [117], it can be shown that

$$e^{i\omega z_*} = \frac{1}{(\omega r_* s)^q} \sum_{l=q}^{\infty} (2l+1) i^{l+q} j_l(\omega r_*) P_l^q(c), \tag{2.87}$$

where q is a positive integer. Making use of equation (2.87) with $q = 2$, and using further recursion relations we find the following useful ways to expand $e^{i\omega z_*}$,

$$e^{i\omega z_*} = \frac{1}{(\omega r_* s)^2} \sum_{l=2}^{\infty} (2l+1)(i)^{l+2} j_l(\omega r_*) P_l^2(c), \tag{2.88a}$$

$$= \frac{1}{(\omega r_* s)^2 c} \sum_{l=2}^{\infty} (2l+1)(i)^{l+2} \zeta_l(\omega r_*) P_l^2(c), \tag{2.88b}$$

$$= \frac{1}{(\omega r_* s c)^2} \sum_{l=2}^{\infty} (2l+1)(i)^{l+2} \eta_l(\omega r_*) P_l^2(c), \tag{2.88c}$$

where

$$\zeta_l(\omega r_*) \equiv \frac{2 j_l(\omega r_*)}{\omega r_*} - j_l'(\omega r_*), \tag{2.89}$$

$$\eta_l(\omega r_*) \equiv \left(\frac{l(l+1)+6}{(\omega r_*)^2} - 1 \right) j_l(\omega r_*) - \frac{6 j_l'(\omega r_*)}{\omega r_*}. \tag{2.90}$$

Equations (2.88) allow us to expand the plane wave metric perturbation components purely in terms of spherical harmonics,

$$e^{i(2\phi-\chi)} s^2 = \frac{1}{(\omega r_*)^2} \sum_{l=2}^{\infty} \frac{(2l+1)(i)^{l+2}}{c_{l2}} j_l(\omega r_*) Y_l^2(\theta,\phi) e^{-i\omega t}, \tag{2.91}$$

$$e^{i(2\phi-\chi)} s^2 c = \frac{1}{(\omega r_*)^2} \sum_{l=2}^{\infty} \frac{(2l+1)(i)^{l+3}}{c_{l2}} \zeta_l(\omega r_*) Y_l^2(\theta,\phi) e^{-i\omega t}, \tag{2.92}$$

$$e^{i(2\phi-\chi)} s^2 c^2 = \frac{1}{(\omega r_*)^2} \sum_{l=2}^{\infty} \frac{(2l+1)(i)^{l}}{c_{l2}} \eta_l(\omega r_*) Y_l^2(\theta,\phi) e^{-i\omega t}, \tag{2.93}$$

where c_{l2} is given by equation (2.29). From equations (2.91) to (2.93), the orthogonality of spherical harmonics equation (A.2), and the property $Y_{l,-m} =$

$(-1)^m\bar{Y}_{lm}$, the following integrals can be deduced:

$$I_1^{lm} \equiv \int s^2 \mathrm{Re}\{e^{i(2\phi-\chi)}\}\bar{Y}_{lm}\,d\Omega = \frac{(2l+1)i^{l+2}j_l}{2c_{l2}(\omega r_*)^2}\left[e^{-i\omega t}\delta^2_m + (-1)^l e^{i\omega t}\delta^{-2}_m\right], \tag{2.94}$$

$$I_2^{lm} \equiv \int cs^2 \mathrm{Re}\{e^{i(2\phi-\chi)}\}\bar{Y}_{lm}\,d\Omega = \frac{(2l+1)i^{l+3}\zeta_l}{2c_{l2}(\omega r_*)^2}\left[e^{-i\omega t}\delta^2_m + (-1)^{l+1} e^{i\omega t}\delta^{-2}_m\right], \tag{2.95}$$

$$I_3^{lm} \equiv \int c^2 s^2 \mathrm{Re}\{e^{i(2\phi-\chi)}\}\bar{Y}_{lm}\,d\Omega = \frac{(2l+1)i^{l}\eta_l}{2c_{l2}(\omega r_*)^2}\left[e^{-i\omega t}\delta^2_m + (-1)^l e^{i\omega t}\delta^{-2}_m\right], \tag{2.96}$$

$$I_4^{lm} \equiv \int s^2 \mathrm{Re}\{ie^{i(2\phi-\chi)}\}\bar{Y}_{lm}\,d\Omega = \frac{(2l+1)i^{l+3}j_l}{2c_{l2}(\omega r_*)^2}\left[e^{-i\omega t}\delta^2_m + (-1)^{l+1} e^{i\omega t}\delta^{-2}_m\right], \tag{2.97}$$

$$I_5^{lm} \equiv \int cs^2 \mathrm{Re}\{ie^{i(2\phi-\chi)}\}\bar{Y}_{lm}\,d\Omega = \frac{(2l+1)i^{l}\zeta_l}{2c_{l2}(\omega r_*)^2}\left[e^{-i\omega t}\delta^2_m + (-1)^l e^{i\omega t}\delta^{-2}_m\right], \tag{2.98}$$

$$I_6^{lm} \equiv \int c^2 s^2 \mathrm{Re}\{ie^{i(2\phi-\chi)}\}\bar{Y}_{lm}\,d\Omega = \frac{(2l+1)i^{l+1}\eta_l}{2c_{l2}(\omega r_*)^2}\left[e^{-i\omega t}\delta^2_m + (-1)^{l+1} e^{i\omega t}\delta^{-2}_m\right]. \tag{2.99}$$

Note that $I^{l(-m)} = \bar{I}^{lm}$.

Beginning with h_{rr}^{lm}, and making use of equation (2.94), it can be seen that

$$h_{rr}^{lm} = \int h_{rr}\bar{Y}_{lm}\,d\Omega = HI_1^{lm}. \tag{2.100}$$

Clearly, $h_{tt}^{lm} = 0 = h_{tr}^{lm}\ \forall\ l, m$. Note that $h_{rr}^{l,\pm 2} \sim r^{-3}$ as $r \to \infty$, using the asymptotic property of the spherical Bessel function, equation (2.33). The Weyl tensor components obtained from this part thus scale as r^{-5} in the far field, and are non-radiative. This is consistent with equation (2.79) which implies $h_{rr}^{\mathrm{rad}} = 0$.

Following the procedure outlined in section 2.3.2, the other MP-functions for a plane wave are found to be

$$j_t^{lm} = 0, \tag{2.101}$$

$$h_t^{lm} = 0, \tag{2.102}$$

$$j_r^{lm} = \frac{Hr}{l(l+1)}\left[\omega r_* I_5^{lm} + 3I_1^{lm}\right], \tag{2.103}$$

$$h_r^{lm} = -\frac{Hr}{l(l+1)}\left[\omega r_* I_1^{lm}\right], \tag{2.104}$$

and

$$K^{lm} = -\frac{1}{2}HI_1^{lm}, \tag{2.105}$$

$$G^{lm} = -\frac{H}{l(l-1)(l+1)(l+2)}\left[(\omega r_*)^2\left(I_1^{lm} + I_3^{lm}\right) - 8\omega r_* I_5^{lm} - 12 I_1^{lm}\right], \tag{2.106}$$

$$h_2^{lm} = -\frac{Hr^2}{l(l-1)(l+1)(l+2)}\left[(\omega r_*)^2 I_5^{lm} - 8\omega r_* I_1^{lm} - 2\right]. \tag{2.107}$$

With the MP-functions in hand, we can find the gauge invariant master functions for the distorted plane wave (equation (2.86)) using equations (2.68) and (2.73). We are interested in their asymptotic form in the far field, where we will subtract them from a total solution to give the scattered component. Checking with `Mathematica` we find that the master functions can be expanded in the far field as

$$\Phi^{\text{plane}}_{l2,-1}(r,t) = \frac{2\pi H c_{l2}}{\omega}\left((-1)^{l+1}e^{-i\omega r_*} + e^{i\omega r_*}\right)e^{-i\omega t} + O\left(r^{-1}\right), \tag{2.108}$$

$$\Phi^{\text{plane}}_{l2,+1}(r,t) = -\frac{2\pi i H c_{l2}}{\omega}\left((-1)^{l+1}e^{-i\omega r_*} + e^{i\omega r_*}\right)e^{-i\omega t} + O\left(r^{-1}\right) \tag{2.109}$$

It follows from the reality condition on $h_{\mu\nu}$ that $\Phi_{l,-m,p} = \bar{\Phi}_{lmp}$. Only the $m = \pm 2$ and $l \geq 2$ modes are needed; all other modes ($l < 2$ or $m \neq \pm 2$) are zero for the plane wave.

2.3.6 Scattering cross section

The energy flux per unit solid angle of a GW in the far field is [86],

$$\left\langle \frac{dE}{dt\, d\Omega} \right\rangle = -\left\langle \lim_{r\to\infty} r^2 A\, T_{rt} \right\rangle \tag{2.110}$$
$$= -\frac{1}{r^2}\frac{1}{32\pi}\left\langle \lim_{r\to\infty} \partial_r h^{AB} \partial_t h_{AB} \right\rangle , \tag{2.111}$$
$$= -\frac{1}{32\pi}\left\langle \sum_{p,l,m} \partial_r \Phi^p_{lm}(r,t)\, X^{AB}_{lmp}(\theta,\phi) \sum_{p',l',m'} \partial_t \Phi^{p'}_{l'm'}(r,t)\, X^{lmp}_{AB}(\theta,\phi) \right\rangle , \tag{2.112}$$

where the second line follows from equation (2.85) and the final line from equation (2.79) (A is given in equation (2.9) for the Schwarzschild exterior).

We want the energy associated with the scattered part of the metric perturbation, which is found by matching to the total metric perturbation and the plane wave via

$$h^{\text{scat}}_{AB} = h^{\text{total}}_{AB} - h^{\text{plane}}_{AB} . \tag{2.113}$$

The total perturbation is found by solving for the master functions with relevant boundary conditions, and the plane wave is discussed in section 2.3.5. The subtraction on the right hand side of equation (2.113) seems simple enough, but it only makes sense if h^{total}_{AB} and h^{plane}_{AB} are calculated in the same gauge. This is where the power of Martel and Poisson's approach helps us, as it allowed us to express both terms in a 'radiation gauge', which we have asymptotic expansions for in the far field. This gives us the gauge invariant master functions for the scattered radiation via

$$\Phi^{\text{scat}}_{lmp} = \Phi^{\text{total}}_{lmp} - \Phi^{\text{plane}}_{lmp} . \tag{2.114}$$

Insisting that the scattered part is all outgoing in the far field,

$$\tilde{\Phi}^{\text{scat}}_{lmp}(r,\omega) \sim \alpha_{lmp}(\omega) e^{i\omega r_*} , \tag{2.115}$$

and that the plane wave has circular frequency ω_0, we obtain

$$\begin{aligned}
\alpha_{lm-}(\omega) &= \beta_{l-}(\omega)\left[\delta_{m2}\delta(\omega_0-\omega)-\delta_{m,-2}\delta(\omega_0+\omega)\right], &(2.116a)\\
\alpha_{lm+}(\omega) &= -i\beta_{l+}(\omega)\left[\delta_{m2}\delta(\omega_0-\omega)+\delta_{m,-2}\delta(\omega_0+\omega)\right], &(2.116b)
\end{aligned}$$

where

$$\beta_{lp}(\omega) \equiv \frac{(2\pi)^2 H c_{l2}}{\omega}\left(e^{2i\delta_l^p(\omega)}-1\right), \tag{2.117}$$

the phase shifts $\delta_l^p(\omega)$ are defined by [1]

$$e^{2i\delta_l^p(\omega)} \equiv S_{lp}(\omega) \equiv (-1)^{l+1}\frac{C_{lp}^{+}(\omega)}{C_{lp}^{-}(\omega)}. \tag{2.118}$$

The boundary conditions and radial equations that fully define the phase shifts are such that

$$S_{lp}(-\omega) = \bar{S}_{lp}(\omega). \tag{2.119}$$

Equations (2.74) and (2.115) to (2.117) determine $\Phi^{\text{scat}}_{lmp}(r,t)$, which we then substitute directly into equation (2.112) to obtain

$$\left\langle \frac{dE}{dt\, d\Omega} \right\rangle = \frac{1}{32\pi} 2\omega_0^2 \left|\left| \sum_{l=2}^{\infty} i\beta_{l-} X^{l2-}_{AB} + \beta_{l+} X^{l2+}_{AB} \right|\right|^2, \tag{2.120}$$

where $||V_{AB}||^2 \equiv V_{AB}\bar{V}^{AB}$. The right hand side of equation (2.120) has been simplified by space-time averaging over time (or radial distance), so that any oscillating terms average to zero.

At this stage it is convenient to translate from the tensor harmonics, X^{AB}_{lmp}, to spin-weighted spherical harmonics, ${}_{-s}Y_{lm}$, using equations (A.9) and (A.10).

---

[1] The symbol delta is used both for the Dirac delta function in e.g. equation (2.116) and to denote phase shifts. The intended use should be clear from the context. If a δ appears in an exponential it denotes a phase shift.

Then

$$\left\langle \frac{dE}{dt\,d\Omega} \right\rangle = \frac{\omega_0^2}{32\pi} \left(\left| \sum_{l=2}^{\infty} \sqrt{(l-1)l(l+1)(l+2)}\,(\beta_{l+} - \beta_{l-})\ {}_2Y_{l2} \right|^2 \right.$$
$$\left. + \left| \sum_{l=2}^{\infty} \sqrt{(l-1)l(l+1)(l+2)}\,(\beta_{l+} + \beta_{l-})\ {}_{-2}Y_{l2} \right|^2 \right). \tag{2.121}$$

The flux of the incident plane wave is

$$\left.\frac{dE}{dt\,dA}\right|_{\text{plane}} = \frac{H^2\omega_0^2}{16\pi}. \tag{2.122}$$

The differential scattering cross section is defined as the energy per unit time scattered into solid angle $d\Omega$, divided by the flux of the incident wave,

$$\frac{d\sigma}{d\Omega} \equiv \frac{dE}{dt\,d\Omega} \div \left.\frac{dE}{dt\,dA}\right|_{\text{plane}}. \tag{2.123}$$

The differential scattering cross section for gravitational plane wave can be expressed as

$$\frac{d\sigma}{d\Omega} = |f_2(\theta)|^2 + |g_2(\theta)|^2, \tag{2.124}$$

where

$$f_2(\theta) \equiv \frac{\pi}{i\omega_0} \sum_{l,p} {}_{-2}Y_{l2}(0)\,{}_{-2}Y_{l2}(\theta) \left[e^{2i\delta_l^p} - 1 \right], \tag{2.125}$$

$$g_2(\theta) \equiv \frac{\pi}{i\omega_0} \sum_{l,p} p(-1)^l\,{}_{-2}Y_{l2}(0)\,{}_{-2}Y_{l2}(\pi-\theta) \left[e^{2i\delta_l^p} - 1 \right]. \tag{2.126}$$

Note that there is no ϕ dependence, which is a consequence of the symmetry of the scattering set up.

For an interpretation of the two amplitudes, note that the perturbation for the scattered waves can be expressed as

$$h_{AB}^{\text{scat}} = \frac{1}{2}\text{Re}\left\{Hre^{i\omega(t-r_*)+2i\phi}\left(f_2(\theta)m_Am_B + g_2(\theta)\bar{m}_A\bar{m}_B\right)\right\}, \tag{2.127}$$

where $m_A = 2^{-1/2}(1, i\sin\theta)$ is a tetrad basis on the sphere. By considering rotations of the tetrad, it can be deduced that the f_2 term has positive helicity and the g_2 term has negative helicity for $\omega > 0$. Since the original plane wave had positive helicity (for $\omega > 0$), f_2 may be called a helicity conserving amplitude, and g_2 helicity reversing [50].

In general, the helicity reversing amplitude is non-zero if a number of partial l-waves satisfy $\delta_l^+ \neq \delta_l^-$. This is the case for Schwarzschild scattering where phase shifts of opposite parity are related by

$$e^{2i\delta_l^+} = \frac{(l-1)l(l+1)(l+2) - 12i\omega M}{(l-1)l(l+1)(l+2) + 12i\omega M}\, e^{2i\delta_l^-}. \tag{2.128}$$

Since $e^{2i\delta_l^+} \sim e^{2i\delta_l^-} + O(l^{-4})$ as $l \to \infty$, large l modes will have a negligible contribution to g_2, and equation (2.126) could be expected to converge reasonably well.

Equation (2.128) was derived by Chandrasekhar [90]. It follows from the 'Chandrasekhar transformation' relating solutions of the Regge-Wheeler equation to solutions of the Zerilli equation (i.e. solutions of equation (2.75) with $p = -1$ and $p = +1$ respectively). Later it was realised that the Chandrasekhar transformation is an example of the more general Darboux transformation [132] [133].

Equations (2.125) and (2.126) were derived in [21] using the Newman-Penrose tetrad formalism throughout (also see references [41, 43]). The phase shifts were calculated by solving the radial Teukolsky equation [89], which reduces to the Bardeen-Press equation for a non rotating black hole [134]. Here we have mostly used the formalism of Martel and Poisson, providing a complementary derivation which may be interesting to current practitioners. We translate to spin-weighted harmonics and the tetrad formalism only at the final steps, which allows the GW energy flux (equation (2.121)), and hence the scattering cross section (equation (2.124)), to be seperated into a sum of two components. Our phase shifts are found by solving the Regge-Wheeler and Zerilli equations (equation (2.75)). It can be shown that these equations are related to the Bardeen-Press equation by another generalised Darboux tranformation [133, 135], which means our phase shifts are the same as those in e.g. reference [21] (provided we impose the same boundary conditions appropriate for a black hole scattering problem).

2.3.7 Absorption cross section

Here we derive the absorption cross section formula for a gravitational plane wave incident on a spherically symmetric compact body using the formalism of [87].

By conservation of energy, the net flow of energy of the GW across the body's surface is equal to the net flow of energy of the GW across any surface containing the body. For simplicity, let us consider a spherical surface with radius tending to infinity.

Integrating equation (2.112) over a sphere (multiplied by −1 since the surface should be oriented inwards), and making use of the properties of the MP spherical harmonics (see appendix A), we obtain

$$\left\langle \frac{dE}{dt} \right\rangle = \sum_{l,m,p} \left\langle \frac{dE}{dt} \right\rangle_{lmp}, \tag{2.129}$$

$$\left\langle \frac{dE}{dt} \right\rangle_{lmp} \equiv \frac{1}{32\pi}\frac{1}{2}(l-1)l(l+1)(l+2)\langle \partial_r \Phi_{lmp} \partial_t \bar{\Phi}_{lmp} \rangle. \tag{2.130}$$

The total solution behaves in the far field as

$$\Phi_{lmp}^{\text{total}} \sim d_{lmp} \left(C_{lp}^{-} e^{-i\omega r_*} + C_{lp}^{+} e^{i\omega r_*} \right) e^{-i\omega t}, \tag{2.131}$$

where d_{lmp} is determined by matching the ingoing component to the plane wave (section 2.3.5). Next, substituting equation (2.131) into equation (2.130) yields

(for $l \geq 2$)

$$\left\langle \frac{dE}{dt} \right\rangle_{lmp} = \begin{cases} \frac{H^2}{64}(2l+1)\left(1 - \left|\frac{C^+_{lp}}{C^-_{lp}}\right|^2\right), & m = \pm 2 \\ 0, & m \neq \pm 2 \end{cases}. \tag{2.132}$$

The absorption cross section is defined as

$$\sigma_{\text{abs}} \equiv \left\langle \frac{dE}{dt} \right\rangle \div \left.\frac{dE}{dt\,dA}\right|_{\text{plane}}. \tag{2.133}$$

It follows from equations (2.122), (2.129) and (2.132) that

$$\sigma_{\text{abs}} = \frac{\pi}{2\omega_0^2} \sum_{l,p} (2l+1)\Gamma_{lp\omega} \tag{2.134}$$

$$= \frac{2\pi^2}{\omega_0^2} \sum_{l,p} \left|{}_{-2}Y_{l2}(0)\right|^2 \Gamma_{lp\omega}, \tag{2.135}$$

where

$$\Gamma_{lp\omega} = 1 - \left|\frac{C^+_{lp}}{C^-_{lp}}\right|^2. \tag{2.136}$$

In the black hole case equation (2.134) is in agreement with the literature [21, 50].

2.4 Conclusions

In this chapter we have discussed scalar and gravitational perturbations on spherically symmetric background spacetimes.

Beginning with the scalar field, we have developed the scattering theory following FHM [21]. This includes the difficulty associated with defining a plane wave that arises due to the long range of the gravitational field. It was resolved by instead using a distorted plane wave analogous to Coulombic scattering studies.

Gravitational waves introduce additional technical difficulties associated with helicity and gauge invariance. Using the powerful perturbation formalism presented by Martel and Poisson [87] (which built on the work of others, see [136–139]), we have developed the scattering theory for compact bodies with a Schwarzschild vacuum exterior. We have derived the main quantities of interest, the scattering and absorption cross sections, and obtained agreement with previous work that used the Newman-Penrose tetrad formalism [21]. Our approach is in some ways less powerful, since it is limited to non-rotating spacetimes. However, an advantage is that it is reasonably simple to combine with perturbation formalisms already developed for non-vacuum spherically symmetric spacetimes, such as the interior of a star [29, 92, 98, 140]. It may also be a suitable starting point for an extension to scattering on slowly rotating, non-vacuum spacetimes [140].

The long range nature of the effective potential results in divergent partial wave sums that define the scattering amplitudes (equations (2.39) and (2.125)). This may be overcome by utilising the series reduction method of Yennie *et al.* [141], which was adapted for fundamental fields scattering from black holes by Dolan [50], and is immediately applicable to other compact objects. We will discuss this in more detail in chapters 3 and 4. In chapter 6 we discuss how complex angular momentum techniques can be used to sidestep this divergence issue in some situations.

With the theory presented in this chapter, we our now in a position to consider specific scattering models which will be the subject of chapters 3 to 5. In chapter 6 we discuss the complex angular momentum approach to scattering, and compare it with the partial wave methods discussed here.

Chapter 3

Rainbow scattering of scalar waves by a compact body

The atmospheric rainbow is a familiar yet fascinating everyday phenomena, due to the internal-reflection and refraction of light by water droplets. It has occupied the minds of many physicists, from René Descartes in the 17th century to present day practitioners [68, 142]. Descartes' considered parallel rays incident on a spherical water droplet. Using Snell's law, he concluded that rays undergoing one internal reflection were scattered by an angle Θ in the range $-180° \leq \Theta \lesssim -138°$ (an attractive scattering has a negative deflection angle by convention). Scattered rays are highly concentrated near the 'rainbow ray' at angle $\Theta_r = -138°$, and this is the heuristic explanation for the brightness of the rainbow. The rainbow ray is an envelope of the ray system, i.e., a caustic. The word caustic originates from the Greek verb *kaiein - to burn*.

This geometric optics model also accounts for the chromatic separation of the bow; different wavelengths of light are refracted different amounts when passing in and out of the water droplet, and so have slightly different values of Θ_r. According to geometric optics, the differential scattering cross section is divergent near an extrema of the deflection function, such as the rainbow angle. This infinity is 'softened' by taking into account diffraction of light. When conditions are favourable, it is sometimes possible to see a secondary rainbow, in which the colours are arranged in reverse order compared to the primary bow. This secondary bow is due to light rays that undergo two internal reflections. In theory, a tertiary bow also exists, but in practice it cannot be seen because it is so faint and it is washed out by glare from the Sun.

Another feature of rainbow scattering is supernumerary arcs, which required an explanation invoking the wave nature of light. Two rays of different impact parameter may be deflected by the same angle. In 1804 Young reasoned that, depending on the optical path difference between them, the two rays will interfere destructively or constructively. The optical path difference, and thus the interference, depends on the angle of observation. On the illuminated side of the rainbow angle, this interference effect leads to supernumerary peaks and troughs. For more on the mathematics of rainbows and the history, see the review by Adam [142] or Chapter 3 of the monograph by Nussenzveig [68].

Nuclear scattering experiments [67, 143] have shown a phenomena analogous to the atmospheric rainbow. An alpha particle incident on a light nuclei has a maximum possible deflection angle. Again, this leads to a singularity in the deflection function. In the quantum mechanics wave picture this singularity transmutes into a maximum in the differential scattering cross section. This has been observed in numerous experiments [67, 143]. Of course, a bow is not actually formed here, as there is only one scatterer, rather than a cloud of them. However, since the underlying mathematics is essentially the same, it is apt to refer to this as nuclear rainbow scattering. In their work on semi-classical scattering, Ford and Wheeler define any extrema of a classical deflection function as a ‘rainbow angle’, and scattering in the neighbourhood of a rainbow angle as ‘rainbow scattering’ [33].

This chapter outlines yet another regime where rainbow scattering can, at least in principle, occur. We find that a massless scalar wave incident on a compact object such as a neutron star will exhibit a rainbow interference pattern. A scalar field corresponds to a particle with zero spin, such as the Higgs boson or hypothetical cold dark matter candidates [144]. Higher spin fields, such as GWs or the electromagnetic field, may propagate in a similar fashion to the scalar wave. Since the massless scalar is the simplest field to investigate from a technical point of view, we choose to begin our scattering study with it.

Ray scattering is treated in section 3.2, and a semiclassical analysis is given in section 3.4 following reference [33]. A numerical method for the partial wave approach (outlined in chapter 2) is given in section 3.5. As with the atmospheric rainbow, using a range of complementary mathematical approaches to the problem is key to a full understanding. In chapter 4, we extend our analysis to gravitational waves and a variety of compact body models. We show that rainbow scattering is a generic feature of massless waves scattered by the gravitational field of horizon-less compact bodies. Part of this work is presented in references [62] and [64], and was done in collaboration with S.R. Dolan. All data and figures appearing in this chapter are the result of the authors own work.

3.1 Perfect fluid stars

Let u_μ be the four velocity of a fluid moving thorough spacetime. If each infinitesimal element of fluid has mass-energy density ρ, and isotropic pressure p in its rest frame, then it is called a perfect fluid. No heat conduction or viscosity is present in a perfect fluid (for more details see references [70, 131]). The stress-energy tensor of a perfect fluid is

$$T_{\mu\nu} = (\rho + p)u_\mu u_\nu + pg_{\mu\nu}. \tag{3.1}$$

We are considering a model where the fluid is static ($u^i = 0$), and since $u_\mu u^\mu = -1$, we have $u^t = (-g_{tt})^{-1/2}$. The next step is to solve Einstein's field equations (EFE)

$$G_{\mu\nu} = 8\pi T_{\mu\nu}, \tag{3.2}$$

where $G_{\mu\nu}$ is the Einstein tensor (see e.g. [70])

$$G_{\mu\nu} = R_{\mu\nu} - \frac{1}{2}Rg_{\mu\nu}. \tag{3.3}$$

It is convenient to define a function $m(r)$ in terms of the metric function B (see equation (2.2)) via

$$B(r) = 1 - \frac{2m(r)}{r}. \tag{3.4}$$

The (t,t) component of the EFE gives

$$\frac{1}{A}\frac{dA}{dr} = -\frac{2}{\rho + p}\frac{dp}{dr}, \tag{3.5}$$

and the (r,r) component gives

$$\frac{dm}{dr} = 4\pi r^2 \rho. \tag{3.6}$$

From the conservation of energy-momentum, ${T^{\mu\nu}}_{;\nu} = 0$, one can derive the Tolman-Oppenheimer-Volkov (TOV) equation of hydrostatic equilibrium for the interior of the star,

$$\frac{dp}{dr} = -\frac{(\rho + p)(m + 4\pi r^3 p)}{r(r - 2m)}. \tag{3.7}$$

For details see e.g. Chapter 10 of Schutz [131]. The system of equations (3.6) and (3.7) can be solved once an equation of state, $p(\rho)$, has been specified. The speed of sound inside a fluid is

$$c_s^2 = c^2 \frac{\partial p}{\partial \rho}, \tag{3.8}$$

where the derivative is taken at constant entropy S. A perfect fluid is adiabatic, i.e. the entropy of a fluid element remains constant, $u^\mu S_{,\mu} = 0$. This does not imply that S has the same values at all points. However, for the situations we wish to consider later (e.g. a typical cold white dwarf or neutron star), the temperature is effectively zero. Thus $kT \ll E_F$ where k is Boltzmann's constant and E_F is the Fermi energy. This means the system has only one state available to it (the ground state), and hence the entropy is zero everywhere within the model star. The constant entropy assumption allows us to use an equation of state of the form $p(\rho)$. For more details on this argument see e.g. Chapter 5 of [145] and Chapter 4 of [131].

3.1.1 Schwarzschild's interior solution

One of the earliest solutions to Einsteins equations was Schwarzschild's interior solution for an incompressible fluid [146]. It describes a spherically symmetric, perfect fluid ball of uniform density, and radius R. This serves as a simple, instructive model for a star. A constant density star of radius R and mass $M = m(R)$ has pressure,

$$p(r) = \rho \frac{\sqrt{3 - 8\pi R^2 \rho} - \sqrt{3 - 8\pi r^2 \rho}}{\sqrt{3 - 8\pi r^2 \rho} - 3\sqrt{3 - 8\pi R^2 \rho}}, \tag{3.9}$$

and density

$$\rho = \frac{3M}{4\pi R^3}. \tag{3.10}$$

With the density and pressure in hand, the metric functions are found using equations (3.4) to (3.6),

$$A(r) = \begin{cases} \dfrac{1}{4R^3}\left(\sqrt{R^3 - 2Mr^2} - 3R\sqrt{R - 2M}\right)^2, & r \leq R \\ 1 - \dfrac{2M}{r}, & r > R \end{cases}, \tag{3.11}$$

and

$$B(r) = \begin{cases} 1 - \dfrac{2Mr^2}{R^3}, & r \leq R \\ 1 - \dfrac{2M}{r}, & r > R \end{cases}. \tag{3.12}$$

The metric function $A(r)$ and its first derivative are both continuous across $r = R$, but the second derivative is discontinuous. The metric function $B(r)$ is continuous and its first derivative is discontinuous across $r = R$. We shall see later that this has important implications for solving the field equations for perturbations at the stellar surface. The discontinuity in B' and A'' at $r = R$ can be traced back to the fact that $\rho(R) \neq 0$ (see equations (3.4) to (3.7)).

Schwarzschild showed that [146], in order for the pressure to be finite at the origin, a constant density star must satisfy the bound

$$R/M > 9/4. \tag{3.13}$$

Buchdahl showed that this bound also applies to any perfect fluid sphere with a barotropic equation of state and a monotonically decreasing density $\rho(r)$ [111]. Known as ”Buchdahl's bound”, equation (3.13) was strengthened to $R/M > 8/3$ by imposing the dominant energy condition [147]. This was further improved by also demanding a sublimnal speed of sound, which resulted in a numerically calculated constraint $R/M \gtrsim 2.74997$ [148]. Compact bodies can be characterised by their 'tenuity' α, or inverse compactness,

$$\alpha \equiv R/M. \tag{3.14}$$

Some typical and instructive tenuities are summarised in table 3.1 using geometric units. For a Schwarzschild black hole, one can use the gravitational (event horizon) radius, R_s to obtain a 'tenuity' to compare with stellar objects, $R_s/M = 2$. The Buchdahl bound implies that there is not a sequence of equilibrium solutions with α tending towards the black hole tenuity. However, in the case of anisotropic stars [149], α can become arbitrarily close to 2. Yagi and Yunes have considered a sequence of such anistropic stars in the context of I-Love-Q relations which relate the bodies moment of inertia, tidal deformability, and quadrupole moment [150]. The I-Love-Q relations are exact for black holes, and approximate for compact stars. It may be interesting to consider this sequence in other contexts such as scattering, but here we focus only on isotropic models. The progenitor neutron stars from the binary merger detected by the LIGO collaboration [2, 151] have tenuities that fall in the range $4.4 \lesssim \alpha \lesssim 7.7$ with 90% credibility (assuming that the equation of state must support stars with mass greater than $1.97M_\odot$ as required by electromagnetic observations [152]).

	Earth	Sun	typical white dwarf	massive white dwarf (Sirius B)	neutron star	Buchdahl's bound
R/M	1.4×10^9	4.7×10^5	9.4×10^3	1.4×10^3	≈ 6	$> 9/4$

Table 3.1: Typical tenuities R/M for astrophysical objects, and Buchdahl's bound for a perfect fluid sphere [111].

3.2 Geodesics

Geodesics are the paths taken by particles under the influence of no forces except gravity (which isn't regarded as a force in general relativity). The geodesic equation can be derived using the principle of least action. A typical choice of the action $\hat{S}$ is the space-time interval between two events

$$\hat{S} = \int \sqrt{-g_{\mu\nu}\frac{dx^\mu}{d\sigma}\frac{dx^\nu}{d\sigma}}\, d\sigma, \tag{3.15}$$

where σ is an affine parameter. One could also choose the action

$$\hat{S}' = \int \mathcal{L}\, d\sigma, \tag{3.16}$$

with the Lagrangian

$$\mathcal{L} = \frac{1}{2} g_{\mu\nu}\frac{dx^\mu}{d\sigma}\frac{dx^\nu}{d\sigma}. \tag{3.17}$$

Varying the action of equation (3.16) with respect to the world line x^μ, yields the Euler-Lagrange equations

$$\frac{\partial \mathcal{L}}{\partial x^\mu} - \frac{d}{d\sigma}\frac{\partial \mathcal{L}}{\partial \dot{x}^\mu} = 0, \tag{3.18}$$

where a dot denotes differentiation with respect to σ. For the Lagrangian of equation (3.17) the Euler-Lagrange equations give the geodesic equation

$$\frac{d^2 x^\mu}{d\sigma^2} + \Gamma^\mu{}_{\alpha\beta}\frac{dx^\alpha}{d\sigma}\frac{dx^\beta}{d\sigma} = 0, \tag{3.19}$$

where ${\Gamma^\mu}_{\alpha\beta}$ is the Christoffel symbol

$$
{\Gamma^\mu}_{\alpha\beta} \equiv \frac{1}{2} g^{\mu\nu} \left(g_{\nu\alpha,\beta} + g_{\nu\beta,\alpha} - g_{\alpha\beta,\nu} \right). \tag{3.20}
$$

If the metric is independent of a coordinate x^μ then so is $\mathcal{L}$. Thus by equation (3.18)

$$
\frac{\partial \mathcal{L}}{\partial \dot{x}^\mu} = \text{constant}. \tag{3.21}
$$

For the spherically symmetric metric expressed in Schwarzschild coordinates (equation (2.2)) there are two constants of motion that follow from this reasoning

$$
\hat{E} \equiv A\dot{t}, \qquad \hat{L} \equiv r^2 \dot{\phi}. \tag{3.22}
$$

A projectile incident from infinity with velocity v has impact parameter b related to the constants of motion via

$$
b = \frac{\hat{L}}{v\hat{E}}. \tag{3.23}
$$

We are interested in null geodesics, and the null condition $\mathcal{L} = 0$ implies

$$
\dot{r}^2 = BA^{-1} \left(\hat{E}^2 - V_{\text{geo}}(r) \right), \qquad V_{\text{geo}}(r) \equiv A\hat{L}^2/r^2. \tag{3.24}
$$

A re-parametrisation defined by $d\lambda/d\sigma = \sqrt{B/2A}$ gives

$$
\frac{1}{2} \left(\frac{dr}{d\lambda} \right)^2 + V_{\text{geo}}(r) = \hat{E}^2, \tag{3.25}
$$

which can be recognised as the equation for a classical unit mass particle with energy $\hat{E}^2$ in a one dimensional potential $V_{\text{geo}}(r)$. It is natural to think of V_{geo} as an effective potential for the radial geodesic motion. From figure 3.1, it can be seen that $V_{\text{geo}}(r)$ has no stationary points for $R > r_c = 3M$; one stationary point for $R = r_c$; and two for $R < r_c$. When there are two stationary points, the outer ($r = r_c$) corresponds to an unstable circular null orbit (or rather, a family of circular orbits known as a 'photon sphere'). The inner stationary

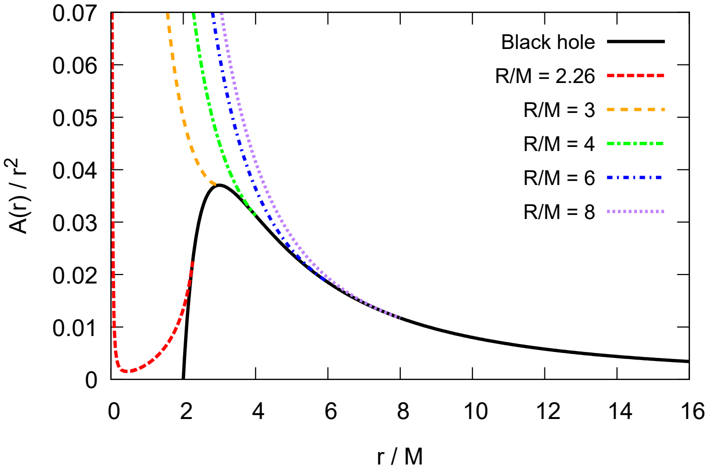

Figure 3.1: Null geodesic effective potential $V_{\text{geo}}/\hat{L}^2 = A(r)/r^2$, for a black hole and for constant density stars of radius $R = 2.26M$, $3M$, $4M$, $6M$ and $8M$.

point corresponds to a stable circular null orbit. The circular null orbits may alse be referred to as 'light rings'. When there is one stationary point, it is an inflection, and corresponds to the unstable light ring at $r = r_c$.

One immediate result from equation (3.24) for an object of radius R is the null grazing-ray impact parameter ($v = c = 1$),

$$b_{gr} = \frac{R}{\sqrt{1 - 2M/R}}, \tag{3.26}$$

defined by the requirement that $\dot{r} = 0$ at $r = R$. Another is the critical impact parameter for objects that posses a light ring,

$$b_c = \sqrt{27}M, \tag{3.27}$$

defined by the requirement that $\dot{r} = 0$ at $r = r_c$.

A null ray incident from infinity will be deflected by an angle

$$\Theta_{\text{geo}} \equiv \pi - \Delta\phi, \tag{3.28}$$

where $\Delta\phi$ is the change in ϕ along the geodesic

$$\Delta\phi = 2\int_{r_0}^{\infty} \frac{\hat{L}}{r^2\sqrt{\hat{E}^2 - V_{\text{geo}}(r)}}\sqrt{\frac{A}{B}}dr, \tag{3.29}$$

and r_0 is the (outer) turning point that satisfies $V_{\text{geo}}(r_0) = \hat{E}^2$. It can be seen that the deflection function is a function of only one constant, the impact parameter b,

$$\Theta_{\text{geo}}(b) = \pi - 2b\int_{r_0}^{\infty} \frac{1}{r^2\sqrt{1 - Ab^2/r^2}}\sqrt{\frac{A}{B}}dr. \tag{3.30}$$

With the deflection function it is possible to calculate the classical scattering cross section (for a corpuscular theory of massless particles),

$$\left.\frac{d\sigma}{d\Omega}\right|_{\text{cl}} = \sum_i \frac{b_i}{\sin\theta\left|\frac{d\Theta_{\text{geo}}}{db}\right|}, \tag{3.31}$$

where the sum over i takes into account rays with different impact parameter scattered by the same net deflection angle. Here we distinguish between the angle of observation $\theta \in [0, \pi]$ and the angle of deflection Θ, related by

$$\theta = |\Theta| \bmod \pi. \tag{3.32}$$

Many features of wave scattering can be understood with reference to the geodesic deflection function and classical cross section. We show the deflection function for a variety of stars and a Schwarzschild black hole of the same mass in figure 3.2. The integral on the right hand side of equation (3.30) is evaluated numerically. A ray with impact parameter $b = 0$ is not deflected, and as $b \to \infty$, $\Theta_{\text{geo}}(b) \to 0$. Like the potential, the deflection functions can be classified according to the stars radius R/r_c.

If $R > r_c$, then at some finite value b_r, the deflection function has a global minimum Θ_r, and we could expect to find rainbow scattering. The wave-optics argument of Young applied to the scattering of light rays by water droplets

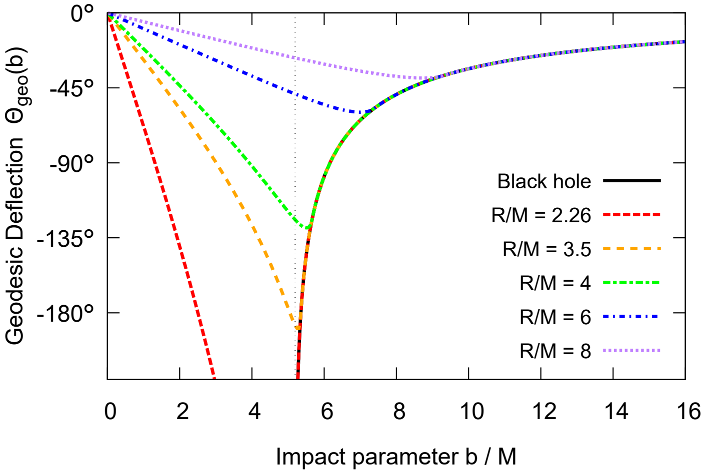

Figure 3.2: The geodesic deflection functions for a constant density star with a range of tenuities R/M, as well as a Schwarzschild black hole. The vertical line corresponds to the critical impact parameter b_c (see equation (3.27)).

translates to the scattering of a massless field (such as the electromagnetic field) plane wave by a compact body in general relativity. In this scenario, rays with impact parameter either side of b_r may be deflected to the same angle $\Theta > \Theta_r$. The path difference of the two rays varies with Θ and should give rise to supernumerary peaks and troughs. The classical cross section (equation (3.31)) diverges at the rainbow angle, which softens into the primary bow for wave scattering.

We find the rainbow impact parameter b_r numerically, and for the models we consider it satisfies $b_r \approx b_{gr}$, where b_{gr} is the grazing impact parameter of equation (3.26). Thus, for deflection functions with only one minimum ($R > r_c$) we can loosely associate the branches either side of the minimum to rays that pass through the body ($b < b_{gr}$) and rays that pass through the exterior only ($b > b_{gr}$).

If $R \leq r_c$, then there is a divergence in the deflection function at the critical impact parameter b_c of equation (3.27). The same divergence is also present in the deflection function for a Schwarzschild black hole. In both cases, it arises due to the presence of the unstable null orbit. An incoming ray with critical impact parameter asymptotes to the unstable circular orbit, and in principle can be deflected by an arbitrarily large angle. Interference between rays deflected by $\theta, \theta + 2\pi, ... \theta + 2\pi k$, where k is an integer, gives rise to the 'orbiting' phenomena seen in black hole wave scattering studies [21, 37, 45].

A further category is bodies with $R \lesssim 3.5M$ (which may or may not satisfy $R \leq r_c = 3M$). The deflection function for these cases passes through $-\pi$ (see figure 3.2). The value $R \approx 3.5M$ is found by calculating the deflection functions for each model (parametrised by R/M) and searching for the root of $\Theta_r(R/M) = -\pi$. The solution for our model is $R/M = 3.554$ to three decimal places. According to ray theory, there is a divergence in the differential scattering cross section (equation (3.31)) whenever the deflection function passes through a multiple of π. Let the impact parameter b_π correspond to the ring of rays that completely back scatter so that $\Theta_{\text{geo}}(b_\pi) = -\pi$. Heuristically, if we consider a wave as a congruence of rays, then rays with $b = b_\pi$ will focus onto the point on the celestial sphere corresponding to the centre of the incoming wave, and constructively interfere. This constructive interference is called a *backwards glory.* Sanchez discovered the backwards glory was a feature of black hole scattering in the 70s [37]. More recently, Crispino *et al.* proposed that one could infer a black hole's charge from the backscattered electromagnetic radiation in a plane wave scattering scenario [53].

Like the rainbow, the word glory has its origin in an atmospheric phenomena, which may be seen from above the clouds when the sun is directly behind the observer. The sunlight is backscattered by the water droplets in the cloud, and the observer will see a shadow of themselves surrounded by a bright halo of light. We will present numerical evidence for glory scattering by compact bodies in section 3.6.

Figure 3.3 shows a congruence of rays with varying impact parameter, impinging from the left hand side onto a star of tenuity (a) $\alpha = 6$ and (b) $\alpha = 8$. As the tenuity is increased, the rainbow impact parameter increases, and the rainbow angle decreases. We can see that the rainbow ray has a distance of closest approach that is just inside the star's surface. At this point it is worth mentioning that we assume no interaction between the massless particle and the compact body, other than that conveyed by the gravitational field of the

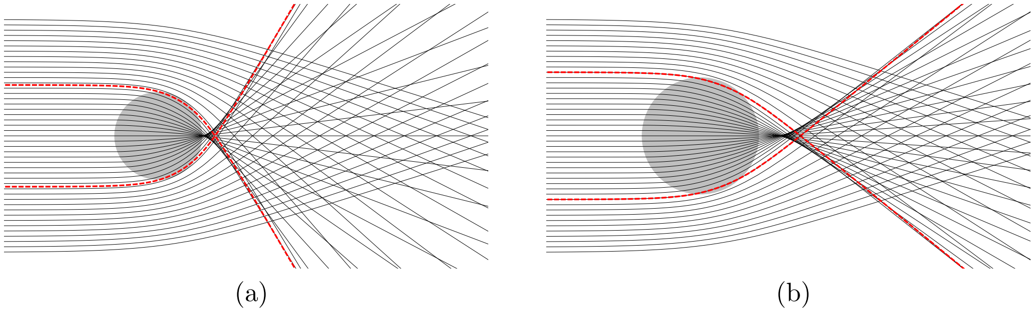

(a)

(b)

Figure 3.3: A congruence of geodesics incident on a constant density star with radius (a) $R = 6M$ and (b) $R = 8M$. In dashed red is the rainbow ray, which forms a caustic downstream where it is the envelope of the outgoing rays.

body. This is not justified if one wants to consider light scattering off any visible astrophysical object. It is however a useful approximation for gravitational wave scattering, or other weakly interacting, light matter fields such as the neutrino. Another more speculative scenario this could provide a toy model for is scattering by dark objects, such as dark matter boson stars.

3.3 Geometric optics

Why should we believe that geodesic motion sheds any light on the question of scalar field scattering? One argument has its origins in the study of light propagation. For high-frequency electromagnetic waves one can use the geometric optics approximation (see chapter 3 of reference [153]). In geometric optics the energy of a wave is transported along straight lines corresponding to light rays (for a homogeneous medium). The main quantities of interest are thus the rays themselves, and the concentration of them which will determine the amplitude of the wave at a given point. Light rays may be bent by inhomogeneous media with varying refractive index. “High-frequency” waves is short hand for the assumption that the wavelength is small in comparison to other relevant length scales, and the inverse frequency is small in comparison to relevant time scales.

Geometric optics is the usual approach used when considering light propagation on curved space-time [70, 154] as well as for flat space. This approximation approach can also be applied to other perturbative fields on curved backgrounds such as the scalar and gravitational fields [155]. In all cases, the energy of the wave is transported along massless geodesics. The radiation intensity varies according to the change in cross-sectional area of an infinitesimal area element on the wave-front. We will summarise the important elements of the method for the scalar field following Dolan [155]. The geometric optics ansatz for the scalar field Φ is

$$\Phi = \mathcal{A} \exp(i\omega\Psi), \tag{3.33}$$

where $\mathcal{A}$ is the amplitude, Ψ is the phase, and ω is related to the frequency but we may regard it as an order counting parameter. Substituting equation (3.33) into equation (2.3) yields

$$(-\omega^2 k^\mu k_\mu \mathcal{A} + i\omega(2k^\mu \nabla_\mu \mathcal{A} + \nabla_\mu k^\mu \mathcal{A}) + O(\omega^0) = 0, \tag{3.34}$$

where $k_\mu \equiv \nabla_\mu \Psi$ is the gradient of the phase. Solving equation (3.34) order by order in ω, the leading order term tells us that k^μ is a null vector field ($k^\mu k_\mu = 0$). The null condition, and the fact that k^μ is a gradient implies that it satisfies the geodesic equation, $k^\nu \nabla_\nu k_\mu = 0$. The integral curves of k^μ are spacetime paths $x^\mu(\sigma)$ that satisfy $\frac{dx^\mu}{d\sigma} = k^\mu$, and they are geodesics which lie in a hypersurface of constant phase ($\Psi(x) = \text{constant}$). At order ω, equation (3.34) yields a transport equation

$$k^\mu \nabla_\mu \mathcal{A} = -\frac{1}{2}\vartheta \mathcal{A} \tag{3.35}$$

where $\vartheta \equiv \nabla_\mu k^\mu$ is the expansion scalar. Equation (3.35) ensures the conservation of flux $\nabla_\mu(\mathcal{A}^2 k^\mu) = 0$.

Here we have shown that a congruence of geodesics can at least give a qualitative picture of high frequency scalar wave scattering. One can trace a constant phase wave front, and the concentration of rays at a point indicates the waves amplitude. A more detailed picture is given by Dolan [155].

Perhaps the key feature of our scattering scenario is caustic points (e.g.

the cusp in figure 3.3). The leading order geometric optics approach suffers from divergences at such caustics, and we have not pursued this analysis any further partly for this reason. Instead, to gain quantitative information about the wave propagation using geodesics, we have found it fruitful to use a high frequency approximation applied to the individual radial scalar modes, inspired by semiclassical scattering studies [33, 156].

3.4 Semiclassical scattering

In this section we show how Ford and Wheeler's semiclassical scattering analysis [33], which provides a link between quantum and classical atomic scattering, can be adapted to translate between the scalar plane wave scattering model of chapter 2 and the geodesic congruence model in section 3.2. Note that Nussenzweig uses an analogous 'semiclassical' approach to understand classical scattering of high frequency electromagnetic waves [68], in terms of rays. In addition, Handler and Matzner adapted Ford and Wheeler's methods to scattering of GWs by Kerr black holes [38].

This approximation method is distinct from the geometric optics approach of e.g. [155], in that it is applied at the level of the radial scalar equation equation (2.8), which resembles the time independent Schrödinger equation

$$\frac{\hbar^2}{2m}\frac{d^2\psi}{dr^2} + \left[E - V(r)\right]\psi = 0, \tag{3.36}$$

where E is the energy of a particle with mass m subject to a radial potential $V(r)$. Ford and Wheeler solve equation (3.36) using a Wentzel–Kramers–Brillouin (WKB) approximation. The particles de Broglie reduced wavelength is

$$\lambda\!\!\!^{-} \equiv \frac{\hbar}{\sqrt{2m(E-V)}}. \tag{3.37}$$

For the WKB solution to be valid, we must have $\lambda\!\!\!^{-}$ short in comparison to characteristic length scales for significant variation of the potential. Provided the potential is well behaved this will be the case in the semiclassical limit

$\hbar \to 0$, except near classical turning points where $E - V = 0$. By comparing equation (2.8) with equation (3.36), we see that the corresponding condition for a WKB analysis to be valid for a scalar radial mode we must have

$$\frac{1}{\sqrt{\omega^2 - V_l^{\text{eff}}}} \ll \frac{1}{V_l^{\text{eff}}}\frac{dV_l^{\text{eff}}}{dr}. \tag{3.38}$$

For high frequencies, this condition will be satisfied except at 'classical turning points' r_{tp} which are solutions of $\omega^2 = V_l^{\text{eff}}(r_{\text{tp}})$. For the compact bodies with $R > 3M$, we have only one turning point r_0. In this case a standard 'patching' procedure can be applied to match the WKB solutions either side of it, obtaining a global approximation (a.k.a. WKB connection formulae, see chapter 10 of reference [157]). Then, applying the regularity boundary condition at the origin, yields the WKB phase shift [157],

$$\delta_L^{\text{wkb}} = \frac{L}{2}\pi - \omega r_0^* + \int_{r_0^*}^{\infty}\left\{\sqrt{\omega^2 - V_L^{\text{wkb}}(r)} - \omega\right\} dr_*, \tag{3.39}$$

where

$$V_L^{\text{wkb}}(r) \equiv A\left(\frac{L^2}{r^2} + \frac{B}{2r}\left(\frac{A'}{A} + \frac{B'}{B}\right)\right), \tag{3.40}$$

and we define $L \equiv l + 1/2$ and $r_0^* = r_*(r = r_0)$. Here we have used the 'Langer substitution' $l(l+1) \to (l+1/2)^2$ to obtain increased accuracy [158]. The substitution results in $V_l^{\text{eff}} \to V_L^{\text{wkb}}$. Note that,

$$2\frac{d}{dL}\left[\delta_L^{\text{wkb}}\right] = \pi - 2\int_{r_0}^{\infty}\frac{L}{r^2\sqrt{\omega^2 - V_L^{\text{wkb}}}}\sqrt{\frac{A}{B}}dr, \tag{3.41}$$

which is the same form as equation (3.30) for the geodesic deflection function $\Theta_{\text{geo}}(b)$. This suggests a correspondence between the wave and ray picture, whereby partial waves and geodesics are associated via the mapping

$$\frac{L}{\omega} \leftrightarrow b, \tag{3.42}$$

and one can define a WKB deflection function

$$\Theta_{\rm wkb} \equiv 2\frac{d}{dL}\left[\delta_L^{\rm wkb}\right]. \tag{3.43}$$

Under the mapping of equation (3.42), $V_L^{\rm wkb} \leftrightarrow V_{\rm geo} + O(\omega^{-2})$, and we may expect $\Theta_{\rm wkb} \approx \Theta_{\rm geo}$ in the high frequency regime.

3.4.1 Semiclassical scattering cross section

A further assumption of the semiclassical approach is to use large-l asymptotics for the Legendre polynomials,

$$P_l(\cos\theta) \approx \begin{cases} \left(\frac{1}{2}L\pi\sin\theta\right)^{-1/2}\sin\left(L\theta+\pi/4\right), & L\sin\theta \gtrsim 1 \\ (\cos\theta)^{L-1/2}J_0(L\theta), & L\sin\theta \lesssim 1 \end{cases}, \tag{3.44}$$

where J_n is a Bessel function of the first kind [117]. Note that the scalar scattering amplitude of equation (2.39) can be decomposed into a sum of two amplitudes, the first of which we call $\hat{f}_0(\theta)$ which satisfies [159]

$$\hat{f}_0(\theta) \equiv \sum_{l=0}^{\infty}(2l+1)P_l(\cos\theta) = 2\delta(\cos\theta - 1). \tag{3.45}$$

Using the WKB phase shifts in equation (3.39), equations (3.44) and (3.45), and provided we are not at the poles, the scattering amplitude summation in equation (2.39) can be written as

$$\hat{f}_{\rm sc}(\theta) = -\frac{1}{2\omega}\sum_{l=0}^{\infty}\left(\frac{2L}{\pi\sin\theta}\right)^{1/2}\left(e^{i\Phi_+} - e^{i\Phi_-}\right), \tag{3.46}$$

where

$$\Phi_\pm(L) \equiv 2\delta_L^{\rm wkb} \pm \left(L\theta + \frac{\pi}{4}\right). \tag{3.47}$$

Following Mott and Massey [118], a series of the form

$$\sum_{L=0}^{\infty} X(L) e^{i\Phi(L)}, \tag{3.48}$$

may be well approximated if there is a unique value L_0 such that $\Phi'(L_0) = 0$, where $' \equiv d/dL$ for this section. In this case, the dominant contribution to the sum comes from L values near L_0, and

$$\sum_{L=0}^{\infty} X(L) e^{i\Phi(L)} \approx X(L_0) e^{i\Phi(L_0)} \int_{-\infty}^{\infty} e^{i(L-L_0)^2 \Phi''(L_0)/2}\, dL \tag{3.49}$$

$$\approx X(L_0) e^{i\Phi(L_0)} \left(\frac{2\pi}{i\Phi''(L_0)} \right)^{1/2}, \tag{3.50}$$

where the second line is the stationary phase approximation. The requirement $\Phi'_\pm(L_0) = 0$ is equivalent to

$$\Theta_{\mathrm{wkb}}(L_0) \pm \theta = 0. \tag{3.51}$$

In other words, the scattering cross section at a given angle θ has its main contribution from partial waves with $L \approx L_0$, which have WKB deflection angles $\Theta_{\mathrm{wkb}} \approx \pm\theta$. By convention an attractive deflection corresponds to $\Theta < 0$, and a repulsive deflection corresponds to $\Theta > 0$. Assuming that each partial wave has a unique WKB deflection, then the semiclassical scattering amplitude is

$$\hat{f}_{\mathrm{sc}}(\theta) = -\frac{1}{2\omega} \left(\frac{2L_0}{i\Theta'_0 \sin\theta} \right)^{1/2} \left(\pm e^{\pm i\Phi_\pm} \right), \qquad \Theta'_0 \equiv \left. \frac{d\Theta_{\mathrm{wkb}}}{dL} \right|_{L=L_0}, \tag{3.52}$$

where the choice of sign is dictated by the condition $\Phi'_\pm(L_0) = 0$. The differential scattering cross section is then

$$\frac{d\sigma^{\mathrm{sc}}}{d\Omega} = \left| \hat{f}_{\mathrm{sc}}(\theta) \right|^2 = \frac{L_0}{\omega^2} \frac{1}{\sin\theta\, |\Theta'_0|} \leftrightarrow \frac{b_0}{\sin\theta \left| \frac{d\Theta}{db} \right|_{b=b_0}}. \tag{3.53}$$

We see that in this special case (when the scattering angle is not too near π or 0, and when there is only one point of stationary phase), the semiclassical and classical cross sections (equation (3.31)) are identical under the mapping of equation (3.42). This provides further justification for associating partial waves with rays in this way.

3.4.2 Interference effects

From figure 3.2, we can see that for $\theta < |\Theta_r|$ there will be two points of stationary phase for scattering by a star, and the deflection function may pass through $-\pi$. Whilst the semiclassical analysis becomes more complicated in these cases, it also reveals the rich interference structure of the scattering cross section. We discuss three phenomena - rainbows, glories and oscillating - that can be seen in the scattering pattern. These are defined in full generality in works by Ford and Wheeler [33], Mott and Massey [118], and Berry and Mount [156], from which we draw heavily in this section.

Let a point of stationary phase correspond to impact parameter b_i, angular momentum L_i, phase shift δ_i, deflection function Θ_i with derivative Θ_i', and $\phi_\pm^i \equiv \phi_\pm(L_i)$. Suppose for the case discussed above ($\theta < |\Theta_r|$), that the two points of stationary phase are well separated, $|L_1 - L_2| \gg 1$, then each contribution can simply be summed to find the scattering amplitude. The cross section is the sum of the two classical contributions (see equation (3.53)) and an interference term:

$$\begin{aligned}\frac{d\sigma}{d\Omega} &\approx \frac{1}{4\omega^2 \sin\theta}\left(\sum_{j=1}^{2} \frac{L_j}{|\Theta_j'|} + 2\cos\left(\phi_+^1 - \phi_+^2\right)\left(\frac{L_1 L_2}{\Theta_1' \Theta_2'}\right)^{1/2}\right) \\ &\leftrightarrow \left.\frac{d\sigma}{d\Omega}\right|_{\mathrm{cl}} + \sqrt{\sigma_1^{\mathrm{cl}}\sigma_2^{\mathrm{cl}}}\cos\left[2\left(\delta_1 - \delta_2\right) + \left(b_1 - b_2\right)\omega\theta\right]. \end{aligned} \tag{3.54}$$

where σ_i^{cl} is the classical contribution to the scattering cross section from each ray b_i, i.e. $\left.\frac{d\sigma}{d\Omega}\right|_{\mathrm{cl}} = \sigma_1^{\mathrm{cl}} + \sigma_2^{\mathrm{cl}}$. Note how the frequency of the wave sets the angular width of the oscillating interference term, since in the high frequency limit $\delta_i \ll b_i\omega$.

Recall that for $R > r_c$, there is a global minimum i.e. a rainbow angle Θ_r. For scattering near Θ_r, the parts of the wave that contribute significantly will overlap and we cannot use equation (3.54). Reference [33] details how to derive an approximation that applies near stationary points of Θ_{wkb}, known as Airy's formula

$$\frac{d\sigma}{d\Omega} \approx \frac{2\pi b_r}{\omega q^{2/3} \sin\theta} \mathrm{Ai}^2 \left[(\theta - \Theta_r) q^{-1/3} \right], \qquad q \equiv \frac{\Theta_r''}{2\omega^2}. \tag{3.55}$$

The Airy function is characterised by an oscillating behaviour for large negative argument, and an exponential fall of for large positive argument. This behaviour predicts supernumerary peaks and troughs below the rainbow angle, and a fall off into the shadow zone $\Theta > \Theta_r$. It is interesting that $\Delta\theta = q^{1/3} = [\Theta_r''/(2\omega^2)]^{1/3}$ defines the separation of the supernumerary peaks, and how close the primary peak θ_{p} is to the rainbow angle,

$$\theta_{\mathrm{p}} \approx \Theta_r - 1.01879\Delta\theta \;\rightarrow\; \Theta_r \quad \text{as} \quad \omega \rightarrow \infty. \tag{3.56}$$

It also predicts an intensity at the peak of

$$\left.\frac{d\sigma}{d\Omega}\right|_{\mathrm{p}} \approx 0.286928 \frac{2\pi b_r}{\omega q^{2/3} \sin\theta_p} \tag{3.57}$$

which will diverge in the high-frequency limit. These conclusions are analogous to Airy's original analysis of light scattered by water droplets, where he predicted the (finite) amplitude of the primary atmospheric rainbow, the possibility of supernumerary arcs, and a faster than exponential fall-off of intensity into the classical shadow zone.

If $R \lesssim 3.5M$, the deflection function passes through $-\pi$ (figure 3.2). Scattering near $-\pi$ is referred to as glory scattering (see section 3.2 and [36, 38]. For a Schwarzschild black hole, we see in figure 3.2 that their is a unique glory impact parameter b_g which corresponds to a ray being completely back-scattered. In this case, a semiclassical formula for scattering near the glory angle can be calculated by approximating the form of the deflection function near b_g and using the approximation for Legendre polynomials valid near the poles (see equation (3.44)) [33, 38, 51]. For $\theta \approx \pi$, the scattering amplitude is found to be

$$f_{\mathrm{BH}}(\theta) \approx b_g \left(2\pi\omega \left|\frac{db}{d\Theta}\right|\right)^{1/2} \exp\left[i\left(2\delta_g - \pi\omega b_g\right)\right] J_0(b_g \omega \sin\theta). \tag{3.58}$$

Semiclassical formulae for glory scattering cross sections of massless plane waves on curved spacetimes were also found using a path integration method by Matzner and co-workers [40]. They found a formula for all spins

$$\frac{d\sigma}{d\Omega}_{\mathrm{BH}} \approx 2\pi\omega b_g^2 \left|\frac{db}{d\Theta}\right| J_{2s}^2(b_g\omega\sin\theta), \quad \theta \approx \pi. \tag{3.59}$$

In contrast to the black hole, the deflection function for a very compact body has two branches that pass through $-\pi$. In effect then we have two glories, with associated impact parameters b_{g1} and b_{g2}. Assuming the ray with impact parameter $b_{g2} > b_{g1}$ does not penetrate the interior spacetime of the star, then $b_{g2} = b_g$, and the 'outer glory' effect will be similar to the black hole glory. Since the two contributions are well separated ($|b_{g1} - b_{g2}| \gg 1/\omega$) a valid approximation in this scenario is to simply sum the two glory amplitudes,

$$\begin{aligned}\frac{d\sigma}{d\Omega}_{\mathrm{CO}} \approx& \sum_{n=1}^{2}\left[2\pi\omega b_{gn}^2 \left|\frac{db}{d\Theta}\right|_{b_{gn}} J_0^2(b_{gn}\omega\sin\theta)\right] \\ &+ 2\cos\left[2i(\delta_{g1}+\delta_{g2}) - i\pi\omega(b_{g1}+b_{g2})\right] \prod_{n=1}^{2} 2\pi\omega b_{gn} \left|\frac{db}{d\Theta}\right|_{b_{gn}} J_0(b_{gn}\omega\sin\theta),\end{aligned} \tag{3.60}$$

when $\theta \approx \pi$.

If $R \leq 3M$, the deflection function has a singularity at $b_c = \sqrt{27}M$. The radial effective potential will have three classical turning points for $R < 3M$, and the WKB analysis becomes significantly more involved. Ford and Wheeler concluded that "*there is no semiclassical approximation to the orbiting effect of simplicity or generality comparable to the analysis for rainbow scattering and glory scattering*" [33]. However, recently, Folacci and Ould El Hadj have derived a high-frequency analytical approximation for glory scattering by black holes,

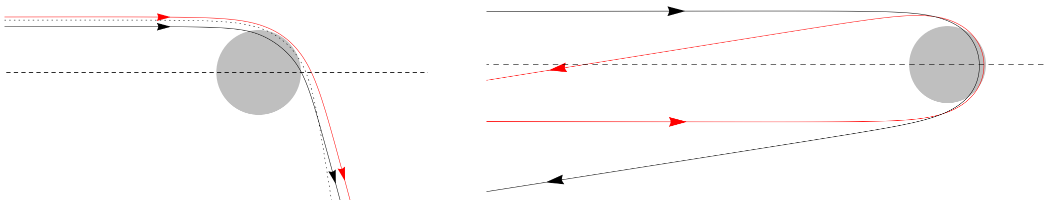
(a) (b)

Figure 3.4: Considering a plane wave as a congruence of geodesics, we can gain a simple picture of the interference phenomena present in the full partial wave numerical analysis. Heuristically, different parts of the wave front scatter to the same angle causing an interference effect such as: (a) rainbow scattering - shown here for a compact body with $R/M = 5$; or (b) a backwards glory - shown here for a compact body with $R/M = 3.5$. Two rays with a deflection $-\pi \pm \delta\theta$, circumventing the body in opposite directions will be deflected to the same observation angle.

based on complex angular momentum techniques [57, 58]. We will postpone further discussion of complex angular momentum until chapter 6.

3.4.3 Geodesic phase shifts

With the correspondence between high frequency wave scattering and geodesics established, it is possible to define 'geodesic phase shifts' δ_l^{geo} in a natural way (see equation (3.43)),

$$\delta_l^{\text{geo}} = \frac{1}{2}\omega \int_0^b \Theta_{\text{geo}}(b')db' + \chi_0, \tag{3.61}$$

where χ_0 is an integration constant which can be fixed by matching to the numerical partial-wave results in the weak-field regime ($b \gg M$) if necessary. We compute $\Theta_{\text{geo}}(b)$ numerically on a grid $0 \leq b \leq b_{\text{max}}$, then interpolate and integrate to obtain δ_l^{geo}.

On a Schwarzschild black hole, the deflection function is known in terms of elliptic integrals. For $b \gg 1$ it is possible to obtain a series expansion (as in e.g. [160]),

$$-\Theta_{\text{geo}}(b) = \frac{4M}{b} + \frac{15\pi M^2}{4b^2} + \frac{128M^3}{3b^3} + \frac{3465\pi M^4}{64b^4} + \frac{3584M^5}{5b^5} + O(b^{-6}). \quad (3.62)$$

Integrating equation (3.62) gives a series for geodesic phase shifts on Schwarzschild,

$$\delta_l^{\text{geo}} = M\omega\left(-2\ln\left(\frac{b}{M}\right) + \frac{15\pi M}{8b} + \frac{32M^2}{3b^2} + \frac{1155\pi M^3}{128b^3} + \frac{448M^4}{5b^4} + O(b^{-5})\right) + \chi_1, \quad (3.63)$$

where we have introduced the constant of integration χ_1.

We expect the geodesic phase shifts to be independent of the nature of the spherically symmetric body (only depending on M) in the limit $b \to \infty$. Rays with large impact parameter ($b > b_g$ where b_g is the 'grazing ray') will not 'feel' the spacetime region inside the classical turning point i.e. the geodesic does not penetrate the interior region of the body $r_{\text{tp}} < R$. For very large b (l) it is convenient to use equation (3.63), with χ_1 chosen so as to match onto the phase shift calculated with equation (3.61) at some large cut-off b_{max}. This may be especially useful for high frequencies, where many phase shifts must be evaluated to calculate the scattering cross section. In practice we find it is not numerically difficult to simply use equation (3.61) to obtain our geodesic phase shifts, and we may compare with equation (3.63) in order to be confident of our results.

Substituting the geodesic phase shifts into equation (2.39), we obtain scattering cross sections, complete with interference phenomena, without solving the wave equation. Cross sections obtained in this way are labelled 'geodesic'. They are a useful check on the numerical method outlined in section 3.5, and assist with interpretation of the results.

3.5 Numerical method for the partial wave approach

To solve equation (2.8), we begin by finding the regular Frobenius series solution at the origin

$$u_l(r) \approx r^{l+1} \sum_{n=0}^{N} a_n r^n. \tag{3.64}$$

This gives initial conditions for $u_l(r)$ and $u_l'(r)$ at $r = \epsilon$ where ϵ is small. Next we use the `NDSolve` function in `Mathematica` to numerically integrate between $r = \epsilon$ and $r = r_{\max}$. In the far field we construct the generalised series solutions

$$u_l(r)^{+} \approx e^{i\omega r_*} \sum_{n=0}^{N'} b_n^{+} r^{-n}, \qquad u_l(r)^{-} \approx e^{-i\omega r_*} \sum_{n=0}^{N'} b_n^{-} r^{-n}. \tag{3.65}$$

Inverting the equations

$$\begin{pmatrix} u_l^{+}(r_{\max}) & u_l^{-}(r_{\max}) \\ u_l^{+\prime}(r_{\max}) & u_l^{-\prime}(r_{\max}) \end{pmatrix} \begin{pmatrix} A_l^{+} \\ A_l^{-} \end{pmatrix} = \begin{pmatrix} u_l(r_{\max}) \\ u_l'(r_{\max}) \end{pmatrix}, \tag{3.66}$$

gives the mode coefficients $A_l^{\pm}$ and the phase shifts $\delta_l = \ln[A_l^{+}/A_l^{-}]/(2i)$ (see equation (2.40)). Typical values we use for the internal parameters are $\epsilon = 10^{-3}, N = N' = 20$ and $r_{\max} = 100M$. In order to check validity we repeat some phase shift calculations for different choices of the internal parameters.

3.5.1 Series convergence

It is known that for Coulomb-like scattering, the scattering amplitude partial wave series are divergent in the ordinary sense [161]. However, they are convergent in the Abel sense, which enables them to be correctly calculated after some manipulation for all angles except the forward direction [113]. The scattering of the radial scalar modes by a spherically symmetric compact body is 'Coulomb-like' as we have discussed in section 2.2.1. An early technique for dealing with divergent partial wave series introduced by Yennie *et al* [141] was adapted for scattering by black holes by Dolan [50, 120], and the technique applies equally well here.

First, define the 'n^{th}-reduced series' $\hat{f}^{(n)}(\theta)$ via

$$\hat{f}(\theta) = (1 - \cos\theta)^{-n} \hat{f}^{(n)}(\theta), \qquad n \in \mathbb{N}, \tag{3.67}$$

where

$$\hat{f}^{(n)}(\theta) = \sum_{l=0}^{\infty} (2l+1) c_l^{(n)} P_l(\cos\theta). \tag{3.68}$$

and $c_l^{(0)} = S_l - 1$. From the recurrence properties of Legendre polynomails [117], it can be shown that the series coefficients $c_l^{(n)}$ satisfy the recurrence relation

$$(2l+1)c_l^{(n+1)} = (2l+1)c_l^{(n)} - (l+1)c_{l+1}^{(n)} - lc_{l-1}^{(n)}. \tag{3.69}$$

We find that the $n = 2$ reduced series is sufficiently convergent for numerical evaluation.

3.6 Results

3.6.1 Scattering coefficients

In figure 3.5 we plot the real part of the scattering coefficients, $S_l \equiv \exp[2i\delta_l]$, for a constant density star of tenuity $R/M = 6$ and for $M\omega = 8$. For comparison we also show the black hole scattering coefficients, S_l^{BH}, and the weak field approximation S_l^{W} given by equation (3.63). Note that for $b \gtrapprox b_g$, the black hole and stellar phase shifts appear to approach the same value. In addition the weak field Schwarzschild approximation appears to be fairly good for $b \gtrapprox b_g$ (where we have chosen the constant χ_1 so that the phase shifts at $l = 100$ match).

Figure 3.6 shows the numerical partial-wave phase shifts and the numerical geodesic phase shifts for the same model (equation (3.61)). We expect these to agree at high frequencies, and note that even for the fairly modest value of $M\omega = 8$ we have reasonably good agreement. This gives us confidence in the

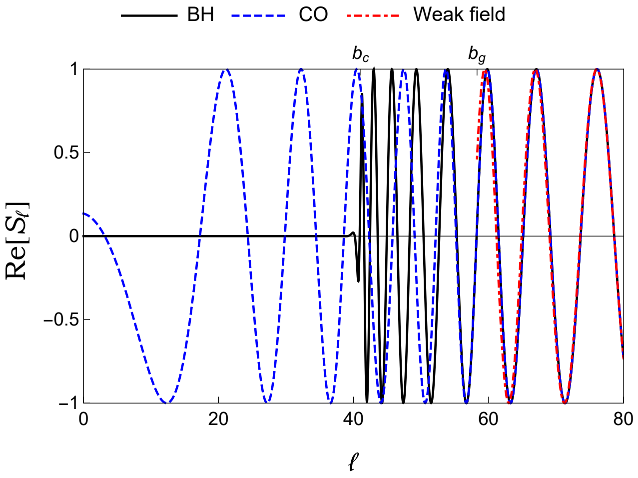

Figure 3.5: Comparison of scattering coefficients for a black hole (BH), compact object consisting of a constant density star (CO), and the weak field approximation (equation (3.63)). Shown for $M\omega = 8$.

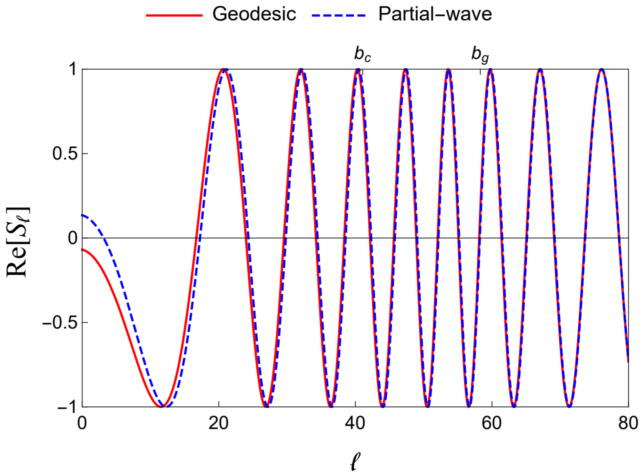

Figure 3.6: Comparison of scattering coefficients for a constant density star calculated exactly (partial wave) and using geodesic phase shifts (equation (3.61)). Shown for $M\omega = 8$.

preliminary numerical results, and indicates that in the high-frequency regime the semiclassical model is a decent approximation.

3.6.2 Scattering cross sections

Rainbow scattering

In this section we discuss scattering by objects with tenuities similar to a neutron star, $4 \lesssim R/M \lesssim 8$. In figure 3.7 we display typical scattering cross sections for a scalar wave of frequency $M\omega = 8$ incident on a constant density star of tenuity $R/M = 8$ and $R/M = 6$. The 'partial wave' cross sections are calculated by solving the wave equation, the 'geodesic' cross sections utilise the geodesic phase shifts of section 3.4.3. In all cases, these two methods show a good agreement. Vertical lines indicate the classical rainbow angle, and we see the primary bow below this as expected from the semiclassical Airy analysis (equation (3.55)). At smaller angles, there are supernumerary bows. Beyond the rainbow angle the partial wave and geodesic cross sections fall off into the classical shadow zone. The rainbow pattern is superposed on a forward divergence expected for Coulombic/Rutherford type scattering equation (2.43).

As the frequency increases, the angular width of the supernumerary oscillations decreases, which can be seen in figure 3.8. In addition the primary peak moves closer to Θ_r and the fall off into the shadow zone becomes steeper. This behaviour is seen even more clearly in figure 3.9 which shows approximate scattering cross sections calculated with the Airy formula (equation (3.55)) which is valid near the rainbow angle. When $M\omega \lesssim 1$, the rainbow pattern is not evident (an example is shown later in figure 4.3). In this case, the incident wave has a wavelength too large to probe the structure of the central scatterer.

Figure 3.7 also shows the contributions to the classical cross section (dashed blue) from each branch of the deflection function either side of the rainbow angle. Both branches diverge at Θ_r , and the outer branch also diverges in the forward direction (since $d\Theta/db \to 0$ as $b \to \infty$). Heuristically we can understand the rainbow interference pattern as the superposition of these two branches - the amplitude of the supernumerary oscillations about the forward

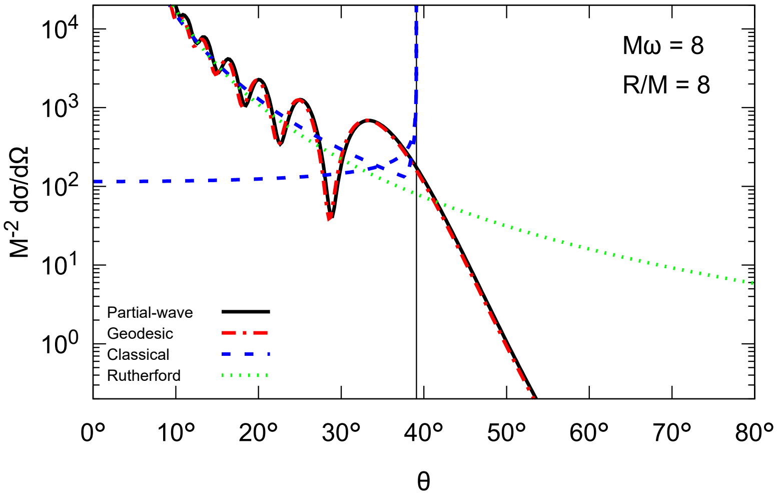

(a) Rainbow scattering for $M\omega = 8$ and $R/M = 8$

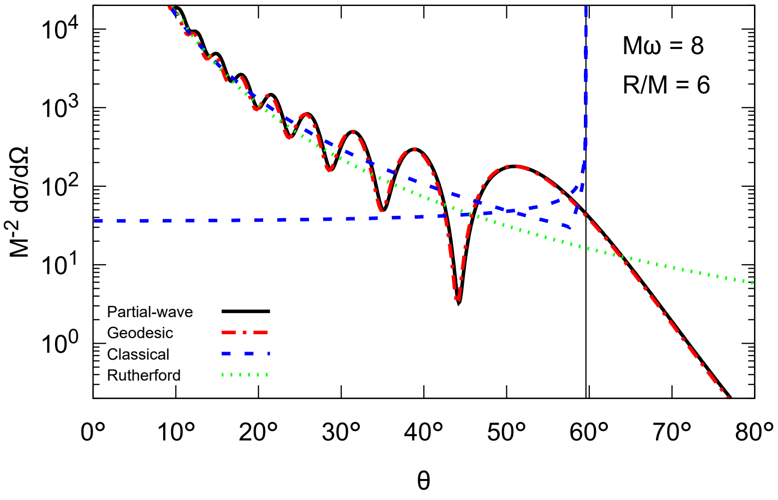

(b) Rainbow scattering for $M\omega = 8$ and $R/M = 6$

Figure 3.7: Rainbow scattering for compact bodies of tenuity $R/M = 8$ and $R/M = 6$, for monochromatic scalar waves of angular frequency $\omega = 8M^{-1}$. The solid lines show the partial-wave cross section calculated from wave-equation phase shifts (black) and geodesic phase shifts (red). The dashed line (blue) shows the classical cross section, equation (3.31), calculated from the geodesic deflection function $\Theta_{\text{geo}}(b)$ of figure 3.2. For comparison, the dotted line (green) shows the Rutherford cross section, $\sim \sin^{-4}(\theta/2)$. A vertical line indicates the geodesic rainbow angle at (a) $\Theta_r = 39.1°$ and (b) $\Theta_r = 59.6°$.

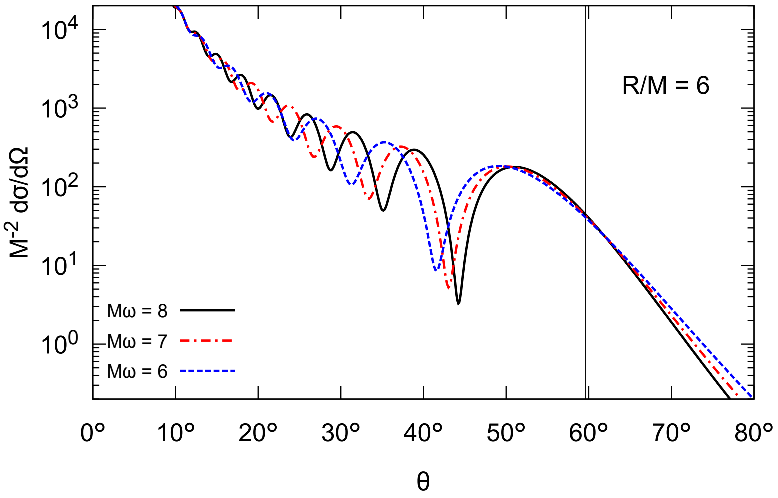

Figure 3.8: Rainbow scattering for a scalar plane wave incident on a compact body with tenuity $R/M = 6$, shown for $M\omega = 8$ (black solid), $M\omega = 7$ (red dot-dashed), and $M\omega = 6$ (blue dashed). A vertical line is at the rainbow angle $\Theta_r = 59.6°$.

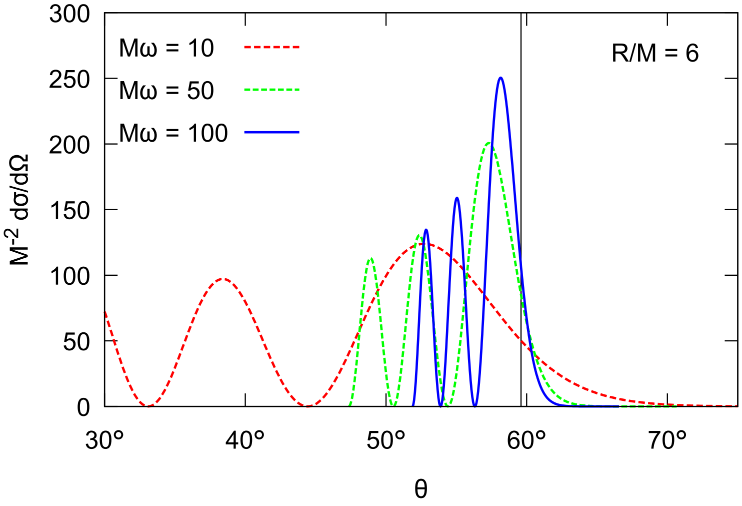

Figure 3.9: The Airy approximation, equation (3.55), for rainbow scattering with $M\omega = 10, 50$ and 100 and $R/M = 6$.

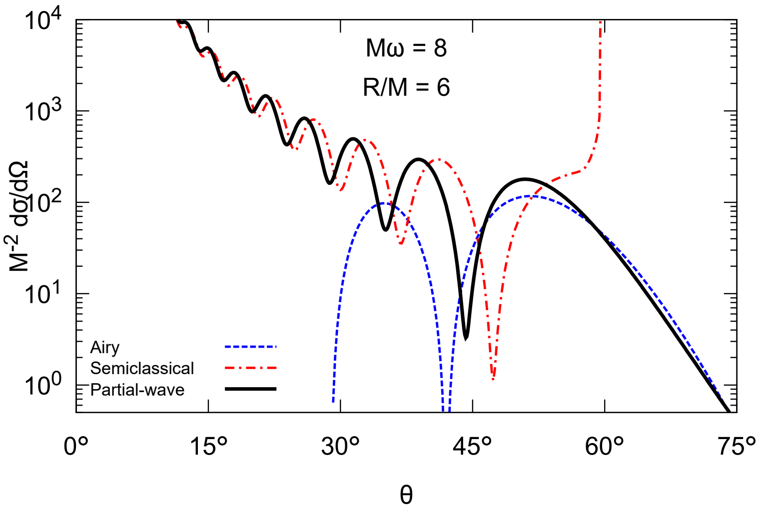

Figure 3.10: Rainbow scattering for a scalar plane wave of angular frequency $\omega = 8M^{-1}$ incident on a constant density star with tenuity $R/M = 6$ (black, solid). The Airy approximation, equation (3.55), for $\theta \approx \Theta_r = 59.6°$ is shown in dotted blue. The semiclassical interference approximation, equation (3.54) , is shown in dot-dashed red.

Rutherford divergence are determined by the inner regular branch.

The semiclassical formula for the interference of the two branches, equation (3.54), explains the supernumeraries qualitatively well. An example is shown in figure 3.10. The approximate interference pattern is however shifted relative to the exact results. Near the rainbow angle the Airy formula, equation (3.55), should be used. This captures the primary peak and the fall off of the cross section for $\theta > \Theta_r$ (see figure 3.10). Both semiclassical formulae appear to be reasonable approximations in their respective regimes of validity, but are not quantitatively accurate.

The rainbow scattering pattern is a robust feature that can be clearly seen in the cross sections for objects with tenuity on the order of a neutron star, however it is sensitive to the tenuity as can be seen in figure 3.11 where we display the partial wave cross sections for $R/M \in \{6, 7, 8\}$. The rainbow angle and thus the interference pattern is shifted to larger angles the more compact the body. For a tenuity of $R/M = 3.5$, the rainbow angle is $\Theta_r \approx -189.5°$.

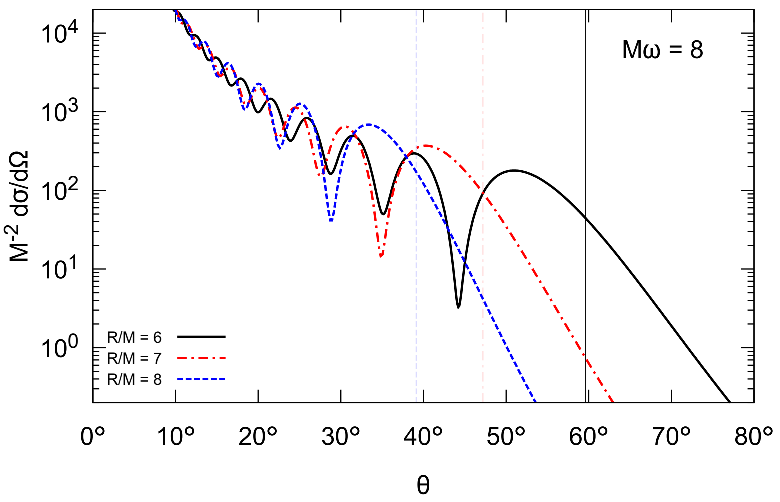

Figure 3.11: Rainbow scattering for a scalar plane wave of angular frequency $\omega = 8M^{-1}$ incident on compact bodies with tenuity $R/M = 6$ (black solid), $R/M = 7$ (red dot-dashed), and $R/M = 8$ (blue dashed). Corresponding vertical lines are shown at the geodesic rainbow angles $\Theta_r = 39.1°, 47.2°$, and $59.6°$ for tenuity $R/M = 8, 7$ and 6 respectively.

Thus, for tenuities $R/M \lesssim 3.5$, the rainbow pattern will 'fold' into itself leading to a complicated structure in the cross section.

Wide angle rainbows and glories

In addition, for $R/M \lesssim 3.5$ we see the backwards glory phenomenon. Some typical examples are shown in figure 3.12. For $R/M = 4$ (figure 3.12a) the two phenomena can be clearly distinguished. For $R/M = 3.5$ (figure 3.12b) the rainbow angle $\Theta_r \approx 189.5°$, and the two effects are superposed on one another. Here, the peak of the oscillations with smaller angular width at $-180°$ is the glory, and the maximum of the oscillations with a larger angular width at approximately $-180°$ is the primary rainbow peak. For this special case we can think of the constructive backscattering as a 'rainbow enhanced glory'.

If $\Theta_r < -\pi$, it makes sense to talk about a superposition of two backward glories from both branches of the deflection function (in a sense the rainbow enhanced glory is just a special case of this 'double glory' effect as we transition

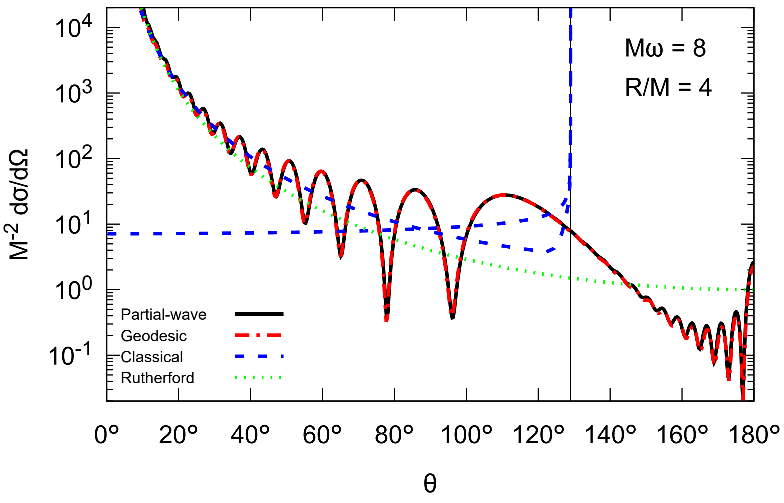

(a) Rainbow and glory scattering for $M\omega = 8$ and $R/M = 4$

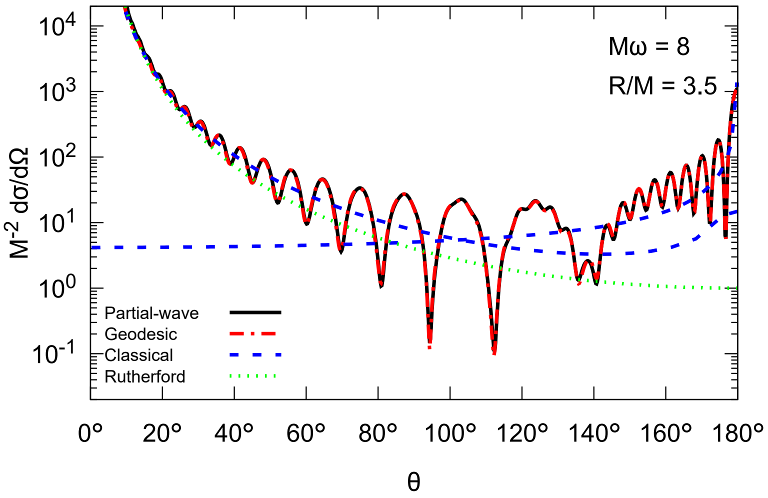

(b) Enhanced rainbow and glory scattering for $M\omega = 8$ and $R/M = 3.5$

Figure 3.12: Scattering cross sections for compact bodies with $R/M = 4$ and $R/M = 3.5$, and an incident wave of angular frequency $\omega = 8M^{-1}$. We show the partial-wave cross section calculated from wave-equation phase shifts (black solid) and geodesic phase shifts (red dot dashed). Also shown is the classical cross section (blue dashed, equation (3.31)) and the Rutherford cross section (green dotted, equation (2.43)). A vertical line indicates the geodesic rainbow angle for figure (a) $\Theta_r = 129.0°$.

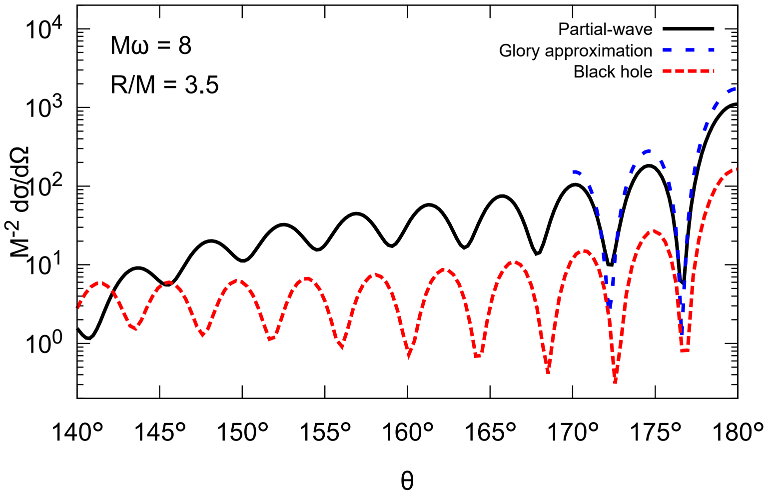

Figure 3.13: Large angle scattering for a scalar plane wave of angular frequency $\omega = 8M^{-1}$ incident on a compact body with $R/M = 3.5$. The numerical partial wave result (black) is compared to the semiclassical glory approximation (blue dashed, equation (3.60)), valid for $\theta \approx 180°$. Also, for comparison we plot the cross section for a Schwarzschild black hole of mass M (red dot dashed).

from no glories to two). The semiclassical approximation for the double glory is shown in figure 3.13, it captures the angular width very well, and the amplitude reasonably well.

Ultra compact objects and orbiting

Note that UCOs do not display rainbow scattering in the sense of Ford and Wheeler's definition, since the deflection function does not possess a minimum, but rather a divergence. We find that $\Theta_r \to -\infty$ as $R/M \to 3^+$. Thus, instead of rainbow scattering, we would expect to see spiral scattering a.k.a. orbiting.

We should not adhere too rigorously to the classical (geodesic) argument for classifying objects that display orbiting as those with a divergence in the cross section (i.e. UCOs). As we have seen, we may have the classical minimum deflection $\Theta_r < -180°$ for $R/M > 3$, so that a particle could undergo at least one full orbit of the scattering body. In addition, in the language of quantum mechanics, a partial wave incident on a compact object with $R \gtrsim 3M$ may

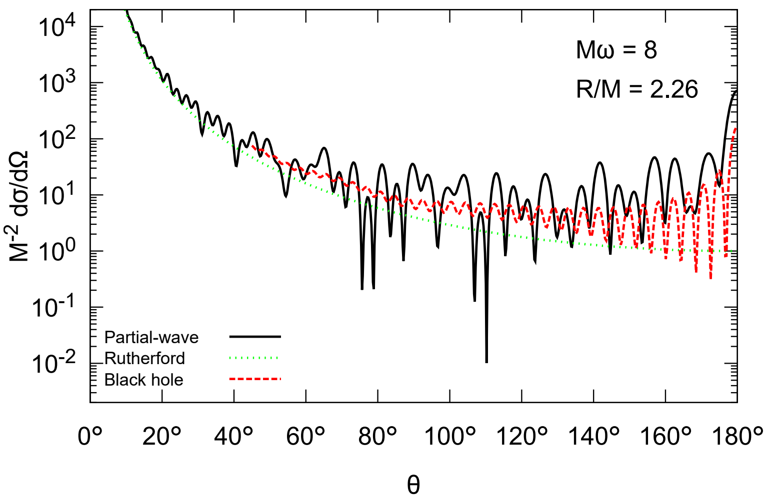

Figure 3.14: Scattering cross section for a scalar plane wave of angular frequency $\omega = 8M^{-1}$ incident on a ultracompact object with $R/M = 2.26$ (black). For comparison we plot the cross section for a Schwarzschild black hole of mass M (red dashed).

tunnel through the effective potential and partly scatter by angles $\Theta < \Theta_r$.

Consequently orbiting oscillations do not suddenly appear in the cross section when $R/M < 3$. Instead they become more prominent, and can be seen at smaller angles, as R/M decreases through the UCO limit (see figure 3.12). Orbiting oscillations are in some sense the 'supernumeraries' of the glory peak.

In figure 3.14 we display the cross section for a star with tenuity $R/M = 2.26$, close to the Buchdahl limit $R/M = 2.25$. Glories, orbiting and the rainbow effect are all present, giving rise to a very complex interference pattern. The enhanced backward glory can be seen in comparison to a glory for a Schwarzschild black hole of the same mass (red dashed line). The orbiting and 'folded rainbow' oscillations are all but impossible to distinguish separately.

3.7 Conclusions

In this chapter we have considered the scattering of a scalar plane wave with angular frequency ω by a constant density star with mass M and radius R.

The process is encapsulated by the dimensionless parameters $M\omega$ and R/M.

At moderate frequencies $M\omega \approx 8$, and for tenuities in the realm of a neutron star, we have found that a rainbow interference pattern appears in the scattering cross section. It is superposed on a forward divergence that is due to the long range nature of the gravitational field and considering a plane wave of infinite extent. The position of the primary rainbow arc, θ_p, depends on the tenuity and $M\omega$. We find that θ_p increases as R/M decreases. The supernumerary rainbow arcs are similarly shifted to larger angles the more compact the body. Beyond the primary rainbow peak, in the classical shadow zone, the cross section falls off to negligible values. As $M\omega$ increases $\theta_p \to \Theta_r$, and the angular width of the supernumerary oscillations decreases (figures 3.8 and 3.10).

Since we have neglected non-gravitational interactions of the field with the body, we would not expect a similar interference effect for light scattering off a neutron star. However, if the central body was a boson star composed of weakly interacting matter, an EM wave should be scattered in a comparable fashion. We do expect the rainbow effect to be inherited by other weakly-interacting fields, such as neutrinos, and we shall see this is the case for GWs in chapter 4.

Recently, Alexandre and Clough have modelled plane wave scattering of neutrinos by a black hole [162]. They found that the downstream flavour oscillation probability displayed a nontrivial interference pattern, which could potentially result in unexpected neutrino detection patterns if source, black hole, and detector were suitably aligned. The consequences of replacing the black hole with a compact body have yet to be considered, yet given our results we might expect it to be similarly nontrivial and long range.

The cross sections are qualitatively similar to experiments of heavy ion scattering [67]. It is intriguing to note that rainbow scattering could in principle provide information on neutron star physics via the mass-radius diagram, just as nuclear rainbow scattering has informed models of nuclear potentials [143]. In chapter 4 we will consider a more general scattering scenario, and we postpone further discussion of astrophysical implications until then.

For sufficiently compact bodies, $R/M \lessapprox 3.5$, the rainbow angle may exceed 180°. In this case the rainbow interference pattern begins to fold in on itself, and the scattering cross section is non negligible at all observation angles. A new interference effect arises - the backwards glory. Tenuities in this regime are beyond reasonable estimates for a neutron star ($4.4 \lesssim \alpha \lesssim 7.7$ [2, 151]), but do find motivation in exotic matter configurations such as boson stars [163].

For ultra compact bodies, $R/M < 3$, the backwards glory is particularly prominent, in fact it can be thought of as a "double glory" with reference to the semiclassical arguments of [33]. We have found that the intensity of a UCO glory is roughly an order of magnitude greater than a Schwarzschild black hole glory. The scattering cross sections of compact bodies with $R/M \approx 6$, UCOs, and black holes are qualitatively very different. Time domain studies have indicated that it may be difficult to distinguish black holes from UCOs (e.g. [26, 27, 164]. It is interesting to note that time-independent scattering does clearly distinguish the two objects. It is reasonable to expect that these compact objects would leave a characteristic 'fingerprint' on a long-lasting, high-frequency incident beam of radiation.

We have also applied a semiclassical analysis to understand scattering at high frequencies, and link the wave picture to massless geodesics. Our results indicate that this is a reasonable approximation even at moderately high frequencies $M\omega \approx 8$. Heuristically, we can consider a plane wave as a congruence of geodesics, some of which pass through the body, and some pass through the exterior (Schwarzschild) spacetime. These two branches interfere, and we have used different approximation methods to examine this interference in different regimes: near a rainbow angle; near a glory; and angular regions far away from rainbows or the poles.

Chapter 4

Scattering of gravitational plane waves by a compact body

The first indirect evidence for gravitational waves came from observations of the Hulse-Taylor binary pulsar PSR 1913+16 [165, 166]. The binary is composed of two neutron stars. One - the pulsar - is spinning and emitting a beam of radiation that is directed at the Earth every 0.05903 seconds with a regularity rivalling atomic clocks [167]. The orbit of the pulsar can be inferred from detection of the Doppler shifted pulses. Four years after the detection of PSR 1913+16, Taylor and colleagues showed that the binary is in-spiralling at a rate consistent with the emission of energy in the form of gravitational waves, as predicted by Einstein's theory of general relativity [166].

GWs are now routinely detected by the laser interferometers of the LIGO and VIRGO collaborations [1, 168], and more detectors are in development [75, 169]. These observations offer a complementary view of astrophysical phenomena, in part because GWs are weakly scattered by interstellar dust and matter between source and detector, in contrast to light. Nonetheless, GWs are subject to the gravitational influence of matter/energy sources by the equivalence principle. A sufficiently strongly curved region of spacetime, such as that of a black hole or neutron star could thus significantly scatter a GW. Scattering of GWs by a BH has been well studied (see e.g. [21, 50, 90]), and here we focus on time-independent scattering of GWs by a simple model of a neutron star with a polytropic equation of state. This builds on the preceding chapter where we considered a scalar plane wave scattered by a constant density fluid sphere.

We find that scattering of GWs by a neutron star is sensitive to the equation of state (EoS). In principle then, observations of GW scattering cross sections could shed light on the nature of nuclear matter at extreme densities. However, the practicality of such observations is at present dubious.

Whilst the astrophysical significance of secondary scattering is certainly overshadowed by the direct detections of GWs, we take the view that it is still worth considering these scenarios for the following reasons: (1) it is of fundamental theoretical interest to understand wave propagation on curved spacetimes; (2) it may be that physical motivation will be found in the future in more sophisticated models as detector capabilities improve, or in analogue systems (for example black-hole analogue spacetimes [73, 103]).

The scattering picture is parametrised by the field spin s, the dimensionless tenuity $Rc^2/(GM)$, the index n of the polytropic equation of state, and the coupling $M\omega$. At low frequencies $M\omega \ll 1$, we expect the scattering cross section for massless plane waves incident on a compact body to be independent of the nature of said body. A plane wave with large wavelength (low frequency) will not be able to resolve the details of the central scatter, being sensitive only to the overall mass. In this limit, the scattering cross sections for a star may be compared to those for a Schwarzschild black hole, namely [44, 49, 170, 171],

$$\lim_{M\omega\to 0}\left(M^{-2}\frac{d\sigma}{d\Omega}\right) = \begin{cases} \dfrac{\cos^{4s}(\theta/2)}{\sin^4(\theta/2)}, & s = 0,\ \dfrac{1}{2} \text{ and } 1 \\ \dfrac{\cos^8(\theta/2)+\sin^8(\theta/2)}{\sin^4(\theta/2)}, & s = 2 \end{cases} . \tag{4.1}$$

The first case is the result for scalar (spin 0), spinor (spin 1/2) and electromagnetic (spin 1) waves. The second case is the result for a gravitational wave (spin 2), where there is an extra ‘anomalous’ term associated with the reversal of the helicity of the incident wave (the low frequency limit of g_{s2} from equation (2.126), see e.g. [49] for a derivation).

We begin this chapter by constructing the background spacetime of a polytropic star in section 4.1. We then discuss the interior perturbation problem in section 4.2 (the exterior problem is summarised in section 2.3). Scattering cross sections calculated numerically are shown in section 4.5 as well as near field scalar scattering profiles. In chapter 3 we found that a rainbow interference pattern is expected for moderate to high frequencies of a scalar plane wave incident on a constant density body. Here, we find that this feature is also present for GW scattering by polytropic stars at moderate to high frequencies. Differences between the scalar and GW scenarios are discussed in sections 4.5 and 4.6, in particular those associated with the additional features introduced for GWs: helicity reversal and fluid perturbation-GW coupling. This work was carried out in collaboration with S.R. Dolan, and part of it is available in reference [64]. All data and figures appearing in this chapter are the result of the authors own work.

4.1 Polytropic equation of state

In section 3.1 we introduced perfect fluids and in section 3.1.1 the Schwarzschild interior solution for an incompressible star. Demanding a constant density allows the Tolman-Oppenheimer-Volkoff equation (3.7) to be solved exactly. A neutron star has nearly uniform density within the core, so this model was a reasonable if simple first approximation for our purposes. However, the model has a potentially serious drawback in that the speed of sound inside a constant density star is infinite.

In this chapter we relax the assumption of uniform density and consider two additional stellar models. These are known as polytropic stars - perfect fluid solutions to Einstein's equations with a polytropic equation of state

$$p(\rho) = \kappa \rho^{1+1/n}, \tag{4.2}$$

where n is the polytropic index and κ is a constant. Part of the reason for introducing these models in this chapter is that gravitational waves couple to fluid pulsations, unlike the scalar wave, and hence it seemed prudent to use a model with density perturbations that travel at subluminal speed. We will see later that the fluid coupling appears to have a negligible effect for plane-wave time-independent scattering and hence we have also shown results for the constant density star. A constant density star is a special case of a polytrope, with $n = 0$, which can be seen by inverting equation (4.2).

Polytropic equations of state were some of the first to be used to model neutron stars and white dwarfs [10, 14, 91] . A neutron star (white dwarf) will cool to zero temperature, and the pressure that keeps it from gravitational collapse is then purely neutron (electron) degeneracy pressure. In this limiting case of zero temperature, Fermi-Dirac statistics for an ideal gas leads to an equation of state of the form of equation (4.2) [145]. For non-relativistic fermions where the rest mass dominates the mass-energy, $n = 3/2$. For the ultra-relativistic case, $n = 3$. Using Newtonian gravity, Chandrasekhar modelled a white dwarf as a polytrope that interpolates between the two polytropic indices with the ultra-relativistic case corresponding to the core. He obtained the maximum mass that such a star could reach before it must succumb to gravitational collapse, the well known Chandrasekhar limit [14] M_{C}. Using more realistic models gives $M_{\mathrm{C}} \approx 1.4 M_{\odot}$ [145]. The equilibrium of the star in this model is determined by balancing the Newtonian gravitational attraction and the repulsion due to pressure.

$$-r^2 \frac{dp}{dr} = G m(r) \rho(r). \tag{4.3}$$

Neutron stars were first predicted by Baade and Zwicky in 1934 [172], who also postulated that they were the remnants of supernovae. The immense gravitational packing energy of the dense neutron star could explain the energy released in a supernova. In this case, it was more important to use general relativity when considering the star's equilibrium.

Tolman found a class of spherically symmetric solutions to Einstein's equations that were relevant to neutron star studies. In an accompanying paper, Oppenheimer and Volkoff modelled neutron stars as a cold Fermi gas obeying the laws of general relativity. In doing so they found an upper mass limit for

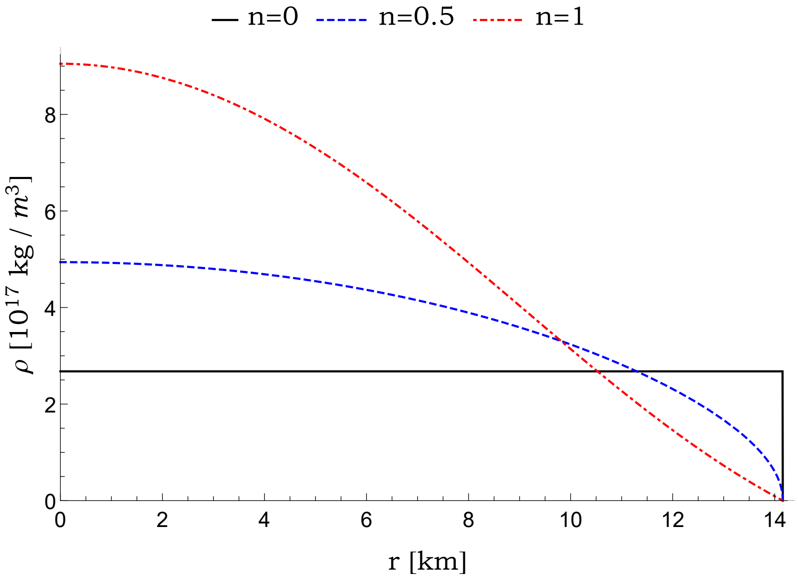

Figure 4.1: Radial density profiles for three spherically symmetric stars with tenuity $R/M = 6$ and polytropic index $n \in \{0, 0.5, 1\}$.

neutron stars (analogous to Chandrasekhar's limit for a white dwarf) of $0.7M_\odot$. This is known as the Tolman-Oppenheimer-Volkoff limit M_{TOV}. The original estimate is not accurate because it does not take into account the strong nuclear force. This provides an additional repulsive force acting against collapse. A recent estimate of the upper limit for non-rotating neutron stars is given by Rezzola *et al* as $2.01 \leq M_{\mathrm{TOV}}/M_\odot \lesssim 2.16$ [173].

The equation of state for a neutron star is a large area of research, partly because the densities in these objects cannot be reproduced in the laboratory [174]. For the equation of state we consider two simple polytropic models with $n \in \{0, 0.5, 1\}$ (equation (4.2)). In practice we fix κ and the central density so that the radius and mass of the resulting solution is consistent with observations. We find that the central density for these models is also of the correct order of magnitude predicted by more sophisticated models [174]. In figures 4.1 and 4.2 we show the radial density and mass profiles for our set of models with tenuity $R/M = 6$. It should be fairly simple to adapt the following methods of this chapter to consider more state of the art equations of state.

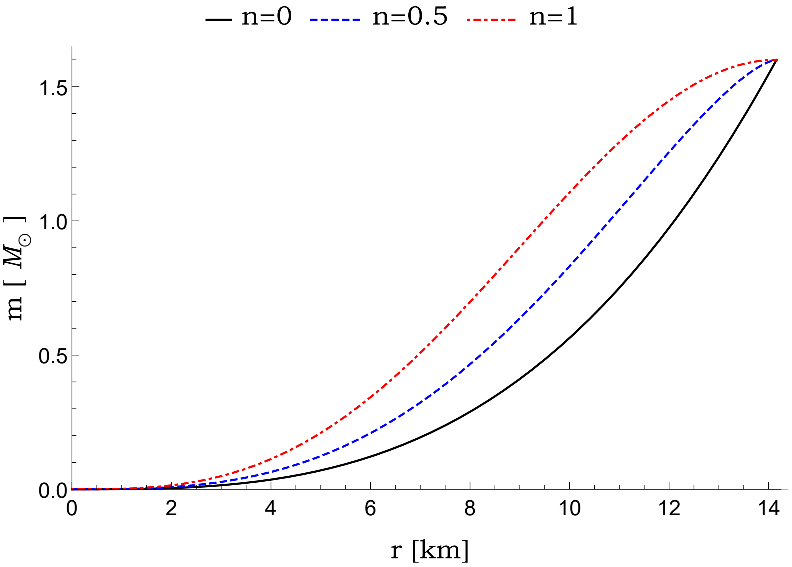

Figure 4.2: “Mass inside radius r” profiles for three spherically symmetric stars with tenuity $R/M = 6$ and polytropic index $n \in \{0, 0.5, 1\}$.

4.1.1 Numerical method

For the polytropes with $n \neq 1$, it is necessary to solve the TOV equations (equations (3.6) and (3.7)) numerically. Here we outline the method for doing so, following Ipser and Price [97].

The TOV equations are subject to the boundary conditions $m(0) = 0$ and $p(0) = p_0$ where p_0 is the central pressure. The integration is terminated at some $r = r_{\max}$ where $p(r_{\max})$ is sufficiently small. At $r_{\max}$ we match the numerical solution onto an ‘atmosphere’ following [97]. That is, we expand the dependent variables, ρ, p and m in powers of $(R-r)$. Near the surface

$$\rho(r) \sim (R-r)^n \sum_{j=0}^{J} \rho_j (R-r)^j, \tag{4.4a}$$

$$p(r) \sim (R-r)^{n+1} \sum_{j=0}^{J} p_j (R-r)^j, \tag{4.4b}$$

$$m(r) \sim M + (R-r)^{n+1} \sum_{j=0}^{J} m_j (R-r)^j, \tag{4.4c}$$

and we take $J = 5$. We estimate R and M by considering the Taylor series for $p(R)$ and $m(R) = M$ about r_{max} and using the numerical solutions. The equation of state and definition of m (equation (3.4)) give m_j and p_j in terms of ρ_j. Substituting the expansions (equation (4.4)) into the TOV equations (equations (3.6) and (3.7)) and solving for each power of $(R-r)$, determines ρ_j. This process is important for solving the radial part of the linearised Einstein equations near the surface. A root finding algorithm (e.g. the inbuilt `FindRoot` function of `Mathematica`) enables us to select a central pressure p_0 that results in a model with the desired tenuity. Using equation (3.8) we can confirm that the speed of sound $c_s < c$ for $n \neq 0$.

4.2 Perturbations of the stellar interior

Given a stellar model, such as a polytrope, that solves Einstein's field equations, the next step is to perturb the EFEs in exactly the same way as was done for the Schwarzschild exterior [122]. The first variation of Einstein's equations is

$$\delta G_{\mu\nu} = 8\pi \delta T_{\mu\nu}, \tag{4.5}$$

where $\delta T_{\mu\nu}$ is the (linearised) perturbation of the stress energy tensor. An additional complexity now is that we are no longer in vacuum ($\delta T_{\mu\nu} \neq 0$). In addition, the variation of the fluid equations of motion (the conservation of stress energy) is

$$\delta\left(T^{\mu}{}_{\nu;\mu}\right) = 0. \tag{4.6}$$

For a spherically symmetric spacetime, equation (4.5) can be decomposed using spherical harmonics as outlined in chapter 2, section 2.3 for the Schwarzschild exterior solution. This was first done by Thorne and Campalatarro [29] using the same gauge and decomposition as Regge and Wheeler (so that for the exterior of the star they have the same formalism) [122]. In Schwarzschild coordinates $\{t, r, \theta, \phi\}$, and Regge-Wheeler gauge, the metric perturbations of each parity are decomposed as follows (see [93]),

$$h^{+}_{\mu\nu} = \sum_{l,m} \begin{bmatrix} AH_0^{lm} & H_1^{lm} & 0 & 0 \\ H_1^{lm} & BH_2^{lm} & 0 & 0 \\ 0 & 0 & r^2 K^{lm} & 0 \\ 0 & 0 & 0 & r^2 \sin^2\theta\, K^{lm} \end{bmatrix} Y^{lm}(\theta,\phi), \tag{4.7}$$

and

$$h^{-}_{\mu\nu} = \sum_{l,m} \begin{bmatrix} 0 & 0 & -(h_0^{lm}/\sin\theta)\partial_\phi & (\sin\theta\, h_0^{lm})\partial_\theta \\ 0 & 0 & -(h_1^{lm}/\sin\theta)\partial_\phi & (\sin\theta\, h_1^{lm})\partial_\theta \\ \bullet & \bullet & 0 & 0 \\ \bullet & \bullet & 0 & 0 \end{bmatrix} Y^{lm}(\theta,\phi), \tag{4.8}$$

where $H_0^{lm}, H_1^{lm}, H_2^{lm}, K^{lm}, h_0^{lm}$ and h_1^{lm} are functions of r and t. In the literature these 'Regge-Wheeler' functions are often assumed to have a harmonic time dependence, writing for example $X(r,t) = X(r)e^{-i\omega t}$. We will mostly be working the frequency domain and X will denote $X(r)$ unless stated otherwise when we refer to Regge-Wheeler functions.

Different choices of gauge, types of tensor spherical harmonics, and choice of decomposition functions lead to different formulations of the equations. Numerous works have been done over the years with different but sometimes closely related approaches (see [175] for a review).

We choose to follow the approach of Allen *et al* for the even parity sector [92], and (e.g.) Kojima [93] for the odd parity sector. Kojima uses the standard Regge-Wheeler gauge and decomposition. Allen *et al.* also use Regge-Wheeler gauge and a closely related decomposition. The important metric functions are $\{\tilde{F}_{lm}, \tilde{S}_{lm}, \tilde{Q}_{lm}\}$ which are related to the Regge-Wheeler functions via

$$\tilde{Q}_{lm} = \frac{\sqrt{AB}}{r} h_1^{lm}, \tag{4.9a}$$

$$\tilde{F}_{lm} = r K^{lm}, \tag{4.9b}$$

$$\tilde{S}_{lm} = \frac{A}{r}(K^{lm} - H_0^{lm}). \tag{4.9c}$$

We also utilise results for the even parity sector from references [97, 124].

4.2.1 Odd parity

In the odd parity sector, the equations for the metric perturbations decouple from the fluid perturbation equations. This means odd parity gravitational waves do not couple to oscillations of the fluid, only to the space time curvature generated by the stress energy of the background fluid configuration. This simplifies the scattering picture enormously. In fact, early studies did not focus on the odd parity sector precisely because of the lack of coupling to fluid oscillations [29]. These investigations were concerned with initial perturbations of the fluid and their damping due to emission of gravitational radiation. It was only when Chandrasekhar and Ferrari looked at the problem in terms of an initial gravitational wave scattering off a star, that this sector was investigated in depth [100].

Working in Regge-Wheeler gauge and in frequency space, the odd parity system of equations reduces to the problem of solving a single second order radial equation for the spacetime variable $\tilde{Q}_{lm}(r, \omega)$ (see for example [93])

$$\frac{d^2\tilde{Q}_{lm}}{dr_*^2} + \left(\omega^2 - \mathcal{V}_l(r)\right)\tilde{Q}_{lm} = 0, \tag{4.10}$$

where

$$\mathcal{V}_l(r) \equiv A(r)\left[\frac{l(l+1)}{r^2} - \frac{6m(r)}{r} - 4\pi(p(r) - \rho(r))\right]. \tag{4.11}$$

In vacuum, $\mathcal{V}_l(r)$ reduces to V_l^- (equation (2.76)), and thus $\tilde{Q}_{lm}$ satisfies the Regge-Wheeler equation. In the exterior $\tilde{Q}_{lm}$ is simply related to $\tilde{\Phi}_{lm}^-$ (see equations (2.73) and (2.74)) by,

$$\tilde{\Phi}_{lm}^-(r,\omega) = \frac{2}{i\omega}\tilde{Q}_{lm}. \tag{4.12}$$

4.2.2 Even parity

In contrast to the odd parity sector, the even-parity metric perturbations do couple to the fluid perturbations. Allen *et al.* looked at gravitational waves from perturbed stars in the even-parity sector [92], working in the time domain. They note that the problem can be reduced to two second order radial wave equations for spacetime variables $S_{lm}(r,t)$ and $F_{lm}(r,t)$ (as was noted before by Ipser and Price using a different decomposition [97]). A constraint equation relates the fluid perturbations to $S_{lm}(r,t)$ and $F_{lm}(r,t)$ and their derivatives. Here, we make use of the two coupled equations derived by Allen *et al.*, working in Fourier space with $\tilde{S}_{lm}(r,\omega)$ and $\tilde{F}_{lm}(r,\omega)$. The relevant equations are

$$\begin{aligned}\frac{d^2\tilde{S}}{dr_*^2} &+ \left[\omega^2 + \frac{A}{r^3}\left(4\pi r^3\left(\rho+3p\right) + 2m - l(l+1)r\right)\right]\tilde{S} \\ &= -\frac{4A^2}{r^5}\left[\frac{\left(m+4\pi p r^3\right)^2}{(r\text{–}2m)} + 4\pi\rho r^3 - 3m\right]\tilde{F}, \end{aligned}\tag{4.13}$$

and

$$\begin{aligned}&\frac{d^2\tilde{F}}{dr_*^2} - \left(1 - \frac{1}{c_s^2}\right)\sqrt{\frac{A}{B}}\frac{1}{r^2}\left(m + 4\pi p r^3\right)\frac{d\tilde{F}}{dr_*} \\ &\quad + \left[\frac{\omega^2}{c_s^2} + \frac{A}{r^3}\left(4\pi r^3\left(3\rho + \frac{p}{c_s^2}\right) - m\left(1 - \frac{3}{c_s^2}\right) - l(l+1)r\right)\right]\tilde{F} \\ &= \left(1 - \frac{1}{c_s^2}\right) r\sqrt{\frac{B}{A}}\frac{d\tilde{S}}{dr_*} + \left[2B + \left(1 - \frac{1}{c_s^2}\right)\frac{l(l+1)}{2} - 8\pi(p+\rho)r^2\right]\tilde{S}, \end{aligned}\tag{4.14}$$

where we have dropped mode labels lm for clarity. In vacuum, the even-parity master function $\tilde{\Phi}^+_{lm}$ (see equations (2.68) and (2.74)) is related to $\tilde{S}_{lm}$ and $\tilde{F}_{lm}$ by

$$\tilde{\Phi}^+_{lm}(r,\omega) = \frac{2}{l(l+1)}\left[\tilde{F}_{lm} + \frac{2}{\Lambda}\left(2A\tilde{F}_{lm} - rA\partial_r\tilde{F}_{lm} + r^2\tilde{S}_{lm}\right)\right]. \tag{4.15}$$

Since $c_s \to 0$ as $r \to R^-$, it is necessary to use an alternative to equation (4.14) to solve for $\tilde{F}$ and $\tilde{S}$ near the surface. Following [92], we keep only the terms that go like c_s^{-2} to obtain

$$\sqrt{\frac{A}{B}}\frac{1}{r^2}\left(m+4\pi pr^3\right)\frac{d\tilde{F}}{dr_*}+\left[\omega^2+\frac{A}{r^3}\left(4\pi pr^3 - 3m\right)\right]\tilde{F} = -r\sqrt{\frac{B}{A}}\frac{d\tilde{S}}{dr_*}+\frac{l(l+1)}{2}\tilde{S}. \tag{4.16}$$

4.2.3 Perturbation junction conditions at the stellar surface

The stellar surface separating the interior and exterior regions of spacetime defines a timelike hyper-surface Σ. There may be discontinuities in the stress energy tensor here, notably for constant density stars or any star with non-zero density at the surface. Thus, carrying solutions to the linearised Einstein field equations over this hypersurface must be done with some care. The prescription for doing so is to insist that the intrinsic and extrinsic curvature of Σ must approach the same value when approached from inside the star as when approached from outside the star (i.e. the first and second fundamental forms should be continuous) [176].

Price and Thorne give the junction conditions for the even parity Regge-Wheeler variables H_0 and K [29, 122] at the stellar surface for a general spherically symmetric solution in appendix B of [30]. The junction conditions for H_0 and K and their first derivatives, together with equation (4.9), imply the following conditions for $\tilde{F}$ and $\tilde{S}$,

$$[\tilde{F}]^+_- = 0, \quad [\tilde{S}]^+_- = 0, \quad [\partial_r\tilde{S}]^+_- = 0, \tag{4.17}$$

where $[z(r)]^+_-$ denotes $\lim_{\epsilon\to 0}[z(R+\epsilon) - z(R-\epsilon)]$. From equations (3.6) and (5.3) in reference [97], it can be deduced that

$$[\partial_r \tilde{F}]^+_- = -\frac{\rho}{2\omega^2 r^2(p+\rho)}\Bigg[r\left(l(l+1) - 2\omega^2 r^2 A^{-1}\right)\tilde{S}_{lm} + r^2 l(l+1)\partial_r \tilde{S}_{lm}$$
$$+\left(\left(l(l+1) - \omega^2 r^2 A^{-1}\right)\partial_r A - 2\omega^2 r^2\right)\tilde{F}_{lm} + 2\omega^2 r^2 \partial_r \tilde{F}_{lm}\Bigg]\Bigg|_{r=R^-} \quad \text{if } \rho(R) \neq 0, \tag{4.18}$$

and

$$[\partial_r \tilde{F}]^+_- = 0 \quad \text{if } \rho(R) = 0. \tag{4.19}$$

The odd parity metric perturbation variable and its first derivative are continuous at the stellar surface for all the models we consider [93]

$$[\tilde{Q}_{lm}]^+_- = 0, \quad [\partial_r \tilde{Q}_{lm}]^+_- = 0. \tag{4.20}$$

4.2.4 Perturbation boundary conditions for the stellar interior

All spacetime variables should be regular at the origin. Only one of the two independent solutions to equation (4.10) satisfies this with

$$\tilde{Q}_{lm} \sim r^{l+1}. \tag{4.21}$$

There are two independent solutions to the even parity system, equations (4.13) and (4.14), that satisfy regularity at the origin,

$$\begin{aligned} \{\tilde{S}^1_{lm}, \tilde{F}^1_{lm}\} &\sim \{r^{l+1}, a_1 r^{l+3}\}, \\ \{\tilde{S}^2_{lm}, \tilde{F}^2_{lm}\} &\sim \{r^{l+3}, a_2 r^{l+1}\} \quad \text{as} \quad r \to 0, \end{aligned} \tag{4.22}$$

where a_1 and a_2 are constants determined by the stellar model. The solution must be a linear sum

$$\mathbf{Y}_{\mathrm{C}} = \alpha_1 \mathbf{Y}^{(1)} + \alpha_2 \mathbf{Y}^{(2)}, \tag{4.23}$$

where

$$\mathbf{Y} = [\tilde{S}_{lm}, \partial_r \tilde{S}_{lm}, \tilde{F}_{lm}, \partial_r \tilde{F}_{lm}]^t, \tag{4.24}$$

and $\mathbf{Y}^{(i)}$ refer to the two independent solutions of equation (4.22).

A second boundary condition for the even parity sector is to require that the Lagrangian variation in pressure at the surface of the star vanishes. Following [97] (see equation (5.2)), this yields the following constraint

$$\begin{aligned}\lim_{r\to R^-} \Bigg\{ \frac{1}{4r^3\omega^2 A} \Bigg[\left(l(l+1)\left(A'r - 2B\omega^2 r^2\right) - \frac{2\omega^2 A' r^3}{A} \right) \tilde{S}_{lm} \\ + \left(l(l+1)A'r^2 - 4\omega^2 r^3 \right) \partial_r \tilde{S}_{lm} \\ + \Bigg(A'\left(l(l+1)A' - 4\omega^2 r \right) - \frac{\omega^2 \left(A'\right)^2 r^2}{A} \\ - 4B\omega^4 r^2 - 4A(B-1)\omega^2 \Bigg) \tilde{F}_{lm} \Bigg] \Bigg\} = 0.\end{aligned} \tag{4.25}$$

4.3 Numerical method

All numerical integrations are performed with the `NDSolve` utility in `Mathematica` [66]. We also use `Mathematica` to find Frobenius series solutions to differential equations.

Odd parity

For the odd parity sector we make use of the regular Frobenius series solution about the origin

$$\tilde{Q}_{lm} = r^{l+1} \sum_{j=0}^{k} q_{2j} r^{2j}, \tag{4.26}$$

where q_n are determined by inserting equation (4.26) into equation (4.10), and also expanding the effective potential given by equation (4.11) about $r = 0$.

Using equation (4.26) for initial conditions at $r = \epsilon$ for some small ϵ, we then integrate equation (4.10) out to $r = R$. With the junction conditions of equation (4.20), we carry the solution over to the exterior spacetime. Then, we may find the Cunningham-Price-Moncrief function $\tilde{\Phi}^{-}_{lm}$ using equation (4.12).

Next, we integrate equation (2.75) from $r = R$ to the far field, $r = r_{\max}$.

Even parity

The ODE system for $\tilde{F}_{lm}$ and $\tilde{S}_{lm}$ can be expressed in matrix form

$$\mathbf{Y}' = \frac{1}{z}\mathbf{M} \cdot \mathbf{Y}, \tag{4.27}$$

where $\mathbf{Y}$ is defined in equation (4.24), $z = |r - r_0|$, $'$ denotes d/dz, and $\mathbf{M}$ is a 4×4 matrix. The system has a regular singularity at $r = 0$, and at $r = R$ if the speed of sound is zero at the surface. Thus, for $r_0 \in \{0, R\}$, we can write

$$\mathbf{M} = \sum_{n=0}^{\infty} z^n \mathbf{M}_n, \tag{4.28}$$

where $\mathbf{M}_j$ are constant matrices found by expanding equation (4.13) and equation (4.14) or equation (4.16) about r_0. In order to make progress we make the ansatz

$$\mathbf{Y} = z^\sigma \sum_{j=0}^{\infty} z^n \mathbf{Y}_j. \tag{4.29}$$

Substituting equations (4.28) and (4.29) into equation (4.27), and equating coefficients of z^σ gives

$$(\mathbf{M}_0 - \sigma \mathbf{I}) \cdot \mathbf{Y}_0 = 0, \tag{4.30}$$

$$[(\sigma + k)\, \mathbf{I} - \mathbf{M}_0] \cdot \mathbf{Y}_k = \sum_{j=1}^{k} \mathbf{M}_j \cdot \mathbf{Y}_{k-j}. \tag{4.31}$$

Equations (4.30) and (4.31) can be solved to find four independent series solutions near the origin ($r_0 = 0$). Two of these are regular, $\{\mathbf{Y}^{(1)}, \mathbf{Y}^{(2)}\}$, satisfying equation (4.22) with eigenvalues $\sigma = l + 1$. We numerically integrate the two solutions from $r = \epsilon$ to $r = R - \epsilon$.

Similarly, near the surface ($r_0 = R$), we use Equations (4.30) and (4.31) to find four independent series solutions for $r \lesssim R$. The solution valid here is thus

$$\mathbf{Y}_{\mathrm{S}} = \sum_{i=3}^{6} \alpha_i \mathbf{Y}^{(i)}. \tag{4.32}$$

Now, at some $r \lesssim R$, we demand that $\mathbf{Y}_{\mathrm{S}}$ matches the solution valid at the origin (see equation (4.23)),

$$\mathbf{Y}_{\mathrm{S}} = \mathbf{Y}_{\mathrm{C}}. \tag{4.33}$$

Equation (4.33) along with the boundary condition equation (4.25), yields five equations for the six unknowns α_i. We are free to set one of them equal to say 1, as this will just scale the overall solution. Now, with $\mathbf{Y}_{\mathrm{S}}$ determined, we carry the solution over the surface of the star using the relevant junction conditions of section 4.2.3. The Zerilli-Moncrief function and its derivative is found outside the star using equations (2.75) and (4.15). We then numerically integrate $\tilde{\Phi}^{+}_{lm}$ out to $r = r_{\max}$.

In the above description, we typically use $\epsilon = 10^{-6}R$, $r_{\max} = 100R$ and we expand series solutions to $k = 15$.

4.3.1 Phase shifts

In the far field, generalised series solutions for the Zerilli-Moncrief and Cunningham-Price-Moncrief master functions, $\tilde{\Phi}_{lmp}$, are given by

$$\tilde{\Phi}^{\mathrm{out}}_{lmp}(r) \approx e^{i\omega r_*} \sum_{n=0}^{N} c_{nlp} r^{-n}, \qquad \tilde{\Phi}^{\mathrm{in}}_{lmp}(r) \approx e^{-i\omega r_*} \sum_{n=0}^{N} d_{nlp} r^{-n}. \tag{4.34}$$

The coefficients (d_{nlp}, c_{nlp}) are found by substituting equation (4.34) into equation (2.75) and solving order by order in $1/r$. Inverting the equations

$$\begin{pmatrix} \tilde{\Phi}^{\mathrm{out}}_{lmp}(r_{\max}) & \tilde{\Phi}^{\mathrm{in}}_{lmp}(r_{\max}) \\ \partial_r \tilde{\Phi}^{\mathrm{out}}_{lmp}(r_{\max}) & \partial_r \tilde{\Phi}^{\mathrm{in}}_{lmp}(r_{\max}) \end{pmatrix} \begin{pmatrix} C^{+}_{lp} \\ C^{-}_{lp} \end{pmatrix} = \begin{pmatrix} \tilde{\Phi}_{lmp}(r_{\max}) \\ \partial_r \tilde{\Phi}_{lmp}(r_{\max}) \end{pmatrix}, \tag{4.35}$$

gives the mode coefficients $C^{\pm}_{lp}$ and the phase shifts $\delta^{p}_{l} = \log[C^{+}_{lp}/C^{-}_{lp}]/(2i)$ (see equation (2.118)). In equation (4.35), $\tilde{\Phi}_{lmp}(r_{\max})$ and $\tilde{\Phi}'_{lmp}(r_{\max})$ have been determined numerically as described above. Typical values for the internal parameters are $N = 20$ and $r_{\text{max}} = 100M$. To check validity some phase shift calculations are repeated for different choices of the internal parameters.

4.4 Gravitational wave scattering amplitudes and cross section

With the phase shifts in hand (section 4.3.1), we seek to compute the helicity conserving and reversing scattering amplitudes ($f_2(\theta)$ and $g_2(\theta)$ respectively) using the partial wave summations given by

$$f_2(\theta) \equiv \frac{\pi}{i\omega} \sum_{l,p} {}_{-2}Y_{l2}(0)\, {}_{-2}Y_{l2}(\theta) \left[e^{2i\delta_l^p} - 1 \right], \tag{4.36}$$

$$g_2(\theta) \equiv \frac{\pi}{i\omega} \sum_{l,p} p(-1)^l \, {}_{-2}Y_{l2}(0)\, {}_{-2}Y_{l2}(\pi - \theta) \left[e^{2i\delta_l^p} - 1 \right]. \tag{4.37}$$

Recall that the scattering cross section is the sum of the absolute values of the two amplitudes squared

$$\frac{d\sigma}{d\Omega} = |f_2(\theta)|^2 + |g_2(\theta)|^2. \tag{4.38}$$

For a derivation of equations (4.36) to (4.38) see chapter 2.

As with the scalar scattering amplitude, the partial wave sum $f_2(\theta)$ diverges. A generalisation of the approach used for scalar wave scattering is given by Dolan [50] for scattering of on-axis plane GWs by Kerr black holes. The technique described in section 5.3 of [50] readily applies to scattering by spherically symmetric compact bodies. For a series reduction method that applies to off-axis scattering see [177].

In contrast, we find that the helicity-reversing scattering amplitude $g_2(\theta)$ converges. This is because the phase shifts become independent of parity in the high-l limit. Then, for a given l, the contributions to $g_2(\theta)$ from each parity mode cancel out. This tells us that the helicity reversing scattering will be due to the lowest-l modes. Indeed in the low frequency limit, only the $l = 2$ partial

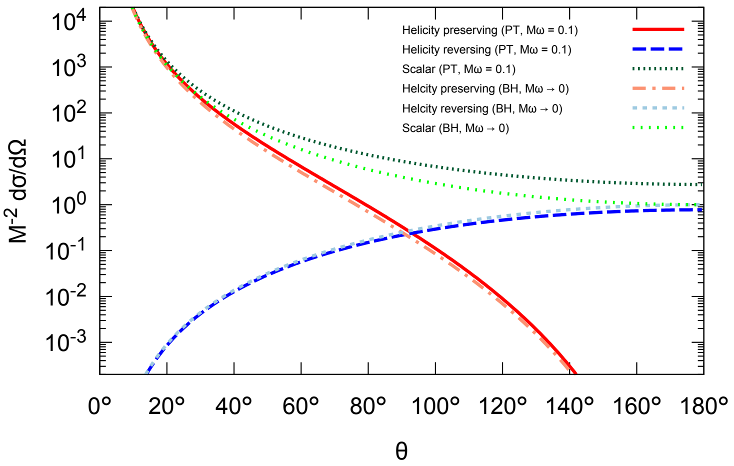

Figure 4.3: Scattering cross sections for massless plane waves of frequency $\omega = 0.1M^{-1}$ incident on a polytrope (PT) of tenuity $R/M = 6$ and polytropic index $n = 1$. For comparison we also plot the low frequency limiting cross sections for massless plane waves scattered by a Schwarzschild black hole of the same mass. Figure reproduced from [64].

wave appears to contribute to the scattering cross section.

4.5 Results

4.5.1 Scattering cross sections

Analytic approximations for scattering by a black hole in the low frequency limit ($M\omega \ll 1$) are given in equation (4.1). These are compared with numerical results for scattering by a compact polytropic star obtained from equations (4.36) to (4.38). Scattering cross sections for a polytrope with tenuity $R/M = 6$, index $n = 1$, and $M\omega = 0.1$ are shown in figure 4.3. The low-frequency BH approximations and numerical polytrope cross sections are very similar. We expect the polytrope cross sections to further approach the low frequency black hole approximations as $M\omega \to 0$. At the beginning of the chapter we posited that large wavelength scattering was independent of the nature of the central body, and the result here is consistent with such a picture.

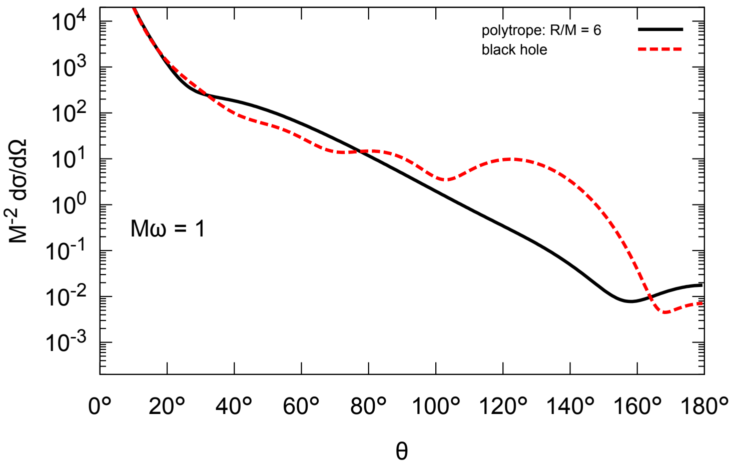

Figure 4.4: Scattering cross sections for a GW of frequency $\omega = 1M^{-1}$ incident on a polytrope (PT) of tenuity $R/M = 6$ and polytopic index $n = 1$. For comparison we also plot the cross section for a GW scattered by a Schwarzschild black hole of the same mass. Figure reproduced from [64].

The scattering cross section becomes sensitive to the central body when the wave is able to probe the internal structure. This corresponds to wavelengths $\lambda/(2M) \lesssim 1$, i.e. moderate to large frequencies, $M\omega \gtrsim 1$. In figure 4.4, the GW cross sections for $M\omega = 1$ are shown for a compact body with $R/M = 6$ and a black hole (both found numerically), and they are markedly different for $\theta \gtrsim 20°$.

In figure 4.5 we display the GW and scalar scattering cross sections for a polytropic star with index $n = 1$ and tenuity $R/M = 6$. At low frequencies the helicity reversing component, $|g_2(\theta)|^2$, of the cross section is significant at large observation angles (see figure 4.5a). As $M\omega$ increases, $|g_2(\theta)|^2$ becomes less significant, and at $M\omega = 4$ it is negligible at all angles. Once $M\omega \gtrsim 2$, the GW and scalar cross sections become hard to visually distinguish (except at the largest angles where the cross section is small). In addition, in this frequency regime a rainbow scattering pattern can be seen as in figures 4.5c and 4.5d. This is the same qualitative cross section structure that we saw for the scalar field on a constant density star ($n = 0$) in chapter 3. To briefly re-iterate the main features: (1) There is a primary peak below the geodesic rainbow

n R/M	0	0.5	1
5	81.1°	92.1°	115°
6	59.6°	66.6°	79.7°
7	47.3°	52.4°	61.5°

Table 4.1: The geodesic rainbow angles, θ_r, for polytropic fluid stars with tenuity R/M and polytropic index n.

angle $\theta_p \lesssim \theta_r$, that approaches the geodesic value as $M\omega \to \infty$; (2) at higher frequencies one can distinguish supernumerary troughs and peaks at smaller angles $\theta < \theta_p$, and the width of these oscillations decreases as $M\omega$ increases; (3) the cross section falls of into the shadow region $\theta > \theta_p$; (4) the rainbow pattern described in points (1)-(3) is superposed on a Rutherford like forward divergence. For a more detailed discussion of points (1)-(4) and semiclassical approximations see chapter 3.

The rainbow scattering feature is sensitive to the stellar structure, in this case parametrised by n and R/M. In figure 4.6 we compare $d\sigma/d\Omega$ for three models with $R/M = 6$, $M\omega = 4$ and $n = 0, 0.5, 1$. As n increases, the rainbow angle increases (see table 4.1), and the interference pattern shifts to larger angles accordingly. This can be understood in terms of the density profiles (see figure 4.1). For larger n, the object is more centrally dense, the star is 'less stiff', and it has a slower internal speed of sound. As a consequence, incident rays have a greater maximum-deflection angle.

4.5.2 Near field scattering profile

For a more complete picture of the scattering process we have also looked at scattering of null rays (see chapter 3, section 3.2) and the near field profile of the scalar field for the three polytropic models $n = 0, 0.5, 1$.

Figure 4.7 shows null geodesics impinging on the three stellar models. For the constant density case (figure 4.7a), a cusp caustic forms near the surface of the body. For higher polytropic indices the cusp caustic is formed deeper inside the body (see figures 4.7b and 4.7c). The cusp caustic envelope defines

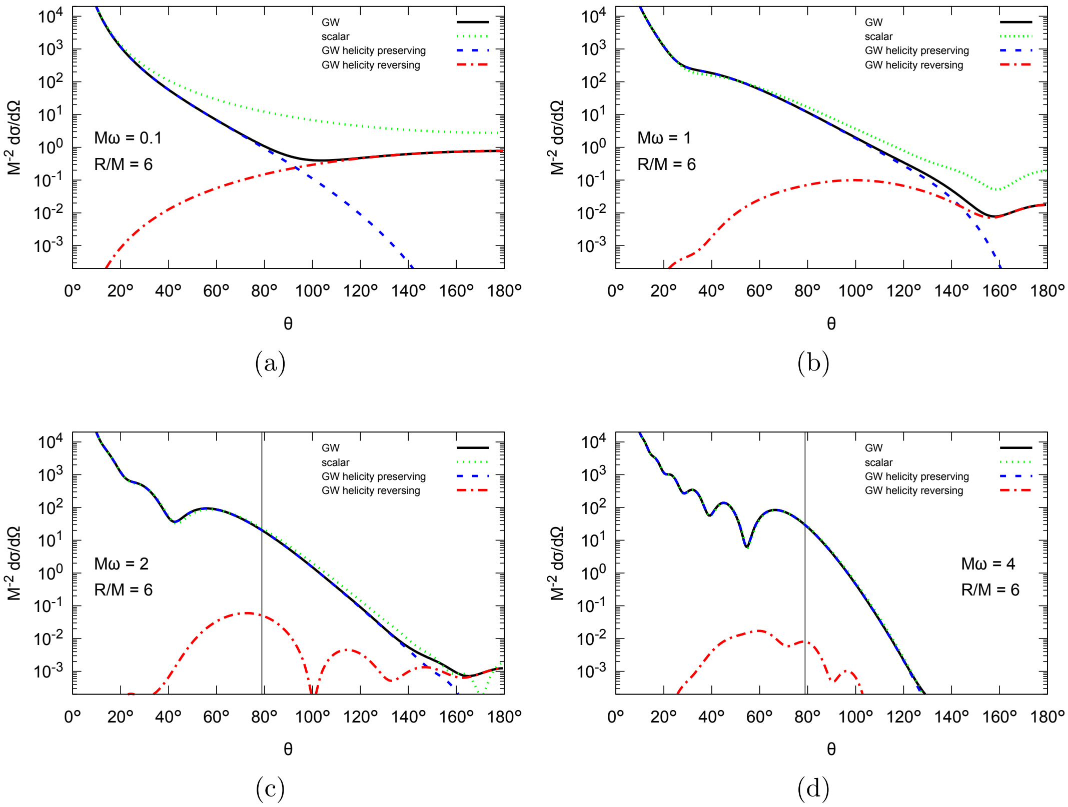

(a) (b)

(c) (d)

Figure 4.5: Scattering cross sections for a polytropic star with $R/M = 6$, polytropic index $n = 1$ and coupling $M\omega = 0.1$ (a), $M\omega = 1$(b), $M\omega = 2$ (c) and $M\omega = 4$ (d). The helicity preserving (reversing) part of the GW cross section is shown in dashed blue (dot-dashed red), and the cross section for a scalar wave is shown in dotted green. The rainbow angle, $\theta_{\text{bow}} \approx 79.7°$, is shown as a solid vertical line for the two higher frequency cases. Figure reproduced from [64].

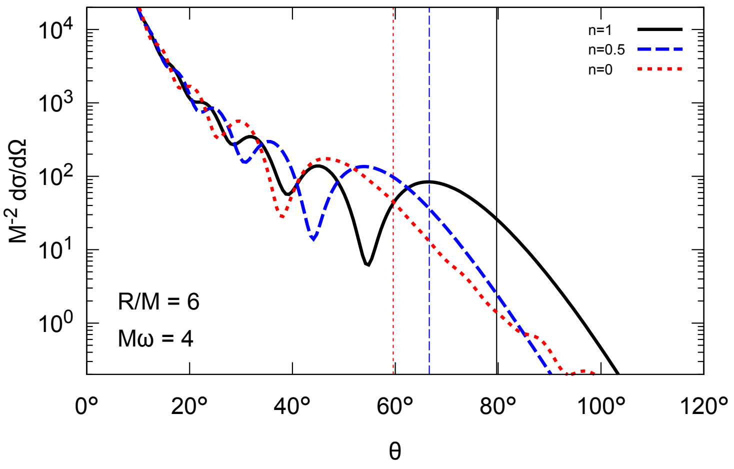

Figure 4.6: Gravitational wave scattering cross sections for polytropes with index $n = 1$ (black solid), $n = 0.5$ (blue dashed), and $n = 0$ (red dashed). Vertical lines indicate the rainbow angles $\theta_r \approx 59.6°$ ($n = 0$), $\theta_r \approx 66.6°$ ($n = 0.5$), and $\theta_r \approx 79.7°$ ($n = 1$). Figure reproduced from [64].

a rainbow wedge with rainbow angle θ_r that can be looked up in table 4.1.

In figure 4.8 we show the scalar field solution corresponding to a scattered plane wave near and inside the central body. We find that for moderate frequencies, $M\omega = 1$, the amplitude of the wave can be increased by a factor of approximately 4 near the formation of the cusp caustic (see figure 4.7c). For higher frequencies the maximum amplification factor increases, and can reach approximately 20 for $M\omega = 8$ as shown in figure 4.8b. In addition, for $M\omega = 8$ it is possible to visually identify constructive interference at a scattering angle of $\theta \approx 79.7°$, corresponding to the primary rainbow peak.

4.6 Conclusions

In this chapter we have generalised the work of chapter 3 to consider scattering of gravitational ($s = 2$) as well as scalar ($s = 0$) monochromatic plane waves by a central compact body, modelled as a spherically symmetric polytrope with index n. We have computed scattering cross sections, $d\sigma/d\Omega$, numerically (figures 4.3, 4.5 and 4.6), and examined the scalar scattering profile near the

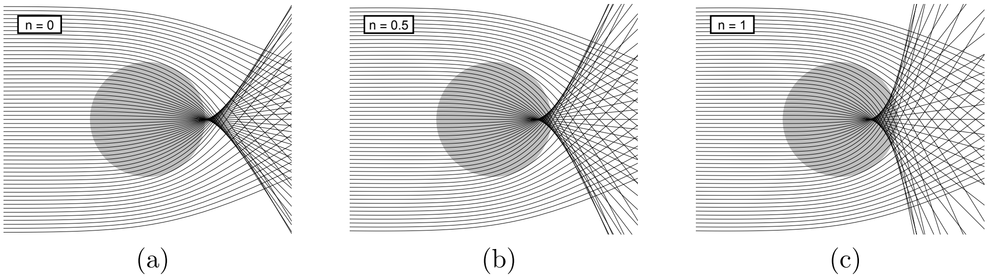

(a) (b) (c)

Figure 4.7: A congruence of geodesics incident on a compact star with tenuity $R/M = 6$ and polytropic index $n = 0$ (a), $n = 0.5$ (b), and $n = 1$ (c). Figure reproduced from [64].

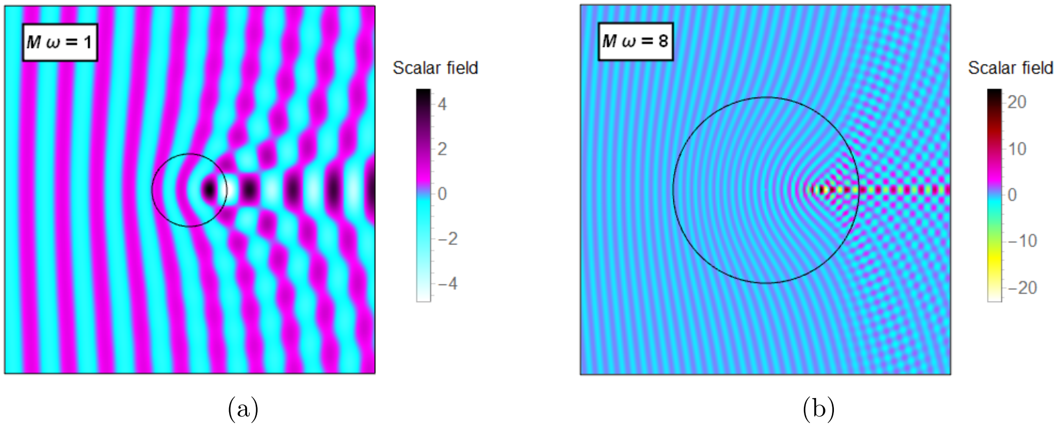

(a) (b)

Figure 4.8: A unit amplitude scalar plane wave scattering off a compact body (black outline) with tenuity $R/M = 6$ and polytropic index $n = 1$. The incident wave has coupling $M\omega = 1$ (a) and $M\omega = 8$ (b). Figure reproduced from [64].

central body (figure 4.8).

At low frequencies $M\omega \ll 1$, we find that $d\sigma/d\Omega$ is essentially only sensitive to the central body's mass, and is well described by the limiting cross section of a Schwarzschild black hole as $M\omega \to 0$, equation (4.1). The incident wave does not probe the details of the scattering body structure since the wavelength $\lambda \gg R_g = 2M$. In this regime, the helicity-reversing amplitude, $|g_2|^2$ has a significant contribution to $d\sigma/d\Omega$ at angles $\theta \gtrsim 90^\circ$ (see figure 4.3).

As the frequency increases, the contribution from the helicity-reversing amplitude decreases. We find that g_2 is essentially negligible for $M\omega \gtrsim 1$. This implies that the odd and even parity phase shifts are approximately equal for the l modes that contribute significantly to $d\sigma/d\Omega$ (leading to cancellations in equation (4.37)). Since the even parity modes couple to the fluid perturbations but the odd parity modes do not, this suggests GW-fluid perturbation coupling is inconsequential for time-independent scattering. Fluid modes might however be key to understanding time-dependent scattering [92], or absorption where one considers energy loss through heat (see discussion in chapter 5).

In chapter 3 we found that a rainbow interference pattern was extant in the scattering cross section for the case $s = 0$, $n = 0$, and $M\omega \approx 8$. Here we have shown that this feature is also present for $s \in \{0, 2\}$, $n \in \{0, 0.5, 1\}$, and $M\omega \gtrsim 4$, indicating its robustness (figures 4.5 and 4.6).

In addition, we have seen that the position of the primary rainbow peak, θ_p, is sensitive to the equation of state, parametrised by n and R/M. For larger n (and/or smaller R/M), θ_p and the supernumerary peaks and troughs are shifted to larger scattering angles (an example is shown in figure 4.6). It would be interesting in future work to consider the inverse problem. That is to say, can the equation of state for a neutron star be constrained by the scattering cross section? This is of course more difficult, there is already the degeneracy of the rainbow peak's dependence on both R/M and n even when only considering polytropic equations of state.

We now turn to the question of the astrophysical relevance of gravitational wave scattering by a compact body. A neutron star has a typical mass $M \approx 1.5M_\odot$ [174], and a gravitational radius of $r_g = 2GM/c^2 \approx 2.2\,\text{km}$. The highest frequency GW sources known are millisecond pulsars with $\omega \sim 10^3$ Hz [76]. The fastest-spinning pulsar yet detected is PSR J1748-2446ad, with a circular frequency of 716 Hz. PSR J1748-2446ad will emit gravitational waves [178, 179] with $\omega = 9 \times 10^3$ Hz provided it is not axisymmetric about its rotation axis. In general then, any essentially time-independent scattering of gravitational waves by a neutron star that could reasonably be expected to occur will satisfy $M\omega \lesssim 1.5 M_\odot \times 10^3\,\mathrm{Hz} \times G/c^3 \sim 10^{-2}$. In this regime, the low frequency approximation (equation (4.1)) is valid, the scattering is essentially insensitive to the bodies structure, and rainbow scattering does not occur.

A larger less compact body such as a white dwarf with tenuity $R/M \sim 1400$ may satisfy the requirements for rainbow scattering (e.g. the Wolf-Rayet star R136a1 of mass $M \approx 315 M_\odot$). However, the interference pattern would be at very small angles and difficult to resolve. Recently it has been shown that scalar waves incident on a black hole with surrounding matter may display rainbow scattering [56], and given the results of this chapter it seems very likely we could expect similar behaviour for GWs. GWs incident on intermediate-mass black holes (10^2–$10^5 M_\odot$) or supermassive black holes ($M \gtrsim 10^5 M_\odot$) with surrounding matter could naturally satisfy the condition $M\omega \gtrsim 1$.

Entertaining the possibility of astrophysical scenarios where (quasi-)time independent scattering of GWs by a compact body does produce a cross section with a rainbow interference pattern, let us consider the issue of detection. Suppose we aimed to sample the primary rainbow peak and subsequent trough of the interference pattern. Firstly, the GW source, scattering body, and detector would need to be aligned in such a way that the detector lay at an angle of observation $\theta_{\mathrm{obs}} \approx \theta_p$. Secondly, since θ_{obs} would be fixed, observations would need to be made over a range of frequencies $\Delta\omega$ instead of a range of angles. Varying ω shifts the diffraction pattern according (roughly) to the semiclassical Airy formula, equation (3.55). To sample the first peak and trough of the rainbow we would require $\Delta\omega/\omega \sim 2q/(\theta_r - \theta_{\mathrm{obs}})$, where $q \equiv \Theta_r''/(2\omega^2)$. A compact binary inspiral could provide a GW source which sweeps out the required frequency range.

Whilst the astrophysical relevance is rather speculative, it is worth reiterating that the results here contribute to a broader, theoretical understanding of wave propagation on compact body space-times. GWs on curved-spacetimes can in some cases have analogies in shallow water wave propagation. Berry has considered tsunamis scattered by submerged islands, and found the formation of a cusp caustic can occur [180, 181]. This corresponds to the amplification of the tsunami downstream with possibly dire outcomes. Analogously, we have found the formation of a cusp caustic when considering geodesics on a compact body spacetime (figure 4.7), and a corresponding amplification of scalar waves incident on a compact body (figure 4.8). Whether there are any physical consequences of the energy focusing in this context is an open question.

Chapter 5

Extreme compact objects: trapped modes and absorption spectra

The detections of gravitational waves by LIGO and Virgo are compelling evidence for the existence of black holes (BH). Numerous detected signals are fully consistent with general relativistic models of two BHs spiralling together and coalescing into a single BH [1]. Other signals are consistent with the merger of two neutron stars (NS) resulting in a BH [2, 168]. More recently there may also be detections originating in NS + BH → BH mergers [182].

The possibility remains however, that the detected signals may not have originated in the mergers of canonical Kerr black holes of the classical theory of general relativity [20, 183]. They could instead have been generated by alternative Exotic/Extreme Compact Objects (ECOs), that can mimick the signal of BH mergers.

ECO proposals include gravastars [116], and BH near horizon modifications motivated by quantum gravity [16, 17]. The horizon may be replaced by a quantum phase transition that arises on the Planck scale. The surface of these objects may be partially reflective, giving rise to an effective cavity between the peak of the external angular momentum barrier (defined by the light ring) and the surface. ECOs may be categorised by their compactness [20]: if they are compact enough to possess a light ring they are known as UltraCompact Objects (UCOs); if they possess a photon sphere and, in addition, a spectrum of modes trapped within the cavity that could provide a clean signal they are known as Clean Photon sphere Objects (ClePhOs). Many ECOs can be ruled out already on theoretical grounds due to the presence of instabilities [183].

The inspiral, merger, and early ringdown stage of a GW signal is currently unable to distinguish between an ECO and BH model [20]. This is predicted to change with the advent of space-based GW detectors and more precise measurements (see e.g. [184]). It is possible to distinguish binary NS mergers by the observation of electromagnetic radiation that follows the gravitational wave [2].

The late-ringdown phase of a merger-endstate ECO displays clear features that differentiate them from BHs. This phase is possible to model using perturbation theory, allowing some physical insight. There has been interest in studying gravitational-wave data from LIGO to search for smoking-gun evidence of ECOs: echoes of the initial ringdown signal corresponding to successive reflections of radiation within the cavity [16, 18, 20, 164, 185, 186]. There has been a claim to have found these echoes already, but it seems inconclusive at present [18, 187, 188]. The consensus is that future, more precise measurements will be required to distinguish ECOs from BHs.

Certain requirements must be met by an ECO for there to be echoes [16]. Barceló and colleagues have proposed compact dark objects without a horizon motivated by a semiclassical model of collapse [17]. These are termed dark stars or quasi black holes and satisfy the requirements for echoes.

Another example of an ECO was proposed by Saravani *et al.* [189], in which spacetime ends at a microscopic distance from black hole event horizons. Abedi and colleagues proposed that the stretched horizon of these ‘empty black holes’ partly absorbs perturbations with frequency greater than the Hawking temperature, $\omega \gg T_H$, and reflects perturbations with $\omega \lesssim T_H$ [18].

In collaboration with C.F.B. Macedo, S.R. Dolan, and L.C.B. Crispino, we have investigated the the absorption cross sections of generic, spherically symmetric ECOs. Part of this material is also presented in reference [63]. All of the data and figures shown here have been generated by the author.

The ECO is characterised by the position of its surface, $R = 2M + \delta R$, and the level of reflectivity/dissipation there. For a UCO $\delta R/M \leq 1$, and for a ClePhO $\delta R/M \lesssim 0.038$ [190]. The ClePhO bound for δR is obtained by demanding that more than 95% of the energy of massless waves initially localised near the photon sphere will have dispersed before a massless particle has the time to make the round-trip from the photon sphere to the the objects surface and back again.

In this chapter we redefine the tortoise coordinate (equation (2.7)) so that the light ring lies at $x = 0$,

$$x(r) \equiv r + 2M \log\left(\frac{r}{2M} - 1\right) - (3 - 2\log 2)M. \tag{5.1}$$

The width of the effective cavity is thus $|x(R)|$. For a ClePhO, $|x(R)| \gtrsim 7.50M$. In this chapter we will calculate ECO transmission factors and absorption cross sections numerically. We will also calculate the trapped mode frequencies. We find that the absorption cross section displays distinctive peaks a.k.a. spectral lines, corresponding to excitation of trapped modes.

In addition, we use a comparison radial equation with a Pöschl-Teller potential that arises naturally for a perturbed Nariai spacetime [191]. This allows an analytic derivation of trapped mode frequencies and of the form of the absorption cross section close to the spectral lines. In this model we show that the spacing of the spectral lines is controlled by the width of the effective cavity $|x(R)|$, and the width of the spectral lines is determined by the reflectivity/dissipation properties of the ECO as well as $|x(R)|$. By comparing to our numerical results for the Schwarzschild-ECO model, we find that the spectral line properties are similarly determined by the ECO parameters.

5.1 The ECO model

The exterior of the spherically symmetric ECO is the Schwarzschild geometry, which we discussed in detail in chapter 2. We will draw a veil over the model dependent interior, and instead consider a generic boundary condition at the surface (see chapter 2 section 2.2.2 for more details).

We consider a scalar field perturbation on the ECO background, and a class of ECOs parametrised by a boundary condition for the field at their surface,

$$u_l^s(r) = \begin{cases} e^{-i\omega x} + \mathcal{K}_l(\omega) e^{-2i\omega x_0} e^{+i\omega x}, & x \to x_0 \\ C_l^- e^{-i\omega x} + C_l^+ e^{+i\omega x}, & x \to \infty \end{cases}, \tag{5.2}$$

where $x_0 = x(R)$, and $u_l(r)$ is a radial mode of angular frequency ω.

The boundary condition is parametrised by the (possibly) frequency dependent 'reflectivity' $\mathcal{K}_l(\omega)$ [192]. As a starting point we will consider some simple cases where $\mathcal{K}_l(\omega) = \mathcal{K}$ is a constant and independent of ω and l (hence we will drop the subscript). For example we could consider Dirichlet ($\mathcal{K} = -1$), Neumann ($\mathcal{K} = 1$), and BH type ($\mathcal{K} = 0$) boundary conditions. To capture the effects of partial absorption, which may be induced by a coupling to the ECO or some dissipation mechanism in the interior, we also consider $|\mathcal{K}| < 1$. Recently it was pointed out that $\mathcal{K}$ may in general be complex, and the phase introduces non-trivial effects in the late-ringdown signal of a perturbed ECO such as polarization mixing [164]. For the scalar case we need not worry about polarization mixing, but this should be kept in mind for possible future studies into absorption of GWs and other fields by black holes.

5.2 Absorption cross section

Recall that the absorption cross section is

$$\sigma_{\text{abs}}(\omega) = \frac{\pi}{\omega^2} \sum_l (2l+1)\Gamma_{\omega l}, \tag{5.3}$$

where the transmission factors $\Gamma_{\omega l}$ are defined by the mode coefficients $C_l^{\pm}$ of equation (5.2),

$$\Gamma_{\omega l} \equiv 1 - \left|\frac{C_l^+}{C_l^-}\right|^2 = \frac{1 - |\mathcal{K} e^{-2i\omega x_0}|^2}{\left|C_l^-\right|^2}. \tag{5.4}$$

We now seek to write $\Gamma_{\omega l}$ in terms of the IN and UP modes introduced in chapter 2. Recall that the BH mode coefficients are related by equation (2.19), which we will make use of in the following analysis.

By considering Wronskian relations between the ECO perturbation, u_l^s, and the black hole IN and UP perturbation modes we arrive at

$$C_l^- \approx B_l^+ - B_l^- \tilde{\mathcal{K}}, \tag{5.5a}$$

$$A_s^+ \approx \frac{1}{A_l^-}\left(A_l^+ C_l^- + \tilde{\mathcal{K}}\right), \tag{5.5b}$$

where $\tilde{\mathcal{K}} \equiv \mathcal{K}e^{-2i\omega x_0}$. The relations of equation (5.5) are approximate, they are valid in the limit $\delta R/(2M) \to 0$, and depend critically on the choice of δR and the formulation of the conditions in equation (5.2) (in particular the choice of an overall phase multiplication at the surface). We now assume that equations (5.5) hold exactly.

The transmission factor diverges where $C_l^- = 0$, or equivalently where the condition

$$\frac{B_l^+}{B_l^-} = \mathcal{K}e^{-2i\omega x_0}, \tag{5.6}$$

is met. Equation (5.6) defines a spectrum of quasinormal modes (QNMs) with complex quasinormal frequencies (QNFs) ω_{ln} (see section 1.1 for a discussion of QNMs). At this stage one may already expect there to be trapped modes in the spectrum, caught between the light ring and the partially reflective surface. Later we will show this is the case, and there exist ω_{ln} with small imaginary part.

The transmission factor is usually evaluated at real values of ω, and when this is near a trapped-mode frequency (i.e. $\omega \approx \omega_{ln}$), it can be shown to be of Breit-Wigner form. We have

$$C_l^- \approx (\omega - \omega_{ln})\frac{\partial C_l^-}{\partial \omega}\Big|_{\omega=\omega_{ln}}, \qquad \text{for } \omega \approx \omega_{ln}, \tag{5.7}$$

and thus by equation (5.4)

$$\Gamma_{\omega l} \approx \sum_n \frac{\mathcal{A}_{ln}}{(\omega - \operatorname{Re}\omega_{ln})^2 + (\operatorname{Im}\omega_{ln})^2}, \tag{5.8}$$

where we allow for a sum over possible nearby modes with amplitudes

$$\mathcal{A}_{ln} = (1 - |\mathcal{K}|^2) \left| \frac{\partial C_l^-}{\partial \omega} \right|^{-2}. \tag{5.9}$$

5.3 The Pöschl-Teller potential or Nariai spacetime comparison problem

As in previous chapters, to obtain the mode solutions on compact body spacetimnes we must resort to numerical or approximate techniques. There are exact analytic solutions to the exterior Regge-Wheeler equation, which are special cases of the confluent Heun function [193]. However, these are not yet sufficiently well understood to obtain for example, the scattering coefficients $C_l^{\pm}$ without ultimately resorting to numerical integration.

Another option is to consider 'comparison potentials' that give exactly solvable differential equations. This can open up the possibility to capture the essential physical features of the system and allow a clearer interpretation. It is a widely used method across physics. For example, Woods-Saxon effective nuclear potentials are frequently used as approximations in atomic scattering studies (e.g. [67, 194]).

Here, we follow previous studies of scalar fields on Schwarzschild spacetime (see [105] and references therein) and consider the Pöschl-Teller potential

$$V_l^{\mathrm{PT}} \equiv \frac{\gamma^2 V_0}{\cosh^2\left(\gamma(x - x_1)\right)}. \tag{5.10}$$

A closest match to the Schwarzschild exterior potential is found with the choice of constants $V_0 = l(l+1), x_1 = 0, \gamma = 1/\sqrt{27}M$ (see figure 5.1). The Pöschl-Teller decays exponentially as $x \to \infty$ and is symmetric about the origin, in

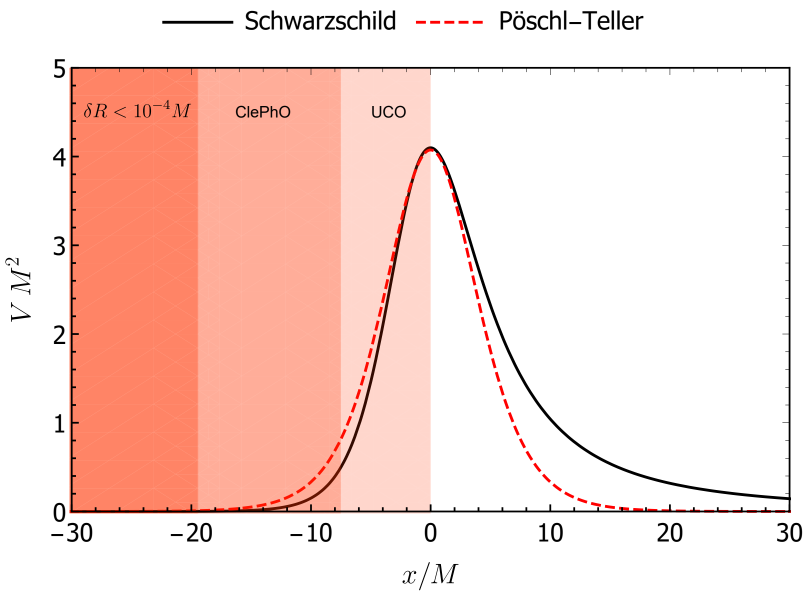

Figure 5.1: The effective radial potential for scalar perturbations on compact body backgrounds. The Schwarzschild (black, solid) and Pöschl-Teller (red, dashed) potentials are plotted as a function of the tortoise coordinate x defined in equation (5.1). The surface radii of compact body categories are depicted with shaded regions.

contrast to the Schwarzschild potential. Both potentials have a single peak, and thus similar classical turning point structure. In this way, scattering and absorption of radial modes may be expected to be qualitatively the same.

As has been noted, the Pöschl-Teller potential actually arises naturally when considering a scalar perturbation of a known solution to Einstein's equations [105]. This solution is the Nariai spacetime [191]. It is the cartesian product of 2-dimensional de Sitter spacetime and the 2-sphere ($dS_2 \times S_2$).

The line element describing the region of the Nariai spacetime we wish to consider for our model is is given by

$$d\hat{s}^2 = -F(z)dt^2 + \frac{1}{F(z)}dz^2 + d\Omega^2 \tag{5.11}$$

where

$$F(z) = 1 - z^2, \tag{5.12}$$

and $z \in (-1,1)$ (see e.g. section III of reference [105] for details). The Klein Gordon equation for a scalar field Φ_N with conformal coupling ξ, on this Nariai background can be solved by decomposing as

$$\Phi_N = \int_{-\infty}^{\infty} e^{-i\hat{\omega}t} \sum_{l=0}^{\infty} \sum_{m=-l}^{m=l} \frac{\hat{u}_{l\hat{\omega}}(r)}{r} Y_{lm}(\theta,\phi)\, d\hat{\omega}. \tag{5.13}$$

The radial equation is

$$\left[\frac{d^2}{d\hat{x}^2} + \hat{\omega}^2 - \frac{L^2 + 4\xi - 1/4}{\cosh^2 \hat{x}}\right] \hat{u}_{l\hat{\omega}} = 0, \tag{5.14}$$

where $L \equiv l + 1/2$ and $\hat{x} = \tanh^{-1} z \in (-\infty, \infty)$. To obtain the Pöschl-Teller potential which has a closest match to the Schwarzschild case we identify

$$\hat{\omega} \leftrightarrow \sqrt{27} M\omega, \qquad \hat{x} \leftrightarrow \frac{x}{\sqrt{27}M}. \tag{5.15}$$

In analogy with the ECO model, we impose boundary conditions as

$$\hat{u}_l(\hat{x}) = \begin{cases} e^{-i\hat{\omega}\hat{x}} + \mathcal{K} e^{-2i\hat{\omega}\hat{x}_0} e^{+i\hat{\omega}\hat{x}}, & \hat{x} \to \hat{x}_0 \\ \hat{C}_l^- e^{-i\hat{\omega}\hat{x}} + \hat{C}_l^+ e^{+i\hat{\omega}\hat{x}}, & \hat{x} \to \infty \end{cases}, \tag{5.16}$$

where $\hat{x}_0$ is the radial coordinate of the 'Nariai-ECO' surface. In analogy with the Schwarzschild in and up modes (see equations (2.16) and (2.17)) standard solutions $\hat{u}_l^{in}$ and $\hat{u}_l^{up}$ may be defined with the following asymptotic behaviour

$$\hat{u}_l^{\text{in}}(\hat{x}) \sim \begin{cases} e^{-i\hat{\omega}\hat{x}}, & \hat{x} \to -\infty \\ \hat{A}_l^+ e^{i\hat{\omega}\hat{x}} + \hat{A}_l^- e^{-i\hat{\omega}\hat{x}} & \hat{x} \to \infty \end{cases}, \tag{5.17}$$

and

$$\hat{u}_l^{\text{up}}(\hat{x}) \sim \begin{cases} \hat{B}_l^+ e^{i\hat{\omega}\hat{x}} + \hat{B}_l^- e^{-i\hat{\omega}\hat{x}}, & \hat{x} \to -\infty \\ e^{i\hat{\omega}\hat{x}}, & \hat{x} \to \infty \end{cases}, \tag{5.18}$$

In fact, $\hat{u}_l^{\text{in/up}}$ are known in closed form [105], and are particularly simple when $\xi = 1/8$ [1] (the conformal coupling factor for three dimensions),

$$\hat{u}_l^{\text{in}} = \Gamma[1 - i\hat{\omega}] P_{iL-1/2}^{i\hat{\omega}}(-z), \tag{5.19}$$

$$\hat{u}_l^{\text{up}} = \Gamma[1 - i\hat{\omega}] P_{iL-1/2}^{i\hat{\omega}}(z). \tag{5.20}$$

Using series expansions for the Legendre functions about $z = 1$, the coefficients are found to be [105]

$$\hat{B}_l^{+} = \frac{\Gamma(-i\hat{\omega})\Gamma(1 - i\hat{\omega})}{\Gamma(\frac{1}{2} + iL - i\hat{\omega})\Gamma(\frac{1}{2} - iL - i\hat{\omega})}, \tag{5.21a}$$

$$\hat{B}_l^{-} = \frac{\Gamma(i\hat{\omega})\Gamma(1 - i\hat{\omega})}{\Gamma(\frac{1}{2} + iL)\Gamma(\frac{1}{2} - iL)}, \tag{5.21b}$$

where $\Gamma(\cdot)$ is the Gamma function. The Nariai potential is symmetric under the transformation $x \leftrightarrow -x$, which implies that $\hat{A}_l^{\pm} = \hat{B}_l^{\mp}$.

5.3.1 Quasinormal mode spectrum

The Pöschl-Teller / Nariai compact body model has a spectrum of modes defined by (in analogy with equation (5.6))

$$\frac{\hat{B}_l^{+}}{\hat{B}_l^{-}} = \frac{\Gamma(-i\hat{\omega})}{\Gamma(+i\hat{\omega})} \cdot \frac{\Gamma(\frac{1}{2} + iL)\Gamma(\frac{1}{2} - iL)}{\Gamma(\frac{1}{2} + iL - i\hat{\omega})\Gamma(\frac{1}{2} - iL - i\hat{\omega})} = \tilde{\mathcal{K}}. \tag{5.22}$$

When $\hat{\omega} \ll L$ (i.e. the mode is trapped deep within the cavity), equation (5.22) can be solved for $\hat{\omega}_{ln}$ approximately,

$$\hat{\omega}_{ln} \approx \frac{\pi(n + 1/2)}{|\hat{x}_0|} + i\frac{\log|\mathcal{K}|}{2|\hat{x}_0|}. \tag{5.23}$$

The spectrum in this regime, $\hat{\omega} \ll L$, thus has an approximately uniform spacing of $\Delta_\omega = \pi/|\hat{x}_0|$ and a constant imaginary part.

---

[1] Note that the closest match to the Schwarzschild effective potential is achieved by choosing $\xi = 0$. However, our aim is to gain a qualitative understanding of a comparison problem that is possible to solve analytically in a simple closed form, so we may as well choose $\xi = 1/8$.

5.3.2 Breit-Wigner amplitude

We now derive an approximation for the Breit-Wigner amplitude appearing in the transmission factor formula valid for circular frequencies close to a QNF (see equations (5.8) and (5.9) with $C_l^- \to \hat{C}_l^-$, $\omega \to \hat{\omega}$).

First, considering Wronskians of the independent mode solutions yields

$$\hat{C}_l^- \approx \hat{B}_l^+ - \hat{B}_l^- \tilde{\mathcal{K}}. \tag{5.24}$$

Differentiating equation (5.24) we find

$$\left.\frac{\partial \hat{C}_l^-}{\partial \hat{\omega}}\right|_{\hat{\omega}=\hat{\omega}_{ln}} \approx \hat{B}_l^+ \left(2i\hat{x}_0 - \frac{\partial}{\partial \hat{\omega}}\left[\log\left(\frac{\hat{B}_l^-}{\hat{B}_l^+}\right)\right]\right)\Bigg|_{\hat{\omega}=\hat{\omega}_{ln}}. \tag{5.25}$$

For $\hat{\omega} \ll L$, the first term of equation (5.25) dominates, so that the Breit-Wigner amplitude for the Nariai-ECO model is

$$\hat{\mathcal{A}}_{ln} \approx \frac{(1-|\mathcal{K}|^2)}{4\hat{x}_0^2} \cdot \frac{1}{|\hat{B}_l^+|^2}. \tag{5.26}$$

Using the reflection identity, $\Gamma(z)\Gamma(1-z) = \pi\csc(\pi z)$, and the identity $\Gamma(z)^* = \Gamma(z^*)$ [117], we can express $|\hat{B}_l^+|^2$ for $\hat{\omega}$ real as

$$|\hat{B}_l^+|^2 = \frac{\cosh\left[\pi\left(L-\hat{\omega}\right)\right]\cosh\left[\pi\left(L+\hat{\omega}\right)\right]}{\sinh^2\left(\pi\hat{\omega}\right)}. \tag{5.27}$$

Assuming $\mathrm{Re}\,\hat{\omega}_{ln} \gg \mathrm{Im}\,\hat{\omega}_{ln}$, substituting equation (5.27) into equation (5.26) gives

$$\hat{\mathcal{A}}_{ln} \approx \frac{(1-|\mathcal{K}|^2)}{4\hat{x}_0^2} \cdot \frac{\sinh^2\left(\pi\hat{\omega}\right)}{\cosh\left[\pi\left(L-\hat{\omega}\right)\right]\cosh\left[\pi\left(L+\hat{\omega}\right)\right]}. \tag{5.28}$$

Equation (5.28) tells us that spectral lines for $L \gg \hat{\omega}$ will be exponentially suppressed. They should become significant for $L \sim \hat{\omega}$.

5.4 Long wavelength approximation

Unruh derived an approximation for the absorption of scalar and spinor particles by a black hole in the limit where the particles wavelength is much larger than the Schwarzschild radius [103] $(M\omega \ll 1)$. For the massless scalar case it is given by

$$\sigma_{\text{BH}} \approx 16\pi M^2. \tag{5.29}$$

Following the method of [103] we will now derive a long wavelength limit for scalar particle absorption by an ECO with boundary conditions given by equation (5.2).

Neglecting the ω^2 terms in equation (2.5), and defining $z \equiv r/M - 1$, one can rewrite the equation for the radial mode in the exterior (see also equation (2.9)) as

$$\left[(1-z^2)\frac{d}{dz^2} - 2z\frac{d}{dz} + l(l+1)\right]\frac{2}{z+1}u_l = 0. \tag{5.30}$$

The general solution to equation (5.30) is

$$u_l = \frac{z+1}{2}(C_I P_l(z) + C_{II} Q_l(z)), \tag{5.31}$$

where $P_l(z)$ and $Q_l(z)$ are the Legendre functions of the first and second kind respectively [117], and C_I and C_{II} are constants determined by the boundary conditions.

5.4.1 Near surface region

Near the surface ($z = 1 + \epsilon$, where $\epsilon \ll 1$) we use the asymptotic forms

$$P_l(z) \sim 1 + O(z-1), \tag{5.32}$$

$$Q_l(z) \sim -\frac{\log(z-1)}{2l!} + a_l + O(z-1), \tag{5.33}$$

where

$$a_l = \frac{1}{l!}\left(\frac{1}{2}\log 2 - \gamma - \frac{\Gamma'(l+1)}{\Gamma(l+1)}\right). \tag{5.34}$$

Therefore, as $z \to 1^+$,

$$u_l \sim \left(C_I + C_{II}(-\log(z-1)/2l! + a_l)\right). \tag{5.35a}$$

$$\left.\frac{\partial u_l}{\partial z}\right|_{r=R} \sim -\frac{C_{II}}{2(l!)}(z-1)^{-1}. \tag{5.35b}$$

Expanding the boundary conditions, equation (5.2), in ω yields

$$u_l \sim (1+\mathcal{K}) + O(\omega), \tag{5.36a}$$

$$\left.\frac{\partial u_l}{\partial z}\right|_{r=R} \sim -\left(1 + \frac{2}{l!(z-1)}\right) iM\omega(1-\mathcal{K}) + O(\omega^2). \tag{5.36b}$$

Applying the conditions of equation (5.36) to the approximate general solution equation (5.35) gives

$$C_I \sim (1+\mathcal{K}), \tag{5.37a}$$

$$C_{II} \sim 4iM\omega(l!)(1-\mathcal{K}), \tag{5.37b}$$

to lowest order in ω (assuming $\mathcal{K} \neq \pm 1$). Defining $D_{II} = C_{II}/(4iM\omega(l!))$ note that

$$\frac{1}{2}\left(C_I D_{II}^* + C_I^* D_{II}\right) = 1 - |\mathcal{K}|^2. \tag{5.38}$$

5.4.2 Far field region

In the far field, the Legendre polynomial solutions have the approximate forms [117]

$$P_l(z) \sim \frac{(2l)!}{2^l (l!)^2} z^l, \tag{5.39}$$

$$Q_l(z) \sim \frac{2^l l!}{(2l+1)!} z^{-l-1}, \tag{5.40}$$

and so

$$u_l \approx C_I \frac{(2l)!}{2^{l+1}(l!)^2}\left(\frac{r}{M}\right)^{l+1} + C_{II}\frac{2^{l-1} l!}{(2l+1)!}\left(\frac{r}{M}\right)^{-l}. \tag{5.41}$$

It is convenient to also use a comparison equation obtained by neglecting terms of $O(2M/r)$ in equation (2.8),

$$\left[r_*^2 \frac{d^2}{dr_*^2}\psi + \omega^2 r_*^2 - l(l+1)\right] u_l \approx 0. \tag{5.42}$$

A set of solutions to equation (5.42) are the spherical Hankel functions, $h_l^{(1)}(\omega r_*)$ and $h_l^{(2)}(\omega r_*)$ [117], with far field behaviour

$$h_l^{(1)}(\omega r_*) \sim (i)^{-l-1}\frac{e^{i\omega r_*}}{\omega r_*}, \tag{5.43}$$

$$h_l^{(2)}(\omega r_*) \sim (i)^{l+1}\frac{e^{-i\omega r_*}}{\omega r_*}. \tag{5.44}$$

In order to match with the boundary conditions in the far field (equation (5.2)), the solution we seek is

$$u_l \approx \omega r_* \left[C_l^-(-i)^{l+1} h_l^{(2)}(\omega r_*) + C_l^+ i^{l+1} h_l^{(1)}(\omega r_*)\right]. \tag{5.45}$$

The spherical Hankel functions are related to the spherical Bessel functions of the first and second kind, $j_l(x)$ and $n_l(x)$, via [117]

$$h_l^{(1)} = j_l + i n_l, \quad h_l^{(2)} = j_l - i n_l, \tag{5.46}$$

with asymptotic expansions

$$j_l(x) \sim \frac{2^l l!}{(2l+1)!}x^l + O(x^{l+2}), \quad \text{as } x \to 0, \tag{5.47}$$

$$n_l(x) \sim -\frac{(2l)!}{2^l l!}x^{-l-1} + O(x^{-l+1}), \quad \text{as } x \to 0. \tag{5.48}$$

Taking the limit $\omega \to 0$ for some finite r_*, the RHS of equation (5.45) is

$$\begin{aligned}\psi \sim \Bigg[&\frac{2^l l!}{(2l+1)!}\omega^{l+1}\left(C_l^-(-i)^{l+1} + C_l^+ i^{l+1}\right) r^{l+1} \\ &- \frac{i(2l)!}{2^l l!}\omega^{-l}\left(C_l^-(-i)^{l+1} - +C_l^+ i^{l+1}\right) r^{-l}\Bigg].\end{aligned} \tag{5.49}$$

Comparing equations (5.41) and (5.49), we see that

$$C_I \approx \frac{2^{2l+1}(l!)^3}{(2l)!(2l+1)!}(M\omega)^{l+1}[C_l^-(-i)^{l+1} + C_l^+ i^{l+1}], \tag{5.50}$$

$$C_{II} \approx -i\frac{(2l)!(2l+1)!}{2^{2l-1}(l!)^2}(M\omega)^{-l}[C_l^-(-i)^{l+1} - C_l^+ i^{l+1}]. \tag{5.51}$$

Provided $\mathcal{K} \neq 1$, by equations (5.37b) and (5.51) we have

$$C_l^+ \approx (-1)^{l+1} C_l^- + O\left(\omega^{2(l+1)}\right), \tag{5.52}$$

and therefore

$$C_I \approx \frac{2^{2l+2}(l!)^3}{(2l)!(2l+1)!}(M\omega)^{l+1} C_l^-(-i)^{l+1}. \tag{5.53}$$

By equations (5.37a) and (5.53)

$$\frac{1}{|C_l^-|} \approx \frac{2^{2l+2}(l!)^3}{(2l)!(2l+1)!}(M\omega)^{l+1} \cdot \frac{1}{|1+\mathcal{K}|}. \tag{5.54}$$

5.4.3 Absorption cross section in the long wavelength limit

Substituting equation (5.54) into the absorption cross section summation, equation (5.3), we see that only the s-wave contributes ($l = 0$) when $\omega \to 0$. Then, we arrive at the $M\omega \ll 1$ approximation for the absorption cross section of our model object,

$$\sigma_{\text{abs}} \approx \frac{1-\mathcal{K}}{1+\mathcal{K}} \cdot 16\pi M^2. \tag{5.55}$$

Reassuringly, when $\mathcal{K} = 0$, this reduces to the black hole approximation, equation (5.29). It also holds as $\mathcal{K} \to +1$, as the absorption cross section should be zero when the object is completely reflective ($\mathcal{K} = 1$). This result does not hold as $\mathcal{K} \to -1$ (see equation (5.37)).

5.5 Numerical method

In order to calculate the absorption cross section, equation (5.3), and mode spectra, we used numerical techniques.

We begin by solving the exterior radial equation (see equation (2.8)) initialised at $R = 2M + \delta R$ with the corresponding boundary condition of equation (5.2). This is done numerically using the `NDSolve` function in `Mathematica`, and we terminate the integration at some $r = r_{\text{max}}$. As in section 3.5, we match the numerical solution to the generalised series solutions (see equation (3.65)) in the far field, to obtain $C_l^{\pm}$.

For the quasinormal mode spectra, we again use direct integration. First, we integrate the solution satisfying the boundary condition at the surface $R = 2M + \delta R$ out to some intermediate $r_1 > R$. Next, we integrate the solution satisfying the outgoing boundary condition (i.e. $C_l^- = 0$) from $r = r_{\text{max}}$ to r_1, initialised with the appropriate generalised series solution. If the Wronskian of the two numerical solutions is zero, then they are linearly dependent. Zeros of the Wronskian correspond to quasinormal mode frequencies. A quasinormal mode solution can be constructed by normalising one of the numerical solutions so they match at r_1. We use the `FindRoot` algorithm in `Mathematica` to search for quasinormal mode frequencies. This appears to be stable for frequencies with small imaginary part, i.e. the trapped modes we are interested in.

Typically we use the condition $r = r_{\text{max}} = 100(l+1)/\omega$ to ensure accuracy of the series solutions in the far field. We check the stability of the results by varying r_1 and r_{max}.

5.6 Results

At low frequencies we have found the numerical results to approach the expected limit obtained analytically (see equation (5.55)). At high frequencies we find that σ_{abs} oscillates about the value

$$\sigma_{\text{abs}} \approx \left(1 - |\mathcal{K}|^2\right) \cdot 27\pi M^2, \tag{5.56}$$

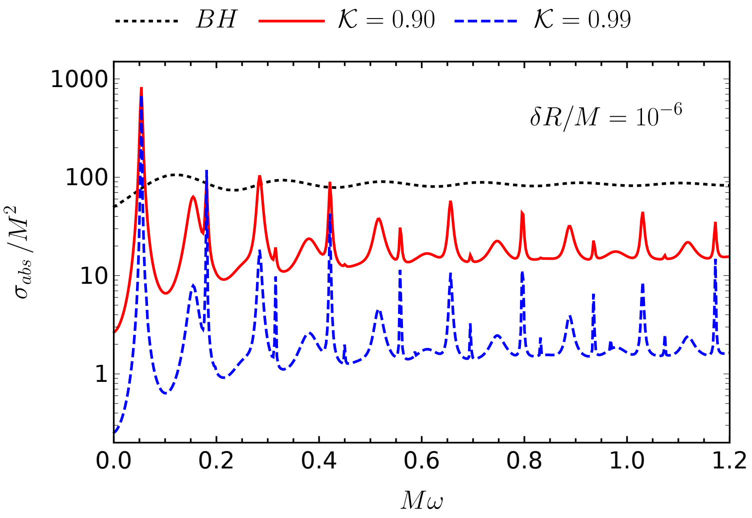

Figure 5.2: Absorption cross section for an ECO with $\delta R = 10^{-6}M$ and $\mathcal{K} = 0.9$ (red, solid) or $\mathcal{K} = 0.99$ (blue, dashed). Also shown for comparison is the absorption cross section for a Schwarzschild BH.

which reduces to the black hole geometric optics limit, $\sigma_{\rm BH} \to 27\pi M^2$, when $\mathcal{K} = 0$. At intermediate frequencies, there is noteworthy structure in $\sigma_{\rm abs}$.

In figure 5.2 we display the absorption cross section for two ECOs with $\mathcal{K} = 0.9$ and $\mathcal{K} = 0.99$. Both have $\delta R = 10^{-6}M$. There are clear spectral lines to be seen in the cross sections, and they are found at frequencies corresponding to the real part of quasinormal mode frequencies of the respective model (see table 5.1).

Not all modes correspond to a peak, as can be seen in figure 5.3. Some may be 'washed out' by other dominant spectral lines. For example, in figure 5.3, the $l = 0$ fundamental ($n = 0$) trapped mode produces a peak in the absorption cross section that obscures possible contributions from other fundamental modes with $l > 0$.

As anticipated by the Nariai / Pösch-Teller comparison model, the real part of the QNFs are relatively insensitive to $\mathcal{K}$. See for example table 5.1 where we tabulate the QNFs for $R = 10^{-6}$ and $\mathcal{K} \in \{0.5, 0.9, 0.99\}$. The spectral line

l	n	$\mathcal{K}$	$\mathrm{Re}\,[M\omega_{ln}]$	- $\mathrm{Im}\,[M\omega_{ln}]$
0	1	0.50	0.053321	0.012164
	1	0.90	0.053535	0.0023733
	1	0.99	0.053579	0.00077809
	2	0.50	0.15252	0.021562
	2	0.90	0.15427	0.012389
	2	0.99	0.15455	0.010888
	3	0.50	0.25353	0.046067
	3	0.90	0.25605	0.036247
	3	0.99	0.25646	0.034653
1	1	0.50	0.062490	0.013634
	1	0.90	0.062445	0.0020724
	1	0.99	0.062444	0.00019810
	2	0.50	0.18063	0.012444
	2	0.90	0.18059	0.0020209
	2	0.99	0.18060	0.00032924
	3	0.50	0.28322	0.014442
	3	0.90	0.28405	0.0055299
	3	0.99	0.28419	0.0040702
	4	0.50	0.37652	0.032500
	4	0.90	0.37890	0.023474
	4	0.99	0.37928	0.022004

Table 5.1: The lowest quasinormal frequencies ω_{ln} for the scalar field. The radius of the compact bodies is $R = 2M + \delta R$ and $\delta R = 10^{-6}M$.

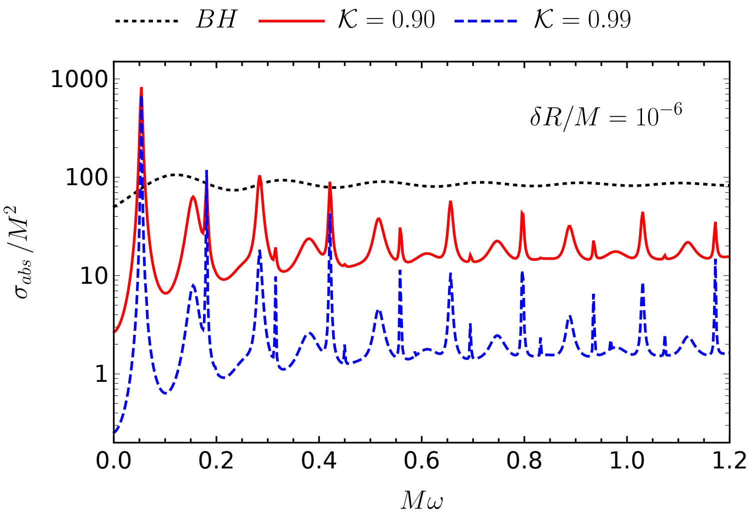

Figure 5.3: Absorption cross section for an ECO with $\delta R = 10^{-6}M$ and $\mathcal{K} = 0.9$. Vertical lines mark the real part of quasinormal mode frequencies, $\mathrm{Re}\,\omega_{ln}$, for $l \in \{0, 1, 2, 3\}$. Spectral lines in the cross section correspond to $\mathrm{Re}\,\omega_{ln}$, and their width is controlled by $\mathrm{Im}\,\omega_{ln}$ (see text for more details).

positions are thus relatively insensitive to $\mathcal{K}$.

The position of the peaks *is* sensitive to $\delta R/M$, as anticipated by the comparison model result, equation (5.23). In figures 5.4 and 5.5 we compare the absorption cross sections for varying values of $\delta R/M \in \{10^{-4}, 10^{-6}, 10^{-20}\}$, keeping $\mathcal{K} = 0.9$ fixed. The lines become more closely spaced as $\delta R/M$ decreases.

The angular width of the peaks are set by the imaginary part of the corresponding QNF. As can be seen from the Breit-Wigner formula, when $|\omega - \mathrm{Re}\,\omega_{ln}| = |\mathrm{Im}\,\omega_{ln}|$, the approximate transmission factor is half its maximum value. The imaginary part of the QNFs, and thus the width of the spectral lines depends on $\mathcal{K}$. The smaller $|\mathcal{K}|$, the smaller $|\mathrm{Im}\,\omega_{ln}|$. Essentially, the more reflective the ECO, the longer lived the trapped modes, as may have been expected. Consequently, the more reflective the ECO, the sharper the spectral lines. This can be seen in figure 5.2. In addition, the width is set by $\delta R/M$, as predicted by equation (5.23). As can be seen in figures 5.4 and 5.5, the smaller $\delta R/M$, the sharper the lines.

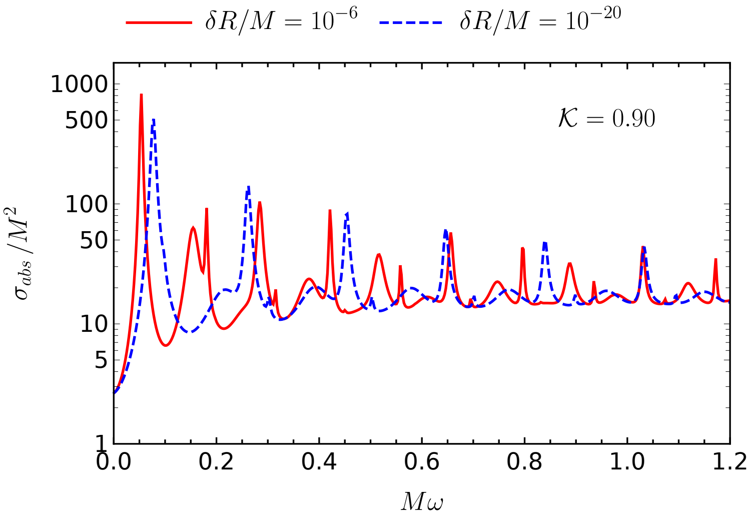

Figure 5.4: Absorption cross section for an ECO with $\mathcal{K} = 0.9$ and $\delta R = 10^{-6}M$ (red, solid) or $\delta R = 10^{-4}M$ (blue, dashed).

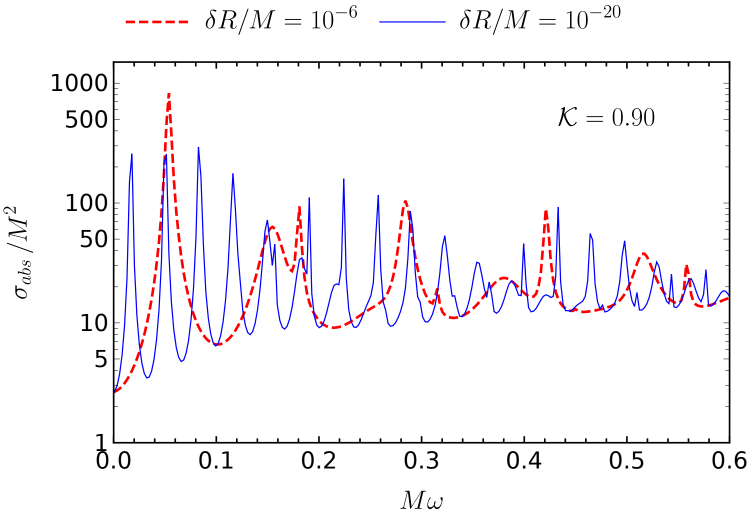

Figure 5.5: Absorption cross section for an ECO with $\mathcal{K} = 0.9$ and $\delta R = 10^{-6}M$ (red, solid) or $\delta R = 10^{-20}M$ (blue, dashed).

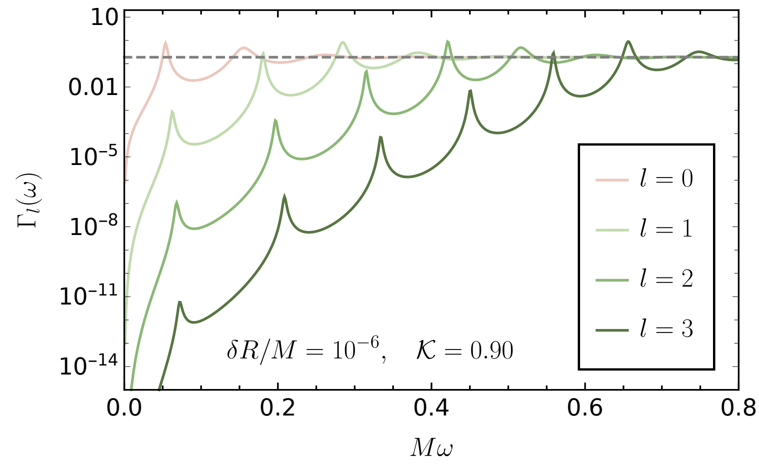

Figure 5.6: Transmission factors, $\Gamma_l(\omega)$, for an ECO with $\mathcal{K} = 0.9$ and $\delta R = 10^{-6}M$. The dashed horizontal line is at $\Gamma_l(\omega) = 1 - \mathcal{K}^2$.

The amplitude of a spectral line peak is set by the transmission factors. In figure 5.6 we plot the transmission factors, $\Gamma_{\omega l}$ for $\mathcal{K} = 0.9$, $\delta R = 10^{-6}M$, and $0 \leq l \leq 3$. For a given multipole, $\Gamma_{\omega l}$ exhibits evenly spaced peaks of Breit-Wigner form. The peaks have approximately the same width, and their amplitude increases exponentially with ω until $\omega \gtrsim (l + 1/2)/(\sqrt{27}M)$. At higher frequencies, the peaks become wider and less prominent, and the transmission factors oscillate about the value $1-\mathcal{K}^2$. The same qualitative behaviour is seen for the transmission factors for the Pöschl-Teller potential model (see section 5.3). The transmission factor peaks are shifted due to the different effective potentials in each model, as can be seen in figure 5.7.

In general, we find that one transmission factor dominates at a spectral line frequency, corresponding to the angular mode number of the corresponding QNM. The visible spectral lines occur at peaks of the transmission factors when $\omega \sim (l+1/2)/(\sqrt{27}M)$, in other words, when the energy ω^2 is near to the height of the potential barrier, $V_0 = (l + 1/2)^2/(27M^2)$. This can be seen in figure 5.8, where we use the Breit-Wigner approximation, equation (5.9), close to the first few spectral lines of a model with $\mathcal{K} = 0.9$ and $\delta R = 10^{-6}M$.

As can be seen in figure 5.2, the spectral lines with the greatest amplitude are seen at lower frequencies $M\omega \lesssim 0.1$ (due to the factor of ω^{-2} in equa-

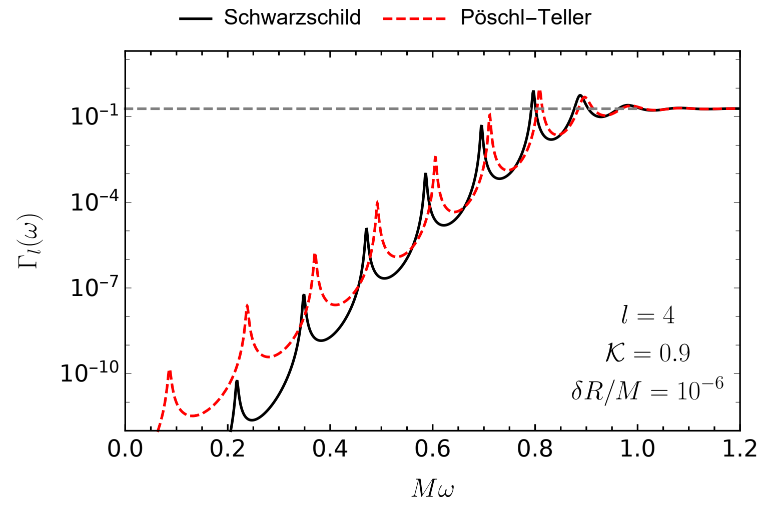

Figure 5.7: Transmission factor, $\Gamma_{l=4}(\omega)$, for an ECO with $\mathcal{K} = 0.9$ and $\delta R = 10^{-6}M$ (black). We also show the transmission factor for the Pöschl-Teller comparison potential (dashed red).

tion (5.3)). In this regime, absorption can exceed the high (and low) frequency limit by more than two orders of magnitude. We note that for objects with small dissipation, $1 > |\mathcal{K}| \gtrsim 0.9$, absorption at the lowest frequency spectral lines may drastically exceed that of a black hole. In these cases, the incoming wave has excited one of the lowest energy trapped modes.

The transmission factors appear to possess an approximate shift symmetry under $l \to l + 1$ and $\omega \to \omega + 1/(\sqrt{27}M)$, as seen in figure 5.6 and predicted by equations (5.23) and (5.28). Thus the dominant peak amplitude for a given $\Gamma_l(\omega)$, that gives rise to a spectral line at $\omega \approx (l + 1/2)/(\sqrt{27}M)$, is insensitive to l. By equation (5.3), we can expect the amplitude of of the spectral lines to therefore scale as ω^{-1} at high frequencies.

Trapped modes may loosely be defined as those with $M\omega_I \lesssim 10^{-2}$ [32]. As shown in figure 5.9, they satisfy $M\omega_R \lesssim (l + 1/2)/\sqrt{27}$, i.e. they have an effective 'energy' ω_R^2 less than the height of the potential barrier at the light ring (see figure 5.1).

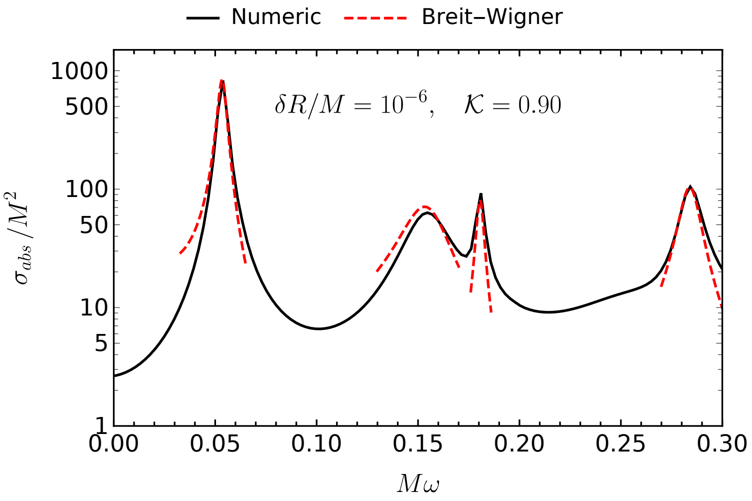

Figure 5.8: Absorption cross section for an ECO with $\mathcal{K} = 0.9$ and $\delta R = 10^{-6}M$ (black, solid) and the Breit-Wigner approximation (equation (5.9)) for frequencies near spectral lines / quasinormal mode frequencies (red, dashed).

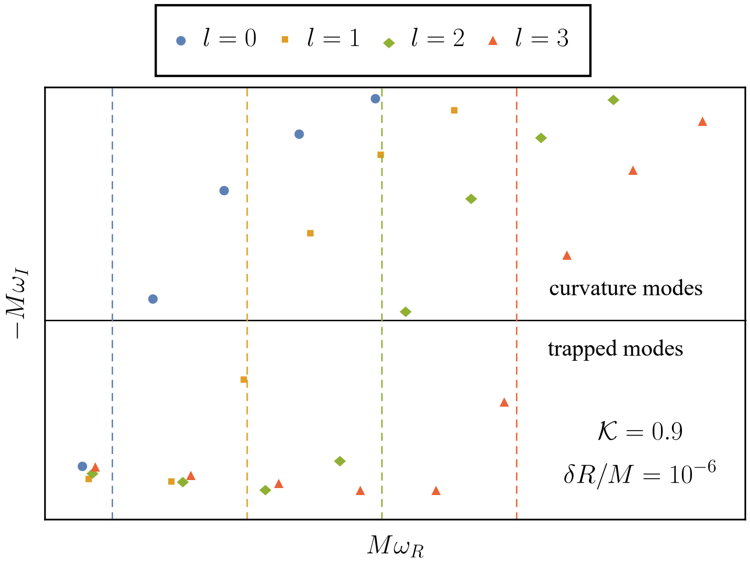

Figure 5.9: Quasinormal frequencies for an ECO with $\mathcal{K} = 0.9$ and $\delta R = 10^{-6}M$. It is easy to distinguish 'trapped' modes by eye as those with $|M\omega_{\rm I}| \lesssim 10^{-2}$ [32]. Trapped modes satisfy $M\omega_{\rm R} \lesssim (l + 1/2)/\sqrt{27}$, shown as dotted vertical lines.

5.7 Conclusions

In this chapter we have shown that a quite generic class of compact objects with partially reflective surfaces and a photon sphere exhibit an absorption cross section with spectral lines.

The frequencies the lines are found at correspond to quasinormal mode solutions that are 'trapped' between the photon sphere and the surface. Physically, we imagine an incident wave of the right frequency exciting a trapped mode, which undergoes successive reflections at the light ring and partial absorption/reflection at the surface. Our study is in the frequency domain, so it makes little sense to speak of a dynamic physical process like this, but we can expect the absorption of long lived, monochromatic waves to display similar properties.

Studies of ECO scattering in the time domain have shown that characteristic GW "echoes" associated with the multiple reflections in the cavity are expected to radiate to the far field [18, 26, 27, 164, 185, 186, 192]. Each echo is dominated by frequencies close to black hole QNM frequencies. The presence of echoes in principle distinguishes the object from a black hole, and the wave form properties can be used to infer $\delta R/M$ and $\mathcal{K}$. The results presented here (section 5.6) suggest a complementary method to diagnose ECO properties.

The spectral lines angular-frequency width is approximately $-\log\mathcal{K}/(2|x_0|)$. They have a spacing of roughly $\pi/|x_0|$, predicted by a comparison model (equation (5.23)). Individual lines are resolvable if the spacing is greater than the (angular-frequency) width. Thus, the more reflective objects have sharper, better resolved lines compared to more dissipative ECOs, i.e., those with smaller values of $|\mathcal{K}|$. This can be seen in figure 5.2. Also, ECOs with a larger cavity ($\delta R/M$ small, $|x_0|$ large) will have sharper and more closely spaced spectral lines, as shown in figure 5.5.

Our model considers a massless scalar field, but we would expect similar absorption spectra for other fields incident on a spherically symmetric ECO with the partially reflective boundary conditions, since the radial equations are similar. There would be some differences, for example radiative electromagnetic and gravitational perturbations (spin $s = 1$ and $s = 2$ respectively) do not have multi-pole components with $l < s$.

If we consider an ECO of mass M_E the strongest spectral lines are at lower frequencies $M_\mathrm{E}\omega \lesssim 1$ which corresponds to $\omega \lesssim 2.0 \times 10^5 (M_\odot/M_\mathrm{E})$ Hz. For an ECO with mass comparable to a stellar black hole $M_\mathrm{E} = 10M_\odot$, considering the electromagnetic spectrum, the strongest spectral lines would be expected for very low frequency radio waves. For the CMB, $10M_\odot\omega \sim 10^7$ in geometric units and we would expect any absorption lines to be highly suppressed due to the $1/\omega$ fall-off.

A more promising possibility is an essentially monochromatic GW signal generated by a massive binary, which may lie in the region $10^{-4}\,\mathrm{Hz} \lesssim \omega \lesssim 10^{-1}\,\mathrm{Hz}$. An ECO of mass $10^6 \lesssim M_\mathrm{E}/M_\odot \lesssim 10^9$ could in principle display strong spectral lines if illuminated by such a source. There is one such candidate at the centre of our galaxy, the supermassive compact object Sagittarius A* (generally believed to harbour a central black hole), with mass $M \approx 4 \times 10^6 M_\odot$ [195].

Even if the parameters in a given scenario are favourable for strong spectral lines, the next question is how would one detect them? Speculatively, one could imagine a binary GW source, with a SMBH candidate fortuitously placed between it and a detector. As the binary swept out a range of frequencies, it may coincide with a trapped mode of the intermediate object, and a conspicuous dip in the detected amplitude might be expected. In this way, the possibility for BH alternatives could be tested using GW spectral lines. In addition, the cavity size and dissipative properties could in principle be inferred from the angular spacing, sharpness, and strength of the absorption lines.

The results displayed here may have some bearing on scattering by neutron stars. In previous chapters we described how GWs couple to fluid oscillations. Our toy models neglected the possibility of energy loss through friction, which could effectively absorb energy from an incident wave. At the right frequency, a GW may excite a fluid mode of a neutron star, which would then decay through heat loss. It seems possible that similar spectral lines may be expected in the absorption cross section for a neutron star.

In addition to absorption lines, we might also expect an ECO to display *emission* lines. The transmission factors are a key ingredient in the calculation of Hawking emission for black holes, in fact the number of particles emitted by a Schwarzschild black hole per unit time per unit frequency can be written in terms of the absorption cross section [121, 196]:

$$\frac{d^2N}{dtd\omega} = \frac{1}{2\pi}\sum_{l=0}^{\infty}\frac{(2l+1)\Gamma_{\omega l}}{e^{2\pi\omega/\kappa}-1} = \frac{\omega^2}{2\pi^2}\cdot\frac{\sigma_{\rm BH}}{e^{2\pi\omega/\kappa}-1}, \tag{5.57}$$

where $\kappa = 1/(4M)$ is the surface gravity. With the above considerations in mind, one may naively expect that ECOs could generate emission spectra with notable deviations from the perfect black body spectrum predicted for black holes [196]. Also, models of rotating ECOs have unstable trapped modes, i.e., modes that grow exponentially over time [164, 192]. These arise due to superradiance which causes an ergoregion instability. An impinging wave could excite an unstable mode of a rotating ECO, leading to stimulated emission lines.

Chapter 6

Regge poles of compact bodies and their application to scattering theory

Chandrasekhar showed that black hole perturbation theory could be formulated in terms of a scattering problem [90]. This picture places the scattering matrix $\mathcal{S}(l,\omega)$ (see equation (2.18)) in a lead role for many calculations one may wish to do. Physically relevant questions rely on the information contained in $\mathcal{S}(l,\omega)$, such as what outgoing gravitational radiation would be detected by an observer far away from a black hole perturbed by some source matter/energy.

Thorne and collaborators first formulated the theory of relativistic stellar perturbations in analogy with the Newtonian approach [29, 30]. The main new relativistic ingredient was that the fluid oscillation modes were damped by a coupling to gravitational waves, which radiated away energy to infinity. In this picture, the initial disturbance is envisaged as a perturbation of the stellar matter.

In a complementary approach, Chandrasekhar and Ferrari presented the oscillations of a star's spacetime as a scattering problem [98–100]. They manipulated the linearised Einstein equations so that the hydrodynamical and space-time perturbation equations decoupled. With the decoupling, one could solve for the space-time perturbations (GWs) *without any reference to the mat-*

ter perturbations [1]. This, in essence, is why one may view the non-radial oscillations of a star purely in terms of scattering by gravitational waves (in the same way as black hole perturbations).

The natural modes of oscillation for a non-rotating compact object are well understood in terms of resonant modes with complex frequencies - a.k.a. quasinormal modes (QNM). A thorough review is given by Kokkotas and Schutz [32]. Recall that these correspond to poles, ω_n, of $\mathcal{S}(l,\omega)$ which is analytically extended to the complex ω-plane for a given integer value of angular momentum l. We have noted the role of trapped resonant modes for exotic compact objects in the previous chapter, and there is a substantial literature on QNMs for many compact objects within general relativity and alternative theories of gravity (see for example [22, 29, 31, 98, 192, 197, 198], and for a more complete reference set see [32]).

A dual-picture is provided by analytically extending $\mathcal{S}(l,\omega)$ (and the mode solutions) into the complex l-plane for a given $\omega \in \mathbb{R}$. It is convention to instead refer to the complex λ-plane where $\lambda \equiv l + 1/2$. This is the complex angular momentum (CAM) picture. It may be that certain complex λ_n exist such that the corresponding mode satisfies an outgoing radiation boundary condition in the far field, and a suitable boundary condition at the objects surface (just as QNMs do [32]). These special values λ_n are called Regge poles, and the modes are another type of resonance sometimes called "Regge modes" [199].

It appears the first application of CAM in relativity was by Chandrasekhar and Ferrari who used it to model the growth of the energy flux inside and outside a star [101]. Later, Andersson and Thylwe presented a CAM formulation of scalar wave scattering by a Schwarzschild black hole [46]. They suggested that Regge pole modes could be associated with surface waves; scalar field disturbances propagating close to the photonsphere at $r = 3M$.

The surface wave interpretation was extended by Décanini, Folacci, and Jensen [71]. They showed how the Regge pole trajectories - the path of $\lambda_n(\omega)$ in the complex plane - could be used to 'semiclassically' construct the QNM

---

[1] However, as shown in chapter 4, one of the space-time variables may in some sense play the role of a fluid perturbation.

spectrum of a Schwarzschild black hole (formally valid when $|\lambda| \to \infty$ but suprisingly accurace at small values of λ). This allowed them to associate resonant frequencies with constructive interference of surface waves. In reference [71], the authors posit that the CAM approach could be usefully extended to perturbations of Kerr black holes and neutron stars. We have taken up the latter suggestion here and in reference [65].

More recent work on CAM in black hole physics includes; a WKB calculation of Regge poles and the interpretation that this allows by Décanini *et al* [200, 201]; efficient and elegant calculations of the high-energy absorption cross section for a Schwarzschild black hole [202]; a description of GWs from a perturbed black hole which complements the usual QNM picture by Folacci and Ould El Hadj [199]; and a CAM description of plane wave scattering of bosonic fields by the same authors [57, 58]. The last of these studies established a procedure for rewriting a partial-wave scattering cross section sum (see equation (2.39)) as a background integral and a sum over Regge-poles. Folacci and Ould El Hadj found a particularly surprising result: that the scattering cross section of a plane wave incident on a black hole is well described by Regge pole contributions alone, and the background integral was negligible except in the forward direction. This contrasts with the majority of scattering CAM calculations in other areas of physics, where the background integral is often significant in multiple scattering regions [68].

CAM is not unique to scattering theory in GR. The origins of CAM theory date back to Watson's study of propagation of radio waves around the Earth [34]. In particular, he wished to understand the penetration of waves from a transmitter to a receiver in the geometrical shadow region. As we have seen in chapter 3, the partial wave sum may suffer from slow convergence, especially at high frequencies. In some cases, CAM methods can be used to avoid this problem. The main motivations for using CAM include the type of numerical advantage described above [57, 58], the possibility of obtaining closed-form approximations for quantities of interest [200–202], and the physical understanding this can allow [46, 71].

Recently, in collaboration with M. Ould El Hadj and S.R. Dolan, we have begun to generalise black hole CAM theory to other compact objects. In particular, we focus on neutron star models as well as more speculative ultra compact objects. This is the subject of this chapter. Part of the material (and some additional material) is also presented in reference [65]. All of the data and figures in this chapter have been generated by the author.

We begin by discussing an accurate method of calculating scalar, electromagnetic, and axial GW Regge pole positions for a general spherically symmetric background in section 6.2. In section 6.2.4 we derive a WKB approximation for a class of scalar and axial-GW Regge poles on a background consisting of a massive body with $R/M > 3$. Section 6.3 outlines the similarities between our model and scattering by an isotropic sphere in flat space. In section 6.4 we present the Regge pole spectra for a scalar field on a constant density star with $R/M = 6$, and $R/M = 2.26$. We apply the CAM approach to scalar plane-wave scattering by the aforementioned models in section 6.5, and discuss our results in section 6.6.

6.1 Regge poles and quasinormal modes

We have discussed how Regge poles and their residues are useful concepts in perturbation theory, both for performing tricky calculations and for aiding with physical interpretation. In addition, the dual concepts of quasinormal frequencies and excitation factors are well understood and powerful tools [32]. The duality means that many of the methods used for determining QNMs can be adapted for finding Regge pole modes.

A well known and stable technique for determining gravitational QNM solutions for a Kerr black hole was introduced by Leaver [197]. In turn, Leaver was inspired by the method for determining electronic spectra of the hydrogen ion used by Jaffé [203]. Leaver's method was based on an analytic representation of a QNM solution, which for a Schwarzschild black hole is given by the series

$$\Phi^{p}_{lm} = \left(\frac{r}{2M} - 1\right)^{-i(2M\omega)} \left(\frac{r}{2M}\right)^{2i(2M\omega)} e^{i\omega(r-2M)} \sum_{n=0}^{\infty} a_n \left(1 - \frac{2M}{r}\right)^{n}, \qquad (6.1)$$

where p is the parity of the mode (see section 2.3.2), and a_n are constants that depend on ω, l and p. By construction, the series solution above satisfies the boundary conditions that define a QNM or Regge pole (radiate inwards at the horizon, and outwards at spatial infinity). The complex frequencies, ω_{ln} ($l \in \mathbb{N}$), for which the series defined by equation (6.1) converges, are the QNM frequencies. Analogously, for a fixed $\omega \in \mathbb{R}$, the complex angular momentum values $\lambda_n(\omega)$ for which the series of equation (6.1) converges are the Regge poles.

Substituting equation (6.1) into equation (2.75) yields a three-term recurrence relation for the coefficients a_n. Exploiting the link between three term recurrence formula and continued fractions allowed Leaver to then accurately calculate the quasinormal frequencies and modes for a Kerr black hole [197].

For the case of Reissner-Nordström (charged) black holes, Leaver found that generalising his method resulted in a four-term recurrence relation [204]. He showed that this can be solved by casting it as an infinite banded matrix equation and numerically searching for roots of the determinant (a.k.a. the Hill determinant method, which Majumdar and Panchapakesan had applied to the Schwarzschild black hole [205]). In addition, Leaver reduced the recurrence-relation to three terms, equivalent to a Gaussian elimination step applied to the matrix equation, and thus could also apply the continued fraction method [204].

Leins *et al.* generalised Leaver's method to consider polar (even parity) gravitational QNMs on a spherically symmetric stellar background [206]. They solve the interior problem numerically (see chapter 4, section 4.2), and extend the mode solution to some finite distance from the surface of the star, $r = b > R$. The next step is to construct a series solution, similar to equation (6.1), which automatically satisfies the numerically determined boundary condition at $r = b$ and the outgoing condition in the far field. This yields a four-term recurrence relation. Benhar *et al.* have calculated axial (odd parity) QNMs for various neutron star models [207], using a modification of the Leins *et al.* method [206].

By Birkhoff's theorem, the vacuum exterior is described by the Schwarzschild metric, and so the Leins *et al.* method is applicable to any spherically symmetric body of finite radius (including black holes, stars, ECOs etc.). The exact details of the central body are efficiently encoded in the boundary conditions at $r = b$.

A significant advantage of Leaver's approach is that it avoids the numerical difficulties encountered if one tries to find QNMs by numerically solving the radial differential equation. It can be seen that for QNM frequencies that decay with time, the outgoing component of a general mode solution that behaves as $\exp[i\omega r_*]$ will diverge as $r_* \to \infty$ as $\mathrm{Im}\,[\omega] < 0$. By contrast, the ingoing component of the mode will grow exponentially small in the far field. Enforcing the outgoing boundary condition is therefore a difficult task to implement numerically, as a small error in the far field could easily introduce a large error at intermediate distances. Of course, this is not an issue for Regge poles as $\mathrm{Im}\,[\omega] = 0$. However, avoiding numerical integration of complex mode solutions to the far field is still a desirable advantage of the series solutions methods over direct integration.

In section 6.2.1, we further generalise the methods described in references [197, 206, 207] to scalar and electromagnetic perturbations on the spacetime of a compact body. We derive a four term recurrence relation and show how to solve it in section 6.2.2 using an adaptation of the Hill-determinant method [204, 205]. In section 6.2.3 we discuss the direct integration method and in section 6.2.4 we derive a WKB approximation for a subset of the Regge poles expected for a compact body with $R > 3M$. Exact (numerical) results for the scalar Regge-pole resonances on the spacetime of a constant density star are displayed in section 6.4.

6.2 Methods

6.2.1 The series solution and recurrence relation

For a spherically symmetric spacetime, the radial wave equation for scalar ($s = 0$), electromagnetic ($s = 1$), and axial gravitational ($s = 2$) perturbations,

$\psi_{ls}(r)$, can be presented in a unified way [183], namely

$$\left[\frac{d^2}{dr_*^2} + \omega^2 - V^{\text{eff}}_{ls}(r)\right] \psi_{ls}(r) = 0, \tag{6.2}$$

with the effective potential

$$V^{\text{eff}}_{ls}(r) = A\left[\frac{l(l+1)}{r^2} + \frac{(1-s^2)}{2r}\left(\frac{A'}{A} + \frac{B'}{B}\right) + 8\pi\,(p-\rho)\,\delta_{s2}\right], \tag{6.3}$$

where $A(r), B(r)$ are the metric functions in equation (2.2). Recall that $p = p(r)$ is the pressure inside the star and $\rho = \rho(r)$ is the density (section 3.1).

Following [206] we express a scalar solution outside the star as a series expansion about some intermediate regular point, $r = b > R$:

$$\psi_{ls}(r) = e^{i\omega r_*} v(r), \quad v(r) \equiv \sum_{n=0}^{\infty} a_n y^n, \tag{6.4}$$

where $y = 1 - b/r$. This satisfies the outgoing boundary condition in the far field (equation (2.21) for $r_* \to \infty$ with $A_l^- = 0$), and an as yet to be determined model-dependent boundary condition at $y = 0$.

Substituting equation (6.4) into equation (6.2) for $r > R$, we find

$$fv'' + (2i\omega + f')v' - \left(\frac{l(l+1)}{r^2} + \left(1 - s^2\right)\frac{f'}{r}\right) v = 0, \tag{6.5}$$

where $' \equiv d/dr$. Now, substituting the series expansion for v into equation (6.5), we obtain

$$\begin{aligned}
2\left(1-\frac{2M}{b}\right)a_2 + \left(\frac{6M}{b}+2ib\omega-2\right)a_1 - \left(\left(1-s^2\right)\frac{2M}{b}+l(l+1)\right)a_0 \\
+\sum_{n=1}^{\infty}\Bigg[\left(1-\frac{2M}{b}\right)(n+1)(n+2)a_{n+2} \\
+\left(\left(\frac{6M}{b}-2\right)(n+1)+2ib\omega\right)(n+1)a_{n+1} \\
+\left(-\left(1-s^2\right)\frac{2M}{b}-l(l+1)+n(n+1)\left(1-\frac{6M}{b}\right)\right)a_n \\
+\frac{2M}{b}\left(n^2+\left(1-s^2\right)-1\right)a_{n-1}\Bigg]y^n = 0. \qquad (6.6)
\end{aligned}$$

Solving equation (6.6) term by term yields a recurrence relation

$$\alpha_n a_{n+1} + \beta_n a_n + \gamma_n a_{n-1} + \delta_n a_{n-2} = 0, \qquad n \geq 2, \qquad (6.7)$$

and a starting equation

$$\alpha_1 a_2 + \beta_1 a_1 + \gamma_1 a_0 = 0, \qquad (6.8)$$

where

$$\alpha_n = \left(1-\frac{2M}{b}\right)n(n+1), \qquad (6.9a)$$

$$\beta_n = \left(\left(\frac{6M}{b}-2\right)n+2ib\omega\right)n, \qquad (6.9b)$$

$$\gamma_n = \left(-\left(1-s^2\right)\frac{2M}{b}-l(l+1)+(n-1)n\left(1-\frac{6M}{b}\right)\right), \qquad (6.9c)$$

$$\delta_n = \frac{2M}{b}\left((n-1)^2+\left(1-s^2\right)-1\right), \qquad n \geq 2, \qquad (6.9d)$$

and

$$\alpha_1 = 2\left(1 - \frac{2M}{b}\right), \tag{6.10a}$$

$$\beta_1 = \left(\frac{6M}{b} + 2ib\omega - 2\right), \tag{6.10b}$$

$$\gamma_1 = \left(\left(1 - s^2\right)\frac{2M}{b} + l(l+1)\right). \tag{6.10c}$$

Continuity of the mode function and its first derivative at $r = b$ $(y = 0)$ implies

$$a_0 = e^{-i\omega r_*}\psi_{ls}\Big|_{r=b}, \tag{6.11a}$$

$$a_1 = e^{-i\omega r_*}\left(\frac{d\psi_{ls}}{dr} - \frac{i\omega}{f}\psi_{l,s}\right)\Bigg|_{r=b}. \tag{6.11b}$$

The right-hand-side of equations (6.11) is found by numerically solving the wave equation (6.2) subject to the boundary conditions of the particular model under consideration at some $r < b$ (chapter 2, sections 2.2.2 and 2.3.3), up to $r = b$. Given a_0 and a_1, we recover a_2 from the starting equation (6.8). All other coefficients a_n follow from equation (6.7).

6.2.2 Hill-determinant method

The four term recurrence relation, equation (6.7), is a (infinite) system of linear equations. It can be recast in the following matrix form

$$\begin{bmatrix} \beta_0 & \alpha_0 & \cdot & \cdot & \cdot & & & & & \\ \gamma_1 & \beta_1 & \alpha_1 & \cdot & \cdot & \cdot & & & & \\ \delta_2 & \gamma_2 & \beta_2 & \alpha_2 & \cdot & \cdot & \cdot & & & \\ \cdot & \delta_3 & \gamma_3 & \beta_3 & \alpha_3 & \cdot & \cdot & \cdot & & \\ \cdot & \cdot & \cdot & \cdot & \cdot & \cdot & \cdot & \cdot & \cdot & \\ & \cdot & \cdot & \cdot & \delta_{n-1} & \gamma_{n-1} & \beta_{n-1} & \alpha_{n-1} & \cdot & \cdot \\ & & \cdot & \cdot & \cdot & \delta_n & \gamma_n & \beta_n & \alpha_n & \cdot \\ & & & \cdot & \cdot & \cdot & \cdot & \cdot & \cdot & \cdot \end{bmatrix} \begin{bmatrix} a_0 \\ a_1 \\ a_2 \\ \cdot \\ \cdot \\ a_{n-2} \\ a_{n-1} \\ a_n \\ a_{n+1} \\ \cdot \end{bmatrix} = 0, \qquad (6.12)$$

where we have introduced

$$\alpha_0 \equiv -1, \qquad \beta_0 \equiv a_1/a_0, \qquad (6.13)$$

defined in terms of the numerically determined, model dependent $a_{0,1}$ (see equation (6.11)). The requirement that equation (6.12) has non-trivial solutions is equivalent to demanding that the determinant is zero,

$$D = \begin{vmatrix} \beta_0 & \alpha_0 & \cdot & \cdot & \cdot & & & & & \\ \gamma_1 & \beta_1 & \alpha_1 & \cdot & \cdot & \cdot & & & & \\ \delta_2 & \gamma_2 & \beta_2 & \alpha_2 & \cdot & \cdot & \cdot & & & \\ \cdot & \delta_3 & \gamma_3 & \beta_3 & \alpha_3 & \cdot & \cdot & \cdot & & \\ \cdot & \cdot & \cdot & \cdot & \cdot & \cdot & \cdot & \cdot & \cdot & \\ & \cdot & \cdot & \cdot & \delta_{n-1} & \gamma_{n-1} & \beta_{n-1} & \alpha_{n-1} & \cdot & \cdot \\ & & \cdot & \cdot & \cdot & \delta_n & \gamma_n & \beta_n & \alpha_n & \cdot \\ & & & \cdot & \cdot & \cdot & \cdot & \cdot & \cdot & \cdot \end{vmatrix} = 0. \qquad (6.14)$$

The information regarding the interior of the star is contained in α_0 and β_0 which are determined by equations (6.11) and (6.13). Let D_n be the determinant of the $n \times n$ sub matrix of that in equation (6.14) (with diagonal $\{\beta_1, \beta_2, ...\beta_n\}$). Generalising the approach of [205], the determinants can be efficiently calculated using a recurrence relation

$$D_n = \beta_n D_{n-1} - \alpha_{n-1}\gamma_n D_{n-2} + \alpha_{n-1}\alpha_{n-2}\delta_n D_{n-3}, \quad n \geq 3, \tag{6.15}$$

with initial conditions

$$D_0 = \beta_0 \tag{6.16a}$$

$$D_1 = \beta_1\beta_0 - \gamma_1\alpha_0 \tag{6.16b}$$

$$D_2 = \beta_2\left(\beta_1\beta_0 - \gamma_1\alpha_0\right) - \alpha_1\left(\gamma_2\beta_0 - \delta_2\alpha_0\right). \tag{6.16c}$$

The determinants $D_n \sim (n^2)!$, so it is convenient to instead work with P_n defined via

$$D_n = \left(n^2\right)! P_n. \tag{6.17}$$

They satisfy

$$P_n = \frac{\beta_n}{n^2}P_{n-1} - \frac{\alpha_{n-1}}{(n-1)^2}\frac{\gamma_n}{n^2}P_{n-2} + \frac{\alpha_{n-1}}{(n-1)^2}\frac{\alpha_{n-2}}{(n-2)^2}\frac{\delta_n}{n^2}P_{n-3}, \quad n \geq 3, \tag{6.18}$$

with initial conditions following from equations (6.16) and (6.17).

From the recursion relation and initial conditions, it can be seen that P_n is a complex polynomial of order $(n-1)$ in $\lambda^2 = (l+1/2)^2$ (fixing $\omega \in \mathbb{R}$). Thus we expect there to be $2(n-1)$ complex roots λ_j of P_n (assuming they are all simple zeros). In addition, if λ_j is a zero then so is $-\lambda_j$. Since the sequence P_n is infinite, this suggests (but does not prove) that there could be an infinite number of Regge-poles λ_j for a spherically symmetric spacetime. Our numerical results in section 6.4 support this conjecture for the models considered.

To summarise, the numerical method for finding Regge-poles (or QNFs), is to fix all physical parameters except l (or ω) which we allow to be complex valued. We then proceed to numerically search for roots of $P_n(l,\omega)$ given by equation (6.18), for some large value of n (typically $n = 10000$).

For each l (ω) we numerically integrate the radial mode solution satisfying regularity at the origin out to $r = b$ ($y = 0$), which determines α_0 and β_0. In turn this allows us to efficiently calculate $P_n(l,\omega)$. A root-finding algorithm is then employed to search for roots of $P_n(l,\omega)$ in the complex l (ω) plane. We use the Newton-Raphson algorithm and check our results by also using the `FindRoot` function in `Mathematica` [66]. We typically choose $b = R$ and confirm our results by repeating the algorithm with another value of $b > R$.

A sophisticated numerical method for finding Regge poles (zeroes of $P_n(l,\omega)$) has been developed by M. Ould El Hadj, based upon Cauchy's residue theorem [208]. His method allows a systematic *scanning* of the complex plane to check for poles, and was the primary technique used for the first exploration of bosonic field Regge poles on a stellar background [65]. The root finding procedure outlined here was used as a secondary method, and agrees with the scanning method by fifteen decimal places for the poles listed in [65]. The power of the scanning method is that it can rule out the presence of poles in a region of the complex plane that may be missed by a standard root finding algorithm.

6.2.3 Direct integration

An alternative 'brute force' approach to the continued fraction / Hill determinant method is 'direct integration'. This was employed in early studies of black hole QNMs. Here it is useful as a verification, since it is more computationally time-consuming than the previously described approach.

First, we integrate the solution satisfying regularity at the origin, $\psi_{ls}(r)$, from $r = \epsilon$ to $r = r_1 > \epsilon$, initialising with the regular Frobenius series. Next, we integrate the solution satisfying the outgoing boundary condition

$$\psi_{ls}^{\text{out}}(r) \sim A_l^+ e^{i\omega r_*}, \quad \text{as } r_* \to \infty, \tag{6.19}$$

(i.e. $A^- = 0$) inwards from $r = r_{\text{inf}}$ to r_1, initialised with the appropriate generalised series solution.

Then we calculate the Wronskian of the two solutions at r_1,

$$W\left[\psi_{ls}, \psi_{ls}^{\text{out}}\right]_{r=r_1} = \left[\psi_{ls}\frac{\partial \psi_{ls}^{\text{out}}}{\partial r} - \psi_{ls}^{\text{out}}\frac{\partial \psi_{ls}}{\partial r}\right]_{r=r_1}. \tag{6.20}$$

If the Wronskian is zero, then the solutions are linearly dependent. Normalising one of the solutions so they match at r_1, we have thus constructed a QNM or Regge-pole mode. Implementing a root finding algorithm for the Wronskian, we check that they agree with the roots of P_n as $n \to \infty$.

6.2.4 WKB approximation

A WKB expansion for the Regge-poles of massless fields on a Schwarzschild black hole background was found by Décanini and Folacci [200]. In addition, Dolan and Ottewill [209] used another high-frequency expansion method to find approximate Regge poles. The two methods are in agreement up to $O(\omega^{-2})$. To zeroth order in $1/\omega$ both groups obtain

$$\lambda_n^{\text{BH}} = 3\sqrt{3}M\omega + i\left(n - \frac{1}{2}\right), \quad n = 1, 2, 3... \tag{6.21}$$

where we follow the convention of enumerating the poles used in [200].

Zhang, Wu and Leung have applied a WKB analysis to determine approximate axial ω-modes for various compact stars [210], building on Berry's analysis of semiclassically weak reflections above potential barriers [211]. Here we adapt the method of Zhang *et al.* to obtain approximations for Regge-poles of massless waves on a stellar background. The results are valid in the high frequency limit, $\omega R_* \to \infty$, where

$$R_* \equiv \int_0^R dr\, \frac{1}{\sqrt{A(r)B(r)}} \tag{6.22}$$

is the tortoise coordinate at the stellar surface.

In practice, we must also have $\omega R_* \gg |l|$ which physically corresponds to wave modes with sufficient energy to penetrate deep into the interior of the body. For this reason they are labelled 'broad-resonances' (B-R). When $\omega R_* \gg |l|$, following [210], the WKB approximation for the solution satisfying equation (6.19) is

$$\psi_{ls}^{\text{out}}(r) = \begin{cases} e^{i\omega(r_*-R_*)} + \mathcal{R}e^{-i\omega(r_*-R_*)} & 1/\omega \leq r_* \lesssim R_*, \\ (1+\mathcal{R})\, e^{i\omega(r_*-R_*)} & R_* \leq r_* < \infty. \end{cases} \tag{6.23}$$

In equation (6.23) we have introduced a reflection coefficient $\mathcal{R}$. One can think of these types of solutions as waves that are weakly reflected by the discontinuity in the effective potential at the surface, shown schematically in figure 6.1. It is a standard calculation in quantum mechanics to show that to leading order in ω^{-1},

$$\mathcal{R} = \frac{1}{4\omega^2}\Delta V = \pm\frac{1}{4\omega^2}\frac{3M(R-2M)}{R^4}, \tag{6.24}$$

where ΔV is the discontinuity in the effective potential at the surface of the star, and the choice of sign is $(+)$ for the scalar case or $(-)$ for the axial GW case. In the more general case where n is the smallest integer such that dV^n/dx^n is discontinuous at the surface, the reflection coefficient can be calculated following the methods of Berry [211], which would allow a generalisation to the polytropic stellar models discussed in chapter 4.

Now, we construct an approximate solution valid deep inside the star. First, note that the metric functions (equations (3.11) and (3.12)) can be expanded in r as

$$A(r) = A_0\left[1 + O\left(\frac{Mr^2}{R^3}\right)\right], \tag{6.25}$$

$$B(r) = 1 + O\left(\frac{Mr^2}{R^3}\right), \tag{6.26}$$

where A_0 is a constant. Secondly, we use an approximate solution for the tor-

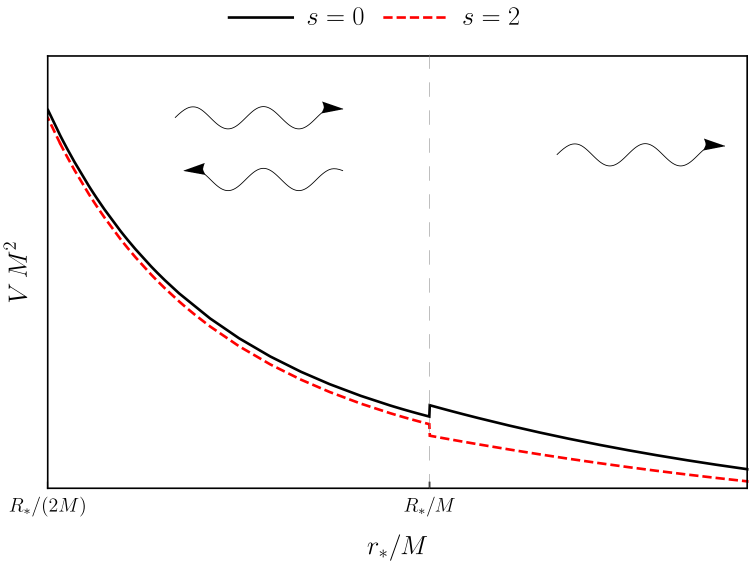

Figure 6.1: Effective radial potential for scalar perturbations (s=0) and axial GWs (s=2) on the background spacetime of a constant density star with $R/M = 6$. Also shown is a schematic of weak reflection within the star caused by the discontinuity at the surface.

toise coordinate near the origin (see equation (2.7)), which yields the equation

$$r = \sqrt{A_0}\, r_* \left[1 + O\left(\frac{M r_*^2}{R^3}\right)\right]. \tag{6.27}$$

Next, we consider the radial equation (equation (6.2)) in the high-frequency limit and with $\ell \gg 1$, such that all but the angular momentum terms in the effective potential may be dropped (see equation (6.3)). Substituting for r_* using equation (6.27) and neglecting the quadratic corrections gives a comparison equation

$$\left[\frac{d^2}{dr_*^2} + \omega^2 - \frac{\ell(\ell+1)}{r_*^2}\right]\psi_{\ell s} = 0. \tag{6.28}$$

We take the regular solution to equation (6.28), i.e.

$$\psi_{ls} = \omega r_* j_{\lambda-1/2}(\omega r_*), \quad 0 \le r_* \le R_*. \tag{6.29}$$

Now, using the high-frequency approximation for the spherical Bessel function

[117] in equation (6.29) gives

$$\psi_{ls} \approx \sin\left[\frac{(\lambda - 1/2)\pi}{2} - \omega r_*\right], \quad 0 \leq r_* \leq R_*, \tag{6.30}$$

for $\omega \to \infty$.

Using the Wronskian condition (6.20) with the approximate solutions of equations (6.23) and (6.30) yields

$$e^{i\pi(\lambda-1/2)-2i\omega R_*} = -\mathcal{R}. \tag{6.31}$$

Solving equation (6.31) for λ we obtain the approximate B-R Regge-pole positions (recall that $+$ and $-$ is for the scalar and axial GW cases respectively)

$$\lambda_n^{\text{B-R}} \approx \frac{2\omega R_*}{\pi} - \left(2n \pm \frac{1}{2}\right) + \frac{2i}{\pi}\log\left[\frac{2R^2\omega}{\sqrt{3M(R-2M)}}\right], \tag{6.32}$$

where $n \in \mathbb{N}$.

From equation (6.32) we deduce that these types of pole are approximately evenly spaced with $|\Delta\lambda_n| \approx 2$. The imaginary part, $\operatorname{Im}\lambda_n^{\text{B-R}}$, is approximately independent of n, and grows logarithmically with frequency ω. In addition, the B-R axial-GW poles lie roughly in-between the corresponding scalar poles.

We consider only the right-half complex λ-plane, i.e., $\operatorname{Re}\lambda > 0$. This places an upper bound on the number of poles in this family

$$N_{\text{B-R}} \leq \left\lfloor \frac{\omega R_*}{\pi} \mp \frac{1}{4} \right\rfloor, \tag{6.33}$$

where $\lfloor\cdot\rfloor$ denotes the floor function.

6.3 Scattering by an isotropic sphere

In this section we outline an analogy between our model and the scattering of scalar/electromagnetic waves by an isotropic sphere in flat spacetime.

If we consider an inhomogeneous, isotropic media with a radially dependent

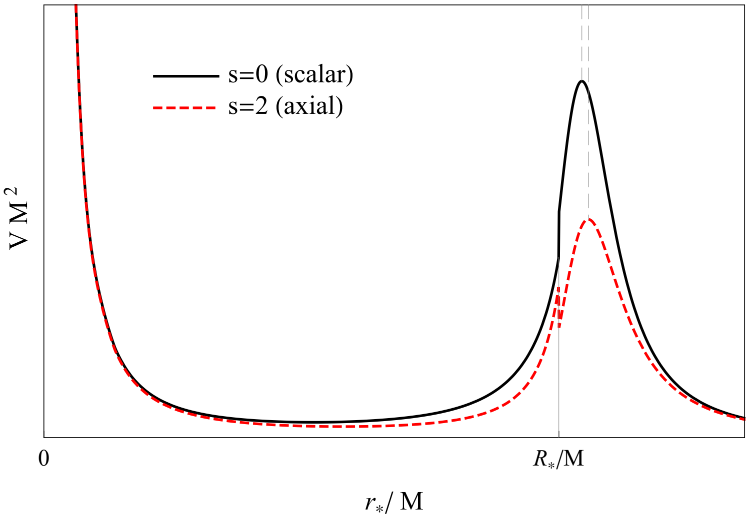

Figure 6.2: Effective radial potential for scalar perturbations (s=0) and axial GWs (s=2) on the background spacetime of a constant density star with $R/M = 2.26$.

refractive index $N(r)$, the radial dependence of a monochromatic electromagnetic wave (or scalar wave) is determined by the equation

$$\frac{d^2 F_l}{dr^2} + \left(\omega^2 N(r)^2 - \frac{l(l+1)}{r^2}\right) F_l = 0. \tag{6.34}$$

In equation (6.34) $F_l(r)$ is the radial function for a mode with angular momentum l and time dependence $e^{-i\omega t}$ (see chapter 5 of [68] for more details). If we substitute

$$N(r) = (1 - \tilde{V}(r)/\omega^2), \tag{6.35}$$

$$\tilde{V}(r) = U(r) - \frac{4\omega^2 M}{r}, \tag{6.36}$$

where $U(r)$ is given by equation (2.12), we recover equation (2.11) - the radial equation for a scalar field on a spherically symmetric spacetime.

Our model can then be compared with scattering by a transparent sphere on flat space with a refractive index given by equations (6.35) and (6.36). This imaginary sphere must have infinite radius, and has a jump discontinuity at $r = R$. In the far field, $N(r) \to 1$ as $r \to \infty$.

The discontinuity at $r = R$ is shared by the model of a homogeneous sphere with finite radius considered by Nussenzweig ($N(r) = N_0$ for $r \leq R$, $N(r) = 1$ for $r > R$) [68]. Scattering of electromagnetic plane waves by a homogeneous sphere is known as Mie scattering [212].

Looking at it from the other angle, the effective potential for a homogenous sphere (figure 9.1 of [68]) has the same classical turning point structure as the scalar potential for a star with $R/M = 6$ (figure 6.1). More similar is the scalar/axial potential for a body with $R/M < 3$ (figure 6.2), which may have a deep cavity region inside the light ring (discussed more in chapter 5).

Two distinct analogies are being made here, first, an analogy between the discontinuity at the star's surface and the surface of a transparent sphere. Secondly, an analogy between the trapped region inside a sufficiently compact star's light ring, and the trapped region inside a transparent sphere. Neither analogy is perfect, yet they are useful in interpreting the results of section 6.4.

6.4 Results: Regge-pole spectra

Using the Hill determinant method described in section 6.2.2, we have calculated the Regge pole spectra for scalar field perturbations on the spacetime of a constant density star (see chapter 3). Recall that the model is parametrised by the dimensionless parameters $M\omega$ and R/M. A neutron star has a tenuity $R/M \approx 6$, and objects with $R/M < 3$ are classified as ultracompact as they possess a unstable photon orbit at $r = 3M$.

In section 6.4.1 we consider the spectra for compact bodies with $R/M = 6$. In section 6.4.2 we look at a particular UCO model with $R/M = 2.26$, just above the Buchdahl limit $R/M = 9/4$ (see section 3.1.1). The axial GW QNMs of this model have been considered before (see e.g. [100]).

We find that the Regge-pole spectra are qualitatively similar to the spectra of electromagnetic waves scattered by transparent spheres with constant refractive index N_0 (see figures 7.6 and 9.2 of [68]). This result is not entirely surprising, since some analogies can be drawn between the transparent sphere model and ours (see section 6.3).

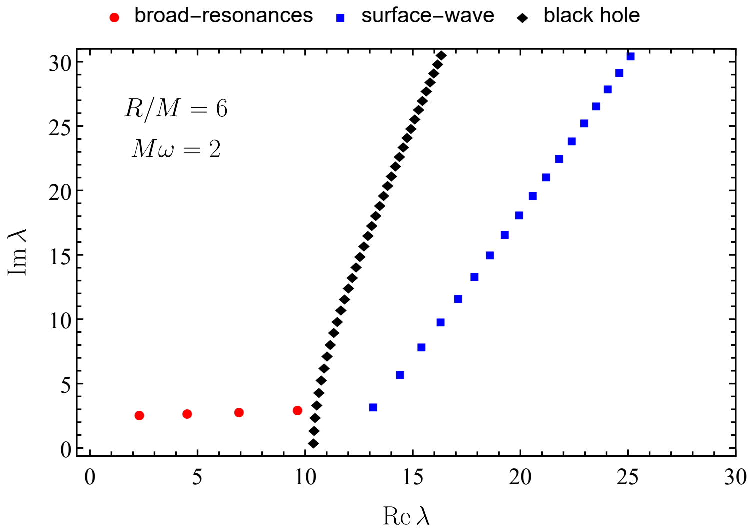

Figure 6.3: The scalar field Regge-pole spectrum for a constant density star with tenuity $R/M = 6$ and $M\omega = 2$. The spectrum is composed of two branches, the broad-resonance (red circles) and surface-waves (blue squares). Also shown for comparison are scalar Regge-poles for a Schwarzschild black hole with $M\omega = 2$ (black diamonds).

The problem of scattering by homogeneous spheres in flat space is exactly solvable and one can obtain the scattering matrix elements in closed form. Nussenzweig has studied these cases in detail, and we borrow the terminology from his monograph [68].

6.4.1 Compact bodies

For a simple stellar model with a tenuity comparable to a neutron star, we find that the Regge pole spectra has two distinct branches (see figures 6.3 and 6.4).

The first branch is roughly parallel to the real λ-axis. It corresponds to the WKB solutions derived in section 6.2.4 (see figure 6.5). Since these modes are associated with the WKB approximate solutions that penetrate deep into the interior region of the star, which feel almost the entire spacetime (in the radial dimension), we call them broad-resonances. Further justification for this label is provided by comparison to the Regge-pole spectra for scattering of

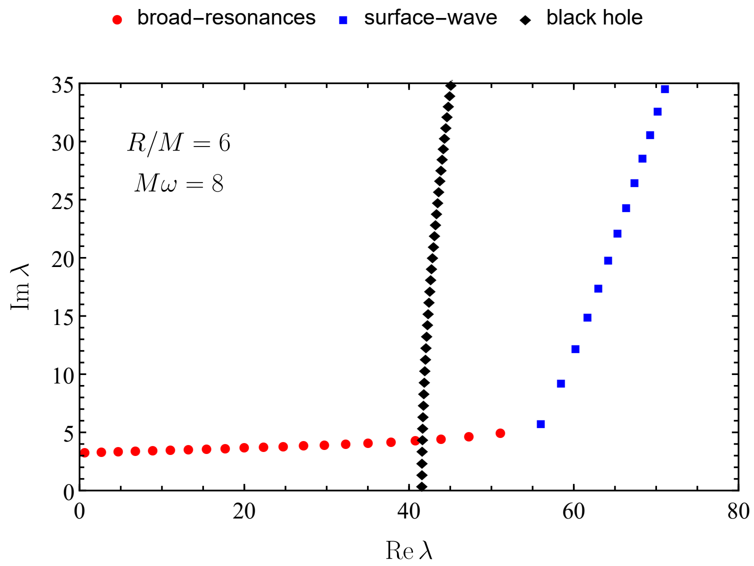

Figure 6.4: The scalar field Regge-pole spectrum for a constant density star with tenuity $R/M = 6$ and $M\omega = 8$. The spectrum is composed of two branches, the broad-resonance (red circles) and surface-waves (blue squares). Also shown for comparison are scalar Regge-poles for a Schwarzschild black hole with $M\omega = 8$ (black diamonds).

electromagnetic waves by hard and transparent spheres [68]. They are displayed as red circles in figures 6.3 and 6.4 and we label them $\lambda_n^{\text{B-R}}$. The number of poles in this numerically determined branch matches the WKB prediction of equation (6.33) for all the examples we have checked.

A second branch, inclined with respect to the real λ-axis, is clearly distinguished and displayed as blue squares in figures 6.3 and 6.4. This branch is somewhat reminiscent of the Regge-pole spectra for Schwarzschild black holes [47, 71]. It is perhaps more similar to the surface-wave poles found in scattering by a hard sphere, which we show for comparison in figure 6.5 (see also [68]). There appears to be an infinite number of surface-wave poles, extending to complex infinity. What we call the first surface-wave pole has the smallest imaginary part and lies near the right end of the broad-resonance branch.

For high frequencies, we find numerical evidence that the first surface-wave

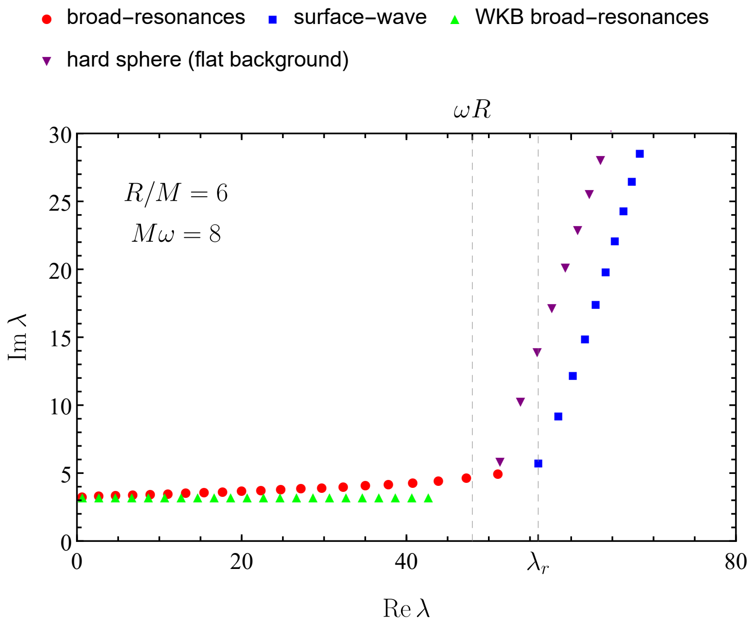

Figure 6.5: The scalar field Regge-pole spectrum for a constant density star with tenuity $R/M = 6$ and $M\omega = 8$. The spectrum is composed of two branches, the broad-resonance (red circles) and surface-waves (blue squares). The two branches meet at $\mathrm{Re}\,\lambda = \lambda_r = b_r\omega$ where $b_r = 6.99895M$ is the impact parameter for a maximally deflected null geodesic. Also shown are the WKB approximations for the broad-resonance branch (green triangles), and hard sphere flat space Regge-poles (purple inverted triangles).

Regge pole has

$$\mathrm{Re}\ \lambda_1^{\text{S-W}} = \lambda_r \equiv b_r\omega, \tag{6.37}$$

where b_r is the impact parameter for a maximally deflected geodesic ray (i.e. a rainbow ray). An estimate for b_r can be given analytically by the grazing ray impact parameter, $b_{gr} = \sqrt{R^3/(R-2M)}$ (see equation (3.26)). This suggests that these resonances are associated with the surface of the star (in contrast to the BH case where the Regge poles surface waves are associated with the photon sphere at $r = 3M$).

The angle of the surface wave branch in the complex plane is found to be $\hat{\theta} \approx 0.37\pi$ for $M\omega = 2$ and $\hat{\theta} \approx 0.35\pi$ for $M\omega = 8$. This is close to the value for the surface-wave Regge pole branch present in scattering by a hard sphere,

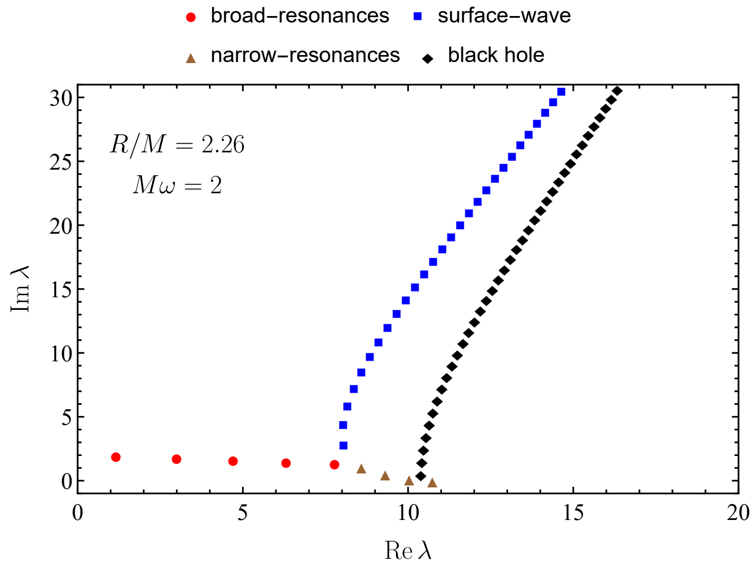

Figure 6.6: The scalar field Regge-pole spectrum for a constant density star with tenuity $R/M = 2.26$ and $M\omega = 2$. The spectrum is composed of three branches, the broad-resonance (red circles), surface-waves (blue squares), and narrow-resonances (brown triangles). Also shown for comparison are scalar Regge-poles for a Schwarzschild black hole with $M\omega = 2$ (black diamonds).

$\hat{\theta} = \pi/3$ [68].

The data for the Regge-poles displayed here is available in section 6.8. Further examples and data can also be found in [65].

6.4.2 Ultra compact objects

A very compact star, with $R/M < 3$, possesses three branches of Regge poles. The two branches that were extant already for $R/M > 3$, broad-resonances and surface-waves, and a third branch which emerges from the point where the first two meet (see figure 6.6).

Again borrowing the terminology from [68], we call the poles in the third branch 'narrow-resonances'. They lie near the real axis and are associated with modes trapped inside the photonsphere of a UCO. The least damped narrow-resonance lies near the first surface wave pole of a Schwarzschild black hole.

In figure 6.6 we plot the spectra for $R/M = 2.26$ and $M\omega = 2$. There are four narrow resonances shown as brown triangles. The number of narrow-resonance poles increases as the star's tenuity approaches the Buchdahl limit $R/M \to 9/4$. In addition, the number of narrow-resonances increases as $M\omega$ increases [65].

Note that for $R/M = 6$, the surface-wave branch satisfies $\mathrm{Re}\lambda_n^{\text{S-W}} > \mathrm{Re}\,\lambda_n^{\text{BH}}$. In other words the branch is to the right of the black hole Regge poles. For $R/M = 2.26$, $\mathrm{Re}\lambda_n^{\text{S-W}} < \mathrm{Re}\,\lambda_n^{\text{BH}}$. The stellar surface-wave branch crosses the black hole branch when $R/M \approx 3$.

The data for the Regge poles displayed here is available in section 6.8. Further examples and data can also be found in [65].

6.5 Complex angular momentum in scattering theory

Here we will recall the method of Folacci and Ould El Hadj who successfully applied complex angular momentum to the problem of scattering by black holes [57]. The majority of their method is immediately applicable to scattering by any spherically symmetric body with a Schwarzschild exterior. However, the properties of the scattering matrix element S_l depend on the type of body considered, so care must be taken when applying the approach outlined in reference [57] to our model. For this reason, we reproduce their argument here and highlight any differences.

The first step is to rewrite the scattering amplitude, equation (2.39), as a complex contour integral. This is accomplished with the use of Cauchy's residue theorem which states: Given a simply connected region D of the complex λ-plane, enclosed by the curve C, let $G(\lambda)$ be holomorphic on D except at a finite list of points λ_n. Then,

$$\oint_C G(\lambda)\, d\lambda = 2\pi i \sum_n \mathrm{Res}\left[G(\lambda), \lambda_n\right], \tag{6.38}$$

where the contour is integrated over in an anticlockwise direction. Each residue can be calculated by applying the theorem,

$$\operatorname{Res}\left[G(\lambda), \lambda_n\right] = \frac{1}{2\pi i} \oint_\gamma G(\lambda)\, d\lambda, \tag{6.39}$$

where γ is a closed contour enclosing just one λ_n. Standard techniques exist for performing these contour integrals [213].

If a complex function $F(\lambda)$ is analytic inside the contour C (shown in figure 6.7) then by Cauchy's theorem, it can be shown that

$$\sum_{l=0}^{\infty} (-1)^l F(l+1/2) = \frac{i}{2} \int_C \frac{F(\lambda)}{\cos(\pi\lambda)}\, d\lambda. \tag{6.40}$$

Equation (6.40) is known as the Sommerfeld-Watson transformation [34]. The contour C is explicitly

$$C = \lim_{\epsilon \to 0^+} \Big\{ \,]\infty + i\epsilon, i\epsilon] \cup [i\epsilon, -i\epsilon] \cup [-i\epsilon, \infty - i\epsilon[\, \Big\}, \tag{6.41}$$

and it encircles the positive real axis of the λ-plane in an anticlockwise direction.

A key advantage of CAM is the freedom to deform the contour C. The deformation can be judiciously chosen to *"concentrate the contributions to the integral into the neighbourhood of a small number of points in the complex λ-plane"* [68]. These are known as *critical points*, the main types being *Regge-poles* and *saddle points*. Nussenzweig's monograph *"Diffraction Effects in Semiclassical Scattering"* contains a trove of results obtained when applying CAM to scattering by a homogeneous sphere.

Noting that the Legendre polynomials satisfy $P_l(\cos\theta) = (-1)^l P_l(-\cos\theta)$, and applying the Sommerfeld-Watson transformation to the partial wave sum, equation (2.39), results in

$$f(\theta) = \frac{1}{2\omega} \int_C \frac{\lambda \left[S_{\lambda-1/2}(\omega) - 1\right] P_{\lambda-1/2}(-\cos\theta)}{\cos(\pi\lambda)}\, d\lambda, \tag{6.42}$$

where $\lambda \equiv l + 1/2$. Poles of the integrand in equation (6.42) are located where $l \in \mathbb{N}$ (which is how the transformation works) and also away from the real λ

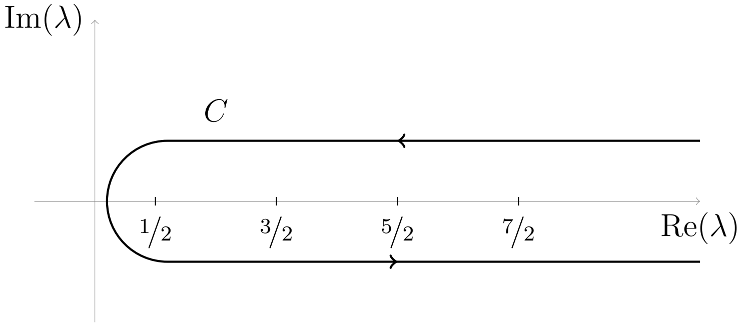

Figure 6.7: The Sommerfeld-Watson transformation converts a sum over poles located at $\lambda = l + 1/2$ where $l \in \mathbb{N}$, to a contour integral C in the complex λ plane.

axis at the poles of $S_{\lambda-1/2}(\omega)$, i.e., the Regge poles $\lambda_n(\omega)$.

The analytic extension of the Legendre polynomials is the Legendre function of the first kind, denoted by $P_{\lambda-1/2}(z)$. It may be defined in terms of a hypergeometric function [117]

$$P_{\lambda-1/2}(-\cos\theta) = F(1/2-\lambda, 1/2+\lambda; 1, (1+\cos\theta)/2). \tag{6.43}$$

We also analytically extend the mode solutions $\psi_{ls}(r)$ to complex angular momentum values. We define $\psi_{\lambda-1/2,s}(r)$ as the solution to equation (6.2) with $l \to \lambda - 1/2$ where $\lambda \in \mathbb{C}$, subject to the boundary condition

$$\phi_{\omega,\lambda-1/2}(r) \sim r^{\lambda+1/2} \qquad \text{as } r \to 0. \tag{6.44}$$

The modes have the usual asymptotic behaviour as $r \to \infty$, which defines the analytic extensions of the coefficients $A_l^{\pm}$ ($A_{\lambda-1/2}^{\pm}$), and S_l, denoted by

$$S_{\lambda-1/2}(\omega) \equiv e^{i\pi(\lambda+1/2)} \frac{A^{+}_{\lambda-1/2}(\omega)}{A^{-}_{\lambda-1/2}(\omega)}. \tag{6.45}$$

For black hole scattering, it can be shown that the S matrix satisfies a symmetry property [46]

$$e^{i\pi\lambda} S^{\mathrm{BH}}_{-\lambda-1/2}(\omega) = e^{-i\pi\lambda} S^{\mathrm{BH}}_{\lambda-1/2}(\omega). \tag{6.46}$$

For our model and analytic extension (equations (6.44) and (6.45)), this symmetry is not satisfied (since the boundary conditions depend on λ, unlike the black hole boundary conditions).

At this point it is helpful to note the asymptotic properties of the quantities in the integrand on the right-hand-side of equation (6.42). For $\mathrm{Re}\{\lambda\} > 0$, we have:

$$P_{\lambda-1/2}(-\cos\theta) \sim \frac{1}{(-2\pi\lambda\sin\theta)^{1/2}} \left(e^{i(\lambda\theta-\pi/4)} + e^{-i(\lambda\theta-\pi/4)}\right), \text{ as } |\lambda\sin\theta| \to \infty. \tag{6.47}$$

Equation (6.47) may be derived from equation (8.10.7) in reference [117] and Stirling's approximation for the Gamma function

$$\Gamma(z) = \sqrt{\frac{2\pi}{z}} \left(\frac{z}{e}\right)^z \left[1 + O\left(\frac{1}{z}\right)\right]. \tag{6.48}$$

In addition,

$$|S_{\lambda-1/2}(\omega)| \sim e^{i\pi(\lambda+1/2)}, \text{as } |\lambda| \to \infty. \tag{6.49}$$

The next step is to apply Cauchy's residue theorem to the right-hand-side of equation (6.42), which allows us to 'deform' the contour C. This is shown schematically in figure 6.8. The contours $\Gamma_{\pm,\infty}$ are arcs joining the imaginary axis to $\Gamma_{\pm}$. When the arc radii is allowed to tend to infinity, $C = \Gamma_+ \cup \Gamma_-$. Thus,

$$f(\theta) = \frac{1}{2\omega} \int_{\Gamma_+} \frac{\lambda \left[S_{\lambda-1/2}(\omega) - 1\right] P_{\lambda-1/2}(-\cos\theta)}{\cos(\pi\lambda)} d\lambda \tag{6.50}$$

$$+ \frac{1}{2\omega} \int_{\Gamma_-} \frac{\lambda \left[S_{\lambda-1/2}(\omega) - 1\right] P_{\lambda-1/2}(-\cos\theta)}{\cos(\pi\lambda)} d\lambda. \tag{6.51}$$

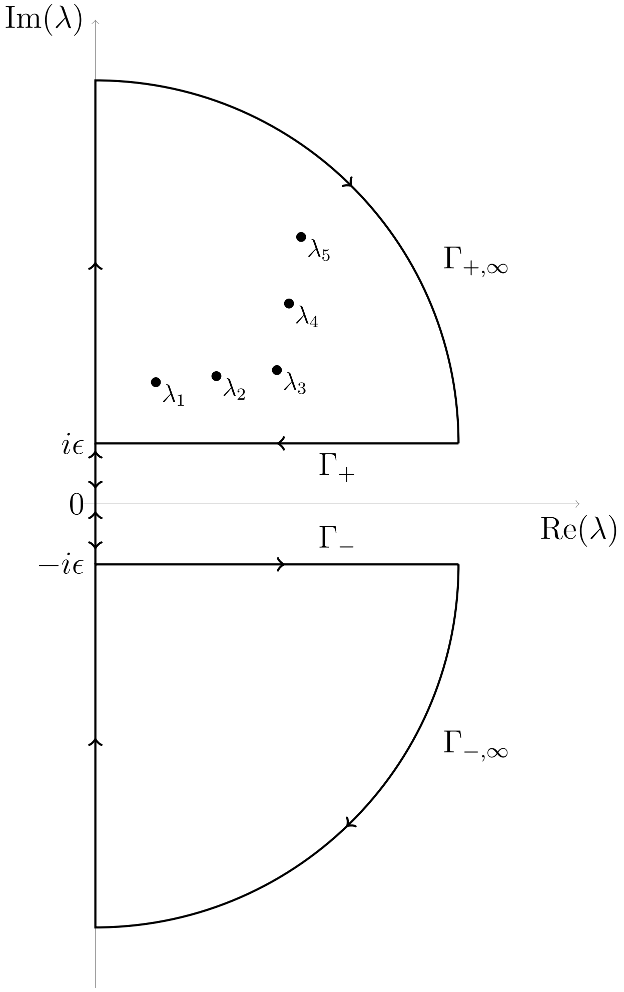

Figure 6.8: The contour integral of figure 6.7, $C = \Gamma_+ \cup \Gamma_-$, and its deformation. We also show a collection of Regge poles $\lambda_n(\omega)$, whoes exact distribution depends on the compact body model and scalar mode angular frequency ω. For $\omega > 0$, Regge poles are located in the first quadrant only.

First we consider the integral along Γ_+. By Cauchy's residue theorem

$$\begin{aligned}\int_{\Gamma_+} \frac{\lambda}{\cos(\pi\lambda)} \left[S_{\lambda-1/2}(\omega) - 1\right] P_{\lambda-1/2}(-\cos\theta)\, d\lambda \\ = -\int_0^{i\infty} \frac{\lambda}{\cos(\pi\lambda)} \left[S_{\lambda-1/2} - 1\right] P_{\lambda-1/2}(-\cos\theta)\, d\lambda \\ - 2i\pi \sum_{n=1}^{\infty} \frac{\lambda_n(\omega) r_n(\omega)}{\cos\left(\pi\lambda_n(\omega)\right)} P_{\lambda_n-1/2}(-\cos\theta).\end{aligned} \quad (6.52)$$

The integral over $\Gamma_{+,\infty}$ may be neglected for $\theta \neq 0, \pi$, since

$$\lambda \cdot \left(\frac{\lambda}{\cos(\pi\lambda)} \left[S_{\lambda-1/2}(\omega) - 1\right] P_{\lambda-1/2}(-\cos\theta)\right) \to 0$$
$$\text{as } |\lambda \sin\theta| \to \infty,\ \operatorname{Im}\lambda > 0. \quad (6.53)$$

which follows from equations (6.47) and (6.49). The second term on the right-hand-side of equation (6.52) is a sum over poles $\lambda_n(\omega)$ of $S_{\lambda-1/2}(\omega)$ with residues

$$r_n(\omega) \equiv \oint S_{\lambda-1/2}(\omega)\, d\lambda, \quad (6.54)$$

where the integral is done over a small closed contour around λ_n. The poles of $S_{\lambda-1/2}(\omega)$ are of first order and thus the residue can be calculated using

$$r_n(\omega) = \lim_{\lambda\to\lambda_n} \left[(\lambda - \lambda_n) S_{\lambda-1/2}(\omega)\right] \quad (6.55)$$
$$= e^{i\pi(\lambda_n(\omega)+1/2)} \left[\frac{A^+_{\lambda-1/2}(\omega)}{\frac{d}{d\lambda} A^-_{\lambda-1/2}(\omega)}\right]_{\lambda=\lambda_n(\omega)}. \quad (6.56)$$

Next we consider the contour Γ_- which is closed by $\Gamma_{-,\infty} \cup]-i\infty, 0]$ (see figure 6.8). The integrand of equation (6.42) diverges exponentially as $|\lambda \sin\theta| \to \infty$ for $\operatorname{Im}\lambda < 0$, so we must take a little more care here. First the integral is split into two parts

$$\begin{aligned}\int_{\Gamma_-} \frac{\lambda}{\cos(\pi\lambda)} \left[S_{\lambda-1/2}(\omega) - 1\right] P_{\lambda-1/2}(-\cos\theta)\, d\lambda \\ = \int_{\Gamma_-} \frac{\lambda}{\cos(\pi\lambda)} S_{\lambda-1/2}(\omega) P_{\lambda-1/2}(-\cos\theta)\, d\lambda \\ - \int_{\Gamma_-} \frac{\lambda}{\cos(\pi\lambda)} P_{\lambda-1/2}(-\cos\theta)\, d\lambda. \quad (6.57)\end{aligned}$$

The integrand of the second term is analytic in the fourth quadrant (excluding the real axis) and vanishes faster than $1/\lambda$ as $\lambda \to \infty$ for $\operatorname{Im}\lambda < 0$ (see equation (6.47)). Hence by Cauchy's integral theorem,

$$\int_{\Gamma_-} \frac{\lambda}{\cos(\pi\lambda)} P_{\lambda-1/2}(-\cos\theta)\, d\lambda \;=\; \int_{-i\infty}^{0} \frac{\lambda}{\cos(\pi\lambda)} P_{\lambda-1/2}(-\cos\theta)\, d\lambda. \quad (6.58)$$

The first term on the right-hand-side of equation (6.57) is the origin of the aforementioned divergence, which is dealt with by utilising the identity [117]

$$P_{\lambda-1/2}(-\cos\theta) \;=\; e^{-i\pi(\lambda-1/2)} P_{\lambda-1/2}(\cos\theta) - \frac{2\cos(\pi\lambda)}{\pi} Q_{\lambda-1/2}(\cos\theta + i0), \quad (6.59)$$

where $Q_{\lambda-1/2}(\cdot)$ is the Legendre function of the second kind. We obtain

$$\begin{aligned}\int_{\Gamma_-} \frac{\lambda}{\cos(\pi\lambda)} S_{\lambda-1/2}(\omega) P_{\lambda-1/2}(-\cos\theta)\, d\lambda \\ = \int_{\Gamma_-} \frac{\lambda e^{-i\pi(\lambda-1/2)}}{\cos(\pi\lambda)} S_{\lambda-1/2}(\omega) P_{\lambda-1/2}(\cos\theta)\, d\lambda \\ - \frac{2}{\pi} \int_{\Gamma_-} S_{\lambda-1/2}(\omega) Q_{\lambda-1/2}(\cos\theta + i0)\, d\lambda. \quad (6.60)\end{aligned}$$

Since there are no poles along the real axis for the second term on the right hand side, we can take the limit $\epsilon \to 0$ and express it as an integral along the real λ axis. It can be shown that $S_{\lambda-1/2}(\omega)$ is in fact analytic in the fourth quadrant (there are no poles there), a proof can be found in the appendix of reference [65]. In addition the integrand of the first term in equation (6.60) tends to zero faster than $1/\lambda$ as $|\lambda \sin\theta| \to \infty$ for $\operatorname{Im}\lambda < 0$. Applying Cauchy's integral theorem again, we arrive at

$$\begin{aligned}\int_{\Gamma_-} &\frac{\lambda}{\cos(\pi\lambda)} S_{\lambda-1/2}(\omega) P_{\lambda-1/2}(-\cos\theta)\, d\lambda \\ &= -\int_{-i\infty}^{0} \frac{\lambda e^{-i\pi(\lambda-1/2)}}{\cos(\pi\lambda)} S_{\lambda-1/2}(\omega) P_{\lambda-1/2}(\cos\theta)\, d\lambda \\ &\qquad - \frac{2}{\pi}\int_0^{\infty} S_{\lambda-1/2}(\omega) Q_{\lambda-1/2}(\cos\theta + i0)\, d\lambda. \qquad (6.61)\end{aligned}$$

Now, we collect terms from equations (6.52), (6.58) and (6.61) to obtain

$$\begin{aligned}f(\theta) = f^{\mathrm{RP}}(\theta) + \frac{1}{2\omega}\Bigg[&\frac{2}{\pi}\int_0^{\infty} S_{\lambda-1/2}(\omega) Q_{\lambda-1/2}(\cos\theta + i0)\, d\lambda \\ &- \int_0^{i\infty} \frac{\lambda}{\cos(\pi\lambda)} \left[S_{\lambda-1/2} - 1\right] P_{\lambda-1/2}(-\cos\theta)\, d\lambda \\ &- \int_{-i\infty}^{0} \frac{\lambda e^{-i\pi(\lambda-1/2)}}{\cos(\pi\lambda)} S_{\lambda-1/2}(\omega) P_{\lambda-1/2}(\cos\theta)\, d\lambda \\ &+ \int_{-i\infty}^{0} \frac{\lambda}{\cos(\pi\lambda)} P_{\lambda-1/2}(-\cos\theta)\, d\lambda\Bigg], \qquad (6.62)\end{aligned}$$

where

$$f^{\mathrm{RP}}(\theta) \equiv -\frac{i\pi}{\omega}\sum_{n=1}^{\infty} \frac{\lambda_n(\omega) r_n(\omega)}{\cos\left(\pi\lambda_n(\omega)\right)} P_{\lambda_n-1/2}(-\cos\theta) \qquad (6.63)$$

is the contribution from the Regge poles. By a change of variable $\lambda' = -\lambda$, and using the relation $P_{\lambda-1/2}(z) = P_{-\lambda-1/2}(z)$ [117], we can rewrite the last term of equation (6.62) as

$$\int_{-i\infty}^{0} \frac{\lambda}{\cos(\pi\lambda)} P_{\lambda-1/2}(-\cos\theta)\, d\lambda = -\int_0^{i\infty} \frac{\lambda'}{\cos(\pi\lambda')} P_{\lambda'-1/2}(-\cos\theta)\, d\lambda'. \qquad (6.64)$$

Making the same change of variable for the fourth term of equation (6.62) and simplifying we obtain

$$f(\theta) = f^{\mathrm{RP}}(\theta) + f^{\mathrm{B}}(\theta), \tag{6.65}$$

where

$$f^{\mathrm{B}}(\theta) \equiv f^{\mathrm{B,Re}}(\theta) + f^{\mathrm{B,Im}}(\theta) \tag{6.66}$$

is a background integral contribution composed of an integral along the real $\lambda-$axis

$$f^{\mathrm{B,Re}}(\theta) \equiv \frac{1}{\pi\omega}\int_0^\infty S_{\lambda-1/2}(\omega) Q_{\lambda-1/2}(\cos\theta + i0)\, d\lambda, \tag{6.67}$$

and an integral along the imaginary $\lambda-$axis

$$\begin{aligned} f^{\mathrm{B,Im}}(\theta) \equiv \frac{1}{2\omega}\int_{i\infty}^0 \frac{\lambda}{\cos(\pi\lambda)} &[S_{\lambda-1/2}(\omega) P_{\lambda-1/2}(-\cos\theta) \\ &- S_{-\lambda-1/2}(\omega) e^{i\pi(\lambda+1/2)} P_{\lambda-1/2}(\cos\theta)]\, d\lambda. \end{aligned} \tag{6.68}$$

Equations (6.65) and (6.66) with equations (6.63) and (6.66) to (6.68) present an exact representation of the scalar field scattering amplitude equivalent to the partial wave expansion (equation (2.39)).

6.5.1 Numerical method

To calculate the Regge-pole scattering amplitude, equation (6.63), we need to first locate the Regge-poles and then calculate their residues. The first task is accomplished using the methods described in section 6.2. The residues are then calculated from equation (6.56), where the mode coefficients $A^{\pm}_{\lambda-1/2}(\omega)$ are found using numerical integration (see section 3.5 for details).

The imaginary background integral $f^{\mathrm{B,Im}}(\theta)$ defined in equation (6.68) is found to be convergent. The scattering-matrix elements $(S_{\lambda-1/2}(\omega), S_{-\lambda-1/2}(\omega))$ are calculated on a grid $\lambda_k = (k/100)i$, $k = 1, 2, ...k_{\max}$ using the method detailed in section 3.5. We then interpolate the integrand over the interval $\lambda \in [0, (k_{\max}/100)i]$ using `Mathematica's` in-built `Interpolate` function (a polynomial interpolation of order 4). The `NIntegrate` function is then used to calculate $f^{\mathrm{B,Im}}(\theta)$. We take $k_{\max}$ sufficiently large so that the relative error is approximately 10^{-8}.

The real background integral $f^{\mathrm{B,Re}}(\theta)$ defined in equation (6.67) suffers from a lack of convergence analogous to the partial wave sum, equation (2.39), and with the same root cause (the long range nature of the gravitational field which means $S_l \nrightarrow 1$ as $l \to \infty$). To overcome this we use the method detailed in the appendix of reference [57]. We can then numerically integrate $f^{\mathrm{B,Re}}(\theta)$ on a grid $\lambda_k = (k/100)$ and again take $k_{\max}$ sufficiently large so that the relative error is approximately 10^{-8}.

6.6 Results: Scattering cross sections

Using the CAM techniques of reference [57], adapted for scalar field scattering by a stellar model (section 6.5) we have calculated the scattering cross sections for a plane wave with $M\omega = 2$ incident on a constant density star. Here we compare exact partial wave results (see chapter 3) with approximate cross sections, obtained by considering the Regge-pole contribution to the cross section alone (neglecting the background integrals),

$$\frac{d\sigma}{d\Omega}_{\mathrm{RP}} \equiv |f^{\mathrm{RP}}(\theta)|^2. \tag{6.69}$$

To calculate $f^{\mathrm{RP}}(\theta)$ in practice we must truncate the summation (equation (6.63)) at some finite $n = N$, that is

$$f^{\mathrm{RP}}(\theta) \approx -\frac{i\pi}{\omega} \sum_{n=1}^{N} \frac{\lambda_n(\omega) r_n(\omega)}{\cos\left(\pi \lambda_n(\omega)\right)} P_{\lambda_n - 1/2}(-\cos\theta). \tag{6.70}$$

We display the results obtained this way in figure 6.9 for a model with tenuity $R/M = 6$ and figure 6.12 for $R/M = 2.26$. Exact partial wave results are plotted in black, and the RP approximations in dashed blue.

For $R/M = 6$ we also compare the exact cross sections with those obtained by including the background integral and a large number of Regge-poles,

$$\frac{d\sigma}{d\Omega}_{\mathrm{CAM}} = |f^{\mathrm{RP}}(\theta) + f^{\mathrm{B}}(\theta)|^2, \tag{6.71}$$

where $f^{\mathrm{B}}(\theta)$ is obtained from equation (6.68). Results calculated using equation (6.71) are shown in dashed green.

In figure 6.10 we display relative differences between a partial wave scattering cross section $d\sigma/d\Omega_{\mathrm{PW}}$ (section 2.2.5) and various Regge-pole approximations given by equations (6.69) and (6.70),

$$\Delta\left[\frac{d\sigma}{d\Omega}\right] = \left|\frac{\frac{d\sigma}{d\Omega}_{\mathrm{PW}} - \frac{d\sigma}{d\Omega}_{\mathrm{RP}}}{\frac{d\sigma}{d\Omega}_{\mathrm{PW}}}\right|. \tag{6.72}$$

In figure 6.10f we show the relative difference between the exact (partial wave) cross section and the full CAM cross section of equation (6.71).

6.6.1 Compact bodies

In figures 6.9b and 6.10b we see that a Regge-pole approximation for the neutron star model $R/M = 6$ captures the shadow zone behaviour reasonably well when all the broad resonances and a couple of surface-waves are included in equation (6.69). Recall from chapter 3 that the shadow zone is $\theta > \theta_r$ where $\theta_r \approx 59.6^\circ$ is the rainbow angle (or maximum geodesic deflection angle).

More Regge-poles are needed ($n \geq 10$) to also capture the rainbow maximum at $\theta_p \approx 40^\circ$ for $M\omega = 2$ (see figures 6.9c, 6.9d, 6.10c and 6.10d). To accurately reproduce the cross section at progressively smaller angles requires yet more Regge-poles, as can be seen in figures 6.9e and 6.10e.

Each branch of Regge-poles makes a significant contribution to the scattering cross section, as shown in figure 6.11. The amplitude of both branches has a phase difference, and the summation yields the rainbow interference pattern expected from the partial wave calculations. Since the rainbow pattern is due to interference of rays passing through the exterior and interior regions of the

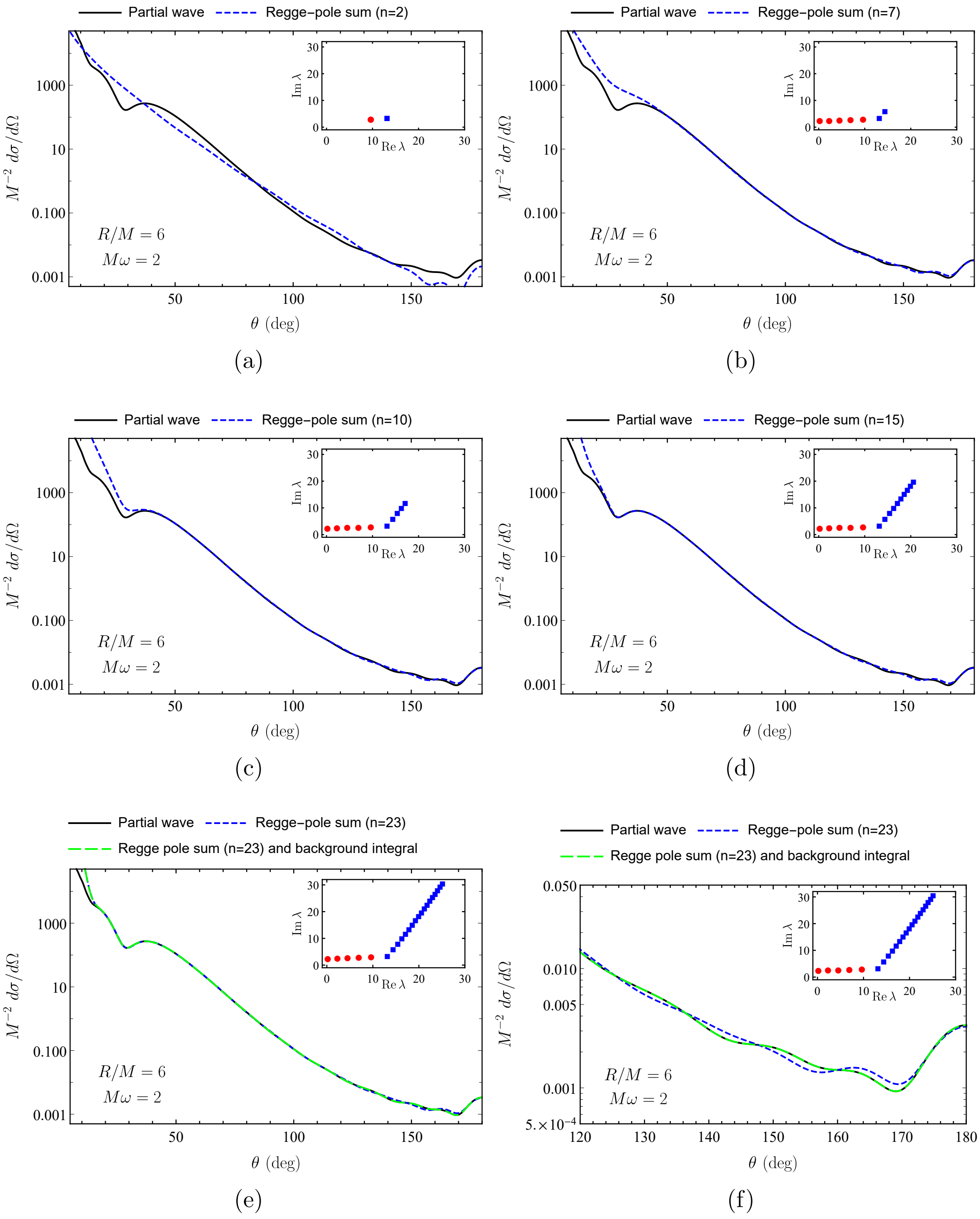

(a) (b) (c) (d) (e) (f)

Figure 6.9: The scalar field scattering cross section for a constant density star with $R/M = 6$ and $M\omega = 2$. Partial wave (exact) calculations are shown in black, Regge-pole approximations in dashed blue, and Regge-pole with background integral approximations in dashed green. The approximations are made by summing over the Regge-poles shown in the inset graph.

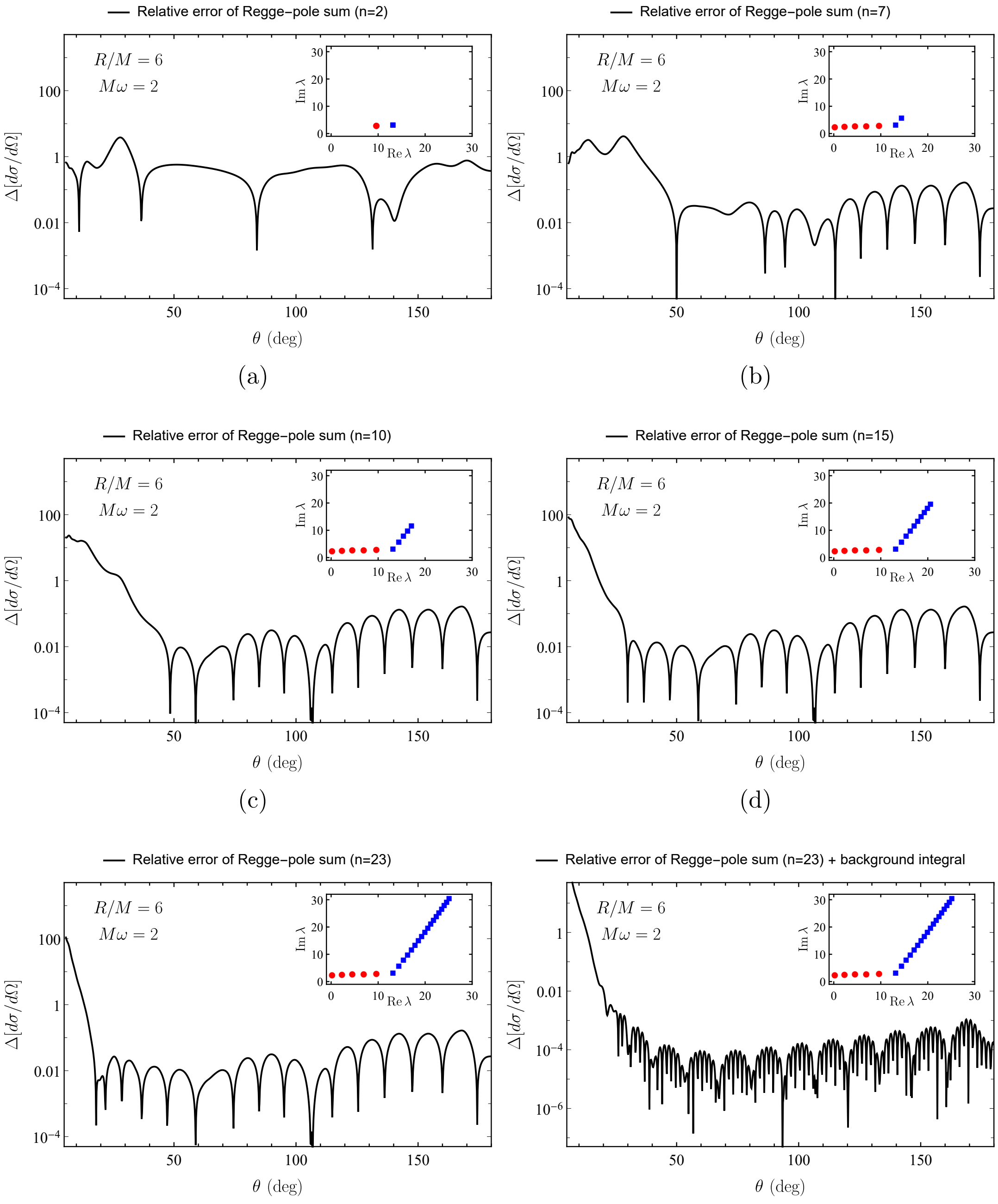

(a) (b)

(c) (d)

(e) (f)

Figure 6.10: The relative difference between scattering cross sections calculated from a Regge-pole sum and from a partial wave sum (equation (6.72)). The scattering cross sections are computed for a constant density star with $R/M = 6$ and $M\omega = 2$. Note that in figure 6.10f we include the background integral contribution.

central body (as discussed in chapter 3) it is not surprising that both branches are needed to reproduce the rainbow peaks and troughs.

The essentially negligible scattering cross section in the backwards direction displays a glory maximum (which smoothly becomes more prominent as $R/M \to 3$ from above, see chapter 3). To reproduce this feature accurately using the CAM calculation we find that the background integral must be included, as shown in figures 6.9f and 6.10f. It is also clear from figures 6.10e and 6.10f that including the background integral in the CAM calculation improves the accuracy considerably over a large range of angles. This should be expected since the partial wave and full CAM expressions for the scattering amplitude are equivalent.

At higher circular frequencies, there are more broad-resonances to take into account (see section 6.4.1). We find that more Regge-poles are needed to accurately capture the cross sections as $M\omega$ increases (see [65]).

6.6.2 Ultra compact objects

In chapter 3 we discussed scattering by UCOs. The cross sections display a complicated interference pattern. This was understood semiclassically as the result of large angle rainbow oscillations, glories, and orbiting all combining.

Here we reconstruct the scattering cross sections using CAM techniques, and find that the Regge pole summations are sufficient to obtain a good approximation. In other words, the background integrals are negligible.

For the parameters considered here ($M\omega = 2$, $R/M = 2.26$) we find that only a handful of Regge-poles are needed to obtain a reasonable approximation for the exact cross section at large observation angles $\theta \gtrsim 140°$ (see figure 6.12b). As shown in figure 6.12a, summing over the single Regge-pole with the largest residue is insufficient at all θ. Much improved approximations are obtained by summing over 9 poles for the region $\theta \gtrsim 140°$ (figure 6.12c) , 14 poles for $\theta \gtrsim 70°$ (figure 6.12d), and progressively more poles for agreement at smaller angles (figures 6.12e and 6.12f).

All three Regge-pole branches make a significant contribution to the scattering cross section, as shown in figure 6.13. The difference in phase between

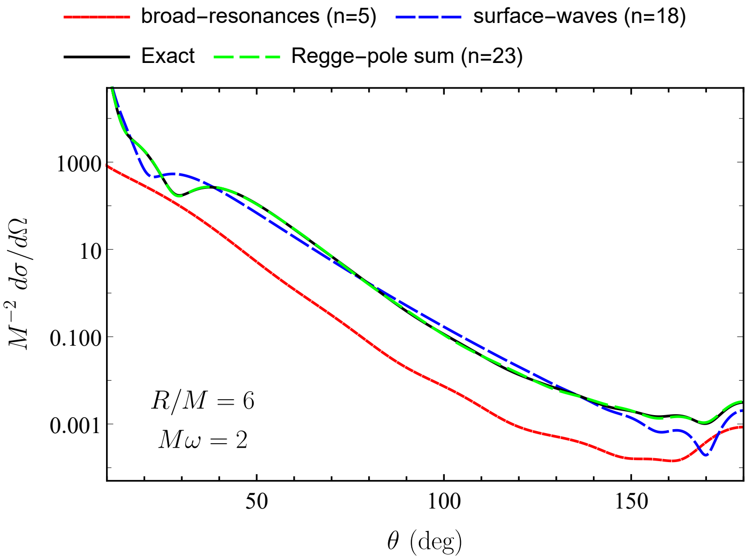

Figure 6.11: The scalar field scattering cross section for a constant density star with $R/M = 6$ and $M\omega = 2$. The partial wave (exact) calculation is shown in black (solid). The Regge-pole contributions from the broad-resonance branch is shown in red (lower solid line), and the surface-wave branch in blue (dashed). The total Regge pole contribution is shown in dashed green and overlays the partial wave (exact) result.

all three yields the interference pattern expected from the partial wave calculations. We find that more Regge-poles are needed to accurately capture the cross sections as $M\omega$ increases (see [65] for further examples).

6.7 Conclusions

In this chapter we have determined the spectrum of scalar field Regge-poles on the background spacetime of a constant density star, in the right-half CAM plane. Our method is applicable to general spherically symmetric spacetimes and could easily be applied to more sophisticated stellar models, or exotic compact objects (chapters 4 and 5). We have applied CAM theory to derive an exact formula for calculating scattering amplitudes as a sum over residues and a background integral, equations (6.63) and (6.65) to (6.68). We have then applied the CAM equations to compute scattering cross sections and demon-

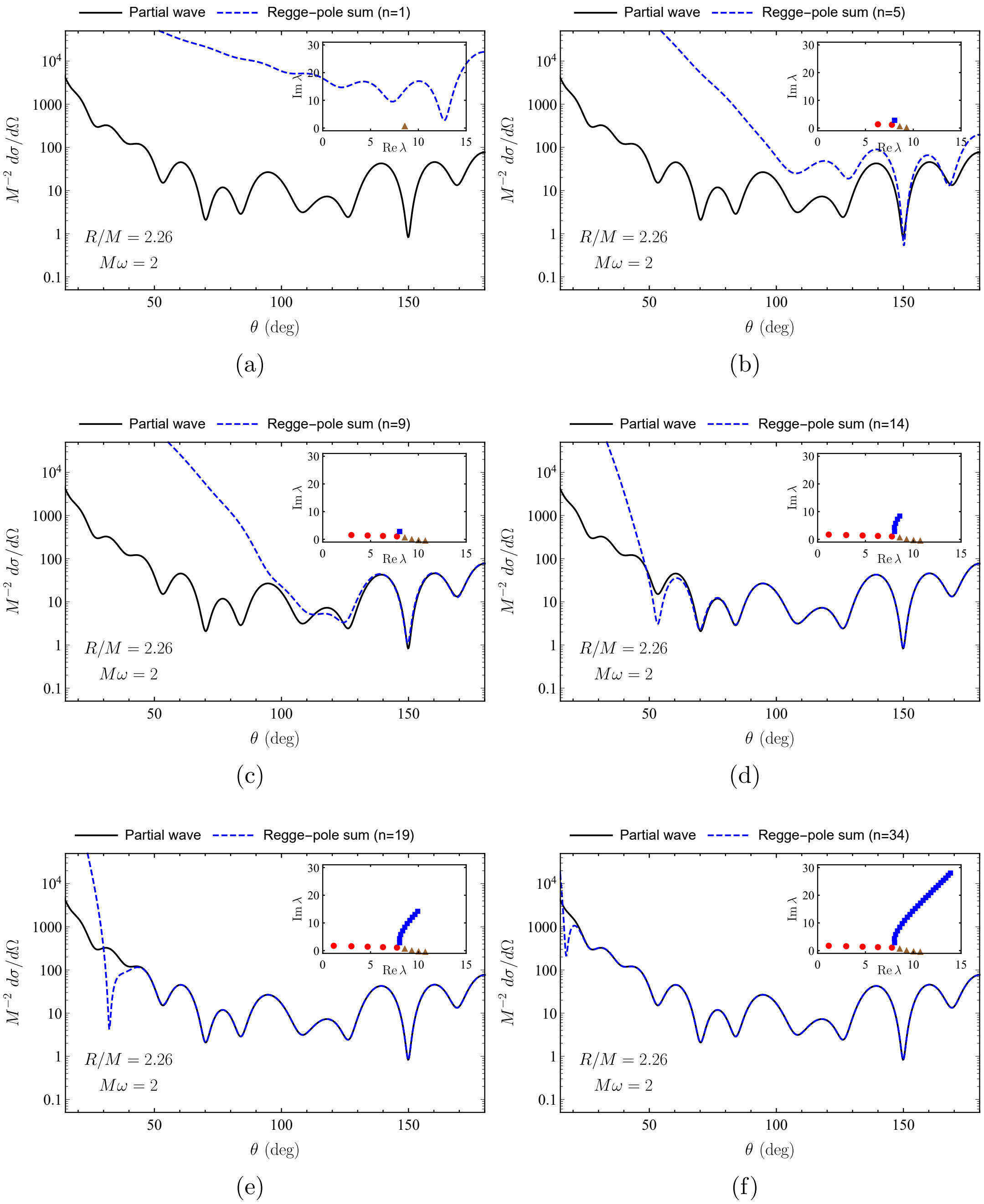

(a) (b) (c) (d) (e) (f)

Figure 6.12: The scalar field scattering cross section for a constant density star with $R/M = 2.26$ and $M\omega = 2$. The partial wave (exact) calculation is shown in black and the Regge-pole approximations in dashed blue. The approximations are made by summing over the Regge-poles shown in the inset graph.

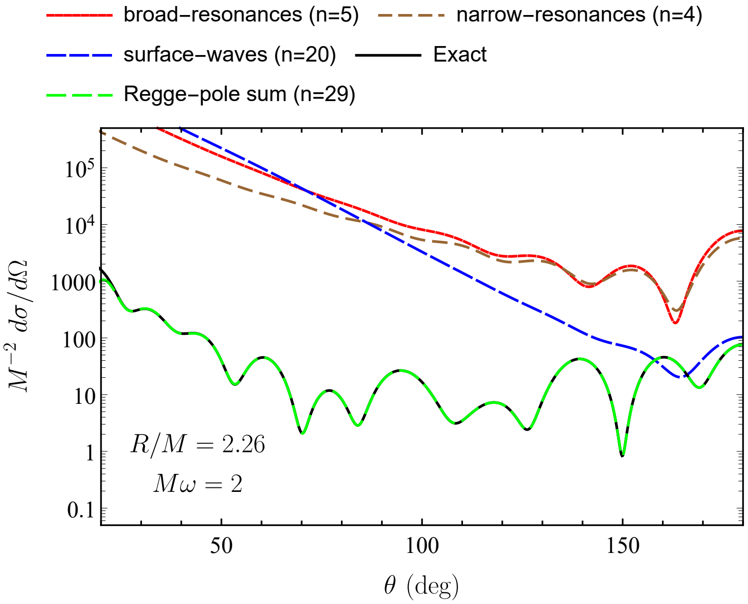

Figure 6.13: The scalar field scattering cross section for a constant density star with $R/M = 2.26$ and $M\omega = 2$. The partial wave (exact) calculation is shown in black (solid). The Regge-pole contributions from the broad-resonance branch is shown in red (solid), the surface-wave branch in blue (dashed), and the narrow-resonance branch in brown (short dashes). The result of combining all 29 Regge-poles is shown in dashed green and is visually indistinguishable from the partial wave result.

strated their equivalence to the partial wave results described in chapter 3.

We have found that the Regge-pole spectra for relativistic, spherically symmetric stellar bodies without a light ring is composed of two branches. The poles in the branch parallel to the real λ-axis we have termed ‘broad-resonances’. The poles in the branch inclined to the real λ-axis we have labelled ‘surface-waves’. Some justification for these labels is provided by considering modes with angular momentum $l = \mathrm{Re}\,\lambda_n - 1/2$, and appealing to semiclassical (high frequency) arguments. In essence, modes with $l = \mathrm{Re}\,\lambda_n^{\text{B-R}} - 1/2$ will penetrate into the interior of the star since the angular momentum barrier is sufficiently small. On the other hand, modes with $l = \mathrm{Re}\,\lambda_n^{\text{S-W}} - 1/2$ in some sense only feel the exterior spacetime and the surface of the star, and exponentially decay in the interior.

We have used a WKB method at zeroth order to derive approximations for the broad resonances. In this picture, the modes undergo a weak internal reflection due to the discontinuity at the surface of the body. The imaginary part of the$\lambda_n^{\text{B-R}}$ is dependent on the magnitude of the discontinuity at the surface, via equations (6.24) and (6.32) (see also figure 6.5).

For UCOs, the Regge-pole spectrum posses an additional third branch of poles, which we have called 'narrow-resonances' (see figure 6.6). The poles in this branch are associated with the effective cavity between the objects light ring at $r = 3M > R$, and the angular momentum barrier.

We have borrowed the terminology for the three Regge-pole branches used by Nussenzweig when examining Mie scattering [68], since they are qualitatively similar (see in particular figures 9.1 and 9.2 in [68] and compare with figure 6.6). As mentioned, the scenarios are not completely analogous and exploring the physical interpretation of the branches we see in the detail that Nussenzweig has for Mie scattering would be an interesting and challenging task beyond the scope of this thesis.

Further worthwhile study would be to consider stellar models with multiple discontinuities in the interior, motivated for example by the possibility of matter phase transitions in neutron stars. As we have seen, the surface discontinuity in our simple constant density model is particularly important for the broad-resonances. If there are multiple discontinuities, could there be further Regge-pole branches?

We are confident for the model considered here that there are no additional branches to be found in the right-half CAM plane for two reasons: (1) neither the root finding algorithm (section 6.2.2) or the rigorous scanning technique of Ould El Hadj [208] has found any additional poles when searching the regions of the complex λ-planes shown in figures 6.3, 6.4 and 6.6 (as well as the examples considered in [65]); (2) the scattering cross sections calculated using CAM and partial-wave methods are in agreement to a high numerical precision, which would not be the case if we had missed poles in the regions mentioned.

There are further, probably infinite poles in the surface wave branches, but these have a negligible effect on the scattering amplitude except at small angles.

There could in principle also be other branches with large imaginary parts and a negligible contribution to the scattering amplitude sum at intermediate and large angles but this seems unlikely. Finally, there most likely are Regge-poles in the left-half CAM plane, as there are in Mie scattering [68]. However, it is not clear what a suitable analytic extension of the mode solutions to this region is at this point. If we simply take the extension defined by equation (6.44), then the modes are divergent at the origin, as is the integrand for CAM scattering (equation (6.42)) as $|\lambda| \to \infty$, Re $\lambda < 0$. This is an avenue for further work, and the results in reference [68] are a good starting point.

We have found that the scattering cross sections for intermediate frequencies can be reconstructed to a good precision using the CAM formulae, except at small angles. The error at small angles is mitigated by including more surface wave poles in the summation. At intermediate and large angles we find a typical relative error of 10^{-2}, which seems to originate from neglecting the CAM background integral. When the background integral is included the relative error is reduced to approximately 10^{-4}. The CAM machinery allows one to sidestep the issue of the partial-wave sum divergence previously dealt with using other methods, provided we can live with a relative error of $O(10^{-2})$. This has been noted previously in black hole scattering, where only a few surface-wave poles are needed to capture the glory and orbiting scattering features [57, 58]. The situation is not quite as elegant for the UCO, since one must also take into account a few surface-wave poles as well as the broad and narrow-resonance poles (which increase in number as ω increases), to accurately reproduce the scattering cross section. In reference [65] the above conclusions are also shown to hold at higher frequencies ($M\omega = 8$).

Again we can look to Mie scattering for inspiration here, where the 'Debye expansion' is used to eliminate broad and narrow-resonances, leaving only surface-wave type Regge poles (see chapter 9 of [68]). The Debye expansion is based on a series of terms corresponding to interactions of the incident wave with the surface of a transparent sphere. We have made some attempts at developing an analogous approach here for a UCO, based on multiple interactions of the incident wave with the *photonsphere*, but have not yet been successful in eliminating the two resonance branches.

Finally we have some speculative comments on the duality of QNMs and Regge poles. Chandrasekhar and Ferrari established a link between the trapped modes of highly compact stars (UCOs) and Regge poles with small imaginary part [101]. These Regge poles are the 'narrow resonances' which we defined in analogy to scattering by a penetrable sphere in flat space. A natural question to ask is if there is a correspondence between the other branches of compact body Regge poles and QNMs.

Décanini *et al.* suggested extending their BH CAM analysis to attempt to interpret neutron star QNMs in terms of surface waves [71]. To do so requires calculating the Regge trajectories, the paths in the complex plane $\lambda_n(\omega)$, $\omega \in \mathbb{R}$. Then, a resonance wave frequency, ω_n^{R}, is found from the Bohr-Sommerfeld type quantisation condition [71],

$$\mathrm{Re}\left[\lambda_n(\omega_n^{\mathrm{R}})\right] = l + 1/2, \quad l = 0, 1, 2\dots \tag{6.73}$$

We have seen that the surface wave poles satisfy $\mathrm{Re}\left[\lambda_n^{\text{S-W}}(\omega)\right] > b_{gr}\omega$ for $R/M > 3$, where b_{gr} is the grazing ray impact parameter (equation (3.26)). Conversely, the broad resonances satisfy $\mathrm{Re}\left[\lambda_n^{\text{B-R}}(\omega)\right] < b_{gr}\omega$, when $R/M > 3$. Thus, for a fixed $l = l_0$ we expect there to be resonant frequencies $\omega_n^{\mathrm{R}} < (l_0 + 1/2)/b_{gr}$ associated with surface waves, and possibly infinite resonant frequencies $\omega_n^{\mathrm{R}} > (l_0 + 1/2)/b_{gr}$ associated with broad resonances. Neutron star models do possess two families of QNM: a possibly infinite number of 'curvature' modes [32], and 'interface' modes that may be associated with scattering from the surface of the star [31]. The interface mode frequencies are smaller than the curvature mode frequencies (see table 1 of [32]). The above considerations suggest that interface modes may be mapped to surface-wave poles, and curvature modes to broad-resonances. In addition, the WKB approximation for broad-resonance Regge poles (section 6.2.4) was adapted from a WKB approach for calculating curvature modes [210]. Unfortunately our code has not proved effective at finding QNMs for typical neutron star models as the imaginary parts are typically large which leads to issues integrating in the radial coordinate, and so we did not investigate this conjecture further. A more rigorous analysis would be required, and desirable, in order to make a stronger statement about the duality of the two types of resonances in compact bodies.

6.8 Regge-pole data

This section is a collection of the data for the Regge-poles and residues for the models $R/M = 6$ and $R/M = 2.26$ with $M\omega = 2$ (see figures 6.3 and 6.6). The branches are enumerated according to their distance from the central meeting point (or the surface wave pole with smallest imaginary part). We also present the Regge-poles calculated for the model with $R/M = 6$ and $M\omega = 8$ (see figure 6.5, and compare the broad-resonances with the WKB formula equation (6.32). Additional data is available in reference [65].

n	$\mathrm{Re}\,[\lambda_n^{\text{B-R}}]$	$\mathrm{Im}\,[\lambda_n^{\text{B-R}}]$	$\mathrm{Re}\,[r_n]$	$\mathrm{Im}\,[r_n]$
1	0.2078589134	2.4037800766	−0.3370928275	0.0178689221
2	2.2964852806	2.5283639620	−0.5392335131	0.1371085210
3	4.5211409166	2.6547369409	−0.6554092430	0.7551927951
4	6.9319724168	2.7898397477	0.7989174999	1.8572064324
5	9.6462574558	2.9496668407	3.8951271197	−3.1005199646

Table 6.1: Broad-resonance Regge-poles for the scalar field on a constant density star with tenuity $R/M = 6$ and $M\omega = 2$.

n	$\mathrm{Re}\,[\lambda_n^{\text{S-W}}]$	$\mathrm{Im}\,[\lambda_n^{\text{S-W}}]$	$\mathrm{Re}\,[r_n]$	$\mathrm{Im}\,[r_n]$
1	13.1571093946	3.1398993509	−12.6188769249	16.0454013304
2	14.4018590904	5.6796001923	59.2266606246	−1.7645406713
3	15.4068773177	7.8223842727	0.2497010582	−106.9838324506
4	16.2933616739	9.7684400587	−147.5386666385	−58.5466764134
5	17.1064353123	11.5852956411	−173.5321734084	120.3763991769
6	17.8675222892	13.3069545636	−32.9374442103	260.4645165757
7	18.5887517106	14.9539722163	177.4464337465	256.4120113608
8	19.2778339843	16.5401100924	340.7781262220	111.7817160542
9	19.9400783025	18.0752025718	388.7283274597	−105.8318358645
10	20.5793565360	19.5666051331	311.3002484882	−317.3799437985
11	21.1986155252	21.0200083237	138.7692682565	−463.4956358904
12	21.8001725668	22.4399315757	−81.1362367687	−514.4481984758
13	22.3858972216	23.8300404914	−300.6553913856	−467.3209734194
14	22.9573291568	25.1933600359	−481.9254532659	−337.9556327652
15	23.5157578586	26.5324230261	−600.7579509812	−152.2906841565
16	24.0622784956	27.8493766536	−646.4266240602	60.7449356351
17	24.5978322543	29.1460608177	−619.0594873833	273.9661921610
18	25.1232362064	30.4240669563	−515.4533056983	464.9975273190

Table 6.2: Surface-wave Regge-poles for the scalar field on a constant density star with tenuity $R/M = 6$ and $M\omega = 2$.

n	$\mathrm{Re}\,[\lambda_n^{\text{B-R}}]$	$\mathrm{Im}\,[\lambda_n^{\text{B-R}}]$	$\mathrm{Re}\,[r_n]$	$\mathrm{Im}\,[r_n]$
1	7.7744358222	1.3005536691	−35.7463341910	−250.6002985536
2	6.3113515934	1.4403982073	47.7322249759	−79.5871577920
3	4.7073116035	1.5900515870	−1.8682316228	−26.7463468623
4	2.9969483227	1.7447759245	−4.9504425616	4.0217462522
5	1.1593932814	1.9098312255	0.1614852296	−1.1022694572

Table 6.3: Broad-resonance Regge-poles for the scalar field on a constant density star with tenuity $R/M = 2.26$ and $M\omega = 2$.

n	$\mathrm{Re}\,[\lambda_n^{\text{N-R}}]$	$\mathrm{Im}\,[\lambda_n^{\text{N-R}}]$	$\mathrm{Re}\,[r_n]$	$\mathrm{Im}\,[r_n]$
1	8.5894199914	1.0905489773	64.6600077923	−128.9301781778
2	9.3098023984	0.5269574852	8.5944268604	−3.6045413616
3	10.0361165037	0.1470067641	0.2922616960	−0.4437231374
4	10.7376054334	0.0064453196	−0.0120914120	−0.0051766969

Table 6.4: Narrow-resonance Regge-poles for the scalar field on a constant density star with tenuity $R/M = 2.26$ and $M\omega = 2$.

n	$\mathrm{Re}\,[\lambda_n^{\text{S-W}}]$	$\mathrm{Im}\,[\lambda_n^{\text{S-W}}]$	$\mathrm{Re}\,[r_n]$	$\mathrm{Im}\,[r_n]$
1	8.0459507022	2.7245439973	−271.8785639876	1,986.8888816303
2	8.0397260117	4.3209876235	2,740.8680505202	−2,720.8784508344
3	8.1639973017	5.7873603892	−4,499.1573311463	−2,411.1830724905
4	8.3575244116	7.1505459327	−3,228.4644583934	4,755.2132870540
5	8.5891987792	8.4327157375	3,392.7683019384	4,966.3076366999
6	8.8424494859	9.6505870601	6,071.4981847061	−203.7224808534
7	9.1079786337	10.8165095354	3,754.8802792320	−4,716.0150474080
8	9.3803278734	11.9396661348	−507.9042965372	−5,907.3571898263
9	9.6561714911	13.0269944632	−4,002.1429048699	−4,207.4142749963
10	9.9334232769	14.0838330257	−5,560.5391639462	−1,143.6052432905
11	10.2107462371	15.1143652731	−5,211.6462129467	1,901.0637414990
12	10.4872715943	16.1219257755	−3,552.1322460630	4,097.5775939170
13	10.7624314992	17.1092140606	−1,292.6758713317	5,145.0150143937
14	11.0358560825	18.0784464066	974.4804548913	5,102.1626654288
15	11.3073082461	19.0314654435	2,853.1489645165	4,216.8623929167
16	11.5766413096	19.9698206237	4,137.3505301899	2,799.9288657569
17	11.8437708984	20.8948282476	4,770.8022981190	1,147.8447808934
18	12.1086559290	21.8076169071	4,798.9874915568	−496.2429529148
19	12.3712855380	22.7091623667	4,326.5363049518	−1,955.9453623296
20	12.6316699697	23.6003146788	3,484.3438866993	−3,120.0076365849
21	12.8898341500	24.4818195111	2,406.6892190141	−3,933.0876096891
22	13.1458131085	25.3543351047	1,216.8626298970	−4,383.6853278949
23	13.3996486925	26.2184458928	19.3155158013	−4,491.9790567175
24	13.6513871939	27.0746735407	−1,103.5584115855	−4,298.9855577101
25	13.9010776287	27.9234859714	−2,091.5786650460	−3,857.6282913209
26	14.1487704866	28.7653048034	−2,905.0702250641	−3,225.8134545644
27	14.3945168243	29.6005115276	−3,522.1578611199	−2,461.3586322300
28	14.6383676087	30.4294526693	−3,935.6537077959	−1,618.5037957670

Table 6.5: Surface-wave Regge-poles for the scalar field on a constant density star with tenuity $R/M = 2.26$ and $M\omega = 2$.

n	$\mathrm{Re}\,[\lambda_n^{\text{B-R}}]$	$\mathrm{Im}\,[\lambda_n^{\text{B-R}}]$	$\mathrm{Re}\,[\lambda_n^{\text{S-W}}]$	$\mathrm{Im}\,[\lambda_n^{\text{S-W}}]$
1	51.1054839401	4.9555954956	56.0094517298	5.7103849263
2	47.2802395843	4.6390754587	58.4465611630	9.1879311322
3	43.8923611192	4.4412977769	60.2037373119	12.1496453608
4	40.7673310730	4.2972583371	61.6770018779	14.8472806975
5	37.8252489752	4.1831707542	62.9862584761	17.3716467021
6	35.0213121669	4.0878840062	64.1860520487	19.7691078243
7	32.3273058738	4.0053096711	65.3064012656	22.0674267572
8	29.7240684052	3.9317952283	66.3658104958	24.2849146553
9	27.1978640192	3.8649888236	67.3765869199	26.4344719730
10	24.7384418829	3.8032927307	68.3473770943	28.5256357023
11	22.3379093557	3.7455747198	69.2845137176	30.5657207317
12	19.9900365371	3.6910043249	70.1927893294	32.5605031223
13	17.6898056541	3.6389545781	71.0759285831	34.5146524402

Table 6.6: The first 13 broad-resonance and surface-wave Regge-poles for the scalar field on a constant density star with tenuity $R/M = 6$ and $M\omega = 8$.

n	$\mathrm{Re}\,[\lambda_n^{\text{B-R}}]$	$\mathrm{Im}\,[\lambda_n^{\text{B-R}}]$	$\mathrm{Re}\,[\lambda_n^{\text{WKB}}]$	$\mathrm{Im}\,[\lambda_n^{\text{WKB}}]$	Error
1	51.1054839401	4.9555954956	40.6615642399	3.2554534592	0.2061
2	47.2802395843	4.6390754587	38.6615642399	3.2554534592	0.1837
3	43.8923611192	4.4412977769	36.6615642399	3.2554534592	0.1661
4	40.7673310730	4.2972583371	34.6615642399	3.2554534592	0.1511
5	37.8252489752	4.1831707542	32.6615642399	3.2554534592	0.1379
6	35.0213121669	4.0878840062	30.6615642399	3.2554534592	0.1259
7	32.3273058738	4.0053096711	28.6615642399	3.2554534592	0.1149
8	29.7240684052	3.9317952283	26.6615642399	3.2554534592	0.1046
9	27.1978640192	3.8649888236	24.6615642399	3.2554534592	0.0950
10	24.7384418829	3.8032927307	22.6615642399	3.2554534592	0.0858
11	22.3379093557	3.7455747198	20.6615642399	3.2554534592	0.0771
12	19.9900365371	3.6910043249	18.6615642399	3.2554534592	0.0688
13	17.6898056541	3.6389545781	16.6615642399	3.2554534592	0.0608
14	15.4331073361	3.5889402680	14.6615642399	3.2554534592	0.0530
15	13.2165290777	3.5405776368	12.6615642399	3.2554534592	0.0456
16	11.0372037871	3.4935572012	10.6615642399	3.2554534592	0.0384
17	8.8926987676	3.4476249031	8.6615642399	3.2554534592	0.0315
18	6.7809326677	3.4025687107	6.6615642399	3.2554534592	0.0250
19	4.7001122482	3.3582088820	4.6615642399	3.2554534592	0.0190
20	2.6486834884	3.3143907476	2.6615642399	3.2554534592	0.0142
21	0.6252932655	3.2709792602	0.6615642399	3.2554534592	0.0118

Table 6.7: Broad-resonance Regge-poles for the scalar field on a constant density star with tenuity $R/M = 6$ and $M\omega = 8$. A comparison of numerical results $\lambda_n^{\text{B-R}}$ and WKB approximations λ_n^{WKB} (see equation (6.32)).

Chapter 7

Summary

In this thesis we have examined and developed the scattering theory for bosonic field plane waves incident on relativistic compact objects. Complementing earlier work on scattering from black holes [21], we have used metric perturbation formalisms [87, 92, 93] to study gravitational waves scattering from spherically symmetric matter configurations such as neutron stars. The definition and derivation of scattering and absorption cross sections for scalar and gravitational waves is presented in chapter 2. A natural extension of this work would be to consider scattering on rotating non-vacuum spacetimes, for example rotating stars. Kojima has derived equations for perturbations of slowly rotating relativistic stars which provides a solid starting point [93].

In chapter 3 we focused on scalar plane wave scattering from a compact star modelled as a fluid sphere of constant density. Using both semiclassical and numerical partial wave approaches we computed scattering cross sections. We found evidence for a rainbow interference pattern when a scalar wave of sufficiently high frequency was incident on a neutron star. In addition glory and spiral scattering were seen for scattering by ultra compact objects.

In chapter 4 we extended our work to consider both gravitational waves and different stellar models. The rainbow interference pattern was shown to be sensitive to the stellar model equation of state and the star's compactness. In practice, gravitational waves of known astrophysical sources are of too large a wavelength (or equivalently too low frequency) to probe the details of a neutron star's curvature, and give rise to this rainbow interference pattern. However, there is the possibility that rainbow scattering could occur due to scattering by other compact matter configurations, such as black holes with surrounding matter, as shown by Leite *et al* [56]. Also, in related work Alexandre and Clough showed that a non-trivial interference pattern for the oscillation probabilities of neutrino flavours would be expected when a black hole was situated between a neutrino source and detector [162].

Interesting avenues for future work that builds on chapters 2 to 4 includes: extending the work in reference [56] to consider gravitational waves, using the formalism we have developed in chapters 2 and 4; generalising to scattering on rotating (non-vacuum) spacetimes; and considering interference patterns for the oscillation probabilities of neutrinos downstream from a compact body, and comparing the findings with those in reference [162].

The absorption of plane waves by exotic compact objects (ECOs) was investigated in chapter 5. A heuristic model was used for the ECO whereby a partially reflective boundary condition was imposed at a small distance above the Schwarzschild radius (where the event horizon would be if the body was a black hole). Clear spectral lines were found in numerically calculated absorption cross sections for scalar waves. These lines were interpreted as enhanced absorption due to the excitation of Breit-Wigner type resonances. The resonances were shown to be modes trapped between the body's surface and light ring. Natural extensions of this work would be to consider electromagnetic, neutrino, and gravitational wave perturbations. In particular, astrophysical gravitational waves incident on super massive black hole candidates which (speculatively) could be ECOs, could give rise to particularly strong absorption lines. It would be interesting to investigate the astrophysical implications of this, if any, in light of upcoming space based gravitational wave detectors [75]. Another option is to consider absorption of plane waves by neutron star models which include a mechanism for dissipation of energy, such as energy loss due to gravitational waves coupling to fluid modes which will then be damped by frictional forces.

In chapter 6 the complex angular momentum (CAM) picture of perturbations on a spherically symmetric compact body space-time was presented. CAM resonant modes known as "Regge modes" were identified for the scalar wave on a constant density star. The theory can easily be applied to other models if desired (such as those in chapter 4, section 4.1, and reference [65]). We showed that at least two families of Regge modes exist for our model, and a third family exists if the star is sufficiently compact to possess a light ring. The families could loosely be interpreted as surface waves (associated with the surface of the star or the light ring if extant), broad resonances that penetrate inside the star, and narrow resonances trapped inside the light ring.

A better understanding of the CAM resonances and their association with quasinormal modes (with complex frequency and real angular momentum) is needed. A good starting point is to follow the work on CAM theory for black hole perturbations undertaken by Décanini, Folacci and Jensen [71], as well as Andersson and Thylwe [46]. In addition the monograph by Nussenzweig provides a thorough analysis of Regge modes for hard and penetrable spheres in flat space using semiclassical techniques [68].

In chapter 6, we made use of the Regge modes and their residues to calculate scattering cross sections and compare with the results from the partial wave method shown in chapter 3. CAM theory has also been applied to time dependent scattering from black holes by Folacci and Ould El Hadj, who accurately modelled the characteristic ringdown of a perturbed black hole [199]. It would be interesting to generalise their method to other compact objects.

Finally, it would be instructive to consider the ECO model from chapter 5 in the CAM picture. Décanini *et al.* have derived an elegant high energy approximation for absorption by black holes using the CAM paradigm [202]. It would be worthwhile to extend their work to further investigate absorption by ECOs, as this could help elucidate the nature of the various Regge modes, their relationship to quasinormal modes, and the physical mechanism behind the spectral lines.

Appendices

Appendix A

Spherical harmonics

Here we collect the definitions and some properties of the usual spherical harmonics $Y^{lm}(\theta, \phi)$ as well as the vector and tensor spherical harmonics introduced by Martel and Poisson [87].

The spherical harmonics $Y^{lm}(\theta, \phi)$ are the eigenfunctions of the differential equation [117]

$$\frac{1}{\sin\theta}\frac{\partial}{\partial\theta}\left[\sin\theta\frac{\partial Y^{lm}}{\partial\theta}\right] + \frac{1}{\sin\theta}\frac{\partial^2 Y^{lm}}{\partial^2\phi} = -l(l+1)Y^{lm}. \tag{A.1}$$

The spherical harmonics are orthogonal on the unit sphere

$$\int \bar{Y}_{lm}Y^{l'm'}\, d\Omega = \delta_{l,l'}\delta_{m,m'}, \tag{A.2}$$

where and over-bar denotes complex conjugation.

The even and odd parity vector spherical harmonics of Martel and Poisson [87] are defined by

$$X_A^{lm+} \equiv D_A Y^{lm} \tag{A.3}$$

and

$$X_A^{lm-} \equiv -\epsilon_A{}^B D_B Y^{lm} \tag{A.4}$$

respectively, where ϵ_{AB} is the Levi-Civita tensor on the unit two-sphere. Here D_A is the covariant differential operator associated with the metric on a two-sphere Ω_{AB}, and the upper case Latin subscript runs over (any choice of) two angular coordinates. With the usual choice (θ, ϕ) the operators are simply $D_\theta = \sin\theta \frac{\partial}{\partial\theta}$ and $D_\phi = \frac{\partial}{\partial\phi}$.

These vector harmonics satisfy

$$\int \bar{X}^A_{lmp} X^{l'm'p'}_A \, d\Omega = l(l+1)\delta_{ll'}\delta_{mm'}\delta_{pp'}. \tag{A.5}$$

Martel and Poisson have also defined tensor spherical harmonics [87]. The even parity tensor spherical harmonics are split into a trace-free part

$$X^{lm+}_{AB} \equiv \left[D_A D_B + \frac{1}{2} l(l+1)\Omega_{AB} \right] Y^{lm}, \tag{A.6}$$

and a trace piece $\Omega_{AB} Y^{lm}$. The odd parity tensor harmonics are

$$X^{lm-}_{AB} \equiv -\frac{1}{2} \left[\epsilon_A{}^C D_B + \epsilon_B{}^C D_A \right] D_C Y^{lm}, \tag{A.7}$$

which are also trace free on the sphere, $\Omega^{AB} X^{lm-}_{AB} = 0$. They satisfy

$$\int \bar{X}^{AB}_{lmp} X^{l'm'p'}_{AB} \, d\Omega = \frac{1}{2} l(l-1)(l+1)(l+2)\delta_{ll'}\delta_{mm'}\delta_{pp'}. \tag{A.8}$$

They are related to spin-weighted spherical harmonics [214] by

$$X^{lm-}_{AB} = \frac{i}{2}\sqrt{(l-1)l(l+1)(l+2)} \left({}_2Y^{lm} \bar{m}_A \bar{m}_B - {}_{-2}Y^{lm} m_A m_B \right), \tag{A.9}$$

$$X^{lm+}_{AB} = \frac{1}{2}\sqrt{(l-1)l(l+1)(l+2)} \left({}_2Y^{lm} \bar{m}_A \bar{m}_B + {}_{-2}Y^{lm} m_A m_B \right), \tag{A.10}$$

where $m_A = 2^{-1/2}(1, i\sin\theta)$. Note $X^{l(-m)p}_{AB} = (-1)^m \bar{X}^{lmp}_{AB}$.

Bibliography

[1] B. P. Abbott et al., GWTC-1: A gravitational-wave transient catalog of compact binary mergers observed by LIGO and Virgo during the first and second observing runs, Phys. Rev. **X9**, 031040 (2019).

[2] B. P. Abbott et al., GW170817: Observation of gravitational waves from a binary neutron star inspiral, Phys. Rev. Lett. **119**, 161101 (2017).

[3] B. Abbott, R. Abbott, R. Adhikari, A. Ananyeva, S. Anderson, S. Appert, K. Arai, M. Araya, J. Barayoga, B. Barish, et al., Multi-messenger observations of a binary neutron star merger, Astrophys. J. Lett. **848**, L12 (2017).

[4] A. Einstein, Approximative integration of the field equations of gravitation, Sitzungsber. Preuss. Akad. Wiss. **1**, 688–696 (1916).

[5] K. Schwarzschild, Über das gravitationsfeld eines massenpunktes nach der Einsteinschen theorie, Sitzungsber. Preuss. Akad. Wiss., 189–196 (1916).

[6] H. Reissner, Über die eigengravitation des elektrischen feldes nach der Einsteinschen theorie, Ann. Phys. Berlin **355**, 106–120 (1916).

[7] G. Nordström, On the energy of the gravitation field in Einstein's theory, Kon. Ned. Akad. B **20**, 1238–1245 (1918).

[8] R. P. Kerr, Gravitational field of a spinning mass as an example of algebraically special metrics, Phys. Rev. Lett. **11**, 237–238 (1963).

[9] E. T. Newman, R. Couch, K. Chinnapared, A. Exton, A. Prakash, and R. Torrence, Metric of a rotating, charged mass, J. Math. Phys. **6**, 918–919 (1965).

[10] J. R. Oppenheimer and G. M. Volkoff, On massive neutron cores, Phys. Rev. **D55**, 374–381 (1939).

[11] D. Lynden-Bell, Galactic nuclei as collapsed old quasars, Nature **223**, 690 (1969).

[12] K. Akiyama et al., First M87 Event Horizon Telescope results. I. The shadow of the supermassive black hole, Astrophys. J. **875**, L1 (2019).

[13] B. F. Schutz, Gravity from the Ground Up (Cambridge University Press, 2003).

[14] S. Chandrasekhar, The maximum mass of ideal white dwarfs, Astrophys. J. **74**, 81 (1931).

[15] F. Mirabel, The formation of stellar black holes, New Astron. Rev. **78**, 1–15 (2017).

[16] C. Barceló, R. Carballo-Rubio, and L. J. Garay, Gravitational wave echoes from macroscopic quantum gravity effects, JHEP **05**, 054 (2017).

[17] C. Barcelo, S. Liberati, S. Sonego, and M. Visser, Fate of gravitational collapse in semiclassical gravity, Phys. Rev. **D77**, 044032 (2008).

[18] J. Abedi, H. Dykaar, and N. Afshordi, Echoes from the abyss: Tentative evidence for Planck-scale structure at black hole horizons, Phys. Rev. **D96**, 082004 (2017).

[19] S. L. Liebling and C. Palenzuela, Dynamical boson stars, Living Rev. Rel. **15**, 6 (2012).

[20] V. Cardoso and P. Pani, The observational evidence for horizons: from echoes to precision gravitational-wave physics, arXiv:1707.03021 (2017).

[21] J. A. H. Futterman, F. A. Handler, and R. A. Matzner, Scattering from black holes (Cambridge University Press, 2012).

[22] C. Vishveshwara, Scattering of gravitational radiation by a Schwarzschild black-hole. Nature **227**, 936 (1970).

[23] W. H. Press, Long wave trains of gravitational waves from a vibrating black hole, Astrophys. J. **170**, L105–L108 (1971).

[24] O. Dreyer, B. J. Kelly, B. Krishnan, L. S. Finn, D. Garrison, and R. Lopez-Aleman, Black hole spectroscopy: testing general relativity through gravitational wave observations, Class. Quant. Grav. **21**, 787–804 (2004).

[25] M. Isi, M. Giesler, W. M. Farr, M. A. Scheel, and S. A. Teukolsky, Testing the no-hair theorem with GW150914, Phys. Rev. Lett. **123**, 111102 (2019).

[26] V. Cardoso, E. Franzin, and P. Pani, Is the gravitational-wave ringdown a probe of the event horizon?, Phys. Rev. Lett. **116**, 171101 (2016).

[27] V. Cardoso, S. Hopper, C. F. B. Macedo, C. Palenzuela, and P. Pani, Gravitational-wave signatures of exotic compact objects and of quantum corrections at the horizon scale, Phys. Rev. **D94**, 084031 (2016).

[28] J. P. Cox, Theory of Stellar Pulsation (Princeton University Press, 1980).

[29] K. S. Thorne and A. Campolattaro, Non-radial pulsation of general-relativistic stellar models. i. Analytic analysis for $L \geq 2$, Astrophys. J. **149**, 591 (1967).

[30] R. Price and K. S. Thorne, Non-radial pulsation of general-relativistic stellar models. II. Properties of the gravitational waves, Astrophys. J. **155**, 163 (1969).

[31] N. Andersson, Y. Kojima, and K. D. Kokkotas, On the oscillation spectra of ultracompact stars: an extensive survey of gravitational wave modes, Astrophys. J. **462**, 855 (1996).

[32] K. D. Kokkotas and B. G. Schmidt, Quasinormal modes of stars and black holes, Living Rev. Rel. **2**, 2 (1999).

[33] K. W. Ford and J. A. Wheeler, Semiclassical description of scattering, Ann. Phys. New York **7**, 259–286 (1959).

[34] G. N. Watson, The diffraction of electric waves by the Earth, Proc. R. Soc. London A **95**, 83 (1918).

[35] N. G. Sanchez, The wave scattering theory and the absorption problem for a black hole, Phys. Rev. **D16**, 937–945 (1977).

[36] N. G. Sanchez, Absorption and Emission Spectra of a Schwarzschild Black Hole, Phys. Rev. **D18**, 1030 (1978).

[37] N. G. Sanchez, Elastic scattering of waves by a black hole, Phys. Rev. **D18**, 1798 (1978).

[38] F. A. Handler and R. A. Matzner, Gravitational wave scattering, Phys. Rev. **D22**, 2331–2348 (1980).

[39] R. A. Matzner, Scattering of massless scalar waves by a schwarzschild "singularity", J. Math. Phys. **9**, 163–170 (1968).

[40] R. A. Matzner, C. DeWitt-Morette, B. Nelson, and T.-R. Zhang, Glory scattering by black holes, Phys. Rev. **D31**, 1869 (1985).

[41] R. A. Matzner and M. P. J. Ryan, Scattering of gravitational radiation from vacuum black holes. Astrophys. J., Suppl. **36**, 451–481 (1978).

[42] B. Mashhoon, Scattering of electromagnetic radiation from a black hole, Phys. Rev. **D7**, 2807–2814 (1973).

[43] P. L. Chrzanowski, R. A. Matzner, V. D. Sandberg, and M. P. Ryan, Zero mass plane waves in nonzero gravitational backgrounds, Phys. Rev. **D14**, 317–326 (1976).

[44] W. K. De Logi and S. J. Kovacs, Gravitational scattering of zero rest mass plane waves, Phys. Rev. **D16**, 237–244 (1977).

[45] T. R. Zhang and C. DeWitt-Morette, WKB cross-section for polarized glories of massless waves in curved space-times, Phys. Rev. Lett. **52**, 2313–2316 (1984).

[46] N. Andersson and K. E. Thylwe, Complex angular momentum approach to black hole scattering, Class. Quant. Grav. **11**, 2991–3001 (1994).

[47] N. Andersson, Complex angular momenta and the black hole glory, Class. Quant. Grav. **11**, 3003–3012 (1994).

[48] K. Glampedakis and N. Andersson, Scattering of scalar waves by rotating black holes, Class. Quant. Grav. **18**, 1939–1966 (2001).

[49] S. R. Dolan, Scattering of long-wavelength gravitational waves, Phys. Rev. **D77**, 044004 (2008).

[50] S. R. Dolan, Scattering and Absorption of Gravitational Plane Waves by Rotating Black Holes, Class. Quant. Grav. **25**, 235002 (2008).

[51] L. C. B. Crispino, S. R. Dolan, and E. S. Oliveira, Scattering of massless scalar waves by Reissner-Nordstrom black holes, Phys. Rev. **D79**, 064022 (2009).

[52] L. C. B. Crispino, S. R. Dolan, and E. S. Oliveira, Electromagnetic wave scattering by Schwarzschild black holes, Phys. Rev. Lett. **102**, 231103 (2009).

[53] L. C. B. Crispino, S. R. Dolan, A. Higuchi, and E. S. de Oliveira, Inferring black hole charge from backscattered electromagnetic radiation, Phys. Rev. **D90**, 064027 (2014).

[54] L. C. B. Crispino, S. R. Dolan, A. Higuchi, and E. S. de Oliveira, Scattering from charged black holes and supergravity, Phys. Rev. **D92**, 084056 (2015).

[55] L. C. S. Leite, S. R. Dolan, and L. C. B. Crispino, Absorption of electromagnetic and gravitational waves by Kerr black holes, Phys. Lett. **B774**, 130–134 (2017).

[56] L. C. S. Leite, C. F. B. Macedo, and L. C. B. Crispino, Black holes with surrounding matter and rainbow scattering, Phys. Rev. **D99**, 064020 (2019).

[57] A. Folacci and M. Ould El Hadj, Regge pole description of scattering of scalar and electromagnetic waves by a Schwarzschild black hole, Phys. Rev. **D99**, 104079 (2019).

[58] A. Folacci and M. Ould El Hadj, Regge pole description of scattering of gravitational waves by a Schwarzschild black hole, Phys. Rev. **D100**, 064009 (2019).

[59] L. C. S. Leite, C. L. Benone, and L. C. B. Crispino, On-axis scattering of scalar fields by charged rotating black holes, Phys. Lett. **B795**, 496–501 (2019).

[60] C. L. Benone and L. C. B. Crispino, Massive and charged scalar field in Kerr-Newman spacetime: Absorption and superradiance, Phys. Rev. **D99**, 044009 (2019).

[61] L. C. S. Leite, S. R. Dolan, and L. C. B. Crispino, Scattering of massless bosonic fields by kerr black holes: On-axis incidence, Phys. Rev. **D100**, 084025 (2019).

[62] S. R. Dolan and T. Stratton, Rainbow scattering in the gravitational field of a compact object, Phys. Rev. **D95**, 124055 (2017).

[63] C. F. B. Macedo, T. Stratton, S. Dolan, and L. C. B. Crispino, Spectral lines of extreme compact objects, Phys. Rev. **D98**, 104034 (2018).

[64] T. Stratton and S. R. Dolan, Rainbow scattering of gravitational plane waves by a compact body, Phys. Rev. **D100**, 024007 (2019).

[65] M. Ould El Hadj, T. Stratton, and S. R. Dolan, Scattering from compact objects: Regge poles and the complex angular momentum method, Phys. Rev. D **101**, 104035 (2020).

[66] W. R. Inc., *MATHEMATICA, Version 10.0*, (Wolfram Research, Inc., Champaign, IL, 2014).

[67] D. A. Goldberg, S. M. Smith, and G. F. Burdzik, Refractive behavior in intermediate-energy alpha scattering, Phys. Rev. **C10**, 1362–1371 (1974).

[68] H. M. Nussenzveig, Diffraction Effects in Semiclassical Scattering (Cambridge University Press, 1992).

[69] T. Regge, Introduction to complex orbital momenta, Nuovo Cim. **14**, 951 (1959).

[70] C. W. Misner, K. S. Thorne, and J. A. Wheeler, Gravitation (W. H. Freeman, San Francisco, 1973).

[71] Y. Decanini, A. Folacci, and B. Jensen, Complex angular momentum in black hole physics and the quasinormal modes, Phys. Rev. **D67**, 124017 (2003).

[72] B. P. Abbott et al., Tests of general relativity with GW150914, Phys. Rev. Lett. **116**, 221101 (2016).

[73] T. Torres, S. Patrick, A. Coutant, M. Richartz, E. W. Tedford, and S. Weinfurtner, Observation of superradiance in a vortex flow, Nature Phys. **13**, 833–836 (2017).

[74] D. Dempsey and S. R. Dolan, Waves and null congruences in a draining bathtub, Int. J. Mod. Phys. **D25**, 1641004 (2016).

[75] P. A. Seoane et al., The gravitational universe, arXiv:1305.5720 (2013).

[76] C. J. Moore, R. H. Cole, and C. P. L. Berry, Gravitational-wave sensitivity curves, Class. Quant. Grav. **32**, 015014 (2015).

[77] J. M. Diego, O. A. Hannuksela, P. L. Kelly, T. Broadhurst, K. Kim, T. G. F. Li, G. F. Smoot, and G. Pagano, Observational signatures of microlensing in gravitational waves at LIGO/Virgo frequencies, Astron. Astrophys. **627**, A130 (2019).

[78] A. Einstein, Lens-like action of a star by the deviation of light in the gravitational field, Science **84**, 506–507 (1936).

[79] J. Wambsganss, Gravitational lensing in astronomy, Living Rev. Rel. **1**, 12 (1998).

[80] S. Seager and D. Deming, Exoplanet atmospheres, Annu. Rev. Astron. Astrophys. **48**, 631–672 (2010).

[81] D. R. Brill and J. B. Hartle, Method of the self-consistent field in general relativity and its application to the gravitational geon, Phys. Rev. **135**, B271–B278 (1964).

[82] R. A. Isaacson, Gravitational radiation in the limit of high frequency. I. The linear approximation and geometrical optics, Phys. Rev. **166**, 1263–1271 (1967).

[83] R. A. Isaacson, Gravitational radiation in the limit of high frequency. II. Nonlinear terms and the effective stress tensor, Phys. Rev. **166**, 1272–1279 (1968).

[84] G. D. Birkhoff and R. E. Langer, Relativity and Modern Physics (Harvard University Press, 1923).

[85] J. T. Jebsen, Über die allgemeinen kugelsymmetrischen lösungen der Einsteinschen gravitationsgleichungen im vakuum, Ark. Mat. Astr. Fys. **15**, 1 (1921).

[86] K. Martel, Gravitational wave forms from a point particle orbiting a Schwarzschild black hole, Phys. Rev. **D69**, 044025 (2004).

[87] K. Martel and E. Poisson, Gravitational perturbations of the Schwarzschild spacetime: A Practical covariant and gauge-invariant formalism, Phys. Rev. **D71**, 104003 (2005).

[88] F. J. Zerilli, Effective potential for even parity Regge-Wheeler gravitational perturbation equations, Phys. Rev. Lett. **24**, 737–738 (1970).

[89] S. A. Teukolsky, Rotating black holes - separable wave equations for gravitational and electromagnetic perturbations, Phys. Rev. Lett. **29**, 1114–1118 (1972).

[90] S. Chandrasekhar, The Mathematical Theory of Black Holes (Oxford University Press, 1985).

[91] R. C. Tolman, Static solutions of Einstein's field equations for spheres of fluid, Phys. Rev. **D55**, 364–373 (1939).

[92] G. Allen, N. Andersson, K. D. Kokkotas, and B. F. Schutz, Gravitational waves from pulsating stars: Evolving the perturbation equations for a relativistic star, Phys. Rev. **D58**, 124012 (1998).

[93] Y. Kojima, Equations governing the nonradial oscillations of a slowly rotating relativistic star, Phys. Rev. **D46**, 4289–4303 (1992).

[94] V. Moncrief, Gravitational perturbations of spherically symmetric systems. II. Perfect fluid interiors, Ann. Phys. New York **88**, 343–370 (1974).

[95] C. T. Cunningham, R. H. Price, and V. Moncrief, Radiation from collapsing relativistic stars. I - Linearized odd-parity radiation, Astrophys. J. **224**, 643 (1978).

[96] C. T. Cunningham, R. H. Price, and V. Moncrief, Radiation from collapsing relativistic stars. II - Linearized even-parity radiation, Astrophys. J. **230**, 870–892 (1979).

[97] J. R. Ipser and R. H. Price, Nonradial pulsations of stellar models in general relativity, Phys. Rev. **D43**, 1768 (1991).

[98] S. Chandrasekhar and V. Ferrari, On the non-radial oscillations of a star, Proc. R. Soc. Lond. A. **432**, 247–279 (1991).

[99] S. Chandrasekhar and V. Ferrari, On the non-radial oscillations of a star - II. Further amplifications, Proc. R. Soc. Lond. A. **434**, 635–641 (1991).

[100] S. Chandrasekhar and V. Ferrari, On the non-radial oscillations of a star - III. A reconsideration of the axial modes, Proc. R. Soc. Lond. A. **434**, 449–457 (1991).

[101] S. Chandrasekhar and V. Ferrari, On the non-radial oscillations of a star - IV. An aplication of the theory of Regge poles, Proc. R. Soc. Lond. A. **437**, 133–149 (1992).

[102] S. Chandrasekhar and V. Ferrari, On the non-radial oscillations of a star - V. A fully relativistic treatment of a Newtonian star, Proc. R. Soc. Lond. A. **450**, 463–475 (1995).

[103] W. G. Unruh, Absorption cross-section of small black holes, Phys. Rev. **D14**, 3251–3259 (1976).

[104] G. Breit and E. Wigner, Capture of slow neutrons, Phys. Rev. **49**, 519 (1936).

[105] M. Casals, S. R. Dolan, A. C. Ottewill, and B. Wardell, Self-force calculations with matched expansions and quasinormal mode sums, Phys. Rev. **D79**, 124043 (2009).

[106] W. W. Hildreth, The Interaction of Scalar Gravitational Waves with the Schwarzschild Metric, PhD thesis (1964).

[107] E. Newman and R. Penrose, An approach to gravitational radiation by a method of spin coefficients, J. Math. Phys. **3**, 566–578 (1962).

[108] S. Dolan, C. Doran, and A. Lasenby, Fermion scattering by a Schwarzschild black hole, Phys. Rev. **D74**, 064005 (2006).

[109] N. Andersson, Scattering of massless scalar waves by a Schwarzschild black hole: A Phase integral study, Phys. Rev. **D52**, 1808–1820 (1995).

[110] N. Andersson and K. D. Kokkotas, Gravitational waves and pulsating stars: What can we learn from future observations?, Phys. Rev. Lett. **77**, 4134–4137 (1996).

[111] H. A. Buchdahl, General relativistic fluid spheres, Phys. Rev. **116**, 1027 (1959).

[112] B. O'Neill, Semi-Riemannian Geometry With Applications to Relativity, Pure and Applied Mathematics (Elsevier Science, 1983).

[113] K. E. Thylwe and J. N. L. Connor, A complex angular momentum theory of modified coulomb scattering, J. Phys. A **18**, 2957–2973 (1985).

[114] P. O. Mazur and E. Mottola, Gravitational condensate stars: An alternative to black holes, arXiv:gr-qc/0109035 (2001).

[115] E. W. Mielke and F. E. Schunck, Boson stars: Early history and recent prospects, in Recent developments in theoretical and experimental general relativity, gravitation, and relativistic field theories. Proceedings, 8th Marcel Grossmann meeting, MG8, Jerusalem, Israel, June 22-27, 1997. Pts. A, B (1997), pp. 1607–1626.

[116] P. Pani, E. Berti, V. Cardoso, Y. Chen, and R. Norte, Gravitational wave signatures of the absence of an event horizon. I. Nonradial oscillations of a thin-shell gravastar, Phys. Rev. **D80**, 124047 (2009).

[117] M. Abramowitz and I. A. Stegun, Handbook of Mathematical Functions (Dover, New-York, 1965).

[118] N. Mott and H. Massey, The Theory of Atomic Collisions (Clarendon Press, 1949).

[119] V. P. Frolov and I. D. Novikov, Black Hole Physics: Basic Concepts and New Developments (Kluwer Academic Publishers, 1998).

[120] S. R. Dolan, Scattering, Absorption and Emission by Black Holes, PhD thesis (University of Cambridge, 2007).

[121] Y. Decanini, G. Esposito-Farese, and A. Folacci, Universality of high-energy absorption cross sections for black holes, Phys. Rev. **D83**, 044032 (2011).

[122] T. Regge and J. A. Wheeler, Stability of a Schwarzschild singularity, Phys. Rev. **108**, 1063–1069 (1957).

[123] S. A. Teukolsky, Perturbations of a rotating black hole. 1. Fundamental equations for gravitational electromagnetic and neutrino field perturbations, Astrophys. J. **185**, 635–647 (1973).

[124] R. H. Price and J. R. Ipser, Relation of gauge formalisms for pulsations of general-relativistic stellar models, Phys. Rev. **D44**, 307–313 (1991).

[125] S. Weinberg, Gravitation and Cosmology (John Wiley and Sons, New York, 1972).

[126] A. S. Eddington, The propagation of gravitational waves, Proc. Roy. Soc. Lond. **A102**, 268–282 (1922).

[127] L. Barack and C. O. Lousto, Perturbations of Schwarzschild black holes in the Lorenz gauge: Formulation and numerical implementation, Phys. Rev. **D72**, 104026 (2005).

[128] V. Moncrief, Gravitational perturbations of spherically symmetric systems. I. The exterior problem. Ann. Phys. New York **88**, 323–342 (1974).

[129] K. Martel, Particles and black holes: Time-domain integration of the equations of black-hole perturbation theory, PhD thesis (University of Guelph, 2004).

[130] J. A. Wheeler, Geons, Phys. Rev. **97**, 511–536 (1955).

[131] B. F. Schutz, A First Course in General Relativity (Cambridge University Press, 1985).

[132] K. Glampedakis, A. D. Johnson, and D. Kennefick, Darboux transformation in black hole perturbation theory, Phys. Rev. **D96**, 024036 (2017).

[133] G. Darboux, On a proposition relative to linear equations, CR Acad. Sci. Paris **94**, 1456–59 (1882).

[134] J. Bardeen and W. Press, Radiation fields in the Schwarzschild background, J. Math. Phys. **14**, 7–19 (1973).

[135] K. Glampedakis and G. Pappas, How well can ultracompact bodies imitate black hole ringdowns?, Phys. Rev. **D97**, 041502 (2018).

[136] U. H. Gerlach and U. K. Sengupta, Gauge invariant perturbations on most general spherically symmetric space-times, Phys. Rev. **D19**, 2268–2272 (1979).

[137] C. Gundlach and J. M. Martin-Garcia, Gauge invariant and coordinate independent perturbations of stellar collapse. 1. The Interior, Phys. Rev. **D61**, 084024 (2000).

[138] J. M. Martin-Garcia and C. Gundlach, Gauge invariant and coordinate independent perturbations of stellar collapse. 2. Matching to the exterior, Phys. Rev. **D64**, 024012 (2001).

[139] O. Sarbach and M. Tiglio, Gauge invariant perturbations of Schwarzschild black holes in horizon penetrating coordinates, Phys. Rev. **D64**, 084016 (2001).

[140] Y. Kojima, S. Yoshida, and T. Futamase, Nonradial pulsation of a boson star. 1: Formulation, Prog. Theor. Phys. **86**, 401–410 (1991).

[141] D. R. Yennie, D. G. Ravenhall, and R. N. Wilson, Phase-shift calculation of high-energy electron scattering, Phys. Rev. **95**, 500–512 (1954).

[142] J. Adam, The mathematical physics of rainbows and glories, Physics Reports **356**, 229–365 (2002).

[143] D. T. Khoa, W. von Oertzen, H. G. Bohlen, and S. Ohkubo, Nuclear rainbow scattering and nucleus-nucleus potential, J. Phys. G **G33**, R111 (2007).

[144] J. Jaeckel and A. Ringwald, The low-energy frontier of particle physics, Ann. Rev. Nucl. Part. Sci. **60**, 405–437 (2010).

[145] S. L. Shapiro and S. A. Teukolsky, Black Holes, White Dwarfs, and Neutron Stars: The Physics of Compact Objects (Wiley, 1983).

[146] K. Schwarzschild, Über das gravitationsfeld einer kugel aus inkompressibler flüssigkeit nach der Einsteinschen theorie, Sitzungsber. Preuss. Akad. Wiss., 424–434 (1916).

[147] D. Barraco and V. H. Hamity, Maximum mass of a spherically symmetric isotropic star, Phys. Rev. **D65**, 124028 (2002).

[148] A. Fujisawa, H. Saida, C.-M. Yoo, and Y. Nambu, Maximum mass of a barotropic spherical star, Class. Quant. Grav. **32**, 215028 (2015).

[149] R. L. Bowers and E. P. T. Liang, Anisotropic spheres in general relativity, Astrophys. J. **188**, 657–665 (1974).

[150] K. Yagi and N. Yunes, I-Love-Q relations: from compact stars to black holes, Class. Quant. Grav. **33**, 095005 (2016).

[151] B. P. Abbott et al., GW170817: Measurements of neutron star radii and equation of state, Phys. Rev. Lett. **121**, 161101 (2018).

[152] J. Antoniadis et al., A massive pulsar in a compact relativistic binary, Science **340**, 6131 (2013).

[153] M. Born and E. Wolf, Principles of Optics (Cambridge University Press, 1999).

[154] V. Perlick, Gravitational lensing from a spacetime perspective, Living Rev. Rel. **7**, 9 (2004).

[155] S. R. Dolan, Geometrical optics for scalar, electromagnetic and gravitational waves on curved spacetime, Int. J. Mod. Phys. **D27**, 1843010 (2017).

[156] M. V. Berry and K. E. Mount, Semiclassical approximations in wave mechanics, Rept. Prog. Phys. **35**, 315 (1972).

[157] C. M. Bender and S. A. Orszag, Advanced Mathematical Methods for Scientists and Engineers I: Asymptotic Methods and Perturbation Theory (Springer Science & Business Media, 2013).

[158] T. Koike and H. J. Silverstone, Rereading Langer's influential 1937 JWKB paper: the unnecessary Langer transformation; the two $\hbar$'s, J. Phys. A **42**, 495206 (2009).

[159] F. W. Olver, D. W. Lozier, R. F. Boisvert, and C. W. Clark, NIST Handbook of Mathematical Functions (Cambridge University Press, 2010).

[160] D. Batic, S. Nelson, and M. Nowakowski, Light on curved backgrounds, Phys. Rev. **D91**, 104015 (2015).

[161] F. Gesztesy and C. B. Lang, On the Abel summability of partial wave amplitudes for Coulomb-type interactions, eng, J. Math. Phys. **22**, 312–319 (1981).

[162] J. Alexandre and K. Clough, Black hole interference patterns in flavor oscillations, Phys. Rev. **D98**, 043004 (2018).

[163] C. F. B. Macedo, P. Pani, V. Cardoso, and L. C. B. Crispino, Astrophysical signatures of boson stars: quasinormal modes and inspiral resonances, Phys. Rev. **D88**, 064046 (2013).

[164] E. Maggio, A. Testa, S. Bhagwat, and P. Pani, Analytical model for gravitational-wave echoes from spinning remnants, Phys. Rev. **D100**, 064056 (2019).

[165] R. A. Hulse and J. H. Taylor, Discovery of a pulsar in a binary system. Astrophys. J. **195**, L51–L53 (1975).

[166] J. H. Taylor, L. A. Fowler, and P. M. McCulloch, Measurements of general relativistic effects in the binary pulsar PSR 1913+16, Nature **277**, 437–440 (1979).

[167] The Nobel Prize in Physics 1993, Press release, NobelPrize.org, Nobel Media AB (2020).

[168] GraceDB — Gravitational-wave candidate event database, https://gracedb.ligo.org/, Accessed: 2020-01-21.

[169] M. A. Sedda et al., The missing link in gravitational-wave astronomy: discoveries waiting in the decihertz range, (2019).

[170] P. J. Westervelt, Scattering of electromagnetic and gravitational waves by a static gravitational field - comparison between the classical (general-relativistic) and quantum field-theoretic results, Phys. Rev. **D3**, 2319–2324 (1971).

[171] P. C. Peters, Differential cross-sections for weak field gravitational scattering, Phys. Rev. **D13**, 775–777 (1976).

[172] W. Baade and F. Zwicky, On super-novae, PNAS **20**, 254–259 (1934).

[173] L. Rezzolla, E. R. Most, and L. R. Weih, Using gravitational-wave observations and quasi-universal relations to constrain the maximum mass of neutron stars, Astrophys. J. **852**, L25 (2018).

[174] F. Ozel and P. Freire, Masses, radii, and equation of state of neutron stars, Ann. Rev. Astron. Astrophys. **54**, 401 (2016).

[175] V. Ferrari, Gravitational waves from perturbed stars, Bull. Astron. Soc. India **39**, 203 (2011).

[176] E. Poisson, A Relativist's Toolkit: The Mathematics of Black-Hole Mechanics (Cambridge University Press, 2009).

[177] T. Stratton, L. C. Leite, S. R. Dolan, and L. C. Crispino, Series reduction method for scattering of planar waves by Kerr black holes, Phys. Rev. D **102**, 044025 (2020).

[178] B. P. Abbott et al., Searches for gravitational waves from known pulsars at two harmonics in 2015-2017 LIGO data, Astrophys. J. **879**, 10 (2019).

[179] B. P. Abbott et al., Narrow-band search for gravitational waves from known pulsars using the second LIGO observing run, Phys. Rev. **D99**, 122002 (2019).

[180] M. V. Berry, Tsunami asymptotics, New J. Phys. **7**, 129 (2005).

[181] M. V. Berry, Focused tsunami waves, Proc. R. Soc. A. **463**, 3055–3071 (2007).

[182] B. Abbott et al., GW190425: Observation of a compact binary coalescence with total mass $\sim 3.4 M_\odot$, Astrophys. J. Lett. **892**, L3 (2020).

[183] V. Cardoso, L. C. Crispino, C. F. Macedo, H. Okawa, and P. Pani, Light rings as observational evidence for event horizons: long-lived modes, ergoregions and nonlinear instabilities of ultracompact objects, Phys. Rev. **D90**, 044069 (2014).

[184] A. Maselli, P. Pani, V. Cardoso, T. Abdelsalhin, L. Gualtieri, and V. Ferrari, Probing Planckian corrections at the horizon scale with LISA binaries, Phys. Rev. Lett. **120**, 081101 (2018).

[185] Z. Mark, A. Zimmerman, S. M. Du, and Y. Chen, A recipe for echoes from exotic compact objects, Phys. Rev. **D96**, 084002 (2017).

[186] R. S. Conklin, B. Holdom, and J. Ren, Gravitational wave echoes through new windows, Phys. Rev. **D98**, 044021 (2018).

[187] J. Westerweck, A. Nielsen, O. Fischer-Birnholtz, M. Cabero, C. Capano, T. Dent, B. Krishnan, G. Meadors, and A. H. Nitz, Low significance of evidence for black hole echoes in gravitational wave data, Phys. Rev. **D97**, 124037 (2018).

[188] G. Ashton, O. Birnholtz, M. Cabero, C. Capano, T. Dent, B. Krishnan, G. D. Meadors, A. B. Nielsen, A. Nitz, and J. Westerweck, Comments on: ”Echoes from the abyss: evidence for Planck-scale structure at black hole horizons”, arXiv:1612.05625 (2016).

[189] M. Saravani, N. Afshordi, and R. B. Mann, Empty black holes, firewalls, and the origin of Bekenstein–Hawking entropy, Int. J. Mod. Phys. **D23**, 1443007 (2015).

[190] V. Cardoso and P. Pani, Testing the nature of dark compact objects: a status report, Living Rev. Rel. **22**, 4 (2019).

[191] H. Nariai, On some static solutions of Einstein's gravitational field equations in a spherically symmetric case, Sci. Rep. Tohoku Univ. Eighth Ser. **34** (1950).

[192] E. Maggio, P. Pani, and V. Ferrari, Exotic Compact Objects and How to Quench their Ergoregion Instability, Phys. Rev. **D96**, 104047 (2017).

[193] P. P. Fiziev, Exact solutions of Regge-Wheeler equation and quasinormal modes of compact objects, Class. Quant. Grav. **23**, 2447–2468 (2006).

[194] M.-E. Brandan and G. Satchler, The interaction between light heavy-ions and what it tells us, Phys. Rep. **285**, 143–243 (1997).

[195] S. Gillessen, F. Eisenhauer, S. Trippe, T. Alexander, R. Genzel, F. Martins, and T. Ott, Monitoring stellar orbits around the massive black hole in the galactic center, Astrophys. J. **692**, 1075–1109 (2009).

[196] S. W. Hawking, Particle creation by black holes, Commun. Math. Phys. **43**, 199–220 (1975).

[197] E. W. Leaver, An Analytic representation for the quasi normal modes of Kerr black holes, Proc. Roy. Soc. Lond. **A402**, 285–298 (1985).

[198] K. D. Kokkotas and B. F. Schutz, W-modes: a new family of normal modes of pulsating relativistic stars, Mon. Not. Roy. Astron. Soc. **255**, 119 (1992).

[199] A. Folacci and M. Ould El Hadj, Alternative description of gravitational radiation from black holes based on the Regge poles of the $\mathcal{S}$-matrix and the associated residues, Phys. Rev. **D98**, 064052 (2018).

[200] Y. Decanini and A. Folacci, Regge poles of the Schwarzschild black hole: A WKB approach, Phys. Rev. **D81**, 024031 (2010).

[201] Y. Decanini, A. Folacci, and B. Raffaelli, Unstable circular null geodesics of static spherically symmetric black holes, Regge poles and quasinormal frequencies, Phys. Rev. **D81**, 104039 (2010).

[202] Y. Decanini, A. Folacci, and B. Raffaelli, Resonance and absorption spectra of the Schwarzschild black hole for massive scalar perturbations: A complex angular momentum analysis, Phys. Rev. **D84**, 084035 (2011).

[203] G. Jaffé, Zur theorie des wasserstoffmolekülions, Z. Phys. **87**, 535–544 (1934).

[204] E. W. Leaver, Quasinormal modes of Reissner-Nordstrom black holes, Phys. Rev. **D41**, 2986–2997 (1990).

[205] B. Majumdar and N. Panchapakesan, Schwarzschild black-hole normal modes using the Hill determinant, Phys. Rev. **D40**, 2568 (1989).

[206] M. Leins, H. P. Nollert, and M. H. Soffel, Nonradial oscillations of neutron stars: A new branch of strongly damped normal modes, Phys. Rev. **D48**, 3467–3472 (1993).

[207] O. Benhar, E. Berti, and V. Ferrari, The imprint of the equation of state on the axial w-modes of oscillating neutron stars, Mon. Not. Roy. Astron. Soc. **310**, 797–803 (1999).

[208] M. Ould El Hadj, Radiation from black holes interacting with massive bosonic fields, PhD thesis (Université de Corse Pasquale Paoli, 2016).

[209] S. R. Dolan and A. C. Ottewill, On an expansion method for black hole quasinormal modes and Regge poles, Class. Quant. Grav. **26**, 225003 (2009).

[210] Y. J. Zhang, J. Wu, and P. T. Leung, High-frequency behavior of w-mode pulsations of compact stars, Phys. Rev. **D83**, 064012 (2011).

[211] M. V. Berry, Semiclassically weak reflections above analytic and non-analytic potential barriers, J. Phys. A **15**, 3693 (1982).

[212] G. Mie, Beiträge zur optik trüber medien, speziell kolloidaler metallösungen, Ann. Phys. Berlin **330**, 377–445 (1908).

[213] H. A. Priestley, Introduction to Complex Analysis (Oxford University Publications, Oxford, 2003).

[214] J. N. Goldberg, A. J. MacFarlane, E. T. Newman, F. Rohrlich, and E. C. G. Sudarshan, Spin-s spherical harmonics and ð, J. Math. Phys. **8**, 2155 (1967).